OPTICAL POLARISATION THEORY IN THE INTERPRETATION OF SS433

by

Vivette Ann Carlaw

Thesis

submitted to the

University of Glasgow

for the degree of

Ph.D.

Department of Physics and Astronomy

University of Glasgow

Glasgow G12 8QW

August 1988

To my mother, who is also one of my closest friends, and to John Montgomery, who has given me the purpose and the strength to finish.

∿ ∿ ∿ ∿ ∿

SUMMARY

Since the discovery of the two systems of moving emission lines in the optical spectrum of SS433, this peculiar object has stimulated intense study and speculation. A generally accepted dynamical model for the binary system comprises an early-type supergiant and a compact object surrounded by a precessing thick accretion disk along the axis of which are ejected two opposing, mildly relativistic, collimated jets. The polarisation of the system, providing information into the distribution of matter in the system is, therefore, a valuable test for this model. Hence, in this thesis, we consider the theory of optically thin, Thomson scattering polarisation and model the observed polarisation of SS433 in order to provide further independent constraints on the dynamical model.

The introductory section of this thesis is contained in the first two chapters. Chapter 1 is a review of the observations that have been made of SS433 as well as a description of the basic kinematic model and its development to the present dynamical model. In Chapter 2, we review the constraints on the system imposed by the observations, and the physica problems which arise from the observations and dynamical model.

In Chapter 3, we develop the theory of Thomson electron scattering polarisation in the optically thin limit. The simple case of a point light source is extended to allow for arbitrary source shapes, the effect of which can be expressed as a 'depolarisation factor'. This factor is found explicitly in the two relevant special cases viz. a spherical (stellar) source and a luminous (accretion) disk source. The equations for the normalised Stokes Parameters for a general coro-

tating scattering region in a binary system are then derived.

A simple geometrical model for the polarisation of SS433 is developed in Chapter 4, including the effect of spherical light sources. Although this model has many limitations, they are either not important to the polarisation or can be compensated for by smoothing the data, particularly if only the precession variation is studied and the size and orbital phasing of the data set permit those data points taken during eclipses to be omitted. Finally, we predict the broad characteristics of the polarisation, such as the expected dominant frequency in the data, based on this model.

In Chapter 5, we analyse the presently available polarisation data of SS433 which span $3\frac{1}{2}$ years of observations. The power spectra of both the observed Q and U Stokes Parameters clearly show the precession period and its first harmonic, as expected from the previous chapter, but no other periods show above the noise. We, therefore, develop an optimisation procedure to fit a simple, precession only models to the data and compare the results of this procedure with others. Finally, we attempt to fit a model including the binary/orbital effects to the data using the best-fit parameter values of the precession only model, thereby reducing the number of free parameters. A significant reduction in the χ^2 parameter is found if only the first harmonic of the orbital period is added to the precession model. No reduction in χ^2 is found when the full model developed in Chapter 4 is fitted to the data.

Chapter 6 investigates the dust grain model developed by Ramaty et al., (1984), to explain the narrow gamma-ray lines claimed to be observed from SS433. Although this model could, in principle, produce

narrow gamma-ray lines, as it is presented by Ramaty et al., it is neither self-consistent nor consistent with the observations at other wavelengths. In particular, the process which produces the gamma-rays is highly inefficient and the grains must, therefore radiate the waste energy deposited in them. This implies an IR flux from SS433 many orders of magnitude greater than observed. Moreover, the restrictions on the dimensions of the emitting region and the small observed polarisation imply that the emitting region must be optically thick in grains and, therefore, that the temperature of the grains would, in fact, be too high for them to survive.

Chapter 7 concludes the thesis with a reprise of the conclusions and suggestions for future work arising from the detailed investigations presented here.

PREFACE

This thesis is concerned primarily with modelling the optical polarisation of SS433. In connection with this, the theory of optically thin polarisation due to Thomson or Rayleigh scattering is adapted to include the effect of an arbitrary source geometry (Chapter 3) and, specifically, the equations in the special cases of a spherically symmetric source and a thin luminous disc are shown to be simply the point source expressions with the electron density distribution weighted by a geometric factor depending purely on the angular radius of the source as seen from the scattering point. Then a simple geometric model for the binary system is developed (Chapter 4) and used in the analysis of the available data (Chapter 5). While the precession period is clearly present in the polarisation data and the inclination angle and precession cone angle can be determined, the data set is too small and too subject to noise to yield accurate parameter values or determine the importance of other effects such as light scattered from the companion star.

The work of Chapter 6, which was carried out in cooperation with Profs. J.C. Brown and V. Icke and Dr. T.V. Cawthorne, is concerned with one of the models for the narrow gamma-ray lines reported from SS433. This model depends on the existence of a large mass of dust grains in the jets of SS433, and the presence of such grains would have important implications for the observed optical polarisation. Hence it is necessary to investigate rigourously whether such grains can indeed survive in the physical conditions of SS433.

The lengthy introduction to the thesis (Chapters 1 and 2) reflects the many different questions posed by this peculiar object, not least of which is: Is SS433 a miniature AGN? While the optical polarisation

should help the understanding of it, the many mysteries of this system are likely to keep Astronomers happily employed for many years to come.

The work of this thesis was begun in the Department of Astronomy. University of Glasgow, and continued through the merger of the Natural Philosophy and Astronomy Departments to form the Department of Physics and Astronomy. I am grateful that I have been able to carry out this research during the headship of Prof. A. E. Roy in a group which is, I believe, unparalleled for its combination of intellectual skill and human warmth and fun. My thanks go especially to my supervisor, Prof. J. C. Brown who has provided the guidance and moral support I needed, despite the vigorous attempts to paperwork and red-tape to smother him. My thanks go also to Dr. Alan Thomson for his invaluable aid in the continual battle to persuade the computers to cooperate; to Prof. Vincent Icke (Leiden), a colleague and friend with whom the work of Chapter 6 was done; and to Prof. P.A. Sweet, a true gentleman and a scholar, for his patience and stimulating discussions.

I am grateful also to Mrs. Williamson who typed this manuscript. While word-processors are available, she has provided the same efficiency and accuracy (or better, considering my own spelling ability) with that human touch. Financial support was provided for three and a half years by a University of Glasgow fellowship, and I am particularly grateful for the six month extension on the initial three year grant. Computing facilities have been provided by the University of Glasgow Computing Services.

Finally, my thanks to all those with whom I have played badminton or gone swimming over the years and particularly to Cary, Liz, Lorna and Margo, the other members of the Queen's Park Baptist Church Dance

Group with whom I have found deep friendship and fulfilment and who have helped to balance the intense intellectual pursuits and pressures of scientific research. Last but not least, I am indebted to Saki, Pinkle and Bogart, who in their feline way have helped to keep me human.

C O N T E N T S

CHAPTER 1

INTRODUCTION TO SS433

1.1 Introduction

SS433, also known as V1343 Aquilae, is a much studied peculiar binary system. Although it was recognised as an object of interest only a decade ago, the intense study and speculation it has stimulated has resulted in a phenomenal volume of published work. Despite the progress that has been made in understanding, it is still surrounded by controversy. In this chapter, we will review briefly how it came to prominence, the basic observations at each wavelength, the most generally accepted model and how it has been developed, and the part the optical polarisation can play in aiding our understanding of this object. Considering the number of papers already published (well into 3 figures), a comprehensive review of the observations and related theory is not possible. We shall therefore, focus only on the highlights and attempt to provide a set of references which can form the basis of a more detailed study into any particular aspect.

SS433 is the most popular and commonly recognised name for this binary system. It derives from the Stephenson-Sanduleak catalogue published in 1977 of strong H_α emission line objects where it made one of its earliest appearances, not surprisingly as number 433. It was independently observed at radio wavelengths (Clark et al. 1975) and in X-rays (Seward et al., 1976), but it was not until a few years later that it was proposed that these sources were in fact the same object (Clark and Murdin, 1978; Seaquist et al., 1979), the former also suggesting an association with the SNR W50. At the same time, the first moderate-resolution spectral data were presented and these

revealed the complexity of SS433.

Quite apart from the strong H_α emission line which led to its inclusion in the Stephenson-Sanduleak catalogue and the accompanying Balmer and HeI lines, SS433 displays a number of prominent, broad emission line features at unfamiliar wavelengths. The typical width of these lines is $\sim 100\text{Å}$ (Margon et al., 1979b). These have been identified as being due to two distinct sets of Doppler-shifted Balmer and HeI lines, one with a huge redshift, the other with a large blueshift. (Figure 1). The Doppler shift of these sets of lines is not constant (Figure 2). They drift through the spectrum by up to 1000 Å in a smooth periodic fashion (Margon et al., 1979 a) & b), Mammano, Ciatti and Vittone, 1980). The maximum redshift is about 50,000 kms^{-1}, the maximum blueshift 30,000 kms^{-1}, while the period of change in λ hovers around 162 days (Margon et al.,(1979a), Anderson, Margon and Grandi,(1983b), see Figure 3). The mean velocity of the red and blue-shifted systems remains approximately constant at 12,000 kms^{-1} which should be compared with the true radial velocity of the system of ~ 70 kms^{-1} as measured from, for example, the 'rest wavelength' Balmer and HeI emission lines (Crampton, Cowley and Hutchings, 1980). It was these unique moving lines which stimulated the interest in SS433.

1.1.1 The Simple Kinematic Model

A number of different models have been proposed for SS433. As Milgrom (1981) points out in his review, all of them have to assume that both the gravitational redshift and $|\underset{\sim}{v}|$, where $\underset{\sim}{v}$ is the velocity of the line-emitting gas, are constant with time to a high degree. The observed changes in wavelength are then attributed to changes in the angle

between $\underset{\sim}{v}$ and the line of sight, due, in most models, to some sort of rotation of the system about a fixed axis. There are 3 basic geometrical configurations, leading to 3 physically different sets of models. These are (Figure 4). a) Radial infall

b) Keplerian motion

c) Radially outflowing opposite beams.

It should be noted that many models in classes (a) and (b) require a central black hole of mass $M \gtrsim 10^6 M_\odot$ to give the observed redshifts. Also, while all 3 classes are compatible with the optical observations both radio (Section 1.3) and X-ray (Section 1.4) observations indicate the presence of outwardly flowing jets. Hence the present preferred model belongs to class(c).

This model has its origins in two of the earliest theoretical papers on SS433 viz Fabian and Rees, 1979, and Milgrom, 1979. Both proposed collimated oppositely ejected jets while the latter also suggested that a periodic rotation of the jet axis could produce the velocity modulation. With the aid of a larger data set, Abell and Margon, 1979 were able to elaborate the Milgrom model. The free parameter values they derived are essentially the same as those presently in use and they predicted the cross-over of the red-and blue-shifted systems which was subsequently observed by Bedogni et al., 1980 and Margon, Grandi and Downes, 1980.

The kinematic model hypothesis is that matter is ejected in two jets that are collimated and oppositely aligned to within a few degrees. The terminal jet velocity is a free parameter, the value of which has remained constant at 0.26 c to within 5% (Milgrom 1981, cf. also Figure 3). The jet axis rotates with a period of $\sim$ 162 days. The inclination of the central axis of the rotation cone and the half angle of this cone are

79^{o} and 20^{o}, although the optical model alone does not distinguish between these angles (cf. discussion of radio observation in section 1.3). The 12,000 kms^{-1} mean value for the Doppler shifts is caused by the second order, transverse, or 'time-dilation' redshift due to the mildly relativistic velocity of the jets. Although the model was first developed primarily to explain the optical doppler-shifted lines, both radio (eg. Gilmore et al., 1981; Hjellming and Johnston 1981 (a) and (b)) and X-ray (e.g. Seward et al., 1980; Watson et al., 1983) imaging observations now provide strong support for the geometry and kinematics of the jet model.

The model, however, leaves unspecified almost all of the physical aspects of the system such as the mechanisms that power, accelerate and collimate the jets and the nature of the underlying star(s). It is simply a convenient device for understanding and predicting the kinematics of the ejected jets. It has, however, formed the basis for most of the theoretical work that has been done on SS433.

Simple source rotation as the cause of the change in the direction of the jet axis has been ruled out since the inferred kinetic energy of the jets is far in excess of the rotational energy of a compact object with such a long period so that rotation would rapidly die out (Abell and Margon, 1979; Katz, 1980). Precession is the most popular mechanism (e.g. Katz, 1980; van den Heuval, Ostriker and Petterson, 1980). To drive the precession and to provide a source of matter to supply the jets and produce the X-ray emission, a close binary system was proposed, and confirmed by the discovery of a 13-day variation in the radial velocity of the'stationary' emission lines (Crampton, Cowley and Hutchings, 1980; Crampton and Hutchings, 1981). The analogy with X-ray binary systems

led to the proposal that an accretion disk be present. To supply the jet mass and energy, substantial mass transfer must occur in the system and a reasonably large object must exist to be precession torqued. Now, it is assumed usually that the primary star precesses and communicates its motion to the jets through a slaved accretion disc. Such a disc also provides a natural symmetry plane to help explain the opposed alignment of the jets. A number of observations now confirm its presence.

As the data base increased, it became clear that higher frequencies were present in the radial velocity variations. Since the orbital period is not negligible compared to the precession period, beat frequencies were not unexpected. The dominant short period superposed on the precession period is $\sim$ 6.28 days, with an amplitude 5-10% of that of the precession period. This period is interpreted as nutation, or a nodding motion of the disk (Katz et al., 1982; Matese and Whitmire 1982; Collins and Newsom 1986). This disk motion is presumed to be reflected in the orientation of the jets, the jets being somehow constrained to follow the disk normal. (This is a model dependent interpretation.)

The precessing disk/jet model has continued to be modified and expanded as observations at many wavelengths have provided more information on the system. By no means all of the physical problems posed by SS433 have been solved, there being still some dispute over even the basic interpretation of the Doppler-shifted lines (e.g. Kundt, 1985, 1987). Before looking at the physical problems, however, we shall review the observations at each wavelength.

1.1.2 Basic Data

The optical source known as SS433 has coordinates $\alpha(1950) = 19^h09^m 21.282^s \pm 0.003^s$, $\delta(1950) = 04^\circ53'54.04'' \pm 0.05''$, epoch of 1980.

Within measurement uncertainties, the position coincides with the compact radio source associated with SS433. The corresponding galactic coordinates are $\ell = 39.7^{o}$, $b = -2.2^{o}$ (Margon, 1984). The proper motion has not been detected optically, so far (Margon et al., 1979a). The distance to SS433 from 21 cm absorption studies (van Gorkom et al., 1982) is in the range 3.7-4.7 kpc while radio observations of the time variable jet structure give a model dependent estimate of 5 kpc (± 0.5 kpc) (Hjellming and Johnstone, 1981a).

Typical optical magnitudes and colours are V = 14.2, (B-V) = 2.1 and (U-B) = 0.6; typical radio flux densities for the central point plus the extended sources are 1Jy at 11 and 20 cm, 0.5Jy at 3.7 and 6 cm and 0.2Jy at 2 cm; the X-ray flux is 5μJy in the 2-10 keV range. (Margon 1984 and references therein). The source, however, shows extensive periodic and aperidoc variations in all these wavelength regions. The estimated bolometric luminosity is $\sim 10^{39}$ erg s^{-1} (Wagner, 1986).

The binary orbital period is 13.081 ± 0.003 days and the precession period is 162.5 ± 0.25 days (Kemp et al., 1986). However, the precession period does show significant instability (Anderson, Margon and Grandi, 1983b).

1.2 Optical and Infrared Observations

1.2.1 Doppler Shifted Spectral Lines

The 'moving' lines have been observed by 2 main groups: Mammano, Ciatti and colleagues at Asiago and Margon and colleagues plus a number of independent observers (see Collins and Newsom, 1986 and refs. therein). In the optical region Balmer and HeI lines are observed, while Pashen

and Brackett lines are observed in the IR (Allen 1979, McAlay and McLaren 1980). No HeII lines have been observed in Doppler shifted sets, although these are present in the stationary spectrum which must be a clue to jet excitation processes. No heavy element shifted lines have been observed in the optical/IR range, though this is probably due to lack of sensitivity since the strength of the HeI features is consistent with a normal H/He ratio. The shifted lines are unpolarised (Liebert et al., 1979). Figure 1 gives an example of an optical spectrum.

Photographic plates do not show these lines well because of their breadth and irregularity. However, modern spectrophotometric devices give good results. The moving lines have a typical base width of a few thousand kms^{-1} while the profiles range from almost perfectly Gaussian (Margon et al., 1984) to highly complex (Margon et al., 1979a); Margon, Grandi and Dowdes 1980; Murdin, Clark and Martin 1980). All the lines in one jet, however, have the same profile at a given time. Sometimes the red and blue lines are mirror images, but this is not always the case (Margon et al., 1979 (a) and (b)). The velocity structure of the lines can change on a timescale of days as can the intensity which is typically a third of the unshifted lines. The moving lines can disappear completely in 10-24 hrs and reappear just as quickly. The profile symmetry and disappearance/reappearance episodes are synchronised in the red and blue-shifted systems with a time delay less than 1 day, implying that less than 10^2 AU separates the two radiating regions (Margon et al., 1984) which is comparable to the length of each optically radiating jet as inferred from the brightness temperature (Davidson and McCray 1980). While the moving lines can be absent for a few days there is no evidence for periods of months when these lines are missing.

In some series of spectra, the lines do not seem to move as a unit. Rather, each line seems to be made up of smaller, narrower lines which do not change their position but increase and decrease in intensity in sequence. This has been described in terms of 'shadows' or 'bullets' (Margon et al., 1979b); Murdin, Clark and Martin 1980) implying that the jets are not continuous smooth streams (cf. also radio observations). This effect is not always observed.

Assuming a distance $d \gtrsim 3.5$ kpc and a value of $E_{B-V} \gtrsim 1.4$ for the reddening of SS433, Begelman et al., (1980) estimated the H_α luminosity of each beam to be $\sim 5 \times 10^{34}$ $(d/3.5 \text{ kpc})^2$ ergs^{-1} (cf. also Davidson and McCray, 1980). Further, they propose that the emission lines are excited by the interaction of the beams with the ambient gas. This gives a lower limit on the kinetic luminosity of the jets as $\sim 10^{40}$ $(d/3.5 \text{ kpc})^{\frac{1}{2}}$ erg s^{-1}, assuming an opening angle of 0.1 radians for the beams and that 10% of the absorbed energy is emitted in H_α. Various estimates for the jet kinetic luminosity range from 10^{36} to 10^{42} erg s^{-1} for mass loss rates in the region 5×10^{-10} to 5×10^{-4} $M_\odot$ yr^{-1} (Watson et al., 1983) with the upper end of the range preferred. This is comparable with the energy needed to distort the shape of W50 (Begelman et al., 1980).

1.2.2 The Stationary Spectrum

This is the set of emission and absorption lines which do not share the large periodic Doppler shifts. These lines are imposed on an extremely red continuum, probably due to interstellar extinction (see below). The spectrum is dominated by intense, broad Balmer and He I emission lines. Most of those who have studied the moving lines have also studied the

stationary component.

The Balmer emission lines are highly variable in equivalent width and, probably, absolute intensity both periodically and aperiodically (Anderson, Margon and Grandi 1983a; Falomo et al., 1987). The latter also show that the line profiles are complex and variable on time-scales as short as 15 mins. The spectrum also displays HeII λ 4686 and λ10,124 emission and the CIII/NIII λ6640-50 emission blend which is attributed in X-ray sources to the Bowen fluorescence mechanism (McClintock Canizares and Tartar, 1975). OI λ 8446 emission is also prominent. Its strength indicates that it may also be due to some preferential emission process such as Lβ fluorescence.

In 1980, Crampton, Cowley and Hutchings reported a 13.1 day periodic variation in the wavelength of the H emission lines which led naturally to binary system models for SS433. The initial mass function from the H emission lines was 0.5 $M_\odot$ which led to models with mass ratios about unity, containing a low mass unseen secondary since the large majority of bright galactic X-ray sources contain neutron stars of 1 $M_\odot$. However, Crampton and Hutchings, 1981 showed that the HeII λ4686 emission line has periodic variations also of 13.1 days but with a substantially different amplitude and phase to the Balmer emission. If this variation indicates the true system orbit, the mass function is 11 $M_\odot$, which necessitates a massive early-type companion.

Since in other X-ray binaries the HeII emission originates from the immediate vicinity of the compact object and since the orbital motion of the H emission occasionally becomes undetectable, Crampton and Hutchings, (1981) argue that the HeII variation shows the true radial velocity curve. This is confirmed by both photometry and the disk 'nodding' motions.

Neglecting the interstellar absorption lines, the spectrum is deficient in absorption features. However, the HeI and Balmer lines do show weak but significant P-Cygni absorption wings. These are more prominent in HeI but the strong Balmer emission may mask strong absorption. The only other prominent absorption features are of very low excitation viz. FeII λ5159 and OI λ7773. These features are highly variable in intensity but can be quite strong Margon et al., 1979(b). Weaker FeII lines in the same multiplet have been reported (Crampton, Cowley and Hutchings, 1980). Such absorption features are often seen in A-F supergiants and shell stars. The FeII absorption equivalent width is phase dependent on the precession (Margon, 1984 and references therein). The maximum absorption strength occurs when the moving lines are near equal Doppler shift, i.e. the time when the accretion disk would be edge on. Therefore, the lines could come from cool matter in the disk or reflect the photometric variation of the disk.

Even without the moving lines the spectrum is unique. The broad emission lines are like systems dominated by accretion disks but there are also features in common with certain early-type stars undergoing considerable mass-loss. There is, therefore, an ongoing debate as to how much each object contributes to the total light of the system.

1.2.3 Interstellar Lines and Extinction

As can be seen even by eye from photographs, the extinction in the region about SS433 is large and patchy. Hence methods which determine the reddening very near to or coincident with the star clearly are preferred, although as many independent estimates as possible should be made.

The prominent interstellar lines and bands which appear in the spectrum confirm that most, or all, of the redness of the continuum must be due to extinction. Among the strong features are the 4430, 5778/80 and 6284 Å diffuse interstellar bands and Ca H, K and Na D (Margon et al., 1979a); Murdin, Clark and Martin, 1980). Numerous weak features are also present.

The reddening can be estimated from the correlation of extinction with the equivalent width of the interstellar features (Clark and Murdin, 1978; Margon et al., 1979(a); Murdin, Clark and Martin, 1980). However, such relations are known to have large scatter and so this method has limited reliability. Decrements in the emission spectrum of the optical filaments of W50 (Kirshner and Chevalier, 1980; Murdin and Clark 1980) provide another estimate, but filaments bright enough for spectroscopy are not close to SS433 which introduces uncertainty. Studies of the extinction of stars near the field have similar difficulties (Crampton, Cowley and Hutchings, 1980). The low energy turnover in the X-ray spectrum gives information on the reddening (Marshall et al., 1979; Seaquist et al., 1982) but this is convolved with the uncertain intrinsic source spectral shape and possible circumstellar X-ray opacity. Infrared spectrophotometry, giving a comparison of Brackett to Balmer emission-line ratios should be reasonably accurate unless QSO complications are applicable to SS433 (Thomson et al., 1979; McAlary and McLaren, 1980). Finally, the continuum slope can be fitted by a combination of underlying spectral type, reddening laws, reddening magnitudes and variable amounts of light of variable spectral slope from, for example the accretion disk. This may be the most sophisticated approach but it also has most free parameters. Margon, 1984 recommends using $A_V \simeq 8$ mag. Most of the above methods give results which are compatible with this figure.

1.2.4 Photometry

Both broadband and narrowband work has been reported on SS433 (for references see Margon 1984, Kemp et al., 1986). The object is variable on virtually all timescales observed except 0.1 ms to 1s. Most of the variation is due to genuine continuum variations and not to the moving spectral lines passing through the bandpass. The precession period and the orbital period with its first harmonic are clearly seen (Mazeh et al., 1987). The precession light curve depends significantly on the orbital phase (Kemp et al., 1986, Fig.4) but the shape seems to require a geometrically thick disk. The orbital light curve indicates mutual eclipses of the companion star and accretion disk (Kemp et al., and references therein). The primary minimum of the 13 day variation agrees with the phase of maximum positive radial velocity of the 'stationary' Balmer emission lines. This is taken as orbital phase 0. Joint optical and X-ray observations (Stewart et al., 1986) show that the 13 day X-ray light curve has a minimum at orbital phase 0. Since the X-ray source is partially obscured at this phase, the primary minimum corresponds to the eclipse of the disk by the (darker) star. The zero phase of the 6.3 day 'nodding motion' of the Doppler-shifted lines (Katz et al., 1982) is offset from the primary minimum by $\sim$0.25 in orbital phase, exactly the same as the offset of the HeII emission line variation from the Balmer. Since the 'nodding motion' must originate from the vicinity of the compact object the HeII emission must reflect the true orbital motion. Hence the true mass function must be 11 $M_{\odot}$.

The 6.28 day 'nodding motion' of the disk also appears in the photometry, being the strongest beat frequency. The ratio of the amplitude of the 6.28 to 162 day photometric variations is $^{1}/3$, $\sim$ 5 times the

corresponding ratio of the radial velocity variations (Mazeh et al., 1987). There is also a phase delay of about 1 day between the photometric and radial velocity maxima. Both these last effects can be explained by the way in which the nodding motion is transmitted from the outer to the inner rings of the disk. (Katz et al., 1982; Matese and Whitmire, 1982; Collins and Newsom, 1986).

Infrared photometry of SS433 has been reported by a number of observers (Kodaira, Nakada and Backman, 1985 and references therein). The infrared light curve for the precession period is similar to the optical curve and is consistent with light modulations due to the changing aspect of a precessing accretion disk. The eclipses seen in the orbital infrared light curve also indicate that the disk is the more luminous source. Evidence for short timescale fluctuations in the infrared on timescales from days down to at least 10 minutes have also been reported (Kodaira and Lenzen, 1983; Kodaira, Nakada and Backman, 1985).

1.2.5 Polarisation

Initial attempts to detect polarised radiation from SS433 were unsuccessful. Liebert et al., 1979 found no circular polarisation in red light while Thompson et al., 1979 found $p = 0.1\%$ in the infrared. Other observers reported linear polarisation of 3 to 4 percent but attributed it mostly to interstellar polarisation. However, more accurate measurements by McLean and Tapia (1980) revealed time variation which implied that at least part of the observed linear polarisation is intrinsic to the source. Further observations strongly suggest that the precession period was present in the data (McLean and Tapia, 1981)

and allowed for the first analysis of the data using simple optically thin electron scattering models. McLean and Tapia (1981) found that the data were compatible with jet scattering models of high inclination ($55^{o} \sim i \sim 80^{o}$) and with disk or ring scattering for $i > 50^{o}$. However, the data set was still too small to determine free parameters with any significance.

Efimov, Piirola and Shakhovskoy (1984) have also observed the linear polarisation of SS433 in a number of wavebands and they confirm the presence of the first and second harmonics of the precession period, the first harmonic being dominant. They also found that, in the R and I wavelength region, the mechanism producing the changing polarisation is nearly wavelength independent and that a significant part of this polarisation is due to scattering from matter concentrated towards the orbital plane. They also suggested that the strong first harmonic of the precession period could be due partly to variations in the direct unpolarised light.

The polarisation can provide information on the scattering geometry and mechanism (cf. Brown et al., 1978). Hence analysis of the polarimetric data may be useful in distinguishing between the various models proposed for SS433. In particular, fitting a polarisation model based on the jet/disc binary system model discussed in Section 1.1.1 to the data should provide independent confirmation of various system parameters such as the inclination of the system and the precession cone angle. (See Chapters 4 and 5).

1.3 Radio Observations

1.3.1 Central Source

SS433 has been observed at radio wavelengths by a large variety of

techniques at many frequencies. It was probably first observed by Gower, Scott and Wills (1967), the positional discrepancy almost certainly due to confusion in the crowded region. The positional coincidence between the optical object and the radio source is now known to be less than 0.2" (Kaplan et al., 1980; Hjellming and Johnstone, 1981a)). The central source has been observed at frequencies from 160 MHz to at least 22 GHz. The typical spectral index at higher frequencies is $\sim$0.6, which is common for non-thermal sources (Seaquist, 1981; Hjellming and Johnstone, 1982). Seaquist et al., (1982) give a spectrum obtained simultaneously over a broad range of frequencies. They show that the spectrum flattens and probably turns over at frequencies below 300 MHz.

The central source intensity is highly variable by at least a factor of 4 at virtually all wavelengths on timescales as rapid as a day and, occasionally hours (eg. Ryle et al., 1978; Heeshen and Hammond, 1980; Seaquist, 1981; Johnston et al., 1981, 1984). From VLBI observations (Geldzahler, Downes and Shaffer, 1981), there is evidence that $\sim$ 5 mas is a lower limit to the angular size of the central radio-emitting source, at 10.65 GHz at least. This angular size corresponds to $\sim$20 AU at 5 kpc (the distance of SS433), and so more rapid variability at these high frequencies is not expected. No analog to the orbital period has been found. However, Bonsignori-Facondi and Braccesi, 1986 report a modulation of a component of the 408 MHz flux density with the precession period. This component also displays short timescale variability and a high brightness temperature implying that the source has a small size and is a coherent radiator. The source size and the precession modulation of the emission place the source in the centre of the accretion disk. From the location and type of source, this component would seem to be direct

evidence for the compact object. Bonsignori-Facondi et al., (1986) studied flaring episodes at 408 MHz. While these showed no relation to either the orbital or the precession periods, the one-day flare activity and one minute variations were correlated possibly with the precession period.

Simultaneous radio and optical observations (Neizvestnyi, Pustilnik and Efremov, 1980; Ciatti et al., 1981) show the possiblity of correlated behaviour between the two wavebands but chaotic variations at both wavelengths and possible time delays between the optical and radio variations make interpretation of the data difficult. The evidence for correlation between X-rays and radio is inconclusive since, of the two occasions when simultaneous observations were made, one gave evidence for correlated behaviour while the other did not (Seaquist et al., 1982).

1.3.2 Extended Components

It became clear that a significant fraction of the radio flux was extended on spatial scales of a few arc seconds, and that the morphology was time variable, soon after intense radio observations began (eg. Spencer, 1979). This extended emission is polarised by up to 20% (Hjellming and Johnston, 1981a). This, plus the nonthermal spectral index, points to highly relativistic synchrotron emission.

Both VLBI and VLA observations have been made (Margon 1984 and refs. therein; Fejes 1986). The VLBI work, with a spatial resolution of 10-100 mas, can probe the central engine where the radio-emitting particles are produced. The VLA resolution is $\sim$1" and the volume studied is large enough to observe the effects of the precession of the beams (but see also Fejes 1986), and hence this work is an excellent probe of the jet kinematics.

The observed morphology changes markedly on a timescale of days giving a 'corkscrew' pattern when projected onto the sky thus identifying the precession axis direction for comparison with W50 and with photometry (Figure 5). This morphology can be analysed to give the radio equivalent to the optical kinematic model, assuming that the pattern is due to ballistically coasting matter ejected from the jets. The results of such an analysis (Hjellming and Johnston 1981(a),(b)) agree to high precision with those inferred from the optical analysis. The twin-jet model is not a unique solution of the optical spectroscopic observations. However, the agreement of the optical and radio results and the fact that the radio maps show that the jets move outwards provides confirmation of this model. Further, the jet linear velocity and the observed proper motion of the jets gives the distance to SS433 as 5 kpc (eg. Fejes 1986). There is no ambiguity between the inclination and the precession cone angles in the radio solution, which also gives the sense of the jet rotation as clockwise. However, rapid changes in the jets, including the effects of the 'nodding' motion cannot be probed. by radio since the radio emitting region is too large.

1.4 X-ray Observations

Ariel V made the first X-ray observations of SS433 in 1974, 75 (Seward et al., 1976). These authors suggested the association of the X-ray source with W50 and, because of its intense variability, suggested it as a possible compact stellar remnant. It was also observed by the Uhuru satellite (Forman et al., 1978). Compared with other bright X-ray sources in the plane of the galaxy, neither the Ariel nor the Uhuru observations suggested anything unusual about the object. The typical

observed flux is $\sim 10^{-10}$ erg $cm^{-2} s^{-1}$ in the 2-10 keV band, but is highly variable. Since there is little correction required for interstellar absorption in this band pass, the X-ray luminosity can be confidently estimated to be $\sim 10^{35}$ $ergs^{-1}$ which is trivial compared to the infrared bolometric luminosity ($\sim 10^{39}$ $ergs^{-1}$, Wagner, 1986), the kinetic energy of the jets ($\sim 10^{40}$ $ergs^{-1}$, Begelman et al., 1980) and to many binary X-ray sources.

Marshall et al., (1979) analysed the spectrum of the source in the 2-30 keV band obtained by the HEAO-1 A-2 experiment but could not distinguish between thermal or power-law spectra. However, both models require a prominent, broad emission line at 6.8 keV, the result of a variety of unresolved transitions of highly ionised iron. The observed equivalent width of this line (580 eV) implies a thermal plasma at a temperature of about 14 keV. A similar feature can be seen in a spectrum from Ariel VI (Ricketts et al., 1981). Stringent upper limits on Si emission near 1.9 keV are given by Grindlay et al., (1984). Since strong Si emission is expected for thermal sources with kT between 0.35 and 1.3 keV, thermal interpretations of the X-ray emission must have substantially hotter plasmas.

The Einstein observations were the first to give information on the spacial structure of SS433. X-ray imaging observations (Seward et al., 1980) show that 90% of the soft (1-3 keV) X-ray flux is coincident with the optical object but 10% is contained in 2 extended jets closely aligned with the major axis of W50. This confirmed the association of SS433 and W50, strengthened the evidence for ejected jets and gave a minimum age for the jets of a few thousand years. Further imaging data (Watson et al., 1983) showed that the spectrum of the X-ray lobes is different

from that of the central source, which is not surprising as the lobe emission must reflect the interaction of the jets with the ambient medium.

SS433 is highly variable on a number of timescales. Significant daily variations have been observed (Seaquist et al., 1982) some, but not all, of which may be correlated with radio variability. There is strong evidence for variation on the orbital period, in particular, the light curve shows a partial eclipse at 0 phase as defined by the 'stationary' HeII radial velocity curves (Grindlay et al., 1984; Stewart et al., referenced in Kemp et al., 1986). There were insufficient observations from Einstein to search for flux variations on the precession period (Grindlay et al., 1984) although Rickets et al., 1981 do discuss this effect based on the more extended Ariel V observations. No variability on timescales less than $\sim$300 s has been observed suggesting an extended X-ray source.

Two groups (Watson et al., 1986; Matsuka, Takano and Makishima, 1986) have reported observations of a Doppler shifted iron emission line, with energy shifts consistent with the kinematic model of the jets. This implies that the X-ray emitting material is associated with the jets. The rest frame energy of the lines (6.7keV) suggests a thermal origin for the line emission. Further, precession phase dependent changes in the visibility of the lines are interpreted by Watson et al., (1986) as being due to obscuration by the precessing accretion disk, implying X-ray line emission in a hot inner jet region.

1.5 Gamma Ray Observations

Lamb et al., 1983 and Lamb (1984) have reported observations of narrow gamma ray lines in the low MeV range in the general direction of

SS433 and have indicated this object as the most likely source of these lines. However, the details of the emission process, and even the reality and correct identification of the lines in terms of nuclear transitions are still controversial (Wheaton et al., 1985; Geldzahler et al., 1985). A number of models have been proposed for these lines (Boyd et al., 1984; Kundt, 1985; Ramaty et al., 1984; Helfer and Savedoff, 1984), though without general agreement on even the number of lines that were observed, and with lack of physical self-consistency of some aspects of the models.

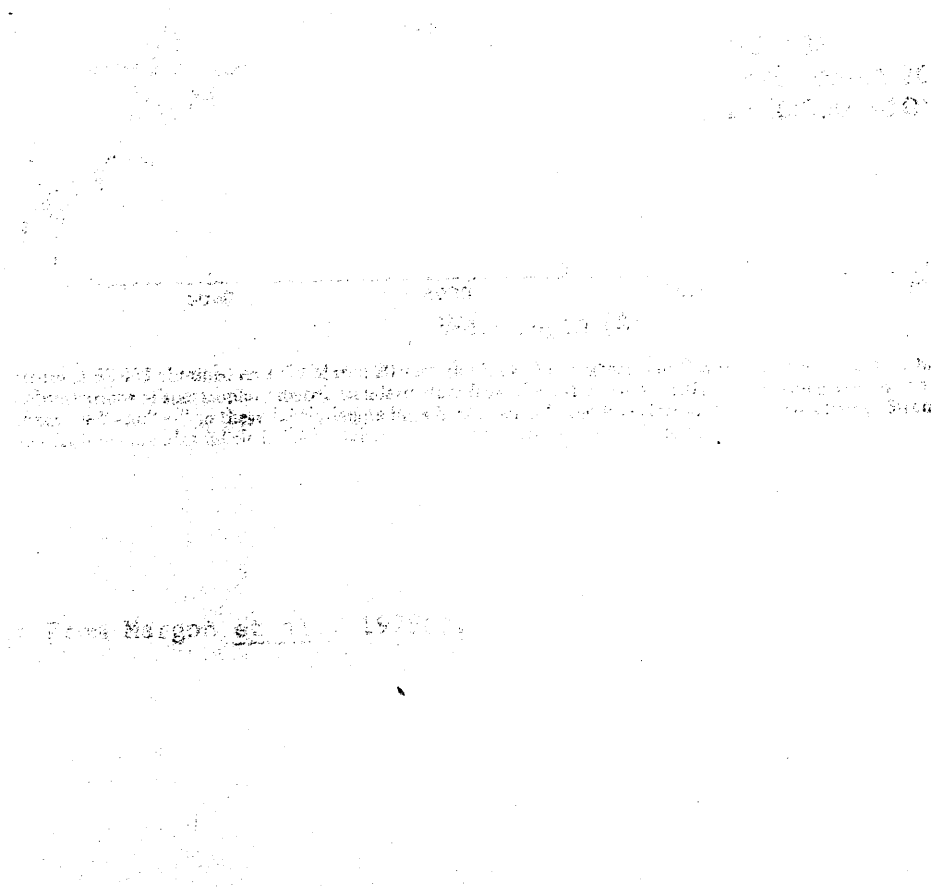

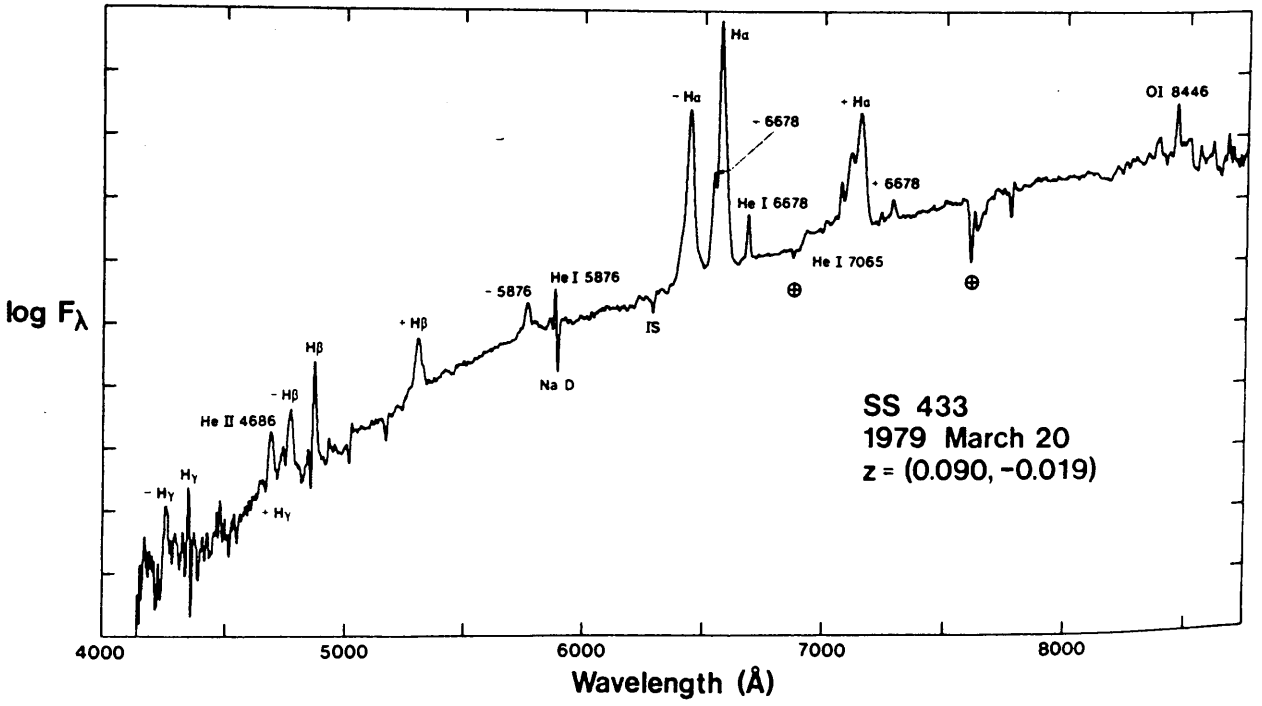

Spectrum of SS 433 obtained on 1979 March 20 with the Lick Observatory 3 m Shane reflector. The data have been converted to flux units via observations of spectrophotometric standard stars from the list of Stone (1977). The principal emission features are identified, and the prefixes "+" and "−" to these labels denote lines in the redshift and blueshift systems, respectively. Stronger interstellar and telluric absorption features are also labeled. Each division on the ordinate corresponds to 0.83 mag.

Figure 1: From Margon et al., 1979b).

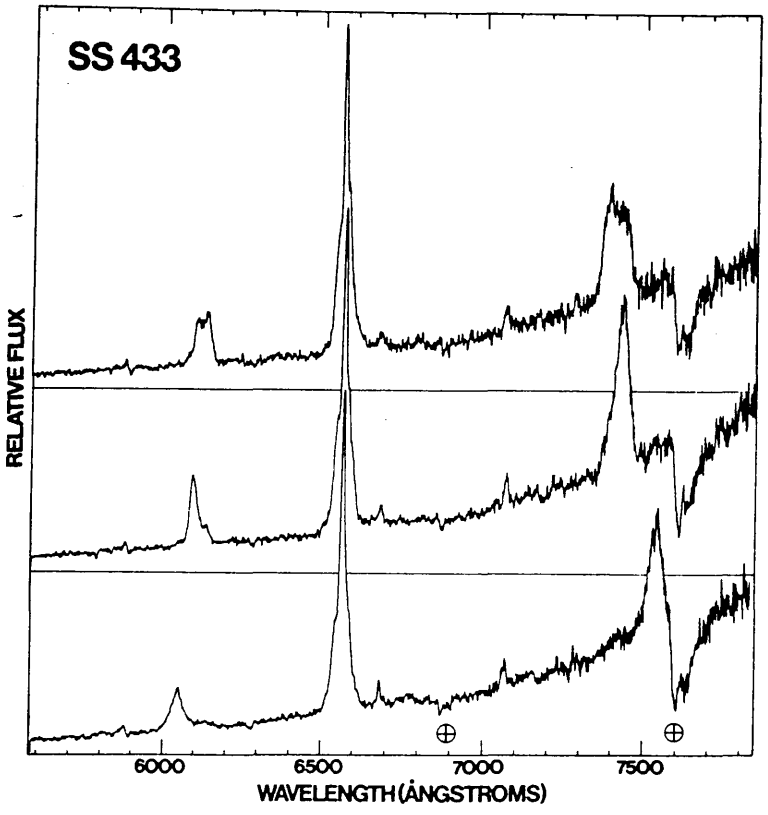

The red/infrared spectrum of SS 433 on three of four consecutive nights, obtained with 10 Å resolution on the Lick 0.6 m reflector. The dramatic changes in both wavelength and profile of the two unidentified emission features flanking Hα are well-illustrated in this example. He I λ5876, 6678, 7065 emission is visible, as are the unresolved interstellar NaD lines and λ6284 band. The emission bands in the $\lambda\lambda$6300–6400 range (cf. Fig. 1) are absent on these particular nights. The telluric A and B bands have been indicated. The upper, center, and lower panels were observed on 1978 October 23, 24, and 26, respectively.

Figure 2: From Margon et al., 1979a).

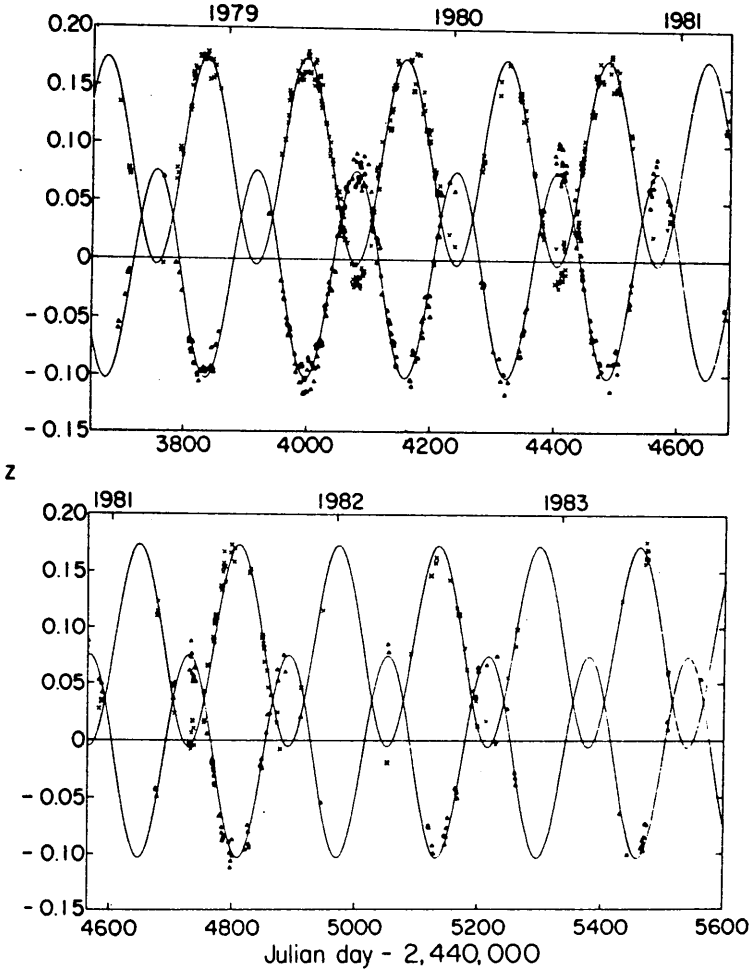

Doppler shifts of SS 433 on 450 nights in the period 1978–83. The majority of these data were obtained by the author and colleagues, supplemented by sources cited in (105). The solid curve is a least-squares best fit to the simple "kinematic model" (1). The free parameter values and their associated 1σ uncertainties (notation as in 105) for this fit are $v/c = 0.2601 \pm 0.0014$, $\theta = 19.80° \pm 0.18°$, $i = 78.82° \pm 0.11°$, $t_0 = \text{JD } 2{,}443{,}562.27 \pm 0.39$, $P = 162.532 \pm 0.062$ days.

Figure 3: From Margon, 1984

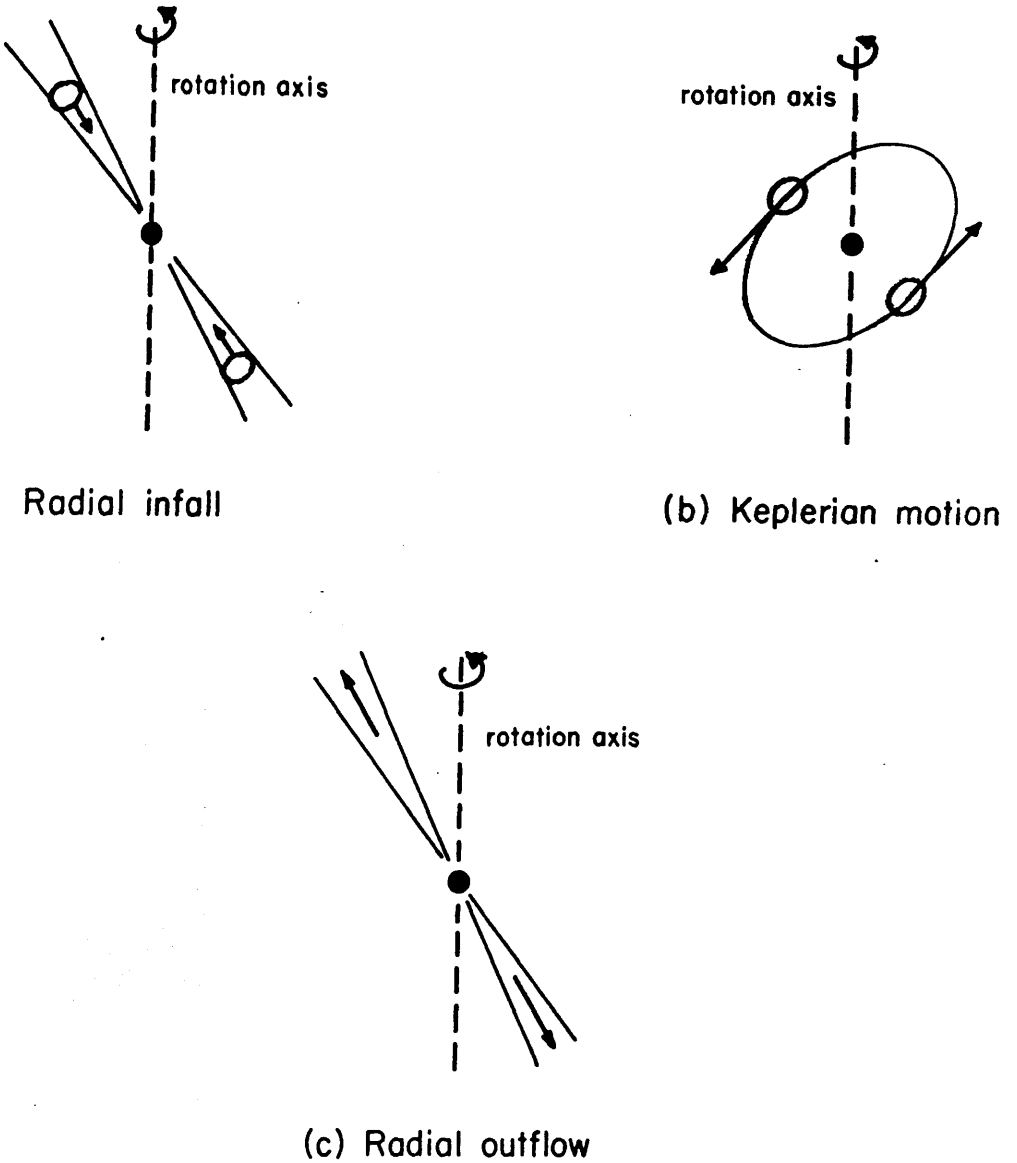

Figure 4: The three possible geometries for the moving systems of emission lines of SS433. The line of sight in each case is inclined to the rotation axis by a constant angle.

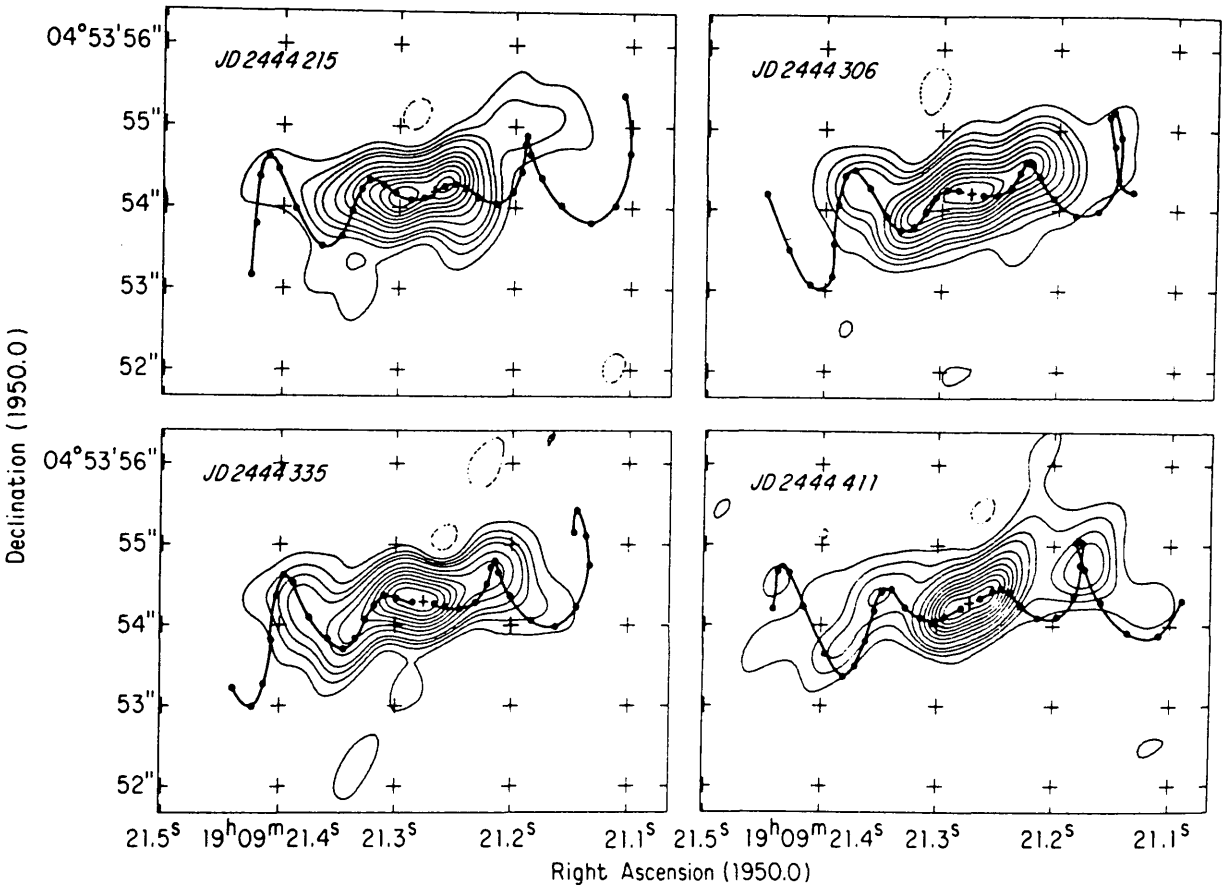

VLA radio contour maps of SS 433 at 4885 MHz for t = JD 2,444,215, 2,444,306, 2,444,335, and 2,444,111 are displayed in a form where the unresolved core radio source (small +) is removed, and the proper motion paths of material ejected at 20 day intervals with the parameters of Table 1 are drawn with filled circles. The contour levels correspond to 90, 80, 70, 60, 50, 40, 30, 20, 15, 10, 5, and −5% of the peak flux density values of 0.070, 0.030, 0.029, and 0.032 Jy per beam area for JD 2,444,215, 2,444,306, 2,444,306, and 2,444,411 maps, respectively.

Figure 5: From Hjellming and Johnstone, 1981b).

CHAPTER 2

PHYSICAL CONDITIONS IN SS433

2.1 Introduction

We now turn to the physical problems based on the twin jet and disc model for SS433, which is the most widely accepted model (see Chapter 1). Before dealing with these problems, however, we will detail the constraints imposed by the observations.

2.1.1 Observational Constraints

The luminosity in the H_α line is $\sim 10^{35}$ erg s^{-1} (Milgrom, 1981), while the estimated bolometric luminosity could be as high as 4×10^{39} erg s^{-1}. though much of this would be obscured by the interstellar extinction, being mostly in the U optical band and the unobserved UV (from optical spectrum fitting, Wagner 1986). The width of the moving optical lines is ~ 100 Å. The temperature in the optical emitting region of the jets must be $\sim 10^4$K, since a higher temperature would lead to stronger HeII lines than observed and we would see lines of higher excitation ions. In comparison, the highest disc photospheric temperature is $\sim 10^7$ K (Katz, 1986) as is the temperature of the inner regions of the jets (Watson et al., 1986) . If the emission is incoherent, the H_α flux and the estimated distance imply a lower limit of $\sim 3 \times 10^{12}\ \theta_{-1}^{-\frac{1}{2}}$ cm for the length of the emitting region, where θ_{-1} is the opening angle of the jets in units of 0.1 radian, which is the inferred opening angle (Bodo et al., 1985). Since changes in the lines occur on timescales of the order of a day this implies that the maximum length of the optical emitting region is $\sim 3 \times 10^{15}$ cm. This can be reduced to $\sim 7 \times 10^{14}$ cm if coherent changes are propagated at the beam velocity.

The jet velocity is remarkably stable (Milgrom, 1981) and uniform in

direction and magnitude across the jets (Milgrom, Anderson and Margon, 1982; Katz and Piran, 1982), indeed the jet speed is more stable than its direction (Margon 1981; Katz and Piran 1982). The kinetic luminosity, L_K, of the jets is highly uncertain. If each atom emits only one H_α photon then $L_K \sim 4 \times 10^{42}$ erg s^{-1}. Other estimates for L_K (eg. Milgrom 1981; Bodo et al., 1985) lead to the conclusion that the filling factor must be very small if L_K is to be much smaller than 10^{42} erg s^{-1} which is highly super-Eddington even for an object of mass 10 $M_\odot$. A lower limit for L_K can be found that is independent of the filling factor, the length of the emission region and the emission mehcnaism (cf. Milgrom, 1981). Since the emission of an H_α photon requires a prior excitation or ionization, an energy, E_{ex}, must have been deposited in the line-emitting gas. Unless this energy is deposited isotropically there will be a simultaneous transfer of momentum $P_{ex} \gtrsim E_{ex}/c$. However, the relative change in the total momentum flux across the emitting region must be less than 0.1 since the observed velocity spread across the region is small. This implies that the total momentum flux must exceed P_{ex} by at least the ratio of the velocity of the line-emitting gas to the maximum spread in that velocity allowed by observation. This gives $L_K \gtrsim 10^{36}$ erg s^{-1} (Shapiro, Milgrom and Rees, 1986).

The observations of the doppler shifted iron K lines (Watson et al., 1986; Matsuoka, Takano and Makishima, 1986) show that the disc obscures one of the X-ray emission regions except (possibly) when the disc is close to being edge on. Hence the inner regions of the jets are at X-ray temperature ($\sim 10^{7.5}$ ^oK). Depending somewhat on the shape and thickness of the disc, the length of the X-ray emitting region must be $\lesssim 10^{12}$ cm for this obscuration to occur. Also, since the X-ray lines are observed to be

shifted by the jet velocity of 0.26c, the jets must be accelerated up to the terminal velocity within $r \simeq 10^{12}$ cm and before being heated to X-ray emission temperatures, or at any rate before the X-ray emission becomes observable.

2.2 The Jets

There are 3 basic physical questions relating to the jets of SS433:

a) What is the energy source of the jets?

b) How are the jets collimated?

c) How are the jets accelerated, and why is the velocity stable at 0.26c?

We will deal with each of these in turn.

2.2.1 The energy source of the jets

Two energy sources have been proposed to power the jets both of which involve a central compact object. These are the rotation of a neutron star or accretion onto a neutron star or black hole. Since there is as yet no evidence from observations suggesting the rapid rotation of the central source and since accretion is normally invoked to supply the mass ejected by the jets, accretion powered models have been more popular. In addition, a very rapidly rotating central neutron star would be needed to sustain L_K >>10 years. Unless the mass flow rate has been severely overestimated or the compact object is extremely massive, the Eddington accretion limit must be exceeded to power the jets, in accretion-type models(for a $1M_\odot$ object the Eddington limit is $\simeq 1.25 \times 10^{38}$ erg s^{-1}).

2.2.2 Collimation of the jets

The phase difference between the radial velocity and the photometric precession periods is evidence that the jets follow the normal to the disk.

For this reason and since the disk provides a natural symmetry plane, it has long been assumed that the disk is involved in collimating the jets (Davidson and McCray 1980; Katz, 1980; Sikora and Wilson, 1981). Despite doubts as to the stability of thick disks (see Section 2.3.1), the funnels formed along the axis of a thick, super-critical accretion disk have been suggested as acceleration regions (see below) and collimators for the jets (eg. Milgrom, 1981; Bodo et al., 1985). De Laval nozzles near the magnetopause of a magnetised neutron star have also been proposed (Begelman and Rees, 1984) and Eichler, (1983) has also pointed out the possible role of the ambient medium.

2.2.3 Jet Acceleration Mechanism

Early in the study of SS433, Milgrom, 1979 pointed out that the observed velocity of the jets, 0.26c, is within a few percent of the value required to doppler shift the hydrogen Lyman continuum limit to the wavelength of L_α. Although it may be a coincidence, this has led to models where the acceleration mechanism is radiative absorption and the terminal velocity is maintained at 0.26c by the phenomenon of line-locking. There are, however, a number of serious problems with such models, not least of which is the huge $\dot{M}$ required by the inferred kinetic luminosity. Shapiro, Milgrom and Rees,(1986 and references therein) have shown that not only must the spectrum of the underlying source exhibit a Lyman jump, but the discontinuity must be of the correct magnitude for line-locking to occur and give a stable terminal velocity. The luminosity of the source must be at least partially collimated along the jet axis, for if it was spherically symmetric the required luminosity would be highly super-Eddington even for a central mass of 20 $M_\odot$. For Hydrogen line-locking, they found that the acceleration

must begin $\sim 2 \times 10^{13}$ cm from the centre of symmetry and the gas must be highly clumped (for recombination to keep the gas neutral) if the required $\dot{M}$ is to be accelerated to the terminal velocity. They also investigated line-locking with heavier elements and found that the minimum acceleration distance and the required clumping was reduced as Z increased. If the line-locking element is Fe, the acceleration distance is $\sim 10^{10}$ cm and no clumping is required but if enough mass is to be accelerated, Fe must be significantly overabundant. They also found that, for the heavier elements, there is a lower limit of $\sim 10^{10}$ cm on the acceleration region since, if acceleration begins closer to the central object, electron scattering will push the jet velocity above the line-locked limiting value. The constraint that the jets must be accelerated to their terminal velocity well within 10^{12} cm (Watson et al., 1986) certainly rules out hydrogen and a number of the heavier elements as the line-locking element. Also the equivalent width of the iron emission lines indicates normal cosmic abundances (Watson et al., 1986) which would rule out line-locking by F_e. As Margon (1984) points out, line-locking may act only as a velocity stabiliser in a hybrid acceleration mechanism.

Two other possible acceleration mechanisms have been proposed by Begelman and Rees (1984) and Bodo et al., (1985). The former authors proposed a magnetised neutron star as the central object, undergoing super-critical accretion. The de Laval nozzles act as exhausts for the excess mass which form the jets accelerated by electron scattering radiation pressure. The power source can be either highly inhomogeneous accretion onto the neutron star's surface or the rapid spin of the neutron star. The velocity, and collimation angle, of the jets are determined by such parameters as the rotation rate, the magnetic field and the mass of the

neutron star and the accretion rate. The velocity, therefore, is not constrained to be 026c in this model. It should also be noted that some analyses of the optical light curve (Leibowitz, 1984) indicate that the central object is too massive to be a neutron star.

Bodo et al., 1985 have adapted a wind-type model first proposed in the context of jet acceleration in active galactic nuclei. They assume that it is possible to form a stable thick disk (see discussion below in Section 2.3.1) and that the gas in the disk funnels is optically thin. The gas of the jets is accelerated in the disk funnels and the terminal velocity can be attained at distances from the central object $\lesssim 10^9$ cm. The exit temperature of the jet gas is $\gtrsim 10^7$ K, consistent with the observed X-ray emission lines (Watson et al., 1986). The jets then cool and fragment, due to thermal instabilities, giving rise to clouds which then have the correct temperature ($\sim 10^4$K) to be the sources of the observed optical moving lines. However, at distances $\sim 10^{15}$ cm the cloud will evaporate due to heat conduction from the hotter surrounding medium and hence no further H_α emission can occur. This distance is in agreement with the inferred length of the optical jets. Again in this model there is no single terminal velocity, this depending on such parameters as the luminosity of the central source and the opening angle of the disk funnels. Indeed, terminal velocity need not be achieved if the mass loss rate is too high for a given source luminosity.

2.3 The Disc

2.3.1 Disc Structure

A number of observations suggest that the disk is geometrically thick, such as the amplitude and shape of the precession photometric light curve (Kemp et al., 1986 and references therein). It has been suggested that the

disk thickness is as much as two-thirds its diameter. The 6.3 day nodding motion also suggests a thick disk (Katz et al., 1982) since the disc must be highly viscous to rapidly transmit the nodding motion from the outer rings of the disc to the inner region where the jets originate and respond to the motion. Also many of the jet collimation mechanisms involve a thick disc.

Paploizu and Pringle (1984) have considered the dynamical stability of thick disks. They show that such disks are unstable to long wavelength fluid perturbations reflecting at the inner boundary of the disk. Such instabilities have a typical growth time of the order of a disk rotation period. However, (cf. Bodo et al., 1985), the presence of streaming onto the central object violates the boundary conditions and may cause the instability to disappear. Moreover, it is uncertain whether such an instability would indeed disrupt the disk as it may simply cause dissipative heating. In practice, most authors still assume that a stable thick disk can exist.

From the amplitude of the precession photometric variations and plausible emissivity limits, Anderson, Margon and Grandi, (1983a)have been able to infer the disc linear dimensions as $\sim 10^{12}$ cm. This is comparable to the separation of the stars. A disk of large radius is required if the torque on it is to be significant (cf. discussion on precession mechanism below).

2.3.2 Disc Precession Mechanism

SS433 is not the only object where precessing disks are invoked, for example, the 35 day X-ray modulation of Hercules X-1 is widely attributed to disc precession. However, precise modelling of the precession mechanism has not yet been accomplished. The early suggestion

that the precession mechanism might be instead the relativistic Lense-Thirring effect (Martin and Rees 1979; Sarazin, Begelman and Hatchett, 1980) requires a highly compact disk, contrary to the inferences of photometry and the nodding motion (see section 2.3.1 above), and therefore can probably be dismissed.

The two most considered mechanisms are classical driven precession, where the normal companion exerts a torque on the disc, and slaved precession, where the compact object causes the misaligned companion star to precess and a short residence time for matter in the disk allows it to follow the companion star's motion. In both these mechanisms the disk precession begins in the outer rings of the disk since in driven precession the torque is significant only for disk rings of large radius and in slaved precession it is the outer part of the disk which is directly slaved to the companion star. The inner region of the disk then follows the outer rings and the jets are generally assumed to follow the inner region of the disk. This is confirmed by the phase delay between the photometric nodding variation and the corresponding radial velocity variations since the photometric maxima appear before the radial velocity ones (Mazeh et al., 1987).

Both these mechanisms have been discussed with respect to SS433 (e.g. De Campli, 1980; Katz, 1980; van den Heuval, Ostriker and Petterson 1980; Whitmire and Matese, 1980; Hut and van den Heuval, 1981). Slaved precession is more popular, indeed Katz et al.,(1982) claim that the observed amplitude of the nodding motion favours slaved over driven precession. However, Papaloizou and Pringle (1982) present strong arguments against the precession of a gaseous star over time scales longer than that needed to circularise the binary orbit. The low orbital eccentricity ($\sim$0.05 Collins and Newsom, 1986) may, therefore, imply that slaved precession cannot be occurring in SS433.

2.4 The Compact Star

The ejection velocity of the jets as well as the X-ray emission from the system have long suggested the presence of a compact object, either a neutron star or black hole. Bonsignori-Facondi and Braccesi (1986) argue that direct evidence of such a compact object has been observed at 408 MHz. So far no rapid variations of the type indicative of a rotating neutron star have been observed, though such an absence is hardly conclusive. Since the system eclipses and is a single line spectroscopic binary, the mass of the compact object can theoretically be estimated using the observed mass function and light curve synthesis. Although such modelling is uncertain as to uniqueness and error estimation, the results of such techniques applied to SS433 have led to estimates for the mass of the compact star which have been both increasing and becoming better constrained. (Margon 1984 and references therein; Watson et al., 1986 and references therein). Leibowitz (1984) estimates the mass of the compact star to be 10-100 $M_\odot$ and therefore certainly a black hole, while the companion star, an early B or O super-massive star, has a mass M_* in the range 20-50 $M_\odot$ such that $M(\text{compact})/M_* \geq 0.8$.

The nature of the compact star has relevance to other aspects of the system, for example the collimation mechanism and the shape of the disc. The cauldron scenario of Begelman and Rees (1984) probably requires a neutron star while thick disk models may well require a central black hole. Incidentally, if the compact object is a neutron star it requires a spin period of the order of 10 ms if its spin-down time is to be longer than the minimum age of SS433 (if rotational kinetic energy is to provide L_K).

2.5 Analogous Objects

Few, if any, astronomical objects are truly unique. Hence it is not

unreasonable to ask if there exist any other objects analogous to SS433. Since the distance to SS433 is measured in kiloparsecs, the galactic population of such objects is probably only a few at most, and it is not improbable that SS433 is the only observable example in our Galaxy. None of the possible candidates so far suggested as analogs to SS433 have stood up to spectroscopy and observations at many wavelengths (Margon, 1984 and references therein) although a number have proved to be very interesting in their own right. From estimates of the absolute luminosity of SS433, it seems likely that an analogous object would be easily observable in the Magellanic Clouds, and even within the reach of large telescopes in M31, if one knew where to search. Since the X-ray luminosity of SS433 is not remarkable, the radio emission or morphology or the peculiar optical emission lines would provide a more distinctive signature. Indeed, surely a necessary requirement for identification as an SS433 analogue would be observational evidence of collimated, near-relativistic, opposed, precessing jets. So far there are no convincing galactic candidates. It is, however, worth noting that collimated relativistic outflow is thought to be the basic phenomenon occurring in a variety of active galactic nuclei with the strong possibility that precession is the cause of the observed curved radio jets (eg. Gower and Hutchings, 1982a,b); Gower et al., 1982). Indeed, the implication that SS433 could be displaying the same basic physical processes in miniature was a primary motivation for the twin-jet model (Fabian and Rees, 1979). If the analogy between SS433 and extragalactic jets is more than a morphological coincidence (cf. e.g. Rees 1982), this would be extremely fortunate. Not only can we observe SS433 in detail with much smaller telescopes but the time scale of observable changes in the SS433 jets is many orders of magnitude faster than in extragalactic cases and we have a precise

unambiguous measurement of the SS433 jet velocity which is not normally available for extragalactic jets. Hence SS433 may provide us with valuable insight into the basic physics of such objects as radio galaxies and quasars.

CHAPTER 3

GENERAL POLARIMETRY OF A ROTATING SYSTEM

3.1 Introduction

In modelling the polarisation due to circumstellar scattering of light from a stellar system, several approaches have been used. One is to seek solutionsof the full radiative transfer equations (cf. Chandrasekhar, 1960) which can,in principle treat an arbitrary source shape and scattering geometry. However, to treat relatistic cases, such an approach nearly always requires very elaborate numerical simulation or Monte Carlo techniques. This not only demands large amounts of computer time but also presents problems when attempting to fit a model to the data. Often a set of parameters can be found for which a particular model reproduces the data but lack of time and money can prevent a full search of parameter space and the estimation of confidence intervals. There is no guarantee that such a model is unique, or that the best fit has been found when the number of free parameters is large.

An alternative approach is to consider the limiting case of optically thin scattering of isotropic, unpolarised light from a point source. This treatment is more likely to yield analytic or semi-analytic expressions as shown for the Thomson (Rayleigh) scattering case by, for example, Brown and McLean (1977)and Brown et al.,(1978). A complete search of parameter space may still be prohibitive but, as shown by Simmons et al. (1980), in the case of a binary system statistical analysis of polarimetric data may yield the best-fit solution and confidence intervals for one or more of the free parameters. (See also Chapter 5).

Simmons (1982, 1983) generalise the Thomson (Rayleigh) results and give expressions for the polarisation produced by arbitrary spherically

symmetric mechanisms in optically thin circumstellar envelopes. The polarisation produced by grain scattering can be approximated using these expressions, assuming the grains are spherically symmetric. To first order, the form of the polarisation versus wavelength function is independent of the density distribution of scatterers and the position angle is independent of the particular scattering mechanism. Thomson and Rayleigh scattering are special cases giving, respectively, wavelength independent and λ^{-4} polarisation. Numerical simulations of the full radiative transfer problem indicate that this single scattering approach gives remarkably accurate results for the variation of polarisation with time, direction and wavelength (Dolan 1984, Daniel 1980, 81).

The magnitude of the linear and circular polarisation observed, its wavelength and its time dependence can provide information into the polarising mechanism, the distribution of matter in, and the orientation of, the system. Hence, independent confirmation of models based on other observations can be provided by analysis of polarimetric data. Moreover, the polarisation may provide extra information, such as the inclination of non-eclipsing spectroscopic binaries (eg.St.Louis et al. 1987), their position angle orientation on the sky (Rudy 1979) and the distribution of matter out of the direct line of sight (Brown and Henricks, 1987).

The case of arbitrary, optically thin envelopes illuminated by point sources is dealt with in Brown and McLean, 1977 and Brown et al. 1978. In the latter paper, expressions for the normalised Stokes Parameters for a general binary system with corotating envelope are derived and data from 3 binary systems are analysed. Rudy and Kemp (1978), also developed a similar theory for determining the inclination of a binary system assuming small photometric variability, no eclipses of the scattering regions and

mirror symmetry about the orbital plane. Their result is shown to hold for extended sources provided the sources are also symmetric about the orbital plane. Cassinelli et al., 1987 have shown for the case of scattering in an axisymmetric optically thin region of light from a spherically symmetric source that the point source expressions still hold when modified by a simple geometric factor.

In this chapter, we extend the point source, optically thin case to include the effect of an arbitrary light source geometry. A general 'depolarising factor' is defined for an arbitrary source and the factor found by Cassinelli et al. is shown to hold for the more general case of a spherically symmetric source, illuminating an arbitrary optically thin electron distribution. Finally, the equations obtained by Brown et al. 1978 are rederived including the effect of extended sources.

3.2 Polarisation from an arbitrary electron distribution illuminated by a point source.

Since the method used to derive the polarisation for an arbitrary source geometry and one scattering electron is essentially parallel to that of deriving the polarisation for a point source and arbitrary scattering region, we here derive the Stokes Parameters for the latter case.

We require the observer's reference frame and the scattering plane for each electron (see Figure 1). The observer's reference frame for the Q,U parameters (X,Y) will be perpendicular to the line of sight. It is not, however, a right-angled system on the sky for the Y-axis is inclined by 45^{o} to the X-axis. The scattering plane for each electron is defined to be the plane containing the position vector of the electron with respect

to the source and the line of sight. The scattering angle, χ, is defined to be the angle between the line of sight and the position vector of the electron. For a given observer's reference frame, each electron will have associated with it the angle between the normal to its scattering plane and the X-axis, here denoted as ψ .

Let L be the luminosity of the light source, then the Stokes Parameters for the whole envelope measured with respect to the observer's reference plane are given by

$$I_1 = \frac{L\sigma_o}{4\pi} \int_V \frac{n(\underset{\sim}{r})}{r^2} (1 + \cos^2 \chi) dV$$

$$I_2 = \frac{L\sigma_o}{4\pi} \int_V \frac{n(\underset{\sim}{r})}{r^2} \sin^2 \chi \cos 2\psi \, dV \qquad (1)$$

$$I_3 = \frac{L\sigma_o}{4\pi} \int_V \frac{n(\underset{\sim}{r})}{r^2} \sin^2 \chi \sin 2\psi \, dV$$

(cf. Equations (1) Brown et al., 1978).

where $n(\underset{\sim}{r})$ is the electron number density distribution with respect to the source and, for Thomson scattering, $\sigma_o = 3\sigma_T/16\pi$, σ_T being the Thomson cross-section per electron. The Stokes Parameters are here denoted by I_1, I_2 and I_3 to be consistent with the notation of Brown et al., 1978. They are, however, measured in Watts/sterad and are not specific intensities. For a source at distance d from the earth, the observed fluxes would be

$$F_i = \frac{I_i}{d^2} \text{ Watts } m^{-2} \qquad (i=1,2,3)$$

Note that only three of the four Stokes Parameters are necessary since single Thomson scattering (in the absence of a magnetic field) gives no circular polarisation. Also, to obtain the first Stokes Parameter, usually denoted by I the total direct light ($L/4\pi$) should be added to I_1.

Since Stokes Parameters add linearly, equation (1) may be generalised

to include any number of point sources simply by summing the individual I_1, I_2, I_3 due to each source, with the integrals performed in coordinate systems centred on each source.

3.3 Polarisation from a single electron illuminated by an extended source

We now derive the polarisation due to one electron scattering from an arbitrary extended source. First, we divide the source into separate elements and treat each element as a point source. For each source element, χ and ψ are defined in an analogous way to that of Section 3.2 using the line of sight, the observer's reference frame and the position vector of the electron with respect to the source element. The total Stokes Parameters for the extended source scattering from one electron are found by integrating over the surface of the source.

Consider an unpolarised, arbitrary source of total luminosity L (integral over 4π) illuminating one electron. Define a cartesian coordinate system with origin within the source and z-axis the position vector $\underset{\sim}{r}$ of the electron with respect to the origin (Figure 2). Then angles α and β define the direction of $\underset{\sim}{\rho}$, the position vector the electron with respect to the source element. Similarly, the line of sight is defined by angles γ and ε. Let the specific intensity of the source as seen from the electron be $I = I(\alpha,\beta)$. If the observer's reference frame is defined by the projection of the z-axis on the sky as the X-axis (i.e. parallel to $\underset{\sim}{\ell}$ in Figure 2) then

$$
\begin{aligned}
I_1 &= \sigma_o \int_\beta \int_\alpha I(\alpha,\beta)(1+\cos^2\chi)\sin\alpha \, d\alpha \, d\beta \\
I_2 &= \sigma_o \int_\beta \int_\alpha I(\alpha,\beta)\sin^2\chi \cos 2\psi \sin\alpha \, d\alpha \, d\beta \\
I_3 &= \sigma_o \int_\beta \int_\alpha I(\alpha,\beta)\sin^2\chi \sin 2\psi \sin\alpha \, d\alpha \, d\beta
\end{aligned}
\qquad (2)
$$

Note that $I(\alpha,\beta)$ is measured in Watts/area/sterad and therefore does not have the same dimensions as I_i (i=1,2,3) (Watts/sterad).

Now expressions for $\cos^2\chi$, $\sin^2\chi\cos 2\psi$ and $\sin^2\chi\sin 2\psi$ in terms of α,β,γ and ε can be found from spherical triangle ZPE (Figure 3). These are:

$$\begin{aligned}
\cos^2\chi &= \cos^2\alpha\cos^2\gamma + \sin^2\alpha\sin^2\gamma\cos^2(\varepsilon-\beta) + \frac{1}{2}\sin 2\alpha\sin 2\gamma\cos(\varepsilon-\beta) \\
\sin^2\chi\cos 2\psi &= -\sin^2\gamma + \sin^2\alpha[\sin^2\gamma + \sin^2(\varepsilon-\beta) - \cos^2\gamma\cos^2(\varepsilon-\beta)] \\
&\quad + \frac{1}{2}\sin 2\alpha\sin 2\gamma\cos(\varepsilon-\beta) \qquad (3) \\
\sin^2\chi\sin 2\psi &= \sin 2\alpha\sin\gamma\sin(\varepsilon-\beta) - \sin^2\alpha\cos\gamma\sin 2(\varepsilon-\beta)
\end{aligned}$$

Since the origin lies within the source, the integration limits are $0 \leq \beta \leq 2\pi$ and $0 \leq \alpha \leq f(\beta)$ where $f(\beta)$ is some function of β that describes the boundary of the source as seen from the electron. In general, $f(\beta)$ will depend on the position of the electron. Substituting equations (3) in equations (2), and using the above limits gives, after some manipulation

$$\begin{aligned}
I_1 &= (1+\cos^2\gamma)A_1 + \frac{1}{2}(1-3\cos^2\gamma)A_2 + \frac{1}{2}\sin^2\gamma(A_3\cos 2\varepsilon + \\
&\quad + A_4\sin 2\varepsilon) + \sin 2\gamma(A_5\cos\varepsilon + A_6\sin\varepsilon) \\
I_2 &= -\sin^2\gamma(A_1 - \frac{3}{2}A_2) + \frac{1}{2}(1+\cos^2\gamma)(A_3\cos 2\varepsilon + A_4\sin 2\varepsilon) \qquad (4) \\
&\quad + \sin 2\gamma(A_5\cos\varepsilon + A_6\sin\varepsilon) \\
I_3 &= 2\sin\gamma(A_5\sin\varepsilon - A_6\cos\varepsilon) - \cos\gamma(A_3\sin 2\varepsilon - A_4\cos 2\varepsilon)
\end{aligned}$$

where

$$A_1 = \sigma_o \int_0^{2\pi}\int_0^{f(\beta)} I(\alpha,\beta)\sin\alpha\, d\alpha\, d\beta$$

$$A_2 = \sigma_o \int_0^{2\pi}\int_0^{f(\beta)} I(\alpha,\beta)\sin^3\alpha\, d\alpha d\beta$$

$$A_3 = \sigma_o \int_0^{2\pi} \int_0^{f(\beta)} I(\alpha,\beta)\, \sin^3\alpha \cos 2\beta \, d\alpha \, d\beta$$

$$A_4 = \sigma_o \int_0^{2\pi} \int_0^{f(\beta)} I(\alpha,\beta)\, \sin^3\alpha \sin 2\beta \, d\alpha \, d\beta \qquad (5)$$

$$A_5 = \sigma_o \int_0^{2\pi} \int_0^{f(\beta)} I(\alpha,\beta)\, \sin^2\alpha \cos\alpha \cos\beta \, d\alpha \, d\beta$$

$$A_6 = \sigma_o \int_0^{2\pi} \int_0^{f(\beta)} I(\alpha,\beta)\, \sin^2\alpha \cos\alpha \sin\beta \, d\alpha \, d\beta$$

For sources with some degree of symmetry, the axes can sometimes be chosen to take advantage of that symmetry, depending on the positon of the electron. This will impose some conditions on $f(\beta)$ and $I(\alpha,\beta)$. For example, for a source with mirror symmetry about some plane and an electron in that plane, then by choosing the x-axis such that it also lies in the symmetry plane, we find that $f(\beta) = f(-\beta)$ and $I(\alpha,\beta) = I(\alpha,-\beta)$. For any source we have $f(2\pi + \beta) = f(\beta)$ and $I(\alpha, 2\pi + \beta) = I(\alpha,\beta)$.

Conditions on $f(\beta)$ and $I(\alpha,\beta)$ simplify equations (5) as follows:

(a) if $f(-\beta) = f(\beta)$ and $I(\alpha,-\beta) = I(\alpha,\beta)$ then $A_4 = A_6 = 0$

(b) if $f(\pi-\beta) = f(\beta)$ and $I(\alpha,\pi-\beta) = I(\alpha,\beta)$ then $A_5 = 0$

(c) if $f(\pi/2-\beta) = f(\beta)$ and $I(\alpha,\pi/2-\beta) = I(\alpha,\beta)$ then $A_3 = 0$.

We will refer to these conditions as the 'symmetry conditions'.

A uniform spherical source satisfies all the above conditions for any electron, but a plane ellipse can never satisfy all three conditions even for an electron on the normal to the centre of the ellipse. A uniform thin disk will satisfy the symmetry conditions only for electrons on the disc axis.

For sources of uniform surface intensity $I(\alpha,\beta) \equiv I$ a constant.

Hence equations (5) become

$$A_1 = \sigma_o I\{ 2\pi - \int_o^{2\pi} \cos f(\beta)\, d\beta$$

$$A_2 = \sigma_o I\{ \frac{4\pi}{3} + \int_o^{2\pi} [\frac{1}{3}\cos^3 f(\beta) - \cos f(\beta)]\, d\beta\}$$

$$A_3 = \sigma_o I\int_o^{2\pi} [\frac{1}{3}\cos^3 f(\beta) - \cos f(\beta)]\cos 2\beta d\beta \qquad (6)$$

$$A_4 = \sigma_o I\int_o^{2\pi} [\frac{1}{3}\cos^3 f(\beta) - \cos f(\beta)]\sin 2\beta\, d\beta$$

$$A_5 = \sigma_o I\int_o^{2\pi} \sin^3 f(\beta)\cos\beta\, d\beta$$

$$A_6 = \sigma_o I\int_o^{2\pi} \sin^3 f(\beta)\sin\beta\, d\beta$$

and if the source satisfies the symmetry conditions above then, using (6), equations (4) reduce to

$$I_1 = \frac{8\pi}{3}\sigma_o I + \frac{1}{6}\sigma_o I(1-3\cos^2\gamma)\int_o^{2\pi}\cos^3 f(\beta)d\beta - \frac{1}{2}\sigma_o I(3-\cos^2\gamma)\int_o^{2\pi}\cos f(\beta)\, d\beta \qquad (7)$$

$$I_2 = \frac{1}{2}\sigma_o I\sin^2\gamma\int_o^{2\pi}[\cos^3 f(\beta) - \cos f(\beta)]\, d\beta$$

$$I_3 = 0$$

If, however, the source has rotational symmetry about the z-axis then $I(\alpha,\beta) \equiv I(\alpha)$ and $f(\beta) = \alpha_o$, a constant. Such a source satisfies the symmetry conditions and, with $\mu = \cos\alpha$, equations (4) become

$$I_1 = \pi\sigma_o \int_{\mu_o}^{1} I(\mu)\,[3-\mu^2]d\mu + \pi\sigma_o \cos^2\gamma \int_{\mu_o}^{1} I(\mu)\,[3\mu^2 - 1]d\mu$$

$$I_2 = -\pi\sigma_o \sin^2\gamma \int_{\mu_o}^{1} I(\mu)\,[3\mu^2 - 1]\,d\mu \qquad (8)$$

$$I_3 = 0$$

where $\mu_o = \cos\alpha_o$. In this situation α_o is the angular radius of the source as seen from the electron.

3.4 Depolarisation Factor

We define the depolarisation factor, D, to be the ratio of the value of I_2 for the extended source to the value of I_2 for an isotropic point source of the same total luminosity as the extended source, denoted by I_{2p}. Note that $I_{3p} = 0$ because of the choice of observer's axes and so a similar definition using I_3 is not possible for these particular axes.

Suppose, however, we measure the Stokes Parameters with respect to axes rotated clockwise from the X-axis through angle δ, and denote these by J_i, J_{ip} $(i=2,3)$ for extended and point source respectively. Then we can define $D_{2\delta} = J_2/J_{2p}$ and $D_{3\delta} = J_3/J_{3p}$. Now.

$$\begin{aligned} J_2 &= I_2 \cos 2\delta - I_3 \sin 2\delta = DI_{2p} \cos 2\delta - I_3 \sin 2\delta \\ J_3 &= I_2 \sin 2\delta + I_3 \cos 2\delta = DI_{2p} \sin 2 + I_3 \cos 2\delta \end{aligned} \qquad (9)$$

from the definition of D, and, since $I_{3p} = 0$

$$J_{2p} = I_{2p} \cos 2\delta \quad ; \quad J_{3p} = I_{2p} \sin 2\delta \qquad (10)$$

i.e. from (9) and (10)

$$\begin{aligned} J_2 &= DJ_{2p} + I_3 \sin 2\delta \\ J_3 &= DJ_{3p} + I_3 \cos 2\delta \end{aligned} \qquad (11)$$

Clearly, in general, $D \neq D_{2\delta} \neq D_{3\delta} \neq D$. However, when the source satisfies the symmetry conditions, $I_3 = 0$, and it can be seen from equations (11) that $D = D_{2\delta} = D_{3\delta}$. Therefore, in the case when the

source satisfies the symmetry conditions, the second and third Stokes Parameters, with respect to any observer's axes, can be found by multiplying the theoretical point source expressions, referred to the same axes, by the depolarisation factor $D = I_2/I_{2p}$. No such general factor can be found for an arbitrary source that applies to any observer's axes and both the second and third Stokes Parameters.

3.4.1 Depolarising factor for a spherically symmetric source

For a uniform spherically symmetric source, the intensity is a constant, I, and there is a simple relation between I and the luminosity, L, of the sphere, viz.

$$I = L/4\pi^2 r_s^2 \qquad \text{for } \mu_s < \mu < 1 \tag{12}$$

where r_s is the radius of the source, $\mu_s = \cos \alpha_s$, where α_s is the angular radius of the source as seen from the electron. If the centre of the sphere is the origin and r is the distance of the electron from the origin, then $f(\beta) = \alpha_s$ and $\cos \alpha_s = \sqrt{1 - r_s^2/r^2}$. Hence equations (7) and (12) give

$$I_1 = \frac{L\sigma_o}{12\pi r_s^2} \{8 [1 - (1 - \frac{r_s^2}{r^2})^{\frac{1}{2}}] + \frac{r_s^2}{r^2} (1 - \frac{r_s^2}{r^2})^{\frac{1}{2}} (3 \cos^2 \gamma - 1)\}$$

$$I_2 = \frac{-L\sigma_o}{4\pi r_s} (1 - \frac{r_s^2}{r^2})^{\frac{1}{2}} \sin^2 \gamma \tag{13}$$

$$I_3 = 0$$

Now the polarisation from a point source of luminosity L scattering from a electron at distance r, with respect to the same observer's axes, is

$$I_{1p} = \frac{L\sigma_o}{4\pi r^2} (1 + \cos^2\gamma) \tag{14}$$

$$I_{2p} = \frac{-L\sigma_o}{4\pi r^2} \sin^2\gamma \quad ; \quad I_3 = 0 \quad .$$

Defining $C = I_2/I_{2p}$, from (13) and (14) we get, therefore,

$$C = \frac{8r^2[1 - (1 - r_s^2/r^2)^{\frac{1}{2}}]}{3r_s^2\,(1 + \cos^2\gamma)} + \frac{(1 - r_s^2/r^2)^{\frac{1}{2}}(3\cos^2\gamma - 1)}{3(1 + \cos^2\gamma)}$$

$$D = (1 - r_s^2/r^2)^{\frac{1}{2}} \qquad (15)$$

When $r = r_s$, $C = \dfrac{8}{3(1+\cos^2\gamma)}$ and $D = 0$

When r_s/r is small $C \sim 1 - \dfrac{r_s^2(3\cos^2\gamma - 1)}{6r^2(1 + \cos^2\gamma)} \longrightarrow 1$ as $r_s/r \longrightarrow 0$

$D \sim 1 - r_s^2/2r^2 \longrightarrow 1$ as $r_s/r \longrightarrow 0$

Note that D is precisely Cassinelli et al's depolarisation factor and that $I_1 \rightarrow I_{1p}$ and $I_2 \rightarrow I_{2p}$ as $r_s/r \rightarrow 0$, while $I_2 \rightarrow 0$ as $r_s/r \rightarrow 1$.

3.4.2 Depolarising factor for an electron on the axis of a uniform thin disc

If r_d is the radius of the disc and r is the distance of the electron from the origin at the centre of a uniform thin disc, then again $I(\alpha,\beta) = I$ and $f(\beta) = \alpha_d$ where this time $\cos\alpha_d = (1 + r_d^2/r^2)^{-\frac{1}{2}}$. Similarly to the previous example $I = L/2\pi^2 r_d^2$, where L is the luminosity of the disc. Then, following the previous example, we find

$$I_1 = \frac{L\sigma_o}{6\pi\, r_d^2}\left\{8\,[1 - (1 + r_d^2/r^2)^{-\frac{1}{2}}] + \frac{r_d^2}{r^2}\,(1 + r_d^2/r^2)^{-\frac{3}{2}}(3\cos^2\gamma - 1)\right\}$$

$$I_2 = \frac{-L\sigma_o}{2\pi\, r_d^2}\,(1 + r_d^2/r^2)^{-\frac{3}{2}}\sin^2\gamma \qquad (16)$$

$$I_3 = 0$$

and $$C = \frac{16\, r^2[1 - (1 + r_d^2/r^2)^{\frac{1}{2}}]}{3r_d^2\,(1 + \cos^2\gamma)} + \frac{2(1 + r_d^2/r^2)^{-\frac{3}{2}}\,(3\cos^2\gamma - 1)}{3(1 + \cos^2\gamma)}$$

$$D = 2(1 + r_d^2/r)^{-\frac{3}{2}} \qquad (17)$$

As $r \rightarrow 0$ $\quad C = \dfrac{16r^2[1-r/(r_d^2+r^2)^{\frac{1}{2}}]}{3r_d^2(1+\cos^2\gamma)} + \dfrac{2r^3(3\cos^2\gamma-1)}{3(r_d^2+r^2)^{\frac{3}{2}}(1+\cos^2\gamma)} \longrightarrow 0$

$$D = 2r^3/(r_d^2+r^2)^{\frac{3}{2}} \longrightarrow 0$$

When r_d/r is small $\quad C \sim 2 - \dfrac{r_d^2(3\cos^2\gamma-1)}{r^2(1+\cos^2\gamma)} \longrightarrow 2$ as $r_d/r \rightarrow 0$

$$D \sim 2 - 3r_d^2/r^2 \longrightarrow 2 \text{ as } r_d/r \rightarrow 0$$

Here as $r_d/r \rightarrow 0$, I_1 and I_2 tend to twice the value predicted by the unmodified point source expressions, while in the case of the sphere, I_1 and I_2 are always less than the point source theoretical value. This is because the flux emitted by a uniform thin disc is not isotropic but is proportional to the cosine of the angle between the line of sight and the normal to the disc. Hence, when the disc is observed edge on the flux is zero; when it is observed face on, the flux is a maximum. Since the luminosity is the flux integrated over 4π steradians, a disc will emit normal to the plane of the disc twice the flux emitted by a point source of the same luminosity. Care must, therefore, be taken in estimating the luminosity of a non-spherical source from the observed flux.

Figure 4 shows the behaviour of the depolarisation factor in these two cases.

3.5 Normalised Stokes Parameters for an electron orbiting a spherically symmetric source

For an electron orbiting a spherically symmetric source, we define a corotating reference frame as follows (see Figure 5a):

Let the origin be at the centre of the source, and let the polar axis be the normal to the orbit of the electron. Define the inclination

of the orbit, i, as the angle between the line of sight and the polar axis and let λ be the azimuthal angle of the line of sight. λ will be a function of time depending on the angular velocity of the electron. Let (r,Θ,Φ) be the polar coordinates of the electron (constant for a circular orbit).

Now, the normalised Stokes Parameters are $Q = I_2/(I_o+I_1)$ and $U = I_3/(I_o+I_1)$, where I_o is the total direct light. Since I_1 is small compared with I_o, we can approximate Q and U by I_2/I_o and I_3/I_o. Therefore

$$Q = \frac{D\sigma_o}{2r^2} \sin^2\chi \cos 2\psi$$

$$U = \frac{D\sigma_o}{r^2} \sin^2\chi \sin 2\psi \qquad (18)$$

where $D = (1 - r_s^2/r^2)^{\frac{1}{2}}$, r_s = radius of sphere

and where angles χ and ψ can be found from figure 5b, viz.

$$\sin\chi \sin\psi = \cos\Theta \sin i - \sin\Theta \cos i \cos(\lambda+\Phi)$$

$$\sin\chi \cos\psi = \sin\Theta \sin(\lambda+\Phi)$$

Hence equations (18) become

$$Q = \frac{D\sigma_o}{2r^2} \{(1-3\cos^2\Theta)\sin^2 i + \sin 2i \sin 2\Theta \cos(\lambda+\Phi) - (1+\cos^2 i)\sin^2\Theta \cos 2(\lambda+\Phi) \}$$

$$U = \frac{D\sigma_o}{r^2} \{\sin i \sin 2\Theta \sin(\lambda+\Phi) - \cos i \sin^2\Theta \sin 2(\lambda+\Phi)\} \qquad (19)$$

Note that $(\lambda+\Phi)/2\pi$ is the phase of the orbit.

As can be seen by inspection of equations (19), the effect of the extended source is merely to reduce the magnitude of Q and U in proportion (i.e. by the same factor D). Hence the shape of the Q,U locus is unchanged from the point source case. Figures 6-9 show the Q,U loci, for one electron in a circular orbit, swept out during one orbital period

for four values of Θ and i. When Θ = i, the line of sight is tangential to the orbit giving a cusp at phase = 0 (See eg. Figure 7). When $\Theta = 90^{\circ}$ or $i = 0^{\circ}$ or 90°, the Q,U locus is described twice.

For an electron in an equatorial orbit of eccentricity e, $\Theta = 90^{\circ}$ and equations (19) become

$$Q = \frac{D\sigma_o}{2r^2} \{\sin^2 i - (1 + \cos^2 i)\cos 2(\lambda+\Phi)\}$$

$$U = \frac{-D\sigma_o}{r^2} \cos i \sin 2(\lambda+\Phi) \qquad (20)$$

where now r is time dependent. If λ_o is the angle between the major axis and the projection of the line of sight on the plane of the orbit then $\lambda + \Phi - \lambda_o$ is the true anomaly of the electron. Hence

$$\tan\left(\frac{\lambda+\Phi-\lambda_o}{2}\right) = \left(\frac{1+e}{1-e}\right)^{\frac{1}{2}} \tan\frac{E}{2}$$

$$r = a(1-e\cos E) \qquad (21)$$

where E is the eccentric anomaly and a is the semi-major axis. However, E is not a linear function of time, but the mean anomaly M = E-esin E is. Now, the phase of the orbit is defined by $\emptyset = (t-t_o)/P$ where P is the period of the orbit and t_o is the time of zero phase, and $\emptyset$ = 0,0.25,0.5 and 0.75 have been marked on the Q,U loci in Figures 13-16, where these are equivalent to M=0, $\pi/2$,π, $3\pi/2$. As can be seen from Figures 13-16, when $i=90^{\circ}$, U=0 and when $\Theta \geq i$, the Q,U locus crosses itself. When e=0 and $\Theta=90^{\circ}$ the locus is a double ellipse.

3.6 Normalised Stokes Parameters for one electron corotating in a binary system

Suppose the binary system consists of two spherically symmetric sources of radii a_1 and a_2 respectively, and that the orbits are circular.

We define a corotating reference frame such that the polar axis is normal to the plane of the orbit and the x-axis is the radius vector of source 1 with respect to source 2 (see Figure 17). Let i and λ be the inclination and phase of the orbit respectively and let the coordinates of an arbitrary electron be (r_1,θ,Φ) with respect to source 1 and (r_2,θ,ϕ) with respect to source 2, where all lengths are measured in units of the separation of the sources. Then the normalised Stokes Parameters for light emitted by source 1 and scattered by the electron are

$$Q_1 = \frac{\sigma_o}{2r_1^2}\left[1-(\frac{a_1}{r_1})^2\right]^{\frac{1}{2}}\{(1-3\cos^2\theta)\sin^2 i + \sin 2i \sin 2\theta\cos(\lambda+\Phi) - (1+\cos^2 i)\sin^2\theta\cos 2(\lambda+\Phi)\}$$

$$U_1 = \frac{\sigma_o}{r_1^2}\left[1-(\frac{a_1}{r_1})^2\right]^{\frac{1}{2}}\{\sin i \sin 2\theta\sin(\lambda+\Phi) - \cos i \sin^2\theta\sin 2(\lambda+\Phi)\} \quad (22)$$

and for scattered light from source 2.

$$Q_2 = \frac{\sigma_o}{2r_2^2}\left[1-(\frac{a_2}{r_2})^2\right]^{\frac{1}{2}}\{(1-3\cos^2\theta)\sin^2 i + \sin 2i \sin 2\theta\cos(\lambda+\Phi) - (1+\cos^2 i)\sin^2\theta\cos 2(\lambda+\Phi)\}$$

$$U_2 = \frac{\sigma_o}{r_2^2}\left[1-(\frac{a_2}{r_2})^2\right]^{\frac{1}{2}}\{\sin i \sin 2\theta\sin(\lambda+\phi) - \cos i \sin^2\theta\sin 2(\lambda+\phi)\} \quad (23)$$

Hence, the total Stokes parameters for an arbitrary electron are

$$Q = f\,Q_1 + (1-f)Q_2 \quad ; \quad U = f\,U_1 + (1-f)U_2 \quad (24)$$

where f is the fraction of the total luminosity emitted by source 1.

Now, from Figure 17 we have

$$\begin{aligned} r_2^2 &= r_1^2 + 1 + 2r_1 \sin\theta\cos\Phi \\ \cos\theta &= r_1/r_2 \cos\theta \\ \sin\theta\sin\phi &= r_1/r_2 \sin\theta\sin\Phi \\ \sin\theta\cos\phi &= r_1/r_2 \sin\theta\sin\Phi + 1/r_2 \end{aligned} \quad (25)$$

We require expressions for $\cos^2\theta$, $\sin 2\theta\cos\phi$, $\sin 2\theta\sin\phi$, $\sin^2\theta\cos 2\phi$ and $\sin^2\theta\sin 2\phi$. These are

$$\cos^2\theta = (r_1/r_2)^2 \cos^2\Theta$$

$$\sin 2\theta \cos\phi = (r_1/r_2)^2 \sin 2\Theta \cos\Phi + 2r_1/r_2^2 \cos\Theta$$

$$\sin 2\theta \sin\phi = (r_1/r_2)^2 \sin 2\Theta \sin\Phi \qquad (26)$$

$$\sin^2\theta \cos 2\phi = (r_1/r_2)^2 \sin^2\Theta \cos 2\Phi + 2r_1/r_2^2 \sin\Theta \cos\Phi + 1/r_2^2$$

$$\sin^2\theta \sin 2\phi = (r_1/r_2)^2 \sin\Theta \sin 2\Phi + 2r_1/r_2^2 \sin\Theta \sin\Phi$$

As in the previous section, equations (22) - (26) are for one electron only. However the Stokes Parameters of an optically thin cloud of N electrons can be approximated by multiplying the relevant equations (i.e. (19) or (20) for one source or (24) for a corotating cloud in a binary) by N and using the coordinates of the centre of the cloud as long as the 'size' of the cloud is small compared to the distance of the cloud from the source. The case of scattering off an extended spatial distribution of electrons is dealt with more fully in the next section.

Figures 18-20 show Q,U loci and Q,U against phase (λ) for a variety of parameter values. Figures 21-29 show Q,U loci for a matrix of i,Θ values. For each locus $a_1 = a_2 = 0.2$ and r_1,f and Φ are constant for each matrix of loci. Figures 30-32 show Q,U loci for a range of f values for 3 sets of parameters. However, the loci for f = 0.8 and f=1 have been scaled down by a factor 2 compared to the others since the size of the shape generally increases with f, the electron being closer to source 1 than to source 2 for the parameter sets chosen. Finally, Figures 33 and 34 show Q,U loci for 2 parameters sets and a range of Φ values. Equal phase intervals of 0.25 have been marked on all loci in Figures 21-34, except on those loci which are too small. Here the phase is equivalent to $\lambda/2\pi$. For all parameter sets, when $i=0^\circ$ or $\Theta = 90^\circ$ the locus is a double ellipse and when $i=\Theta=90^\circ$, U=0. When f=1 or 0, the equations reduce to those of the previous case. Also, as r_1 increases the difference in the angles of incidence of the

light from the two sources at the electron decreases. As a result, the Stokes Parameters for the binary tend to those of a single source at the centre of mass of the system with the same luminosity as the two binary sources as the distance of the electron from the binary increases, (assuming no eclipses of the sources as seen from the electron).

3.7 Extended Scattering Regions

So far we have dealt with an extended light source scattering off only one electron, or two extended sources still scattering off one electron. We now consider the more realistic situation of an extended light source scattering off an extended spatial distribution of electrons, still in the optically thin limit.

Suppose the light source is centred on origin 0 and that the electrons have number density $n(r,\theta,\phi)$ at the point with spherical polar coordinates centred on 0, with ϕ measured from the plane containing the line of sight, which is at angle i to 0Z(Figure 35). Then the equations of the previous sections apply to an elementary scattering volume dV when multiplied by the number of electrons in dV viz. ndV. Now, for scattering volume at S, we measure I_2(or Q) in the plane OSE, perpendicular to OE. For the total Stokes Parameters we wish to integrate the relevant equations over all V. In general, this requires a return to equations (4) and (5) and a simultaneous integration over both α and β and V. since a source which satisfies the symmetry conditions from a particular dV need not satisfy them for all dV. In fact, it can only satisfy the symmetry conditions from all dV for general extended scattering volumes if the source is spherically symmetric, though possibly limb darkened, or if the scattering volume extends only along an axis of symmetry such as an accretion disk illuminating a narrow coaxial jet.

Here we will restrict ourselves to those cases where the source is axially symmetric for all scattering volumes dV.

Some of the scattering material will be occulted by the finite light source and the corresponding ΔV should be omitted from the integral (cf. Milgrom, 1978). However, the material concerned is that which backscatters light, and so it contributes little to the polarisation. Therefore, we will not consider this further.

The direction of the scattering polarisation will vary with the direction $\underset{\sim}{r}$ of the scattering element dV at S, as also will the value of γ (the angle between the line of sight and $\hat{\underset{\sim}{t}}$). To obtain the Stokes Parameters from the entire volume V we must therefore integrate the local contributions ΔI_2 along a common polarimetric reference (Q_o, U_o) with the local γ value. We define Q_o to be in the plane OEZ. Since the source is axially symmetric, the contributions to I_1, I_2 and I_3 from volume dV are, by equations (8)

$$\left.\begin{matrix} dI_1 \\ dI_{Q_o} \\ dI_{U_o} \end{matrix}\right\} = \pi\sigma_o n(\underset{\sim}{r})dV \times \left\{\begin{matrix} \int_{\mu_o}^{1} I(\mu)\,[3-\mu^2]d\mu + \cos^2\gamma \int_{\mu_o}^{1} I(\mu)\,[3\mu^2-1]\,d\mu \\ \sin^2\gamma\cos\,2\Omega \int_{\mu_o}^{1} I(\mu)[3\mu^2-1]\,d\mu \\ \sin^2\gamma\sin\,2\Omega \int_{\mu_o}^{1} I(\mu)\,[3\mu^2-1]d\mu \end{matrix}\right. \qquad (27)$$

where Ω is the rotation of the I_2 axis with respect to the Q_o axis. Here γ and Ω depend on i, θ and ϕ in a way determined by the geometry of Figures 35 and 36.

Now, for an isotropic point source at the origin, of the same total luminosity as the extended source, the corresponding contributions to I_1, I_2 and I_3 are

$$\left.\begin{matrix} dI_1 \\ dI_{Q_o} \\ dI_{U_o} \end{matrix}\right\} = \frac{L\sigma_o n(\underset{\sim}{r})dV}{4\pi\, r^2} \left\{\begin{matrix} (1+\cos^2\gamma) \\ \sin^2\gamma\,\cos\,2\Omega \\ \sin^2\gamma\,\sin\,2\Omega \end{matrix}\right. \qquad (28)$$

Hence, from the definitions of Section 3.4 of C and D we get from equations (27) and (28)

$$C(r,\gamma) = \frac{4\pi^2 r^2 \left[\int_{\mu_o}^{1} I(\mu)(3-\mu^2)d\mu + \cos^2\gamma \int_{\mu_o}^{1} I(\mu)(3\mu^2-1)d\mu\right]}{L(1+\cos^2\gamma)} \qquad (29)$$

$$D(r) = \frac{L\pi^2 r^2}{L} \int_{\mu_o}^{1} I(\mu)(3\mu^2-1)d\mu \qquad (30)$$

Note that D depends on r only, while C depends on r and γ. For a uniform spherically symmetric source D reduces to $(1 - r_s^2/r^2)^{\frac{1}{2}}$ (cf. equations (15)), i.e. Cassinelli et al's depolarisation factor, now extended to arbitrary spatially extended distributions of electrons. Hence, on integrating equations (27) over V with $dV = r^2 \sin\theta\, dr\, d\theta\, d\phi$, and using equations (29) and (30), we get

$$\left.\begin{matrix} I_1 \\ I_{Q_o} \\ I_{U_o} \end{matrix}\right\} = \frac{L\sigma_o}{4\pi} \int_o^{2\pi} \int_o^{\pi} \int_{r_{min}}^{\infty} n(r,\theta,\phi)\sin\theta\, dr\, d\theta\, d\phi \times \left\{\begin{matrix} C(r,\gamma)(1+\cos^2\gamma) \\ D(r)\sin^2\gamma\cos 2\Omega \\ D(r)\sin^2\gamma\sin 2\Omega \end{matrix}\right. \qquad (31)$$

where expressions for $\cos^2\gamma$, $\sin^2\gamma\cos 2\Omega$ and $\sin^2\gamma\sin 2\Omega$ can be found from Figure 36

$$\cos^2\gamma = \cos^2 i \cos^2\theta + \sin^2 i \sin^2\theta\cos^2\phi + \tfrac{1}{2}\sin 2i \sin 2\theta \cos\phi$$
$$\sin^2\gamma\cos 2\Omega = -\sin^2 i + \sin^2\theta[\sin^2 i + \sin^2\phi - \cos^2 i \cos^2\phi] + \tfrac{1}{2}\sin 2i \sin 2\theta \cos\phi \qquad (32)$$
$$\sin^2\gamma\sin 2\Omega = \sin i \sin 2\theta \sin\phi - \cos i \sin^2\theta \sin 2\phi$$

These expressions are essentially identical to equations (3) since we are now integrating over emergent ray paths in precisely the same way as we did before over incident ray paths.

We have shown that, provided we are dealing with a situation where the source looks axisymmetric from all scattering points then D is a function of

r only. Since D appears in the equations for both I_{Q_o} and I_{U_o} we can then calculate these quantities for <u>any</u> spatial distribution of scatterers using the point light source equations if we replace the real number density distribution by a weighted function $n_{eff} = D(r)n(r,\theta,\phi)$. For example, equations (22)-(26), when multiplied by $n(\underset{\sim}{r})dV$ and integrated over the volume V of a corotating Thomson scattering envelope, give equations (7) of Brown <u>et al.</u> 1978 on replacing the number density distribution by n_{eff}, provided the scattered light can be neglected.

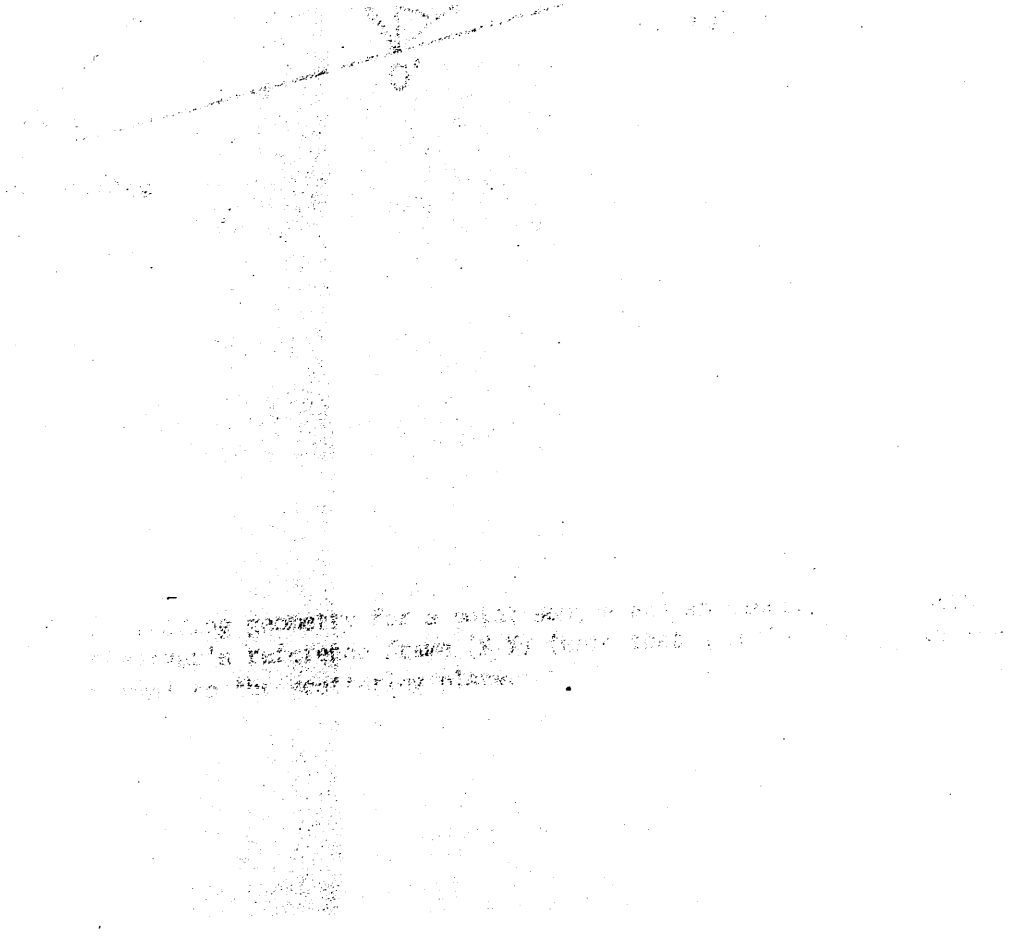

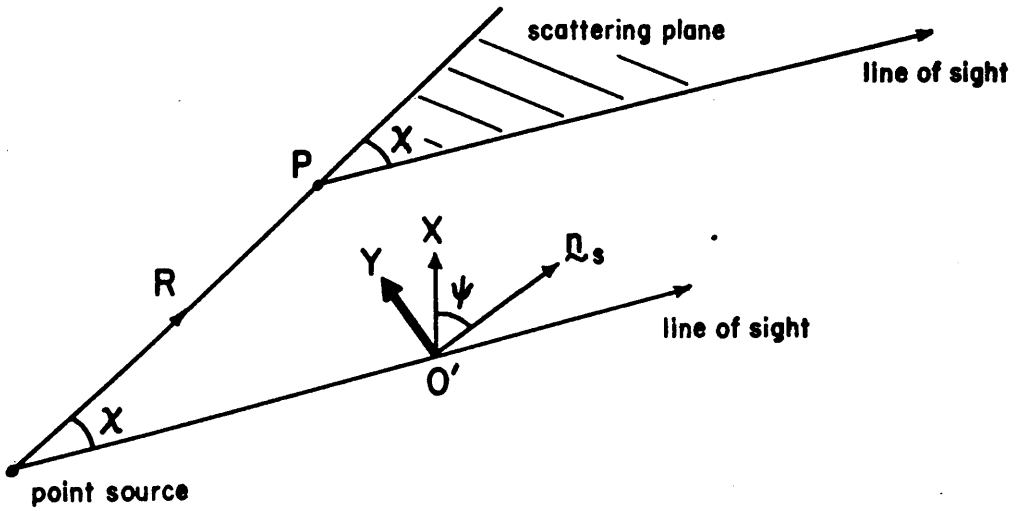

Figure 1: Scattering geometry for a point source and an electron at P with observer's reference frame (X,Y) (note that $\angle XO'Y=45°$). $\underline{n}_s$ is the normal to the scattering plane.

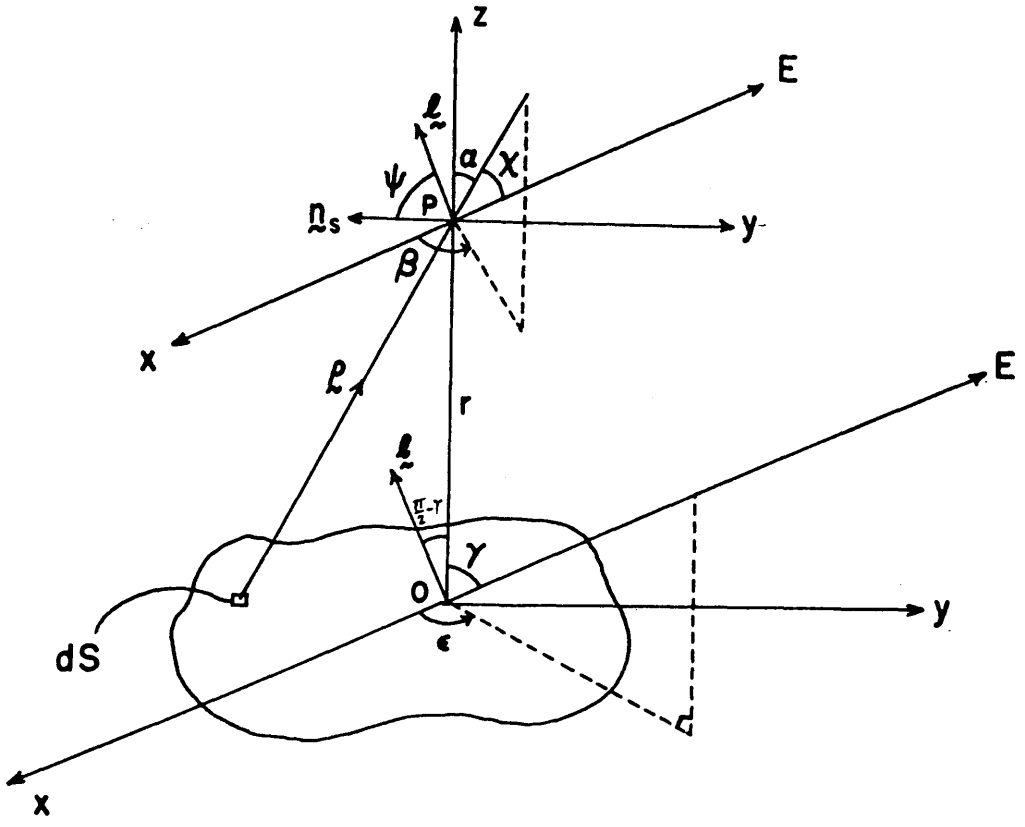

Figure 2: Scattering geometry for a surface element, dS, of an arbitrary source scattering from an electron at P, distance r from origin O. $\underset{\sim}{\rho}$ is the position vector of the electron with respect to the source element, defined by angles (α,β) with respect to the (x,y,z) cartesian coordinate system. OE is the line of sight, defined by (γ,ε). $\underset{\sim}{n}_s$ is the normal to the scattering plane; $\underset{\sim}{l}$ is perpendicular to OE and lies in the same plane as OE and Oz.

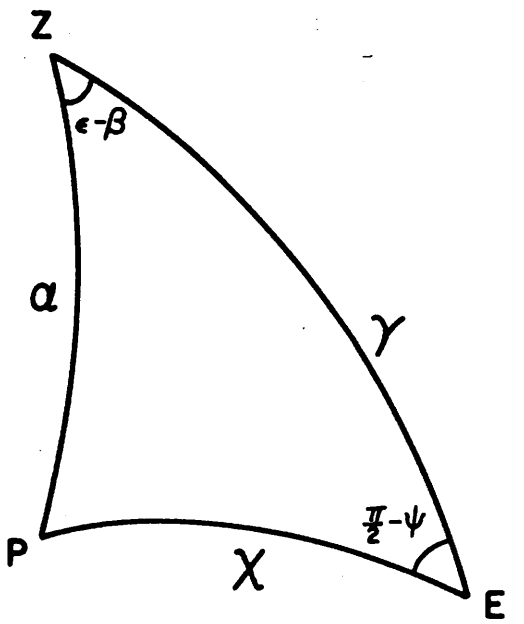

Figure 3: Spherical triangle from Figure 2 for the transformation from (χ,ψ) to (α,β).

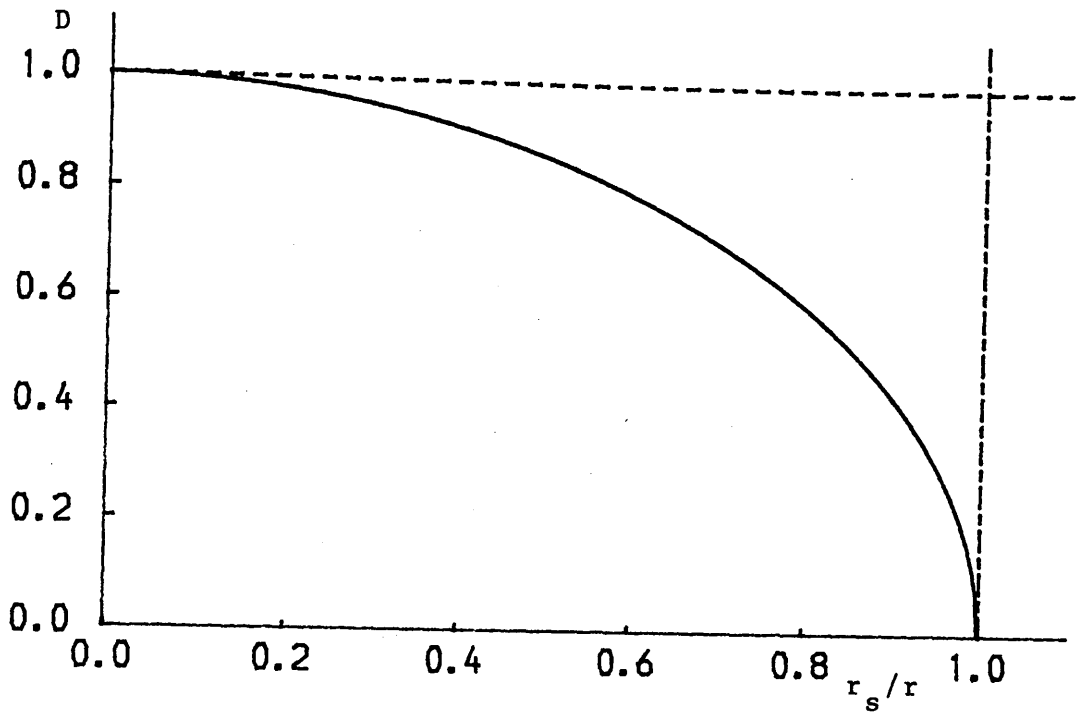

(a)

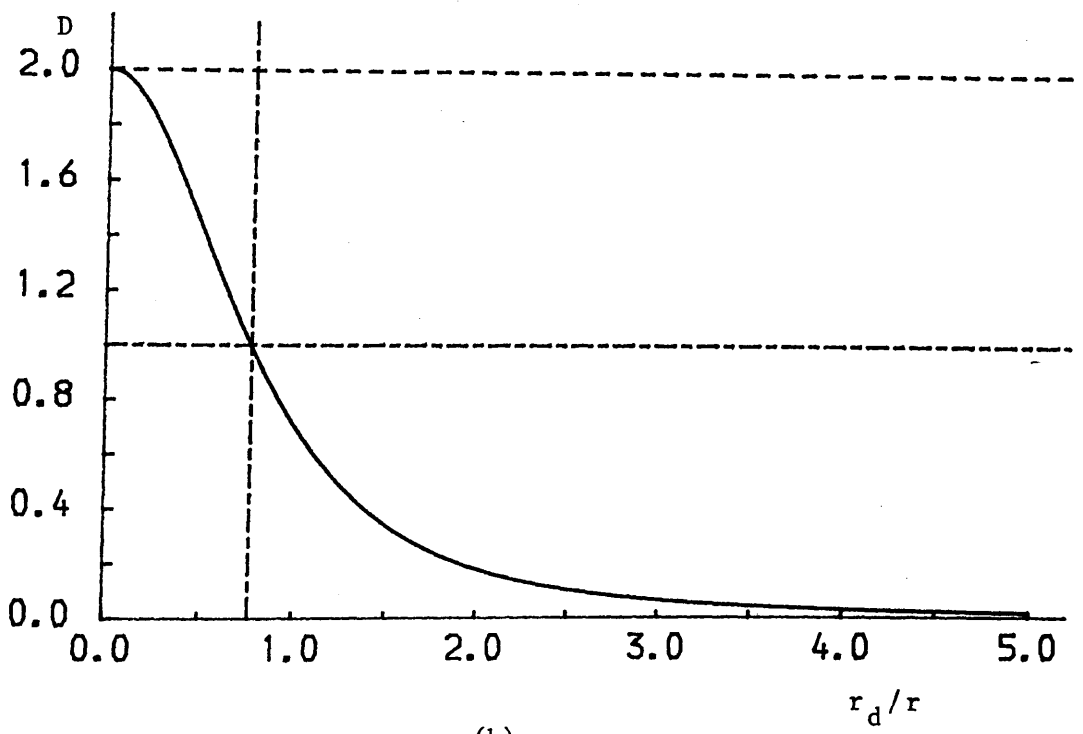

(b)

Figure 4: Depolarisation factor against ratio of radius of source to electron distance for
a) a spherically symmetric source
b) an electron on axis of uniform thin disc

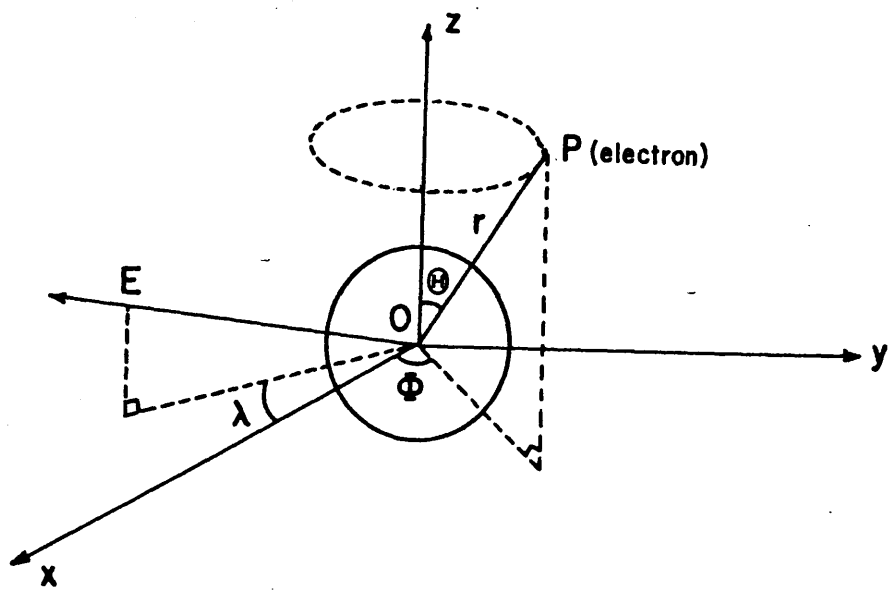

(a)

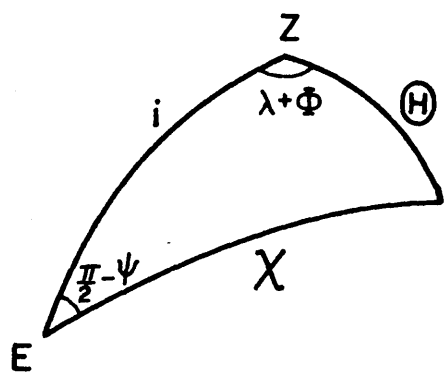

(b)

Figure 5: (a) Scattering geometry for an electron in a circular orbit about a spherical light source. OE is the line of sight. The (x,y,z) coordinate system corotates with the electron.
(b) Spherical triangle from (a) for transformation from (χ,ψ) to (r,Θ,Φ) coordinates.

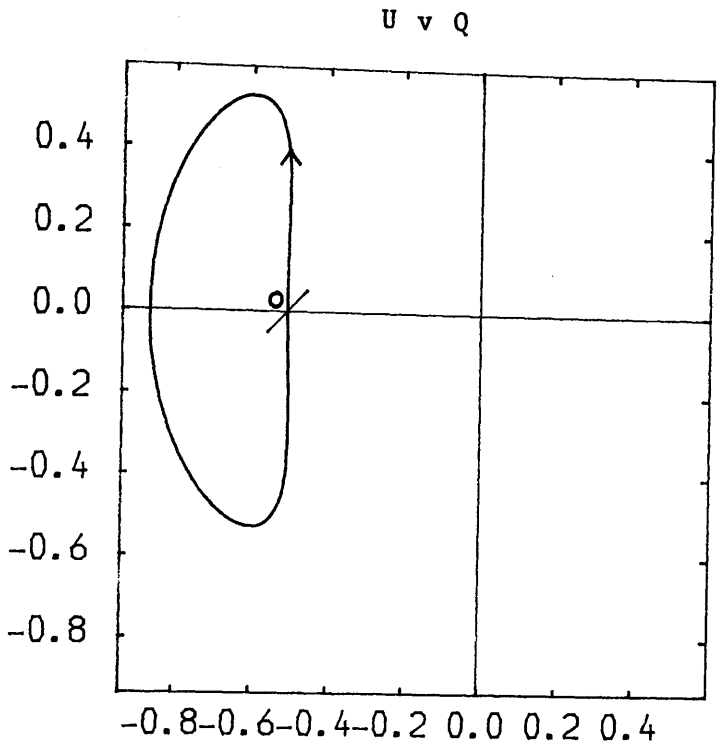

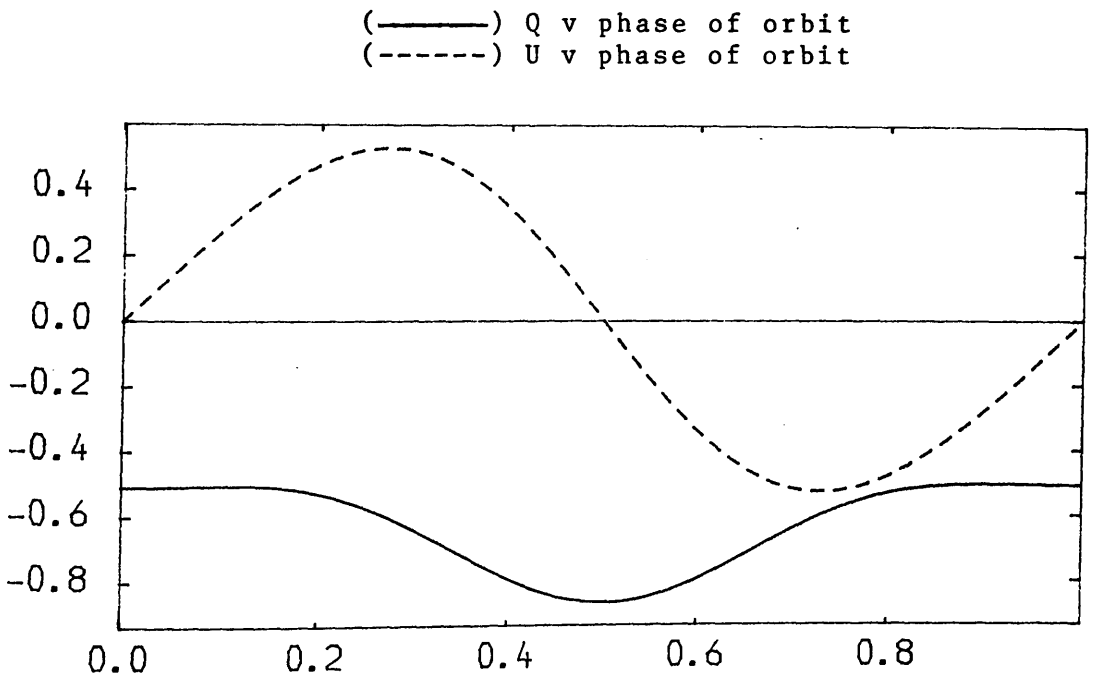

Figure 6: Stokes Parameters for one electron orbiting a spherically symmetric source. The angle between the radius vector and the normal to the orbit, $\Theta = 20°$. The angle between the line of sight and the normal to the orbit, $i = 70°$. The radius of the source, in units of the electron distance from the centre of the source, $R_s = 0.5$

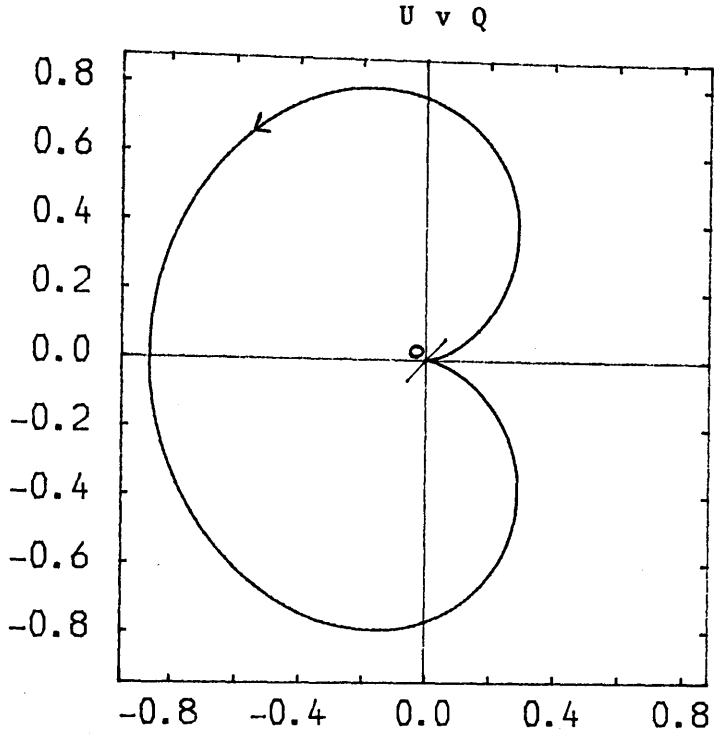

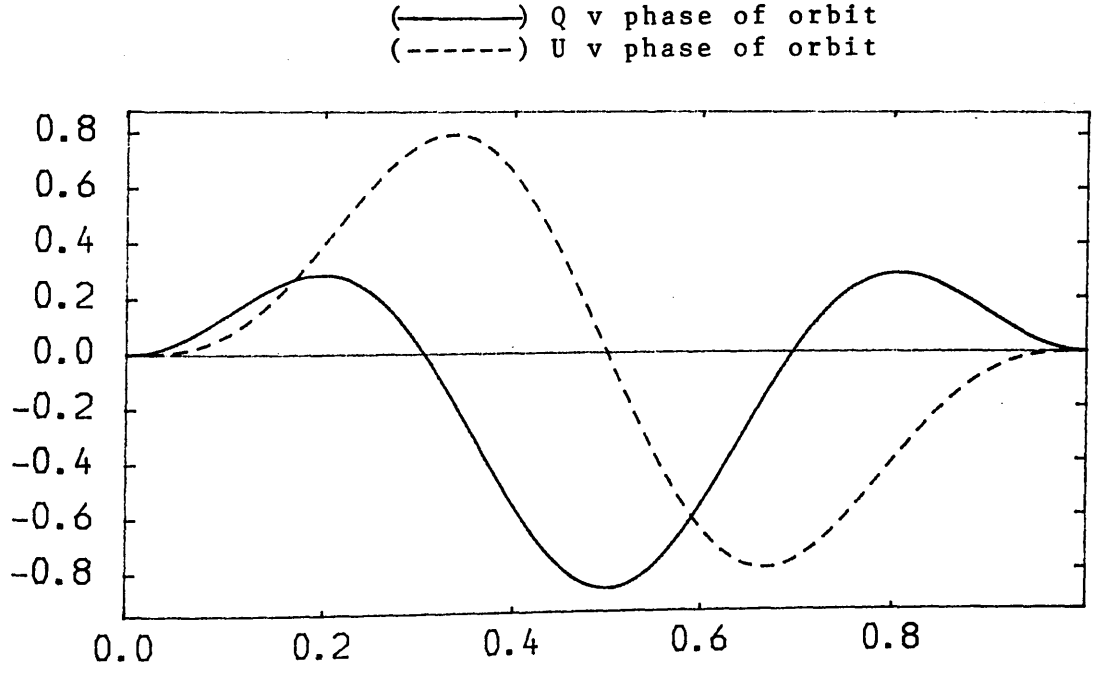

Figure 7: As Figure 6 for $\Theta = 45°$, $i = 45°$

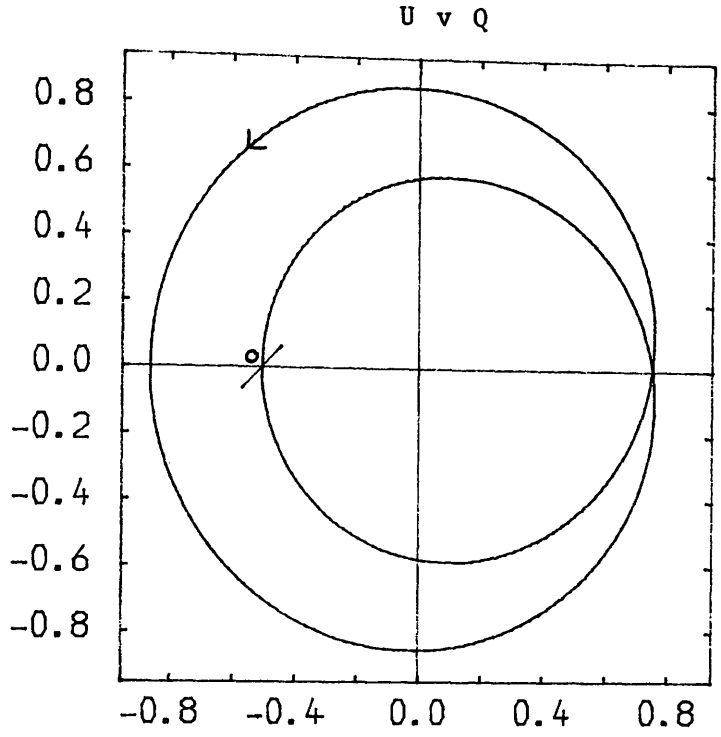

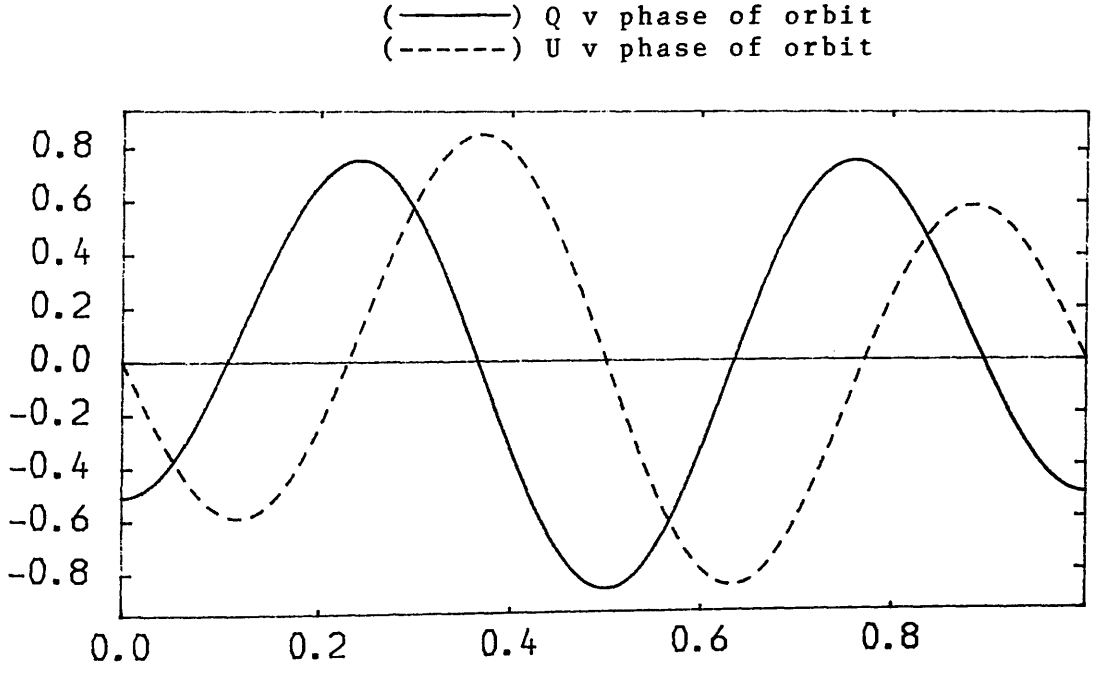

Figure 8: As Figure 6 for Θ = 70°, i = 20°

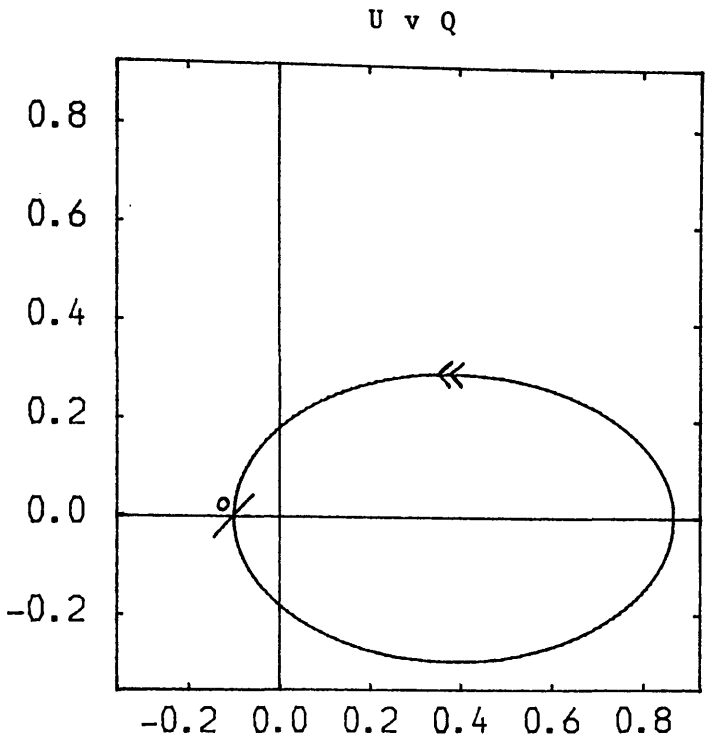

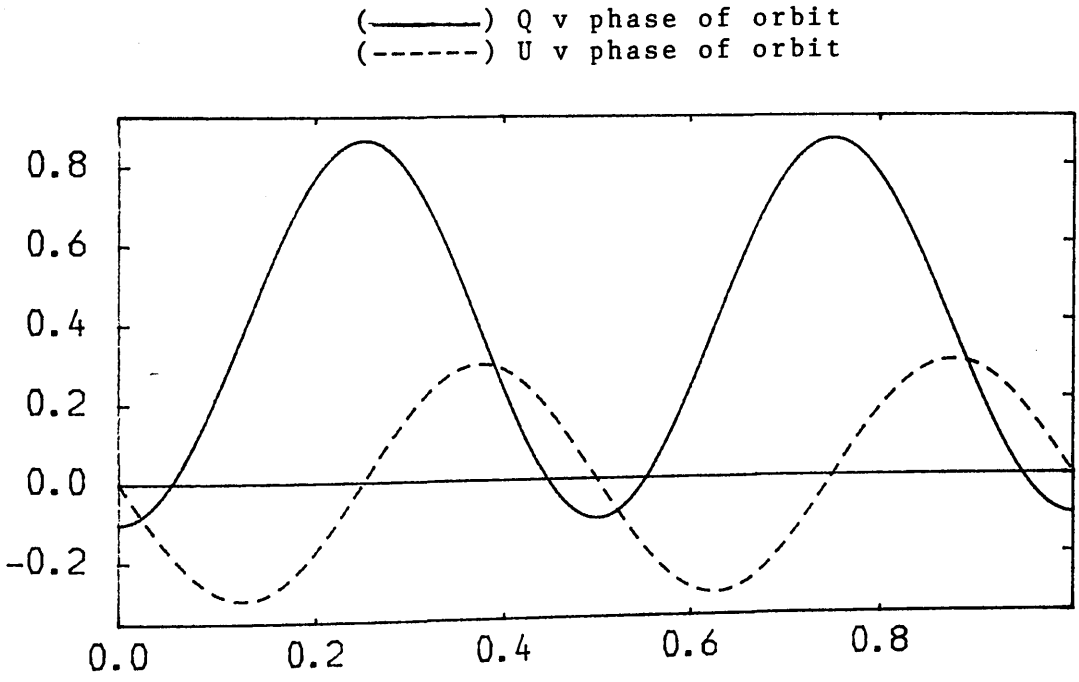

Figure 9: As Figure 6 for $\Theta = 90°$, $i = 70°$, $R_s = 0.5$

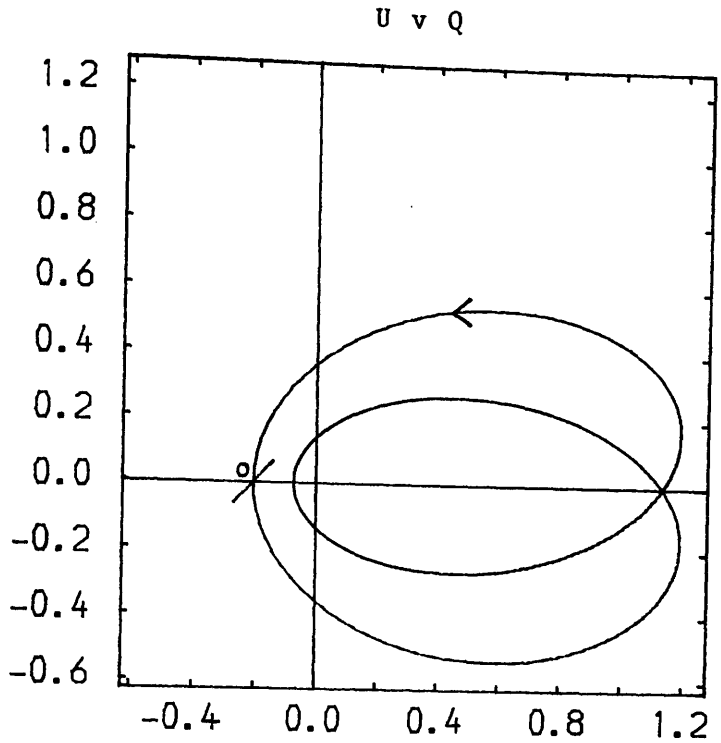

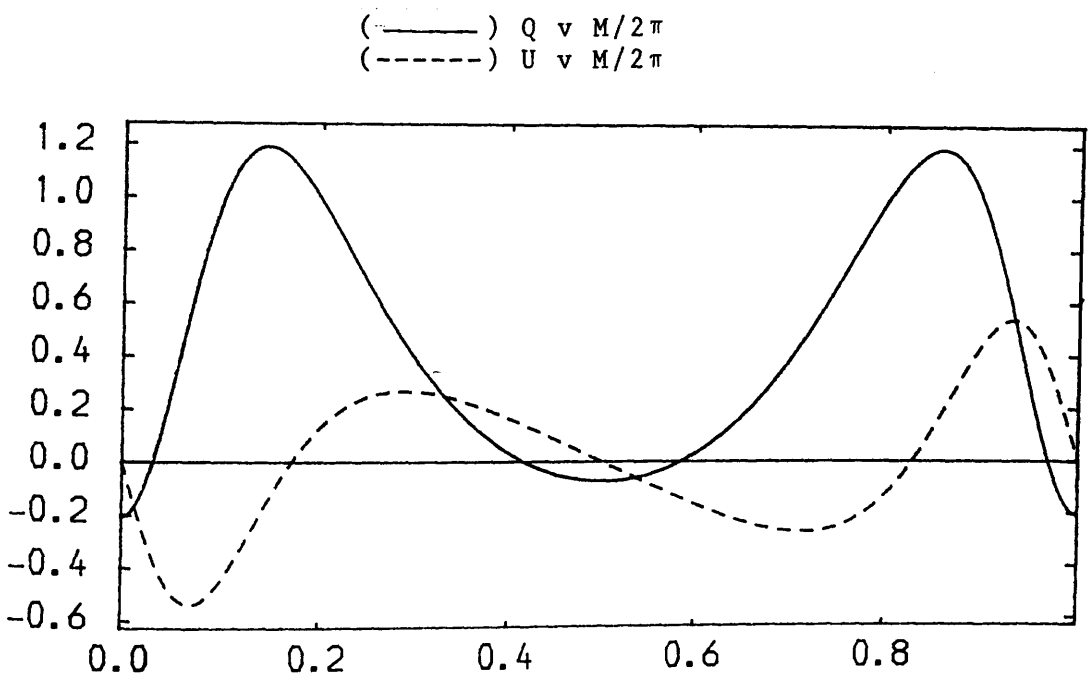

Figure 10: Stokes Parameters for one electron in an eccentric orbit about a spherical source. The angle between the line of sight and the normal to the orbit, i = 70°. The eccentricity of the orbit, e = 0.25. The longitude of periastron, λ_o = 0°. The radius of the source in units of the semi-major axis, R_s = 0.1

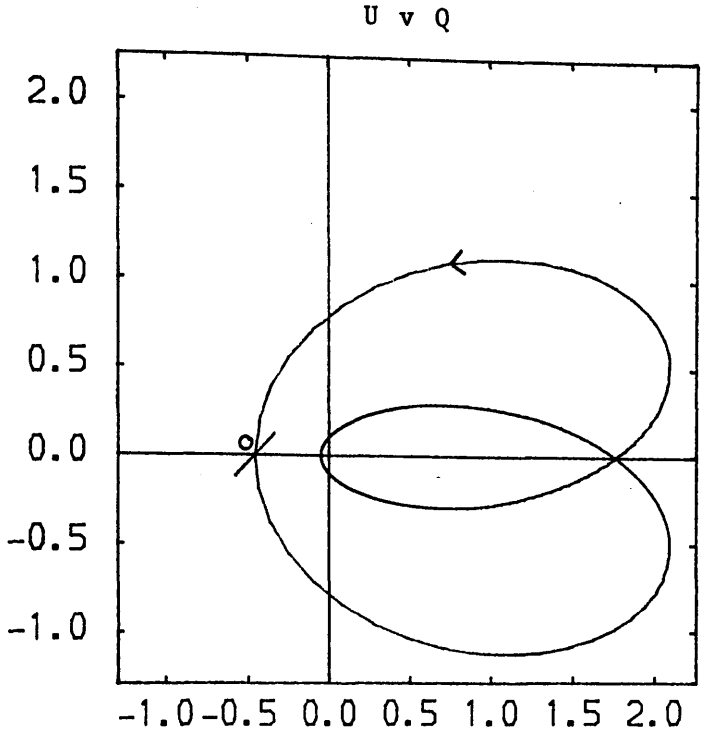

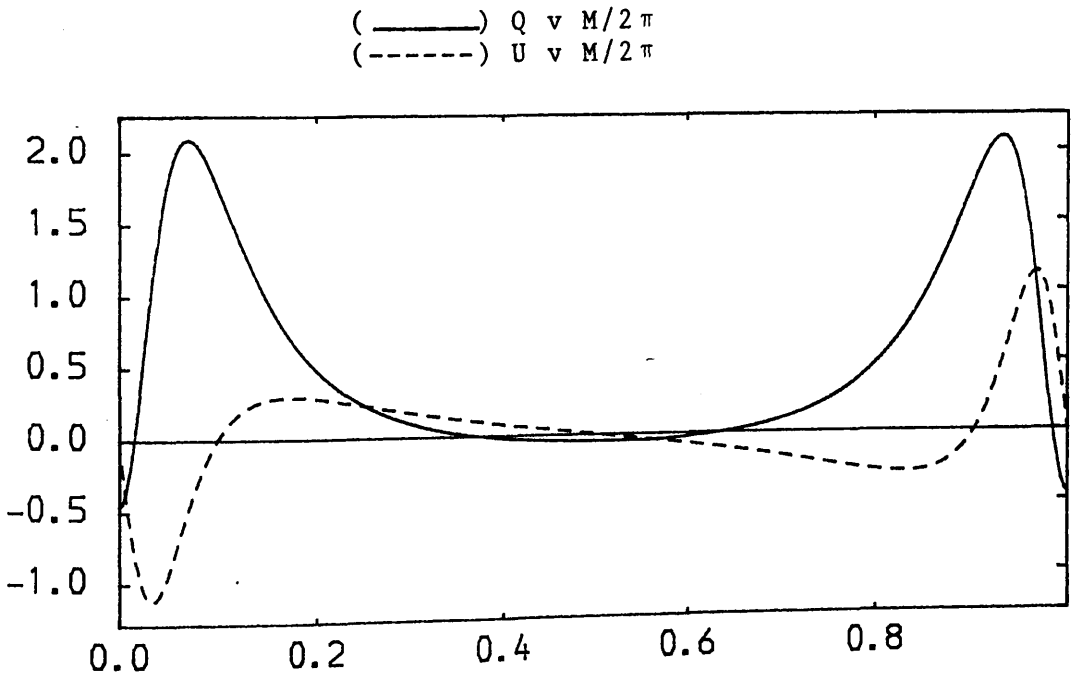

Figure 11: As Figure 10 for e ± 0.5

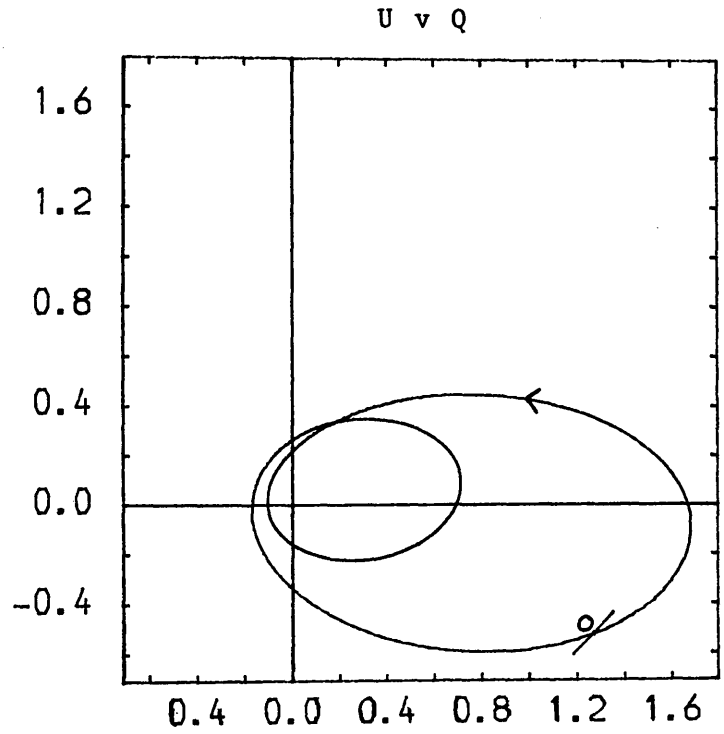

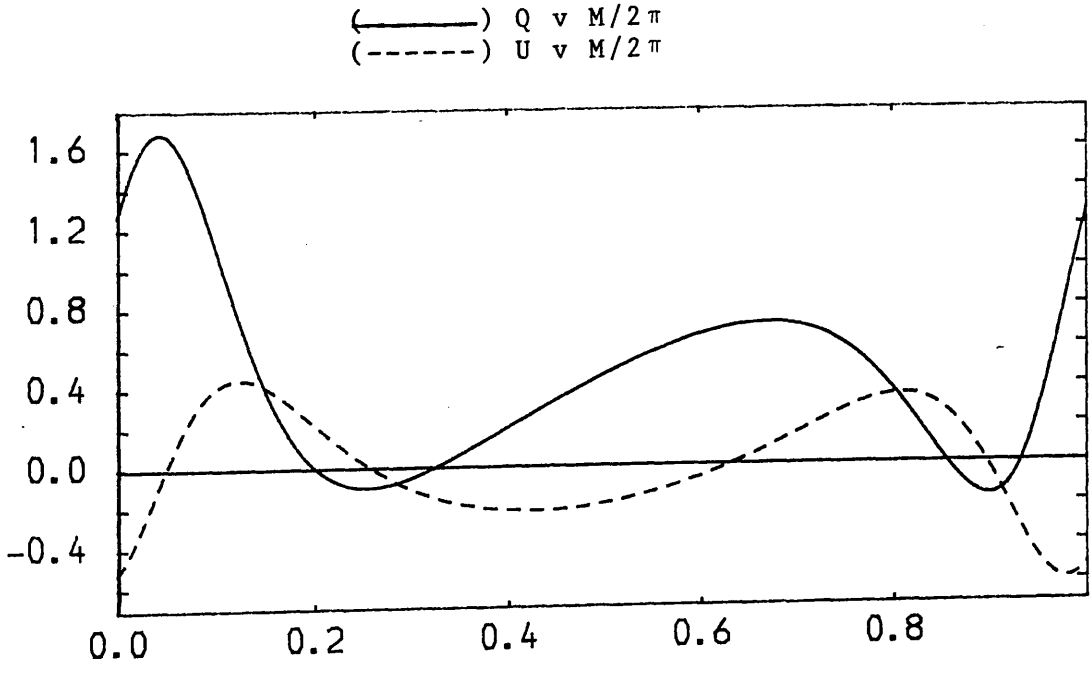

Figure 12: As Figure 10 for $\lambda_o = 60°$

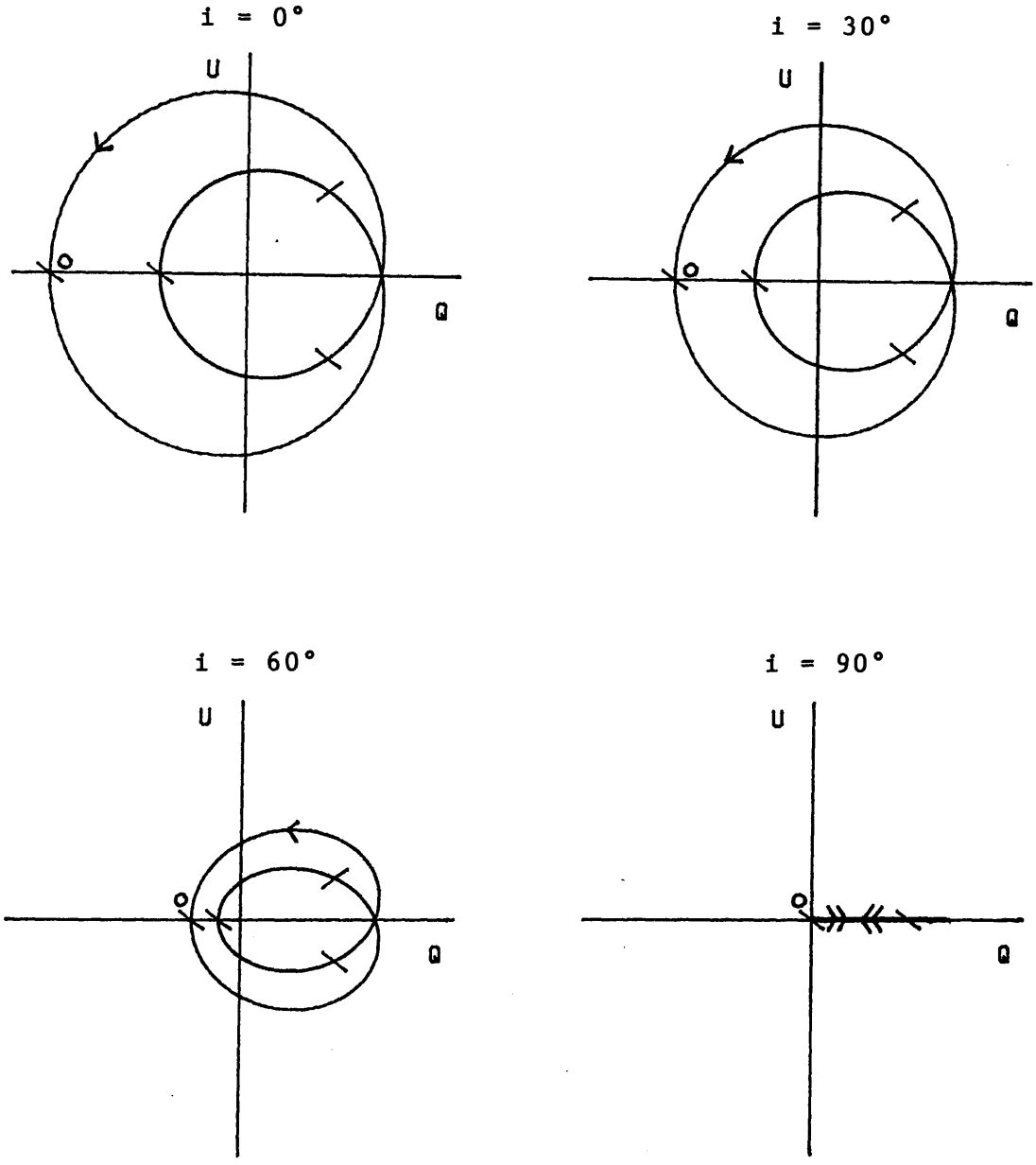

Figure 13: Stokes Parameters for an electron in an eccentric orbit, of eccentricity, e = 0.2 and longitude of periastron, λ_o = 0°, about a spherically symmetric, uniform source for a range of inclination angles, i.

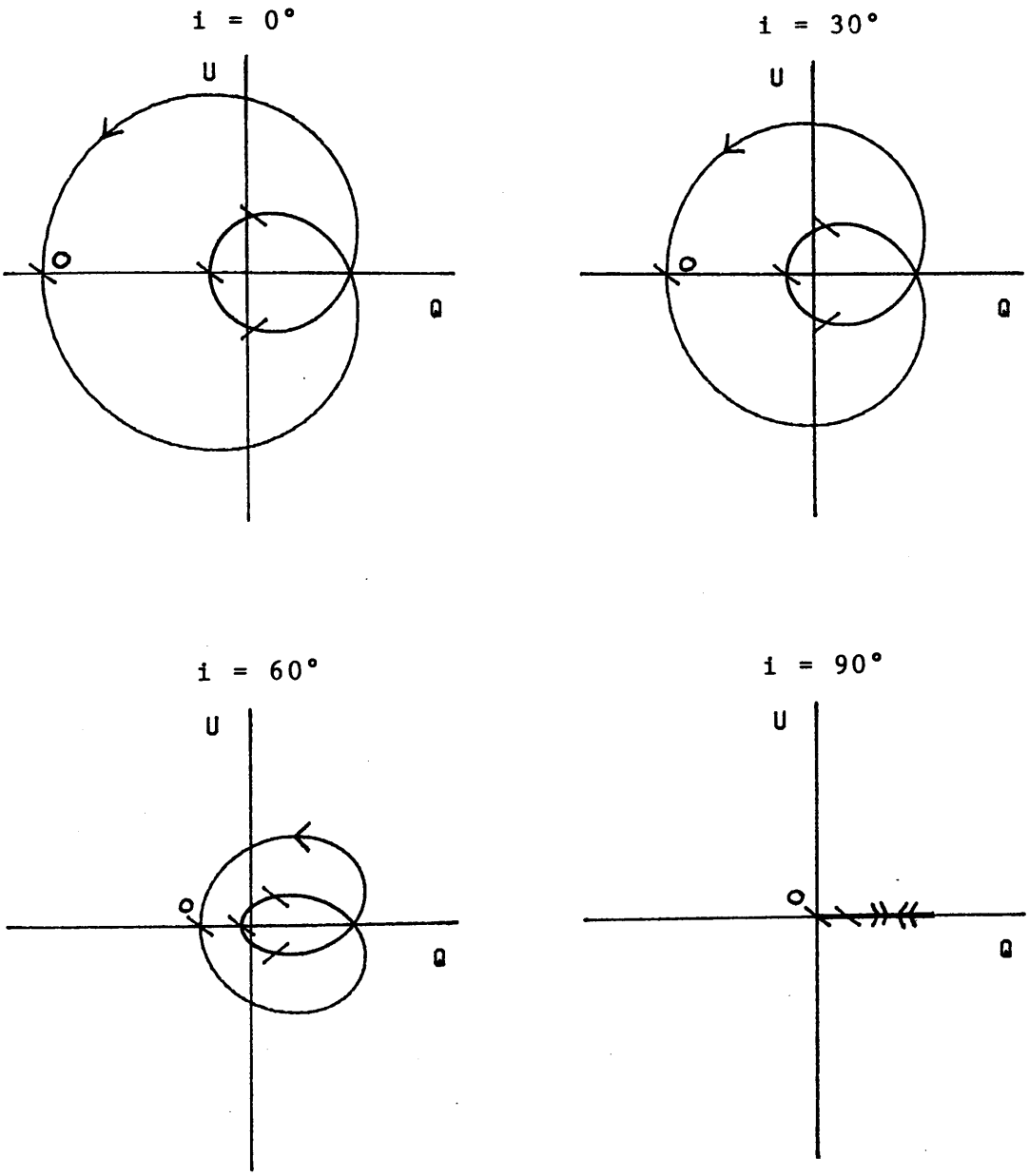

Figure 14: As Figure 13 for e = 0.4 and $\lambda_o = 0^o$

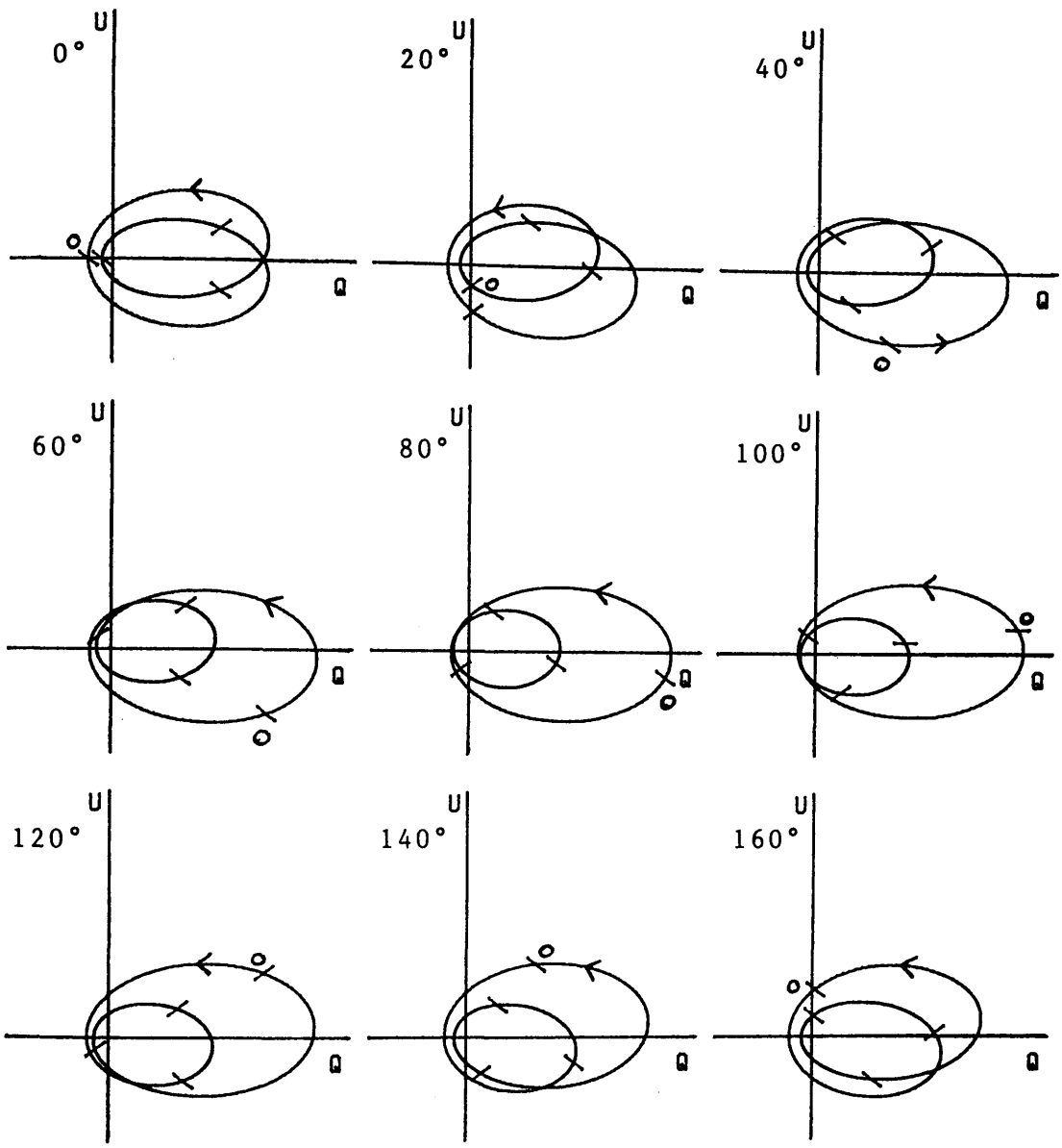

Figure 15: Stokes Parameters for an electron in an eccentric orbit, of eccentricity e = 0.2 and inclination i = 70°, about a spherically symmetric, uniform source, for a range of values of the longitude of periastron, λ_o (degrees).

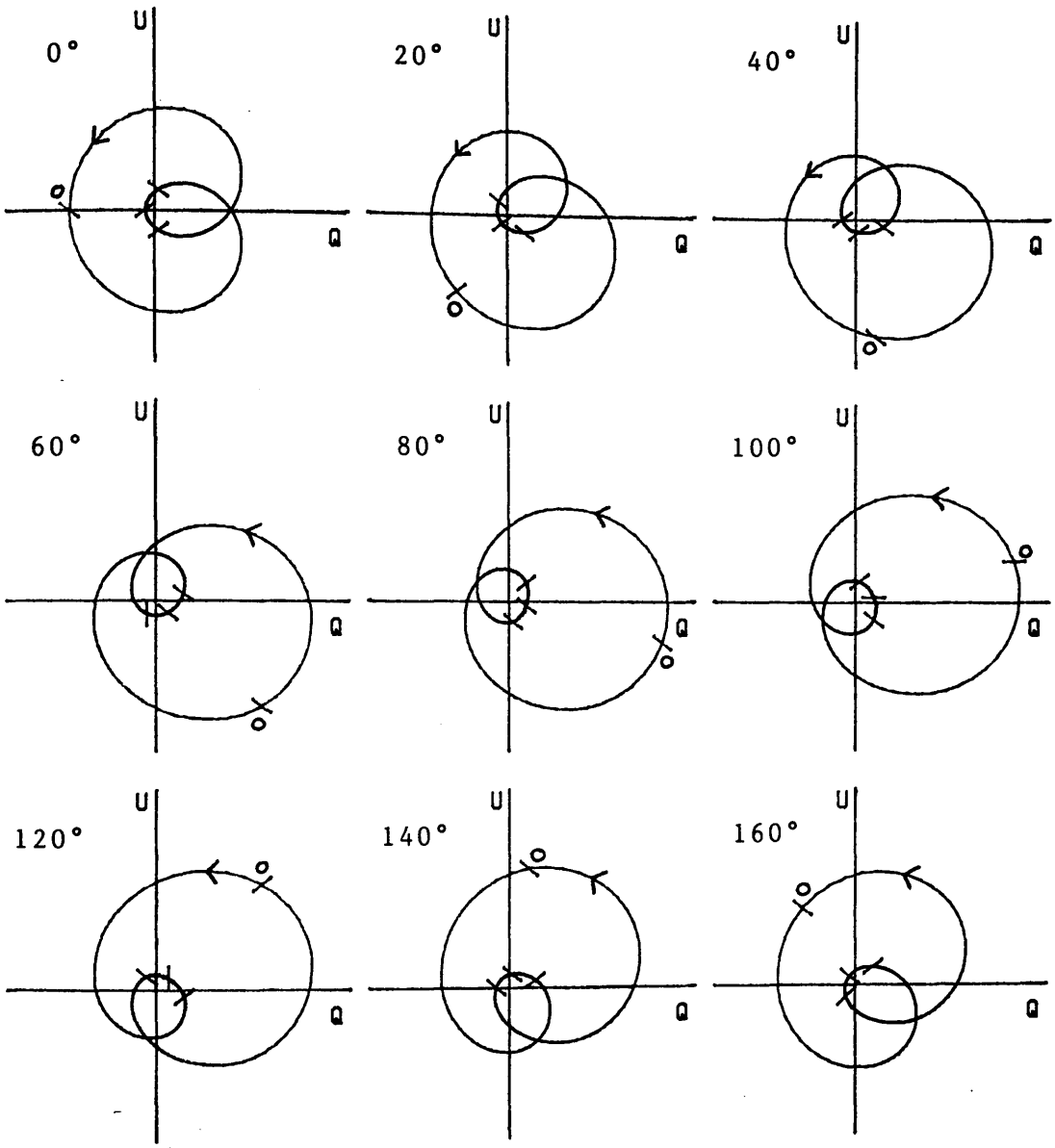

Figure 16: As Figure 15 for e = 0.5 and i = 45°

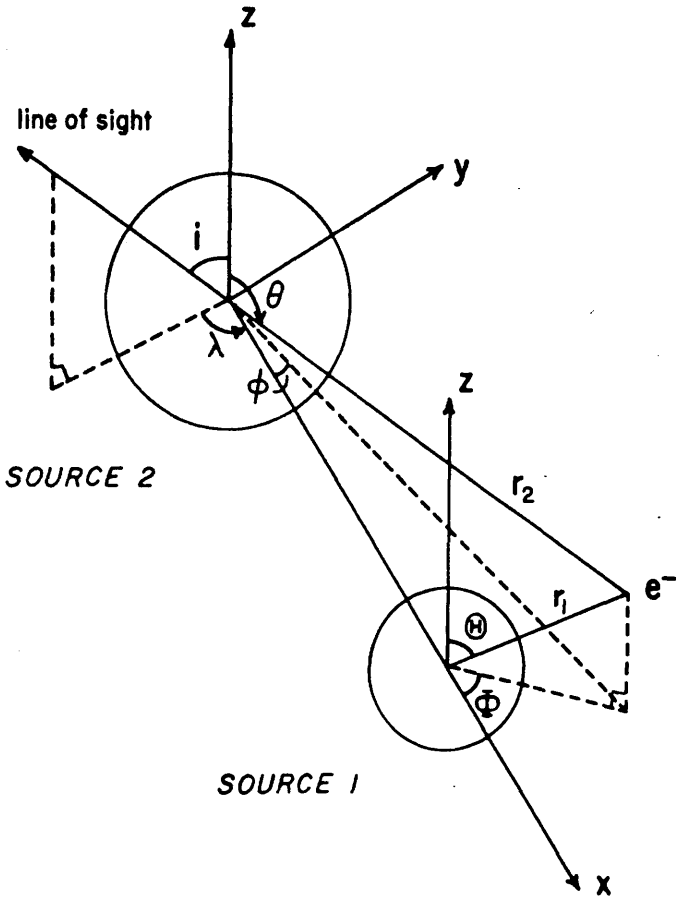

Figure 17: Scattering geometry for an electron corotating in a binary system. The electron has coordinates (r_1,Θ,Φ) with respect to source 1 and (r_2,θ,ϕ) with respect to source 2 in a corotating reference frame. The line of sight is defined by angles i (inclination) and λ (phase of orbit). Note that the z-axis is perpendicular to the orbital plane of the binary.

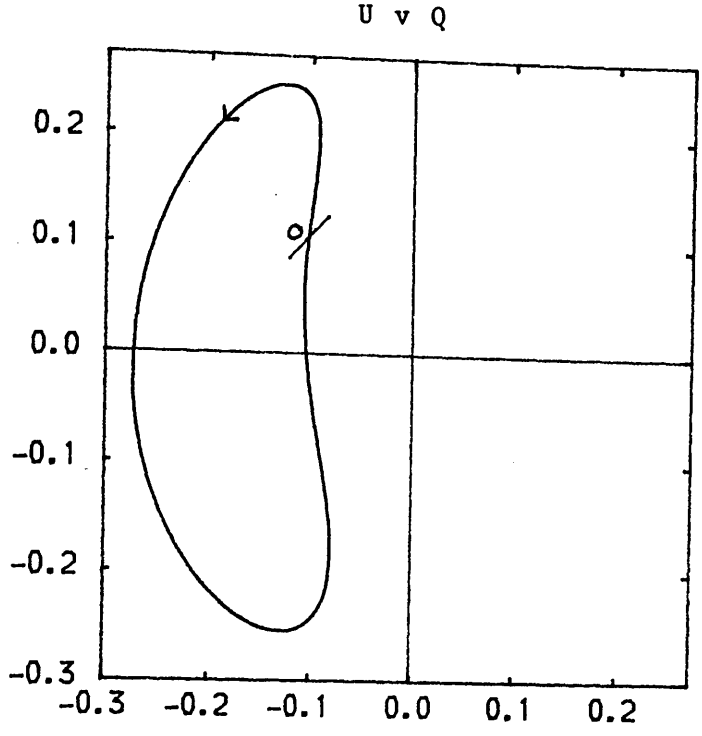

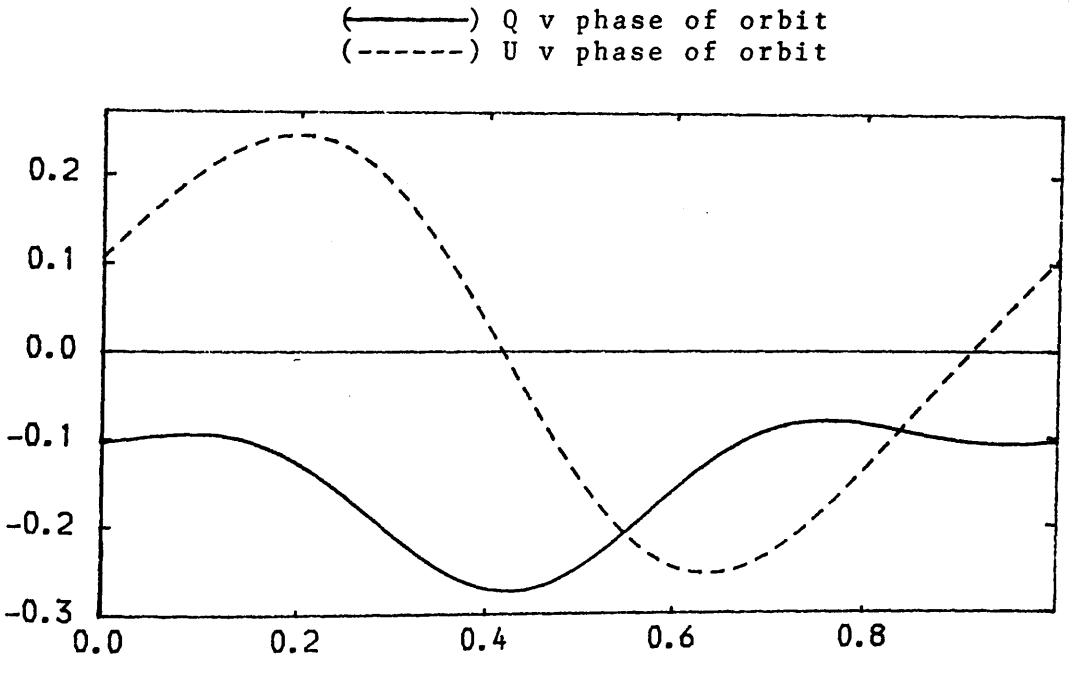

Figure 18: Stokes Parameters for one electron corotating in a circular binary system of unit radius and inclination, i = 70°. The spherically symmetric sources have radii, a_1 = 0.1 and a_2 = 0.8 and the fraction of the total luminosity emitted by source 1, f = 0.1. The position of the electron with respect to source 1 (r , Θ , Φ) is (2,20°,45°).

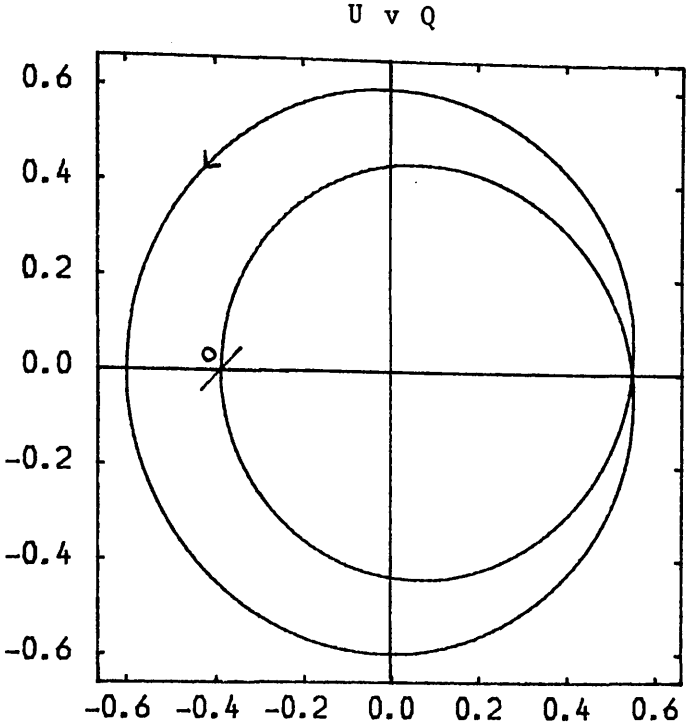

(———) Q v phase of orbit
(------) U v phase of orbit

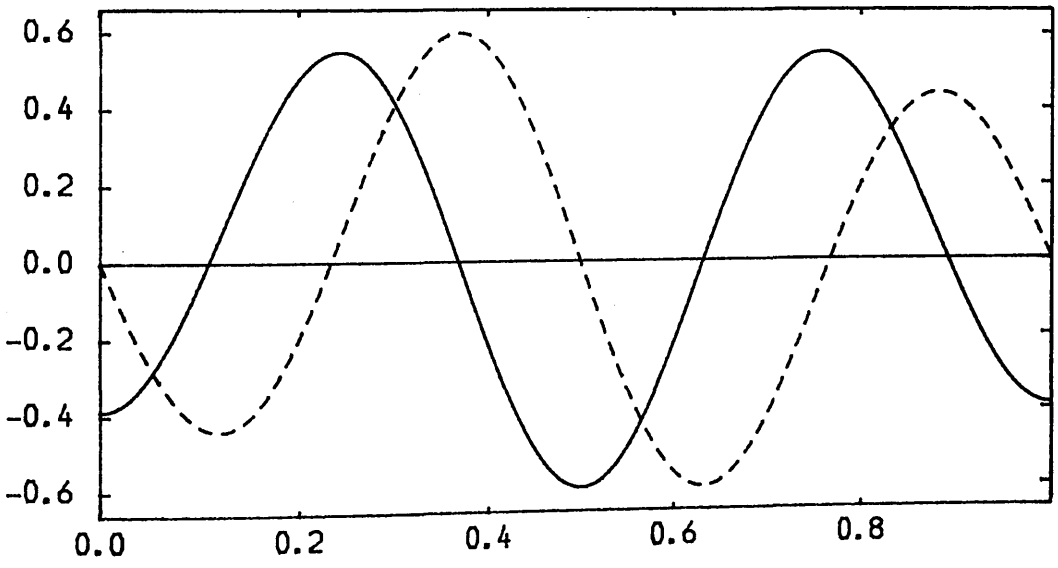

Figure 19: As Figure 18 for i = 20°, a_1 = 0.5, a_2 = 0.1
f = 0.2, r_1 = 1, Θ = 70°, Φ = 0°

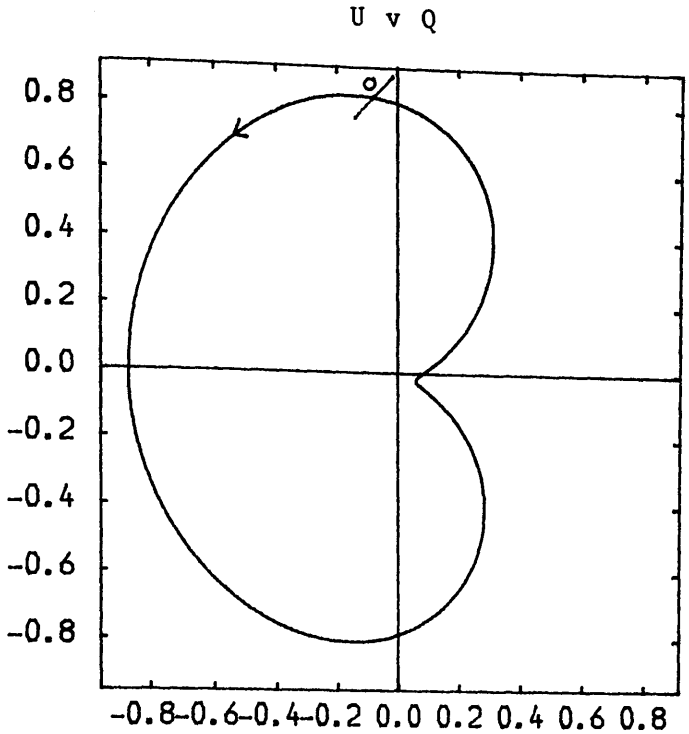

(———) Q v phase of orbit
(------) U v phase of orbit

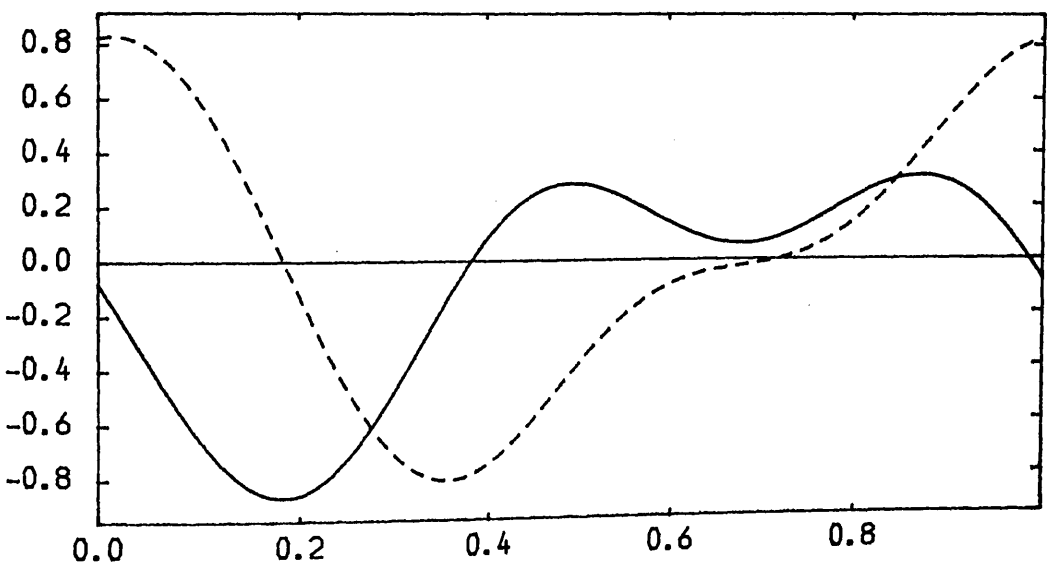

Figure 20: As Figure 18 for $i = 45°$, $a_1 = 0.1$, $a_2 = 0.2$ $f = 0.4$, $r_1 = 2$, $\Theta = 45°$, $\Phi = 120°$

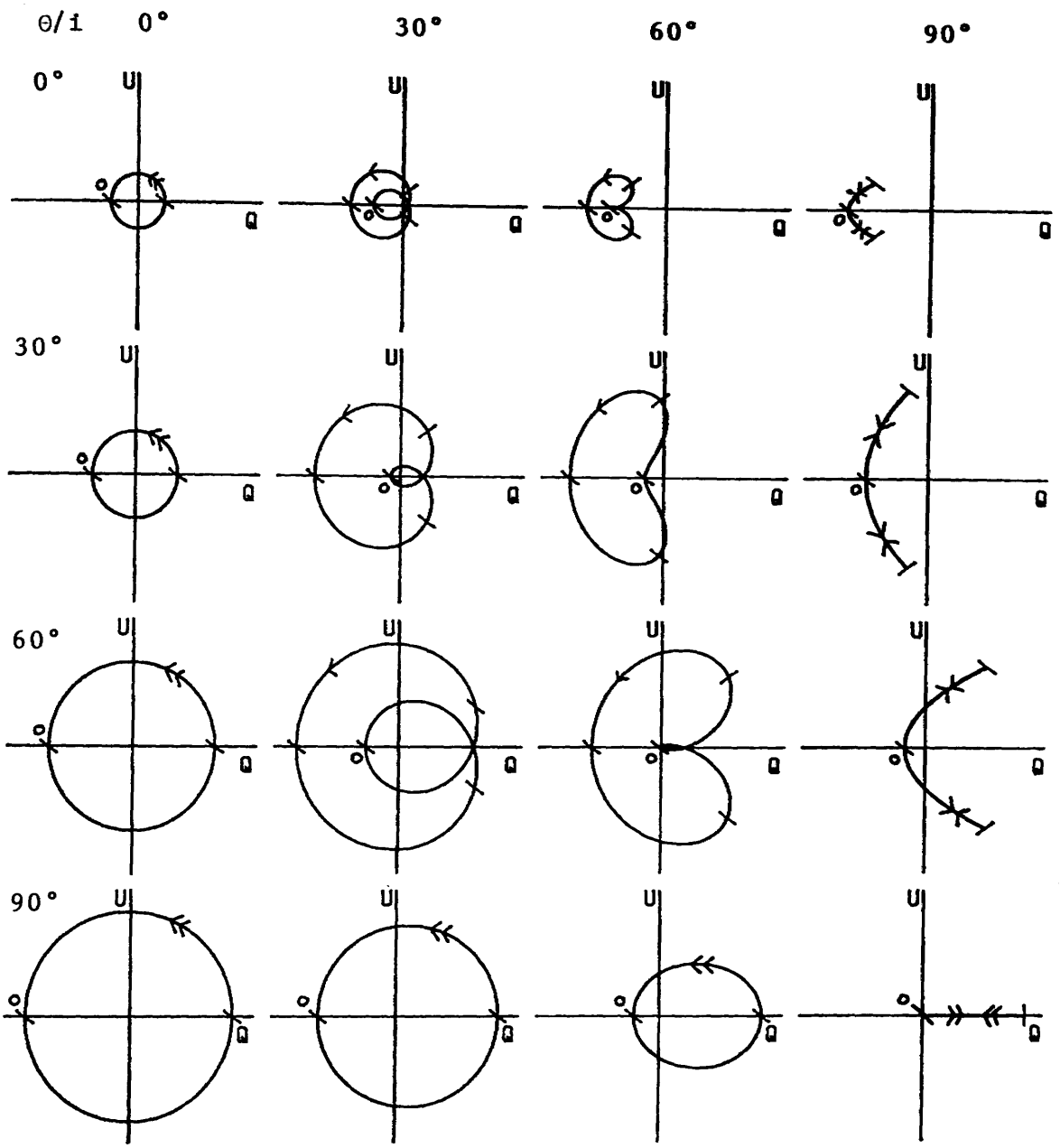

Figure 21: Matrix of Stokes Parameter loci for one electron corotating in a cicular binary system of unit radius and inclination, i. The spherically symmetric sources have radii, a_1 and a_2 = 0.2 and the fraction of the total luminosity emitted by source 1, f = 0.5. The position of the electron with respect to source 1 is (r_1, Θ , Φ), where r_1 = 0.5 and Φ = 0°. Fiduciary marks are shown at quarter orbital phase intervals.

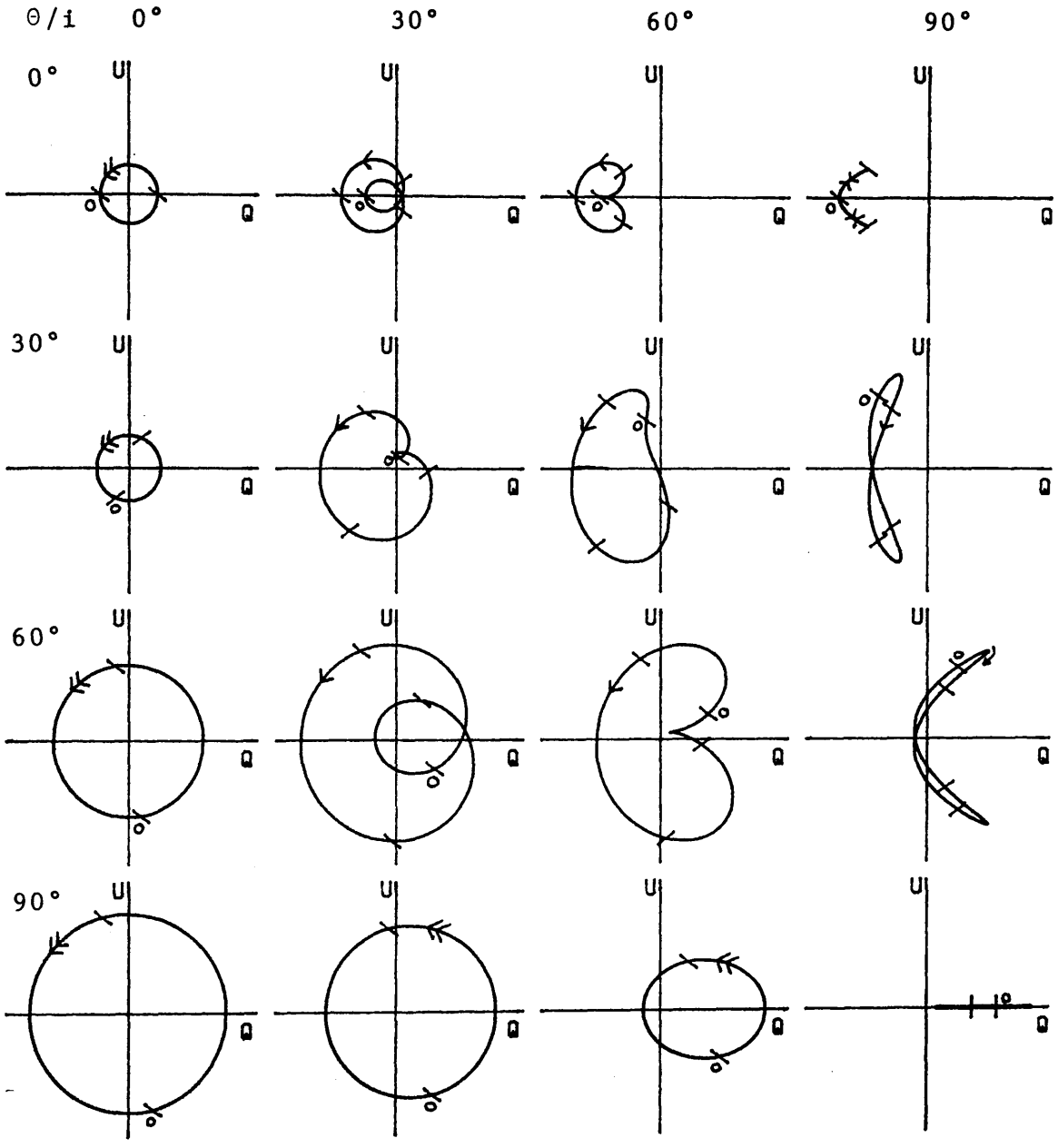

Figure 22: As Figure 21 for $\Phi = 60°$

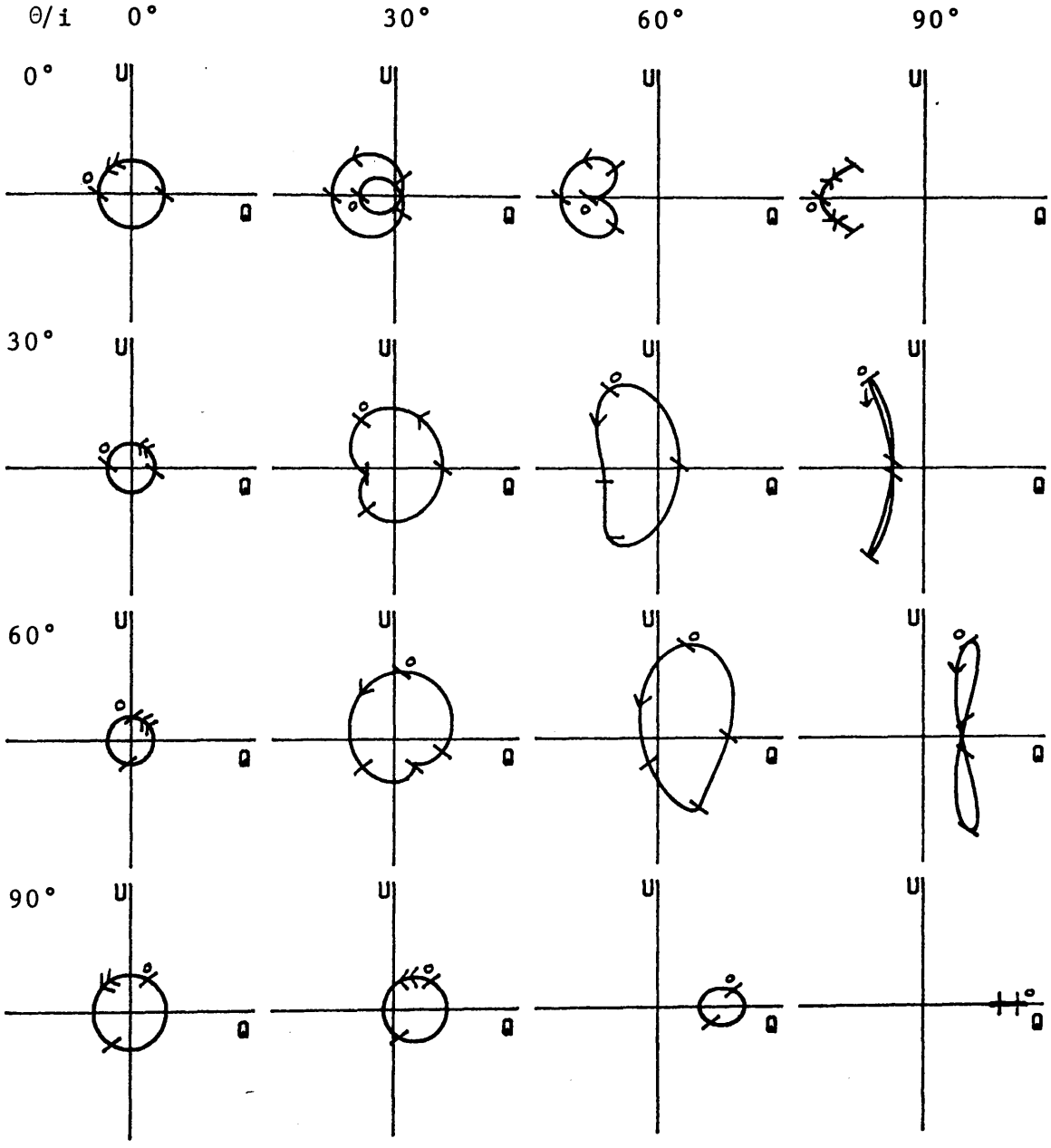

Figure 23: As Figure 21 for $\Phi = 120°$

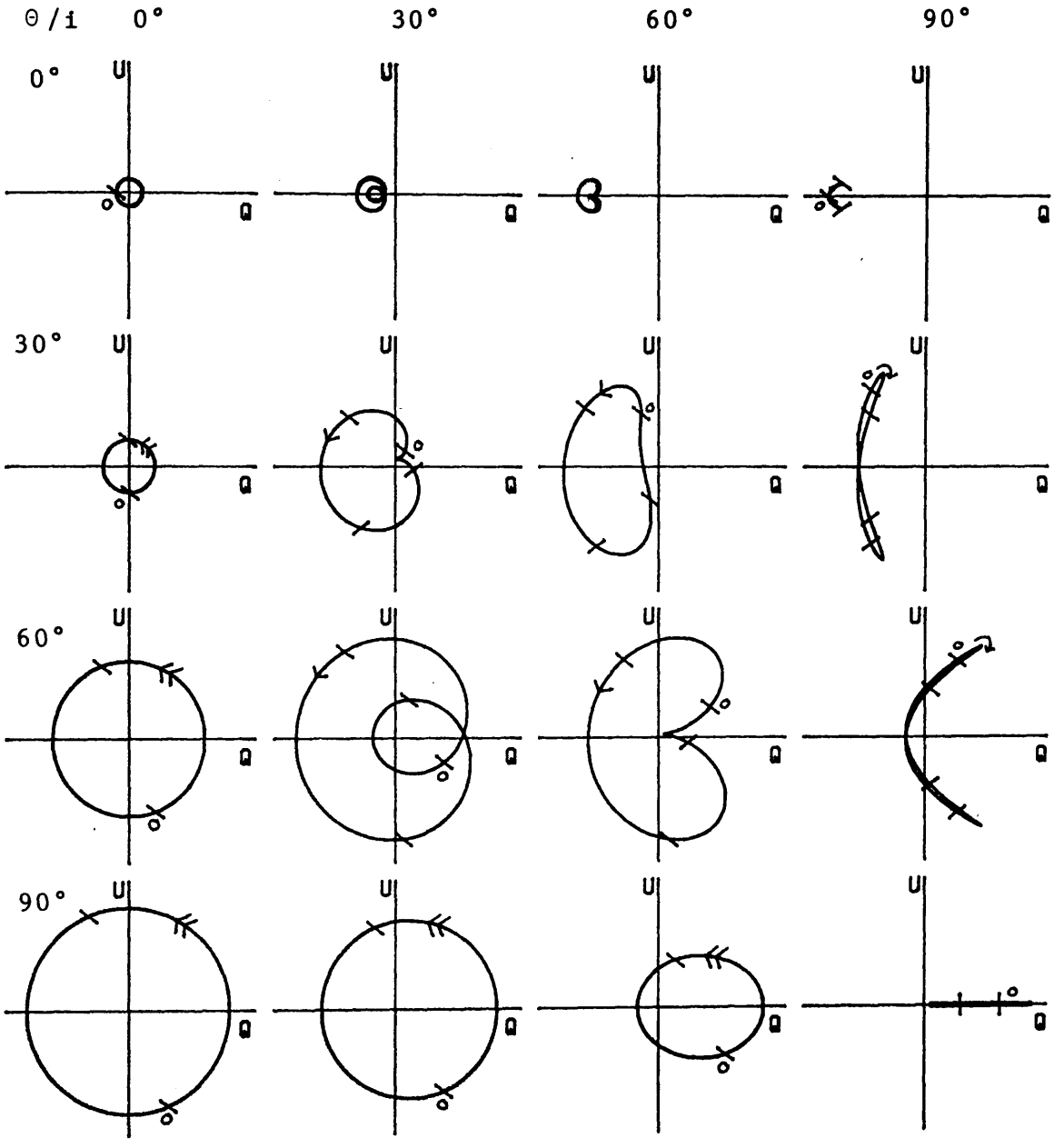

Figure 24: As Figure 21 for f = 0.7 and $\Phi = 60^{o}$

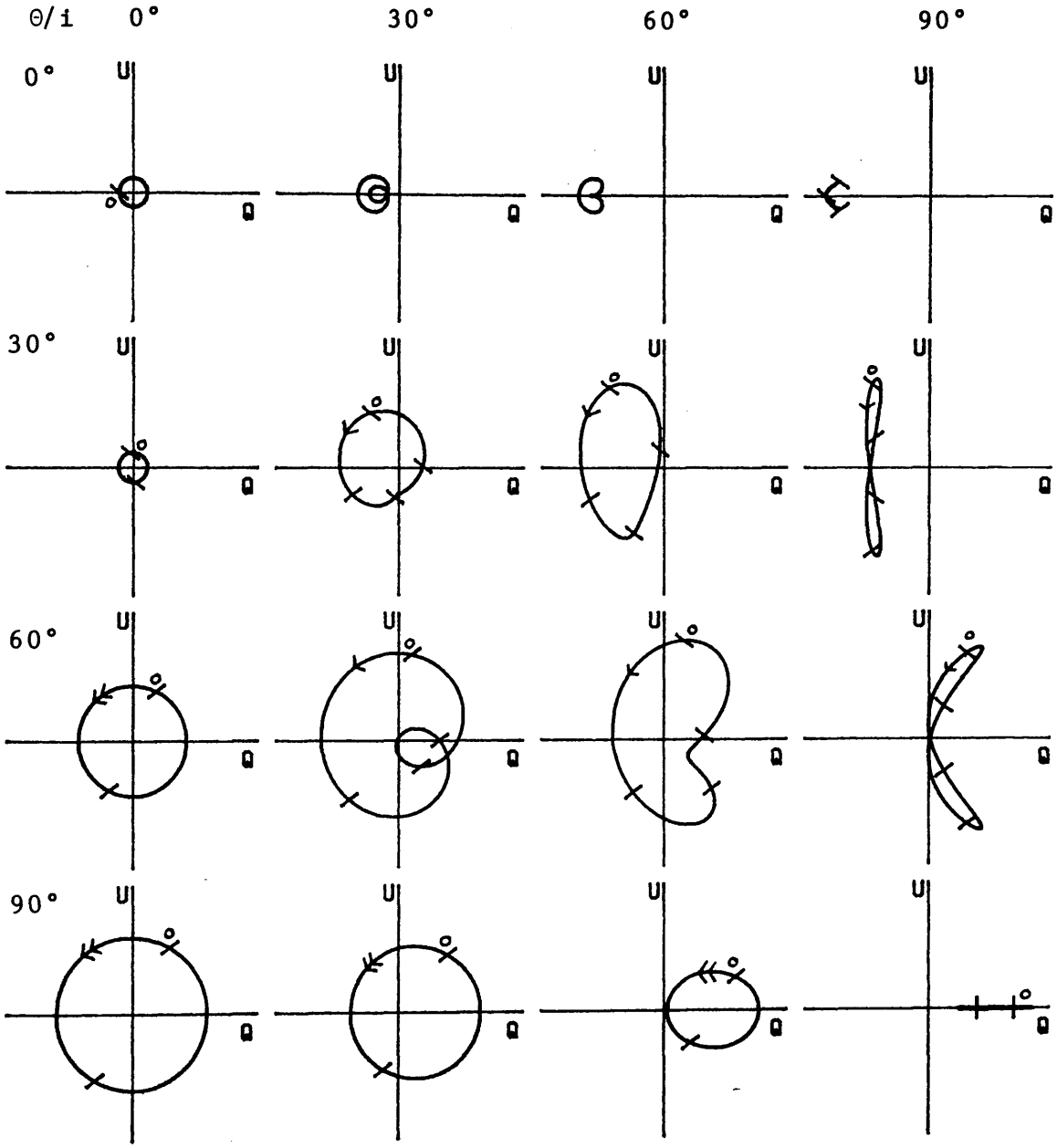

Figure 25: As Figure 21 for f = 0.7 and Φ = 120°

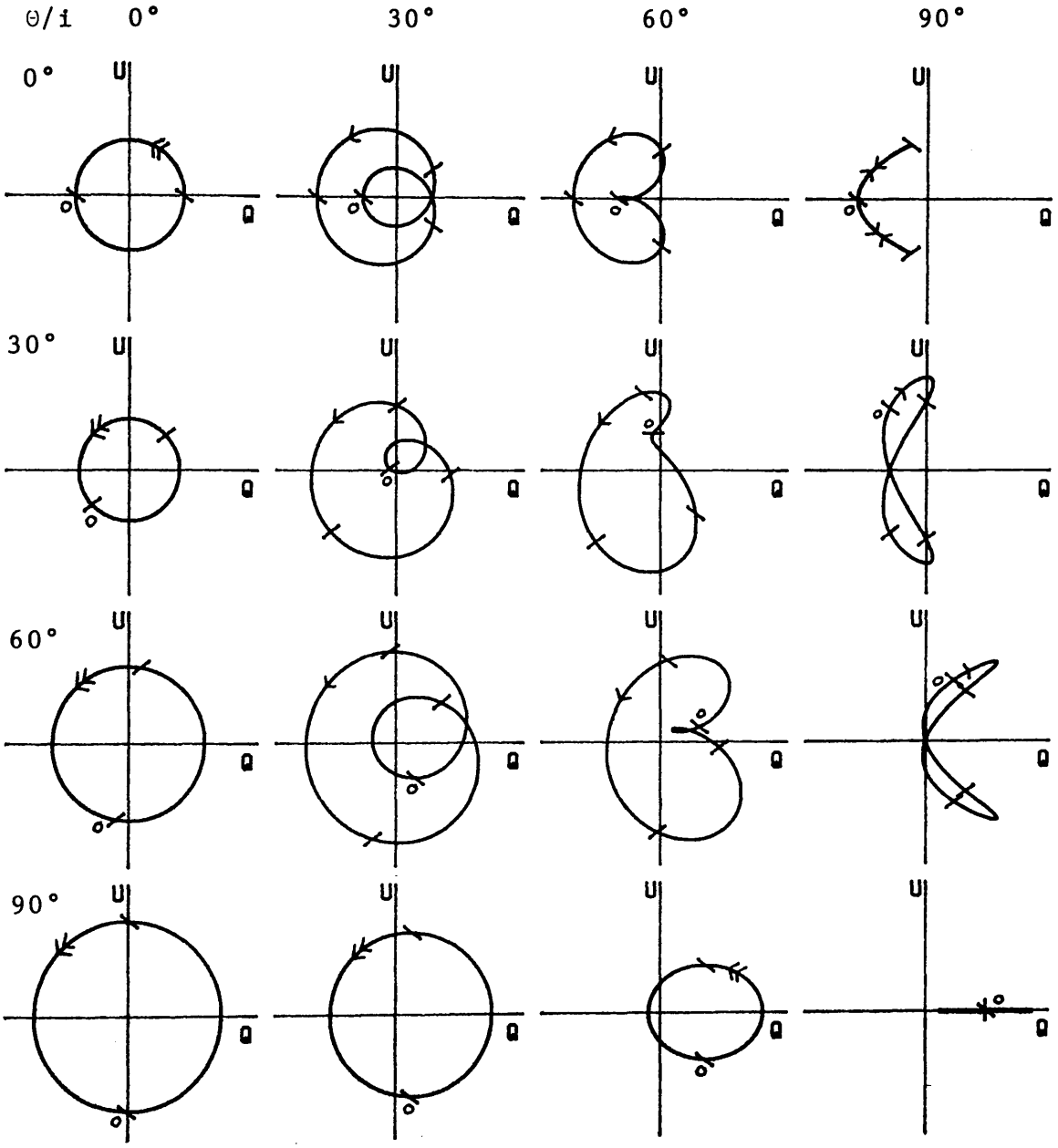

Figure 26: As Figure 21 for f = 0.3 and Φ= 60°

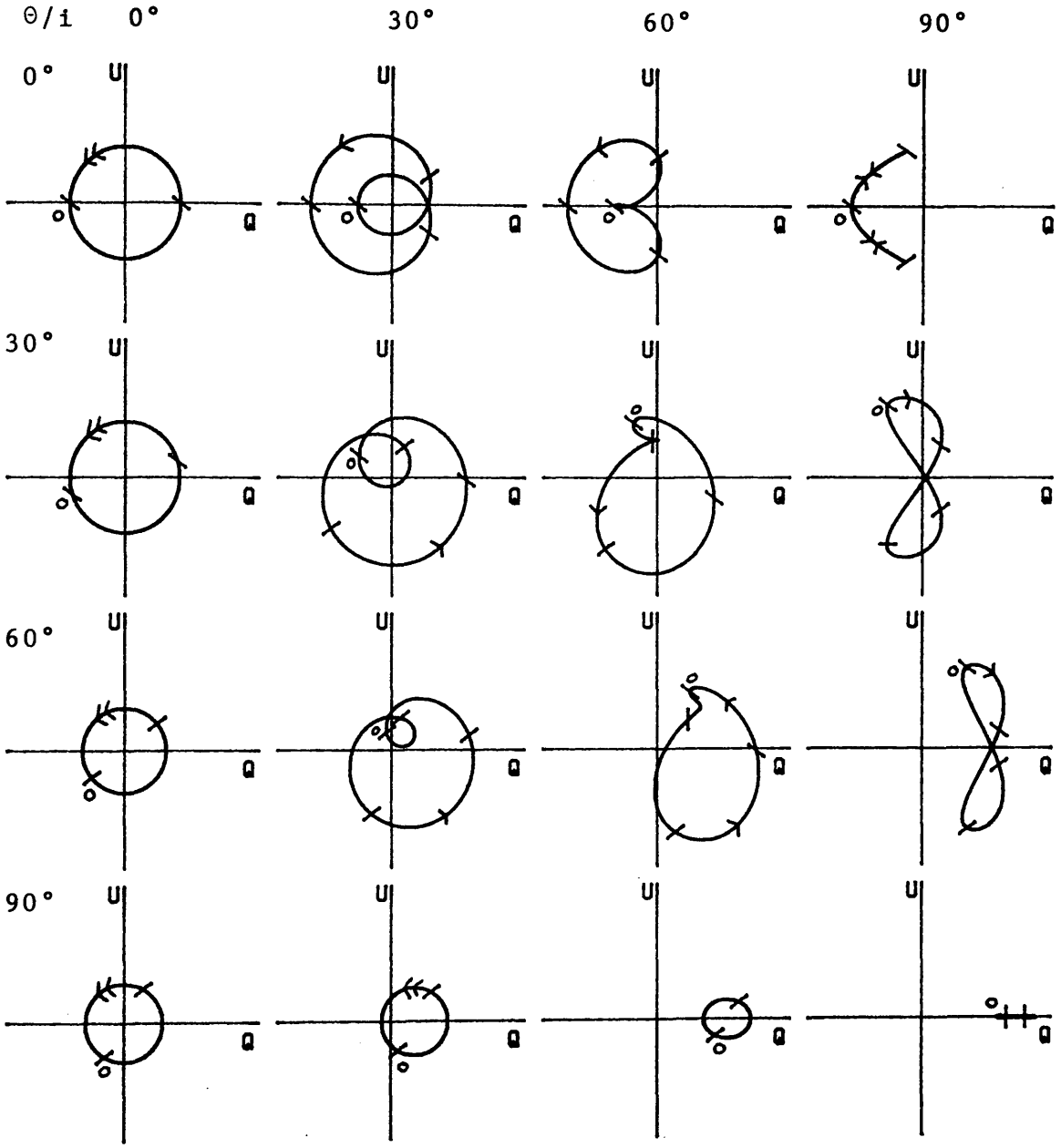

Figure 27: As Figure 21 for f = 0.3 and Φ = 120°

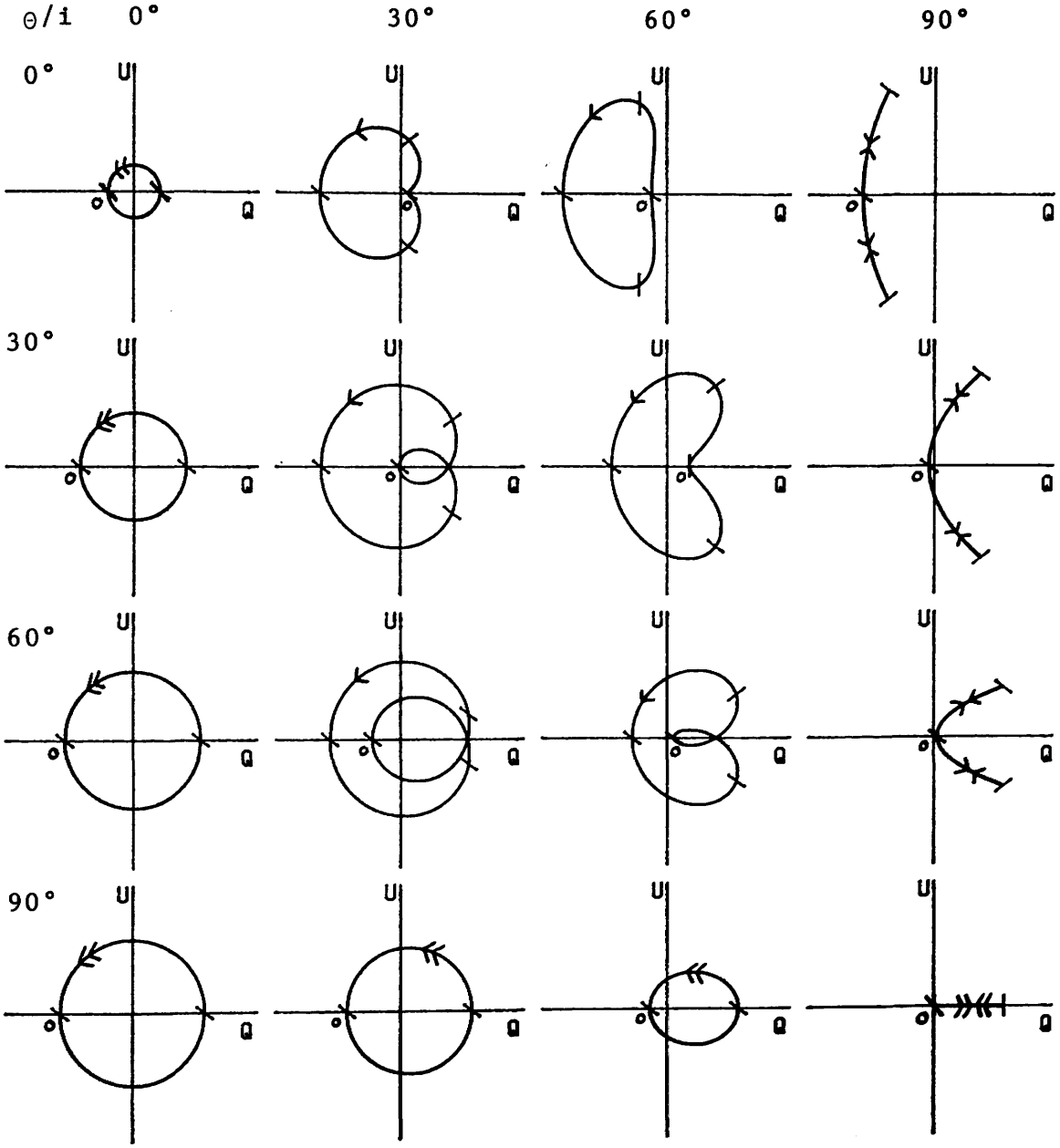

Figure 28: As Figure 21 for f = 0.0 and $r_1 = 2$

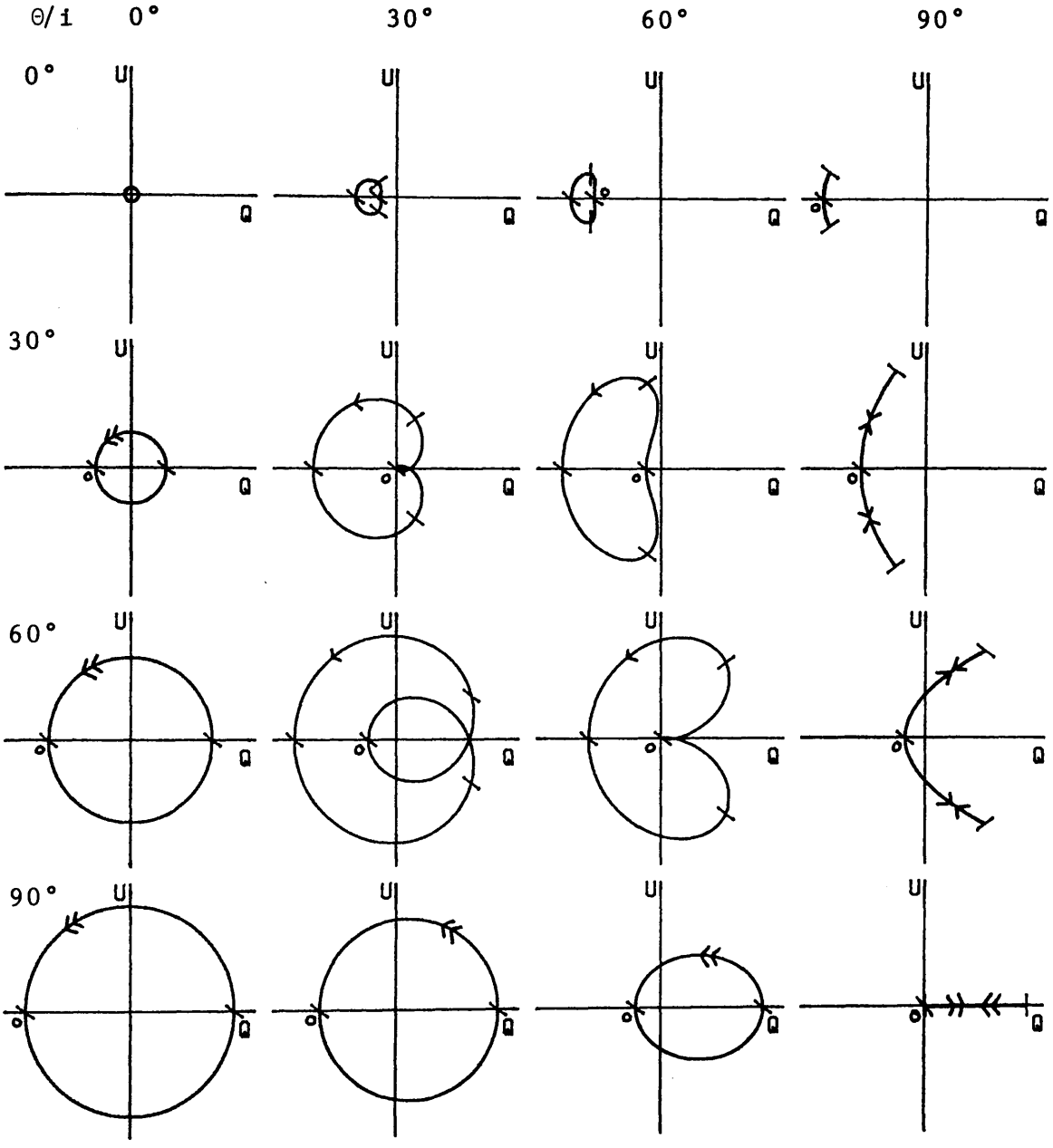

Figure 29: As Figure 21 for f = 0.2 and r_1 = 2

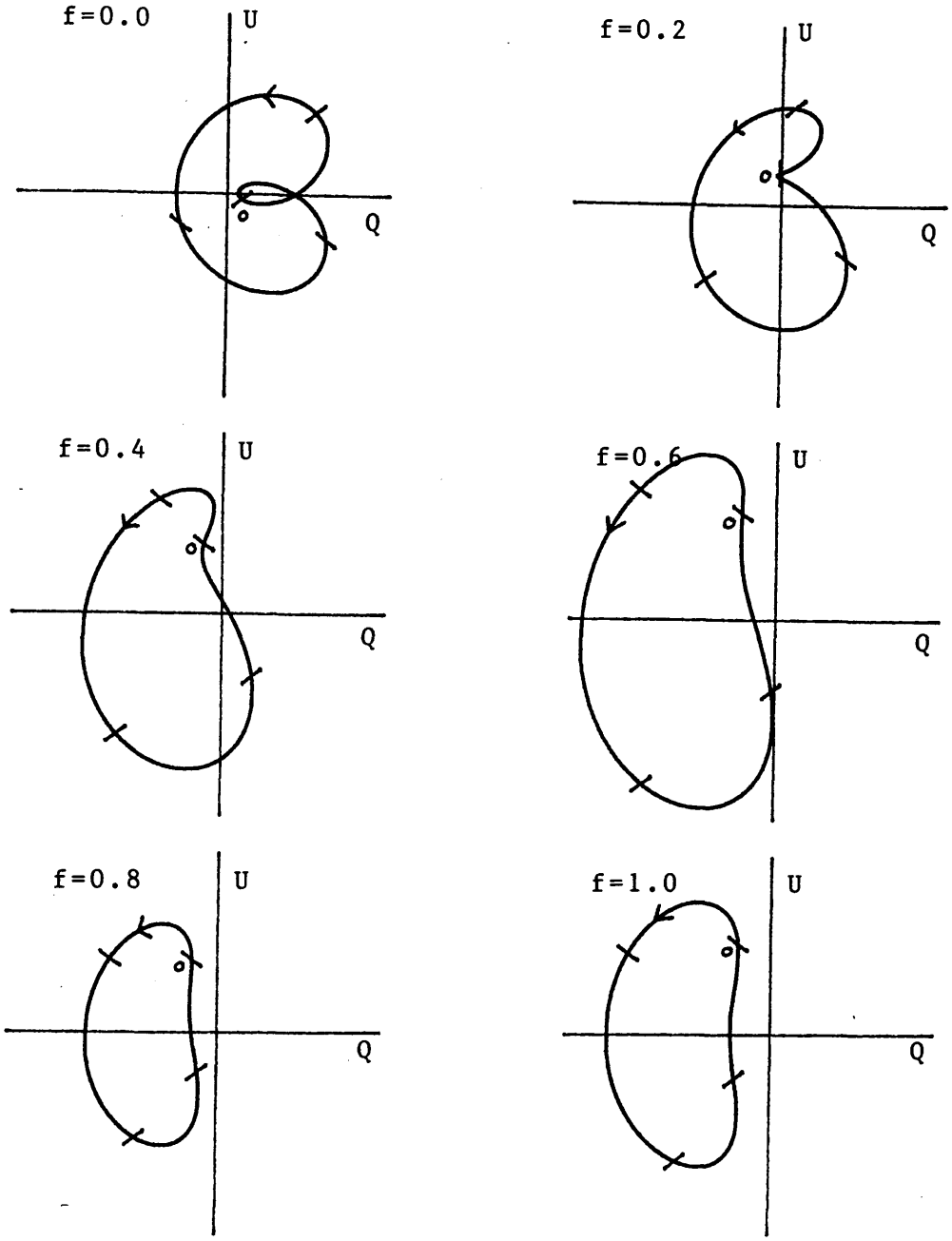

Figure 30: Set of Stokes Parameter loci for one electron corotating in a circular binary system of unit radius and inclination i = 60°. The spherically symmetric sources have radii, a_1 and a_2 = 0.2 and the fraction of the total luminosity emitted by source 1 is f. The position of the electron with respect to source 1, (r_1, Θ, Φ) is (0.5, 30°, 60°). Fiduciary marks are shown at quarter orbital phase intervals. Note that the scale on the loci for f = 0.8 and f = 1.0 has been halved.

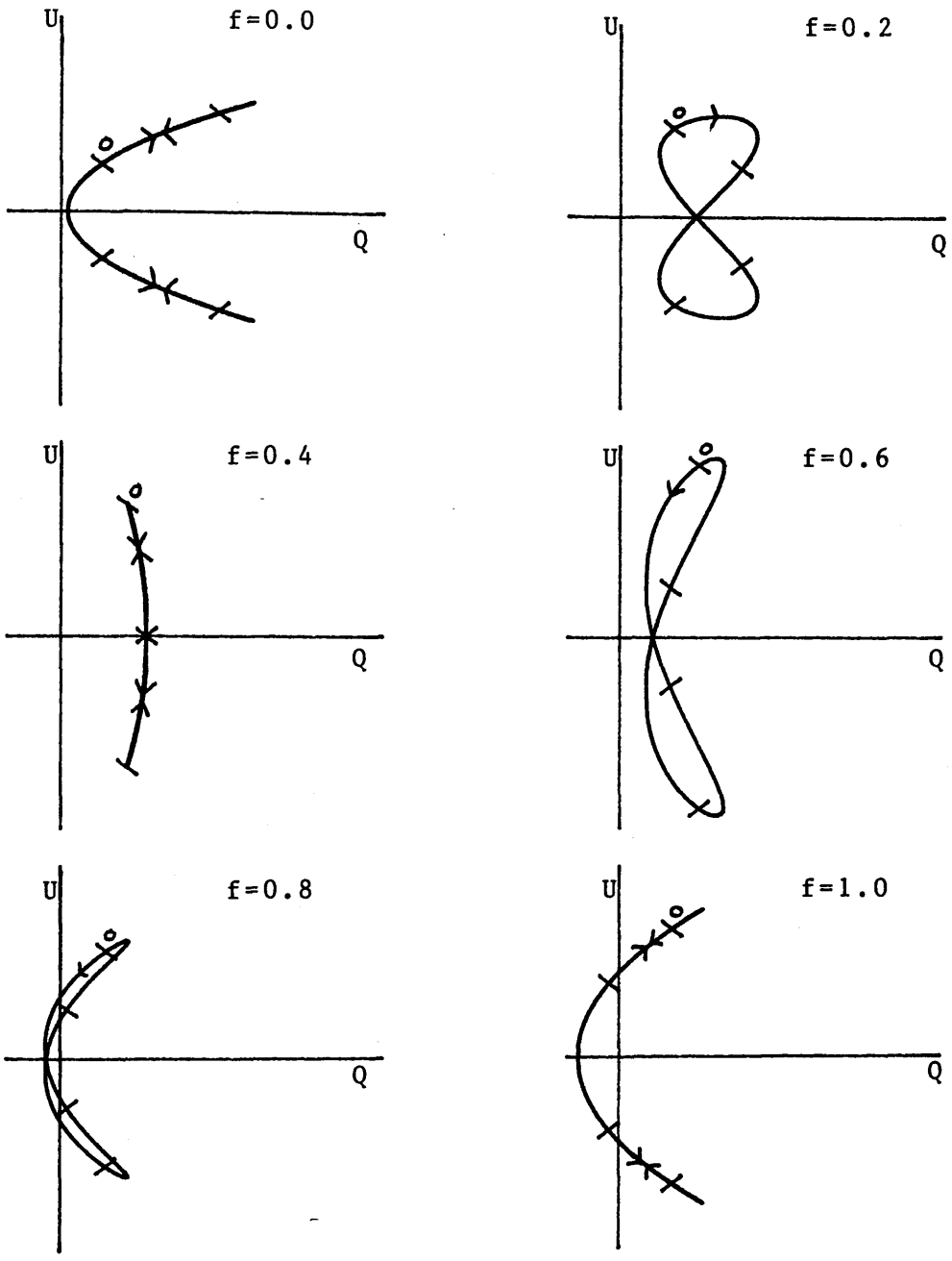

Figure 31: As Figure 30 for i = 90° , Θ = 60° and Φ= 120°.

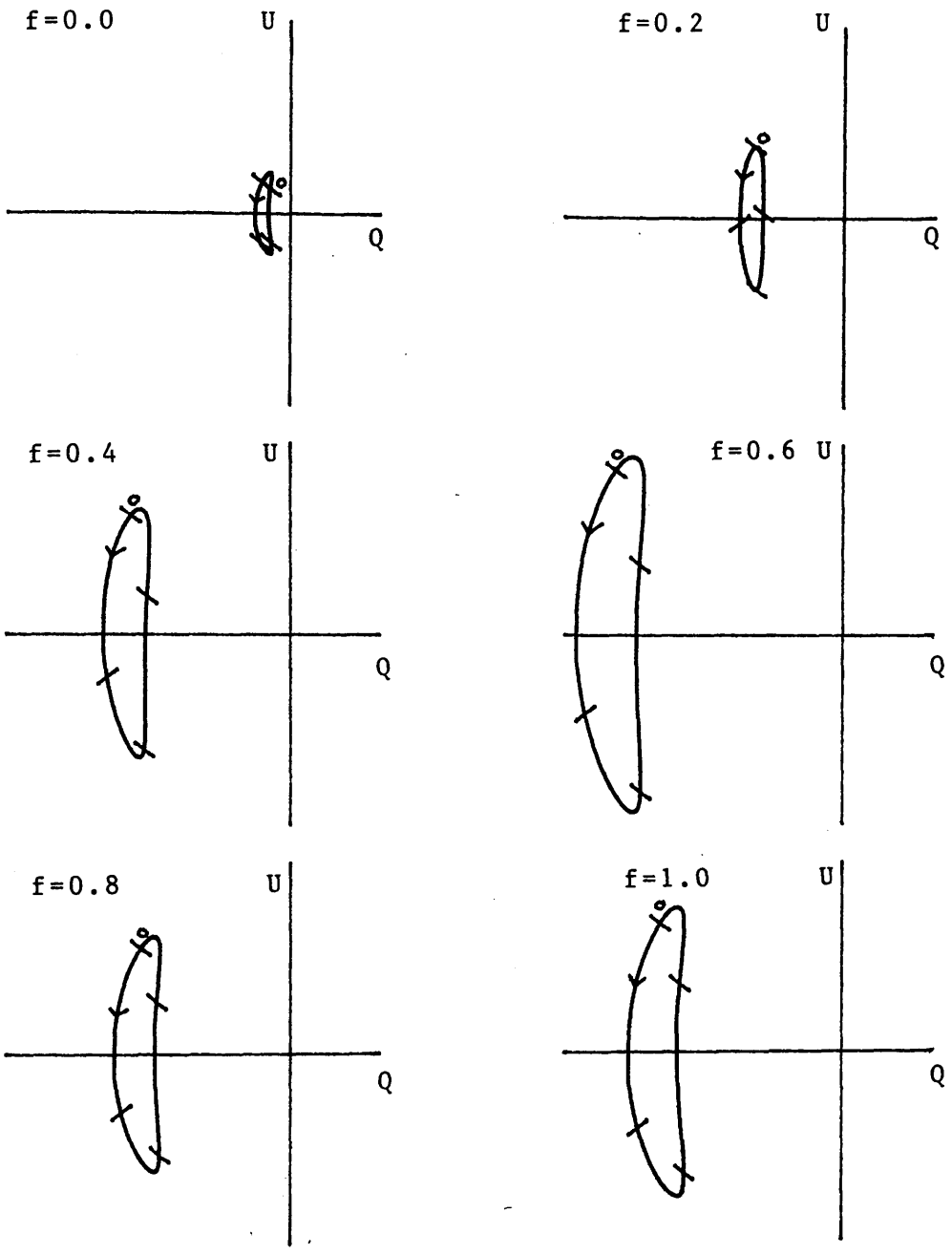

Figure 32: As Figure 30 for i = 80° , Θ = 20°, Φ = 120° and r_1 = 2.

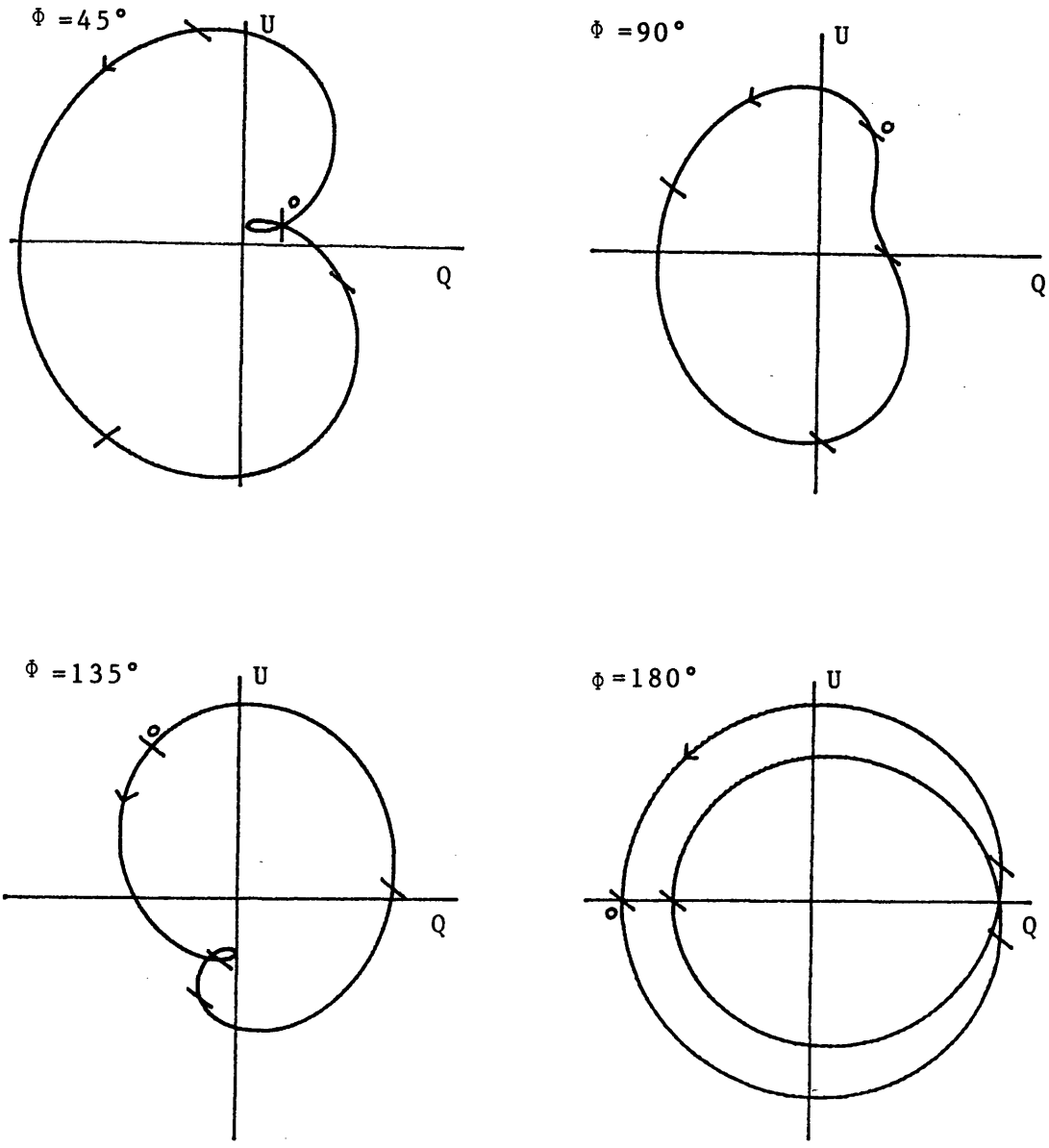

Figure 33: Set of Stokes Parameter loci for one electron corotating in a circular binary system of unit radius and inclination i = 45°. The spherically symmetric sources have radii, a_1 and a_2 = 0.2 and the fraction of the total luminosity emitted by source 1, f = 0.5. The position of the electron with respect to source 1 is (r_1, Θ , Φ) where r_1 = 0.5 and Θ = 45°. Fiduciary marks are shown at quarter orbital phase intervals.

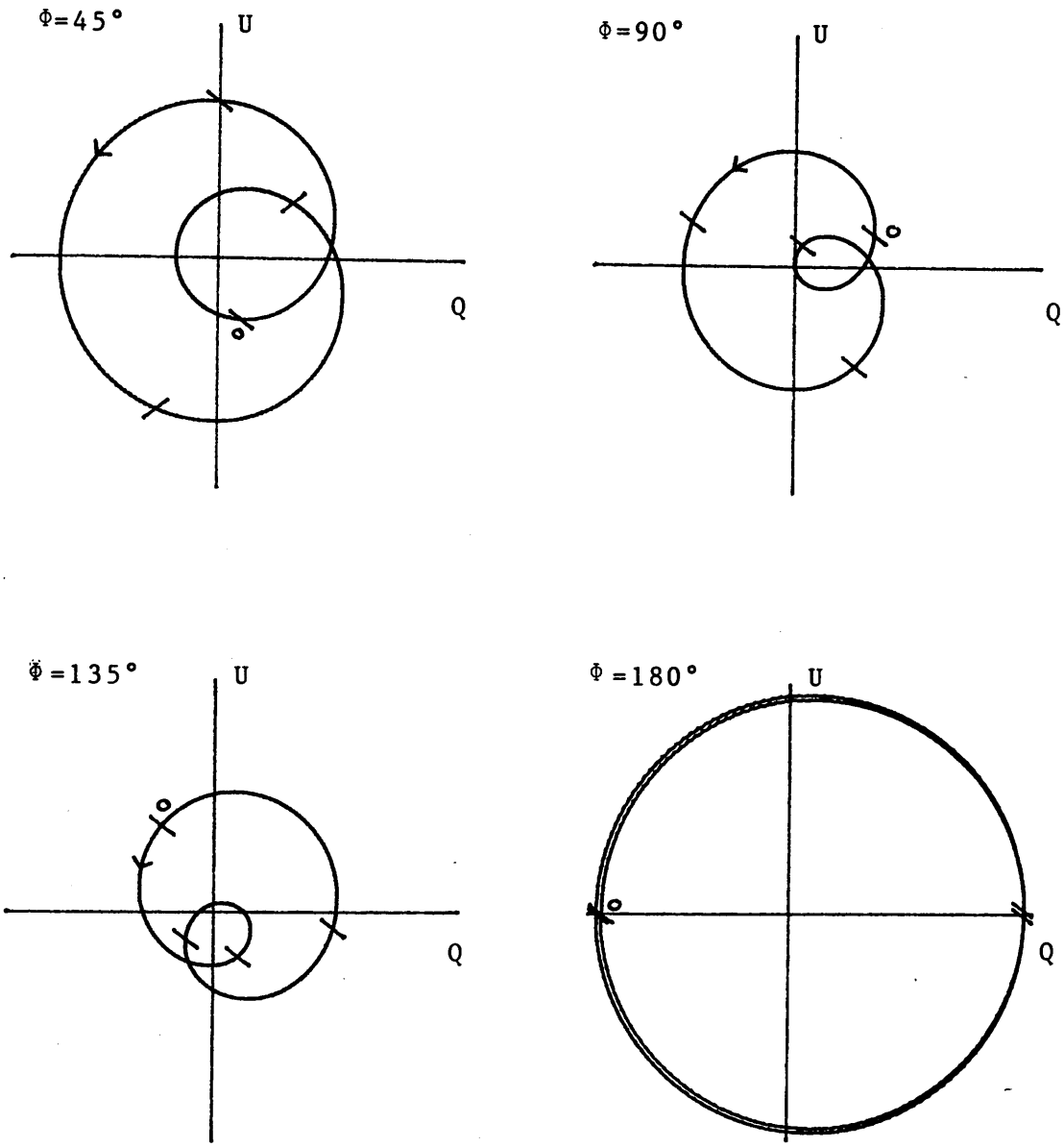

Figure 34: As Figure 33 for i = 30° and Θ = 60°.

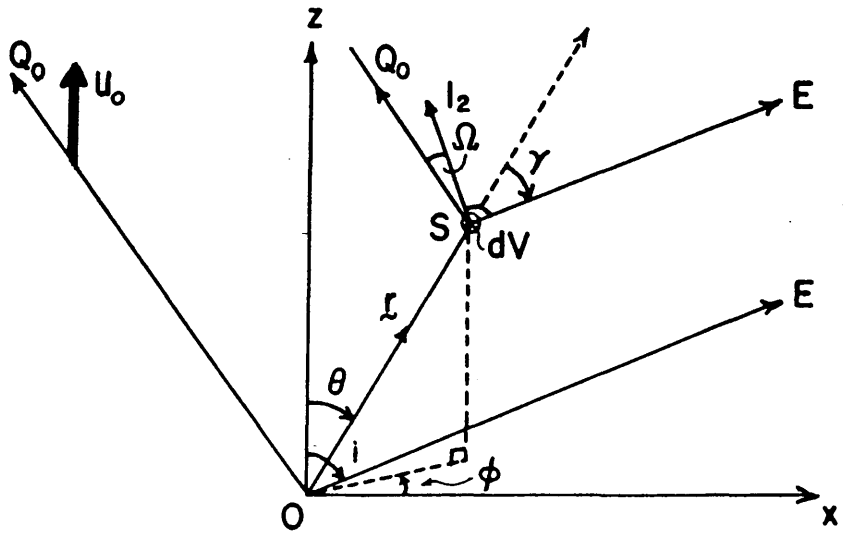

Figure 35: Scattering geometry for an extended source centred on O and scattering element dV at S. OE, in the x,z plane, is the line of sight. (Q_o,U_o) define the observer's reference plane, Q_o being perpendicular to OE in the plane OZE. I_2 is also perpendicular to OE but lies in the plane OSE. The y-axis has been omitted for clarity.

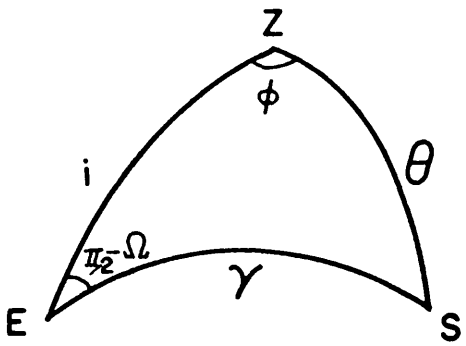

Figure 36: Spherical triangle from Figure 35 for the transformation from (γ,Ω) to (θ,ϕ).

CHAPTER 4

ANALYTIC THEORY OF THE POLARISATION OF SS433

4.1 Introduction

We now apply the equations derived in Chapter 3 to SS433. To do so, we use a much simplified model of SS433 (see Figure 1). The orbit is assumed to be circular (the estimated eccentricity is <0.05, Collins and Newsom, 1986), of radius a, and the companion star is approximated by a sphere of radius r_s. Another spherical source of radius r_c (where $r_c < r_s$) is used to approximate the light emitted by the compact object and the inner region of the disc. For ease of integration, the narrow jets (opening angle $< 5^o$) are approximated by a line of constant number density, n_j, normal to a two-dimensional optically and geometrically thin disc of constant number density per unit area, n_d. The jets and disc are taken to precess as a unit (cf. further discussion in Section 4.5). The inclination, i, of the orbit is the angle between the line of sight and the normal to the orbital plane, and the precession cone angle, Θ, is the angle between the jets and the normal to the orbital plane. Both these angles are assumed to be constant. The reference frame used in the calculation of the Stokes Parameters has polar axis normal to the orbital plane and corotates with the orbit such that the x-axis is the radius vector of the compact object with respect to the centre of the companion star (Figure 2). We define λ to be the longitude of the orbit, i.e. the angle between the x-axis and the projection of the line of sight on the orbital plane, and Ω is similarly defined to be the longitude of precession. Note that Ω is negative for retrograde precession.

In the following two sections, the polarisation of light from each source is treated separately. After the limitations of the model have been discussed (Section 4.5), the absolute value of the polarisation is estimared in relation to mass loss rates and the disc mass.

4.2 Polarisation due to light from source at centre of disc

The jet is symmetrical about the central plane of the disc, but not about the orbital plane, in general. Hence, the Stokes Parameters for scattering from the jet are

$$Q_{cj} = n_j \int_{r_c}^{\infty} [\, Q(r,\Theta,\Phi) + Q(r,\pi-\Theta,\pi+\Phi)]\, dr$$
$$U_{cj} = n_j \int_{r_c}^{\infty} [\, U(r,\Theta,\Phi) + U(r,\pi-\Theta,\pi+\Phi)]\, dr \qquad (1)$$

where $Q(r,\Theta,\Phi)$ and $U(r,\Theta,\Phi)$ are given by equations 3.19 with $D = (1 - r_c^2/r^2)^{\frac{1}{2}}$. Now $Q(r,\pi-\Theta,\pi+\Phi) = Q(r,\Theta,\Phi)$, $U(r,\pi-\Theta,\pi+\Phi) = U(r,\Theta,\Phi)$ and

$$\int_{r_c}^{\infty} (1- r_s^2/r^2)^{\frac{1}{2}} \frac{dr}{r^2} = \frac{\pi}{4r_c} \qquad (2)$$

Hence equations (1) become

$$Q_{cj} = \frac{n_j \sigma_o \pi}{4r_c} \left\{ (1-3\cos^2\Theta)\sin^2 i + \sin 2i \sin 2\Theta \cos(\lambda+\Phi) \right.$$
$$\left. -(1+\cos^2 i)\sin^2\Theta \cos 2(\lambda+\Phi) \right\}$$
$$U_{cj} = \frac{n_j \sigma_o \pi}{2r_c} \left\{ \sin i \sin 2\Theta \sin(\lambda+\Phi) - \cos i \sin^2\Theta \sin 2(\lambda+\Phi) \right\} \qquad (3)$$

where from Figure 2 $\lambda+\Phi = \Omega$.

Note that, because of precession Φ is now time dependent.

To find the Stokes Parameters due to scattering from the disc, we first define α as follows (see Figure 3).

Let OR be the intersection of the plane containing the z-axis and the jet with the disc. Let (r,θ,ϕ) be the polar coordinates of an arbitrary point P in the disc. Then α is defined to be the angle between OR and OP. Hence, the Stokes Parameters for the disc are

$$Q_{cd} = n_d \int_o^{2\pi} \int_{r_c}^{r_d} Q(r,\theta,\phi) r dr\, d\alpha$$
$$U_{cd} = n_d \int_o^{2\pi} \int_{r_c}^{r_d} U(r,\theta,\phi) r dr\, d\alpha \qquad (4)$$

where r_d is the effective outer radius of the disc and $Q(r,\theta,\phi)$, $U(r,\theta,\phi)$ are again found from equations (3.19).

We now substitute for θ and ϕ in terms of Θ,Φ and α. From Figure 4 we find

$$\cos\theta = -\sin\Theta\cos\alpha$$
$$\sin\theta\sin\phi = \cos\Phi\sin\alpha + \sin\Phi\cos\Theta\cos\alpha \qquad (5)$$
$$\sin\theta\cos\phi = -\sin\Phi\sin\alpha + \cos\Phi\cos\Theta\cos\alpha$$

Also $$\int_{r_c}^{r_d} [1 - r_c^2/r^2]^{\frac{1}{2}}\, dr/r = \int_{\sin^{-1}\frac{r_c}{r_d}}^{\pi/2} \frac{\cos^2 x\, dx}{\sin x}$$
$$= -\log\left[\tan\tfrac{1}{2}\left(\sin^{-1}\frac{r_c}{r_d}\right)\right] - \cos\left(\sin^{-1}\frac{r_c}{r_d}\right) \qquad (6)$$

Hence, from equations (5), (6) and (3.19), equations (4) become

$$Q_{cd} = \frac{\pi n_d \sigma_o}{2}\left\{\log\left[\tan\tfrac{1}{2}\left(\sin^{-1}\frac{r_c}{r_d}\right)\right] + \cos\left(\sin^{-1}\frac{r_c}{r_d}\right)\right\}$$
$$\begin{pmatrix} (1-3\cos^2\Theta)\sin^2 i + \sin 2i \sin 2\Theta\cos(\lambda+\Phi) \\ -(1+\cos^2 i)\sin^2\Theta\cos 2(\lambda+\Phi) \end{pmatrix} \qquad (7)$$

$$U_{cd} = \pi n_d \sigma_o \left\{\log\left[\tan\tfrac{1}{2}\left(\sin^{-1}\frac{r_c}{r_d}\right)\right] + \cos\left(\sin^{-1}\frac{r_c}{r_d}\right)\right\}$$
$$\{\sin i \sin 2\Theta \sin(\lambda+\Phi) - \cos i \sin^2\Theta \sin 2(\lambda+\Phi)\}$$

It can be seen from equations (3) and (7) that the polarisation of scattered light emitted by the source at the centre of the disc (hereafter called the central source) does not depend on the orbital phase of the object.

Now, $\log [\tan \tfrac{1}{2} (\sin^{-1}x)] + \cos (\sin^{-1}x) = 0$ for $x = 1$

and $\frac{d}{dx} \{\log [\tan \tfrac{1}{2} (\sin^{-1}x)] + \cos(\sin^{-1} x)\} = \frac{1-x^2}{\sqrt{1-x^2}} > 0$ for $0 < x < 1$

Therefore, $\log [\tan \tfrac{1}{2}(\sin^{-1} r_c/r_d)] + \cos(\sin^{-1} r_c/r_d) < 0$ since $r_c < r_d$.

Hence a comparison of equations (3) and (7) shows that

$$Q_{cd} = - m Q_{cj} \quad \text{and} \quad U_{cd} = - m U_{cj} \tag{8}$$

where $m > 0$. So the Q,U locus has the same shape with precessional phase for jet or disc scattering of light emitted by a spherically symmetric central source, but with a 90^o rotation on the sky or 180^o in the Q,U plane.

The Stokes Parameters for disc and jet scattering from the central source are found from summing equations (3) and (7). The scattering will be jet or disc dominated according as

$$n_d \{\log [\tan \tfrac{1}{2}(\sin^{-1} r_c/r_d)] + \cos(\sin^{-1} r_c/r_d)\} + \frac{n_j}{2r_c}$$

is positive or negative. Figure 5 and 6 show the Q,U loci for a matrix of i and Θ values for (5) jet dominated and (6) disc dominated scattering. When $\Theta = i$, the cusp occurs at precession phase = 0 for then the jet lies along the line of sight and the disc is normal to the line of sight. The polarisation is zero at the cusp since the scattering region is symmetrical about the line of sight.

4.3 Polarisation due to light from the companion star

If (r,θ,ϕ) are the polar coordinates of an arbitrary electron in jet or disc with respect to the centre of the disc and r_1 is its distance from the centre of the companion star then the Stokes Parameters due to light from the companion star scattered by this electron is (cf. equations (3.23, 26).

$$Q_s(r,\theta,\phi) = \frac{(r_1^2-r_s^2)^{\frac{1}{2}}}{2r_1^3}\sigma_o \left[\begin{array}{l} [1-3(\frac{r}{r_1})^2\cos^2\theta]\sin^2 i - \sin 2i \sin\lambda[(\frac{r}{r_1})^2\sin 2\theta\sin\phi] \\ +\sin 2i \cos\lambda[(\frac{r}{r_1})^2\sin 2\theta\cos\phi+\frac{2ar}{r_1^2}\cos\theta] \\ -(1+\cos^2 i)\cos 2\lambda[(\frac{r}{r_1})^2\sin^2\theta\cos 2\phi+\frac{2ar}{r_1^2}\sin\theta\cos\phi+(\frac{a}{r_1})^2] \\ +(1+\cos^2 i)\sin 2\lambda[(\frac{r}{r_1})^2\sin^2\theta\sin 2\phi+\frac{2ar}{r_1^2}\sin\theta\sin\phi] \end{array}\right] \quad (11a$$

$$U_s(r,\theta,\phi) = \frac{(r_1^2-r_s^2)^{\frac{1}{2}}}{r_1^3}\sigma_o \left[\begin{array}{l} \sin i \sin\lambda[(\frac{r}{r_1})^2\sin 2\theta\cos\phi+\frac{2ar}{r_1^2}\cos\theta] \\ +\sin i \cos\lambda[(\frac{r}{r_1})^2\sin 2\theta\sin\phi] \\ -\cos i \sin 2\lambda[(\frac{r}{r_1})^2\sin^2\theta\cos 2\phi+\frac{2ar}{r_1^2}\sin\theta\cos\phi+(\frac{a}{r_1})^2] \\ -\cos i \cos 2\lambda[(\frac{r}{r_1})^2\sin^2\theta\sin 2\phi+\frac{2ar}{r_1^2}\sin\theta\sin\phi] \end{array}\right] \quad (11b$$

where $r_1^2 = r^2 + a^2 + 2ar\sin\theta\cos\phi$.

Note that ϕ is now time dependent, as Φ was in equations (3), because of precession.

Now, the Stokes parameters for scattering from the jet will be (cf. equations (1)).

$$Q_{sj} = n_j \int_{r_c}^{\infty} [Q_s(r,\Theta,\Phi) + Q_s(r,\pi-\Theta,\pi+\Phi)]\,dr$$

$$U_{sj} = n_j \int_{r_c}^{\infty} [U(r,\Theta,\Phi) + U_s(r,\pi-\Theta,\pi+\Phi)]\,dr$$

i.e. using equations (11)

$$Q_{sj} = \frac{n_j \sigma_o}{2a}\left\{\begin{array}{l} [J_o - 3J_1\cos^2\theta]\sin^2 i - \sin 2i\,\sin\lambda[J_1 \sin 2\theta \sin\Phi] \\ + \sin 2i\,\cos\lambda[J_1 \sin 2\theta\cos\Phi + 2J_2\cos\theta\,] \\ -(1+\cos^2 i)\cos 2\lambda[J_1 \sin^2\theta\cos 2\Phi + 2J_2 \sin\theta\cos\Phi + J_3\,] \\ +(1+\cos^2 i)\sin 2\lambda[J_1 \sin^2\theta \sin 2\Phi + 2J_2 \sin\theta \sin\Phi] \end{array}\right\} \qquad (12a)$$

$$U_{sj} = \frac{n_j \sigma_o}{a}\left\{\begin{array}{l} \sin i\,\sin\lambda[J_1 \sin 2\theta\cos\Phi + 2J_2\cos\theta] \\ +\sin i\,\cos\lambda[J_1 \sin 2\theta\sin\Phi\,] \\ -\cos i\,\sin 2\lambda[J_1 \sin^2\theta\cos 2\Phi + 2J_2 \sin\theta\cos\Phi + J_3\,] \\ -\cos i\,\cos 2\lambda[J_1 \sin^2\theta \sin 2\Phi + 2J_2 \sin\theta \sin\Phi] \end{array}\right\} \qquad (12b)$$

where
$$J_o = \int_{R_c}^{\infty}\left\{\frac{f(R)}{[g(R)]^3} + \frac{f(-R)}{[g(-R)]^3}\right\}dR \quad , \quad R_c = r_c/a$$

$$J_1 = \int_{R_c}^{\infty}\left\{\frac{f(R)}{[g(R)]^5} + \frac{f(-R)}{[g(-R)]^5}\right\}R^2 dR$$

$$J_2 = \int_{R_c}^{\infty}\left\{\frac{f(R)}{[g(R)]^5} - \frac{f(-R)}{[g(-R)]^5}\right\}R\,dR \qquad (13)$$

$$J_3 = \int_{R_c}^{\infty}\left\{\frac{f(R)}{[g(R)]^5} + \frac{f(-R)}{[g(-R)]^5}\right\}dR$$

and $f(R) = (R^2+1+2R\,\sin\theta\cos\Phi - R_s^2)^{\frac{1}{2}}$, $R_s = r_s/a$

$g(R) = (R^2+1+2R\,\sin\theta\cos\Phi)^{\frac{1}{2}}$

For scattering from the disc, we have (cf. equations (4))

$$Q_{sd} = n_d \int_0^{2\pi}\int_{r_c}^{r_d} Q_s(r,\theta,\phi)\,r\,dr\,d\alpha$$

$$U_{sd} = n_d \int_0^{2\pi}\int_{r_c}^{r_d} U_s(r,\theta,\phi)\,r\,dr\,d\alpha \qquad (14)$$

where we use equations (5) to substitute for θ and ϕ in terms of Θ, Φ and α, and Q_s, U_s are again given by equations (11). Hence equations (14) become

$$Q_{sd} = \frac{n_d \sigma_o}{2} \Big[\sin^2 i \; [B_1 - \tfrac{3}{2}(B_2+B_3)\sin^2\Theta]$$
$$-\sin 2i \cos\lambda \; [\tfrac{1}{2}(B_2+B_3)\sin 2\Theta\cos\Phi - B_4 \sin\Theta\sin\Phi + 2B_6 \sin\Theta \;]$$
$$+\sin 2i \sin\lambda [\tfrac{1}{2}(B_2+B_3)\sin 2\Theta\sin\Phi + B_4 \sin\Theta\cos\Phi \;]$$
$$-(1+\cos i)\cos 2\lambda [\tfrac{1}{2}(B_3(1+\cos^2\Theta) - B_2\sin^2\Theta)\cos 2\Phi - B_4 \cos\Theta \sin 2\Phi$$
$$+B_5 + 2B_6 \cos\Theta\cos\Phi - 2B_7 \sin\Phi \;]$$
$$+(1+\cos^2 i)\sin 2\lambda [\tfrac{1}{2}(B_3(1+\cos^2\Theta) - B_2 \sin^2\Theta)\sin 2\Phi + B_4 \cos\Theta\cos 2\Phi$$
$$+2B_6 \cos\Theta \sin\Phi + 2B_7 \cos\Phi \;] \Big] \qquad (15a)$$

$$U_{sd} = n_d \sigma_o \Big[\sin i \sin\lambda [-\tfrac{1}{2}(B_2+B_3)\sin 2\Theta\cos\Phi + B_4 \sin\Theta\sin\Phi - 2B_6 \sin\Theta \;]$$
$$-\sin i \cos\lambda [\tfrac{1}{2}(B_2+B_3)\sin 2\Theta\sin\Phi + B_4 \sin\Theta\cos\Phi \;]$$
$$-\cos i \sin 2\lambda [\tfrac{1}{2}(B_3(1+\cos^2\Theta) - B_2\sin^2\Theta)\cos 2\Phi - B_4 \cos\Theta \sin 2\Phi$$
$$+ B_5 + 2B_6 \cos\Theta \cos\Phi - 2B_7 \sin\Phi \;]$$
$$-\cos i \cos 2\lambda [\tfrac{1}{2}(B_3(1+\cos^2\Theta) - B_2\sin^2\Theta)\sin 2\Phi + B_4 \cos\Theta \cos 2\Phi$$
$$+ 2B_6 \cos\Theta \sin\Phi + 2B_7 \cos\Phi \;] \Big] \qquad (15b)$$

where $B_1 = \int_0^{2\pi} \int_{R_c}^{R_d} \frac{(R_1^2 - R_s^2)^{\frac{1}{2}}}{R_1^5} \, R dR \, d\alpha$, $R_c = r_c/a$, $R_s = r_s/a$, $R_d = r_d/a$

$$B_2 = \int_0^{2\pi} \int_{R_c}^{R_d} \frac{(R_1^2 - R_s^2)^{\frac{1}{2}}}{R_1^5} \, R^3 dR \, d\alpha$$

$$B_3 = \int_0^{2\pi} \int_{R_c}^{R_d} \frac{(R_1^2 - R_s^2)^{\frac{1}{2}}}{R_1^5} \cos 2\alpha \, R^3 dR \, d\alpha$$

$$B_4 = \int_0^{2\pi}\int_{R_c}^{R_d} \frac{(R_1^2-R_s^2)^{\frac{1}{2}}}{R_1^5} \sin 2\alpha \; R^3 dR \; d\alpha$$

$$B_5 = \int_0^{2\pi}\int_{R_c}^{R_d} \frac{(R_1^2-R_s^2)^{\frac{1}{2}}}{R_1^5} \; RdR \; d\alpha \qquad (16)$$

$$B_6 = \int_0^{2\pi}\int_{R_c}^{R_d} \frac{(R_1^2-R_s^2)^{\frac{1}{2}}}{R_1^5} \cos\alpha \, R^2 dR \; d\alpha$$

$$B_7 = \int_0^{2\pi}\int_{R_c}^{R_d} \frac{(R_1^2-R_s^2)^{\frac{1}{2}}}{R_1^5} \sin\alpha \, R^2 dR \; d\alpha$$

and $R_1^2 = 1 + R^2 + 2R(-\sin\Phi \sin\alpha + \cos\Theta \cos\Phi \cos\alpha)$.

Note that the lengths in the integrands of equations (13) and (16) have been normalised by the orbital radius so that they are dimensionless.

Figures 7-13 show the Stokes Parameters for scattered light emitted by the companion star. In the integral (equations (13) and (16)), $R_c = 0.001$ for all loci, while $R_d = 0.2$ and $R_s = 0.7$ (cf. van den Heuval et al., 1980) for Figures 7,8,10 and 11 and $R_d = R_s = 0.45$ (cf. Wagner, 1986 and references therein) for Figures 9,12 and 13. Figures 7-9 are for jet only scattering while Figures 10-12 are for disc only scattering. If $\Theta \gtrsim 45^\circ$ (depending on R_s), the jet 'intersects' the companion star and $[f(R)]^2$, in the integrands of equations (13), is negative. There is no similar geometrical restriction on the range of Θ for the disc. When $\Theta = 0$ (Figures 7 and 10), R_s, R_d and R_c affect the scale, but not the shape of the locus, which is an ellipse, whose eccentricity depends on the inclination, that is described twice per orbit. For both jet and disc, when $\Theta = 0^\circ$ and $i = 90^\circ$ then $U = 0$. The loci in all these figures are not smooth because the integrals were calculated in intervals of $\lambda = \pi/10$ over thirteen orbital periods and $P_{prec} \approx 12.5 P_{orb}$ (cf. $P_{prec} = 162.5$ days

and P_{orb} = 13.1 days for SS433 eg. Kemp 1986). In Figures 8,9 and 11-13, the basic ellipse due to the orbital motion of the scattering region, is both modified and displaced by the precession of the jet or disc. The appearance of the locus over one precession period is determined primarily by Θ and i, although in the case of disc scattering, as R_d increases the precessional modification of the orbital double ellipse is more marked. (Note that $R_d + R_s \lesssim 1$). In general, however, the precessional effect in the case of the disc is smaller than for the jet. The scale of the ellipse changes with precessional phase as does the centre of the ellipse, which remains on, or close to, the Q-axis. The shape of the double ellipse changes noticeably only when $\Theta \neq 0$ and i is large (See Figure 12 and 13b for $i=90^{o}$). Although the changing aspect of the disc with respect to the companion star does change the degree of polarisation, the disc can always be approximated by a localised scattering region of slightly varying optical depth in the orbital plane. This cannot be done for the jet when $\Theta \neq 0^{o}$, since, because of precession, the position of the segment of the jet which produces most of the polarisation moves along the jet, being (mostly) in the half of the jet which is tilted towards the companion star. Therefore the 'altitude' of the effective scattering region varies with the precession phase and, hence the changes, with precession phase, in the Q,U locus for the jet for one orbital period. Also, the degree of polarisation given by disc scattering is much less than that given by jet scattering (Figure 13) since $\frac{n_j \sigma_o}{2a}$, $\frac{n_d \sigma_o}{2}$ effectively measure the optical depths of jet and disc respectively.

4.4 Stokes Parameters for the whole system

Let the fraction of the total luminosity of the system emitted by

the central source be f. Then the Stokes Parameters for the whole system are given by

$$Q_{total} = f(Q_{cd} + Q_{cj}) + (1 - f)(Q_{sd} + Q_{sj})$$
$$U_{total} = f(U_{cd} + U_{cj}) + (1 - f)(U_{sd} + U_{sj}) \qquad (17)$$

Figures 14, 15 and 16 show matrices of Q,U loci for a range of i and f values. The constant A can be found from equations (3), (7) and (17) and is equal to

$$\frac{\pi\sigma_o f}{2}\{n_d(\log[\tan\tfrac{1}{2}(\sin^{-1}\frac{r_c}{r_d})] + \cos(\sin^{-1}\frac{r_c}{r_d})) + \frac{n_j}{2r_c}\}.$$

As can be seen from these figures, f must be small, in some cases less than 0.25, before the shape of the Q,U locus does not clearly show the precession variation.

The Stokes Parameters in equations (17) are referred to axes which have Q-axis normal to the orbital plane. When observations are made, this need not be the case. Suppose the angle between an observer's Q-axis and the normal to the orbit is β, measured anticlockwise from the orbit normal to the observer's axis. Then the Stokes Parameters referred to the observer's axes, $Q(\beta)$, $U(\beta)$, are given by

$$\begin{pmatrix} Q(\beta) \\ U(\beta) \end{pmatrix} = \begin{pmatrix} \cos 2\beta & \sin 2\beta \\ -\sin 2\beta & \cos 2\beta \end{pmatrix} \begin{pmatrix} Q_{total} \\ U_{total} \end{pmatrix} \qquad (18)$$

Figures 17 and 18 show the effect of rotating the observer's axes for 2 sets of parameters. The pattern repeats for $\beta > 180^o$.

4.5 Limitations of the model

The simple model of SS433 used in the previous sections does not allow for many of the effects known to be present in the system. These

include eclipses of both light sources and scattering regions, and non-sphericity of the sources. Moreover, the jets do not precess as a rigid rod, for only the inner region is constrained to follow the disc normal, hence the observed 'corkscrew' at radio wavelengths. The disc height may be as much as two-thirds the radius, while the opening angle of the jet is thought to be $\sim 2^{o}$. Both disc and jets are likely to exhibit fluctuations of density that are both position and time dependent, and, certainly close to the compact object, the assumption of optically thin scattering may not hold. SS433 is observed to be variable on many time scales over and above the periodic variations identified with the precession or the orbital period, and such luminosity fluctuations could well change the proportion of the total luminosity emitted by each source (i.e.f). There may be some polarisation due to scattering in the atmosphere of the companion star, which has not been included in the model (but this should mimick that of the companion's light on the jet/disc system) and the eccentricity of the orbit is not well known. Finally, the effects of a magnetic field which may well be present in the environs of the compact object, such as Faraday Rotation, are ignored. These are likely to be small at optical wavelengths.

The chosen geometry of the scattering regions gives the maximum percentage polarisation, $P = (Q^2+U^2)^{\frac{1}{2}}$, per electron. A thick disc or expanding jet will not change the shape of the Q,U locus although the magnitude will decrease as the scattering regions tend to spherical symmetry. Multiple scattering, which will occur if the scattering regions are not optically thin, will also reduce the magnitude of Q and U, and will also give some circular polarisation. However, the temporal and angular polarimetric properties of such a disc/jet which concern us here

can be accurately replaced (cf. Dolan 1984) by an equivalent uniform thin disc/jet.

Polarisation from the jets is proportional to $^1/r^2$ for a thin jet and will decrease even faster for an expanding jet. Only the inner regions of the jet give significant polarisation and hence the jet 'cork-screw' will have a negligible effect, particularly if the disc is the dominant scattering region. Density fluctuations in the jet or disc will affect the shape of the Q,U locus only if they are axisymmetric. Even so, observations over a long period of time should average out such effects. The same is true for non-periodic variations in f.

Many models of SS433 have the companion star filling its Roche Lobe. The central source in this model includes the light emitted by the inner regions of the disc. Hence, both sources are non-spherical. However, the effect of the departure from spherical symmetry of the sources is expected to be less than the effect of replacing a point source with an extended spherical source.

Since the angular size, as seen from the disc, of the companion star is large, any polarisation due to scattering in its atmosphere is likely to be small. Such polarisation will depend only on the orbital period, unless the companion star is singificantly non-spherical and also precesses. If the Q,U variation at the precession phase is dominant, i.e. scattering from the central source is dominant (see Section 4.6), the shape of the precession variation and hence such parameters as i, Θ and β could still be determined. The same is true for non-zero orbital eccentricity, since only the polarisation due to the companion star would be affected.

The major source of inaccuracy in the model lies in the lack of

eclipsing and occultation effects. However, some of these effects depend only on the orbital phase, such as eclipses of the sources and occultation of the disc by the companion star, whereas some depend on the precession phase, such as occultation of part of the jets by the disc. Since the precession and orbit are not phase locked, and since the precession period is much longer than the orbital period, the variation of the polarisation with precession phase can be studied by omitting data taken during eclipses, if the precession is dominant. Then the precession variation can be subtracted from the data and the resultant values analysed.

In general, if the polarisation due to scattering of light from the central source is dominant then the model developed in this chapter should provide values for Θ, i and β, particularly if data taken during eclipses is omitted from analysis, even if SS433 departs significantly from the simple geometrical model shown in figure 1.

4.6 Predicted Characteristics of the Model

In this section we investigate the Stokes Parameters predicted by this model for SS433. If we define

$$\tau_j = \frac{n_j \sigma_o}{a}$$

$$\tau_d = n_d \sigma_o \qquad (19)$$

then τ_j and τ_d are measures of the optical depth in the jet and the disc respectively. (Note that both τ_j and τ_d are dimensionless since n_j and n_d have dimensions L^{-1} and L^{-2} respectively). Now, if $\dot{M}$ is the mass loss rate in the jet, $\dot{M}_T$ is the mass transfer rate from companion star to disc, A_d is the area of the disc and t is the time taken by a proton to spiral in from the outer rim of the disc to the inner radius (in seconds), then

$$n_j = \frac{\dot{M}}{0.26c\, m_p}$$

$$n_d = \frac{\dot{M}_T t}{A_d\, m_p} \qquad (20)$$

and $A_d = a^2\pi(R_d^2 - R_c^2)$

where m_p = mass of proton and 0.26c is the velocity of the jet. Hence, measuring $\dot{M}$ and $\dot{M}_T$ in solar masses per year and a in astronomical units

$$\tau_j = 12.9\ \frac{\dot{M}}{a} \qquad (21a)$$

$$\tau_d = 2.14\ \ 10^{-3}\ \ \frac{t\,\dot{M}_T}{a^2(R_d^2-R_c^2)} \qquad (21b)$$

Let $A = \frac{\pi}{4}\left(\frac{\bar{\tau}_j}{R_c} + 2\tau_d\left[\log\left[\tan\tfrac{1}{2}\left(\sin^{-1}\frac{R_c}{R_d}\right)\right] + \cos\left(\sin^{-1}\frac{R_c}{R_d}\right)\right]\right)$ (22)

Then, (see equations (3) and (7)), the Stokes Parameters for scattering of light from the central source off the disc and jet are

$$Q_c = Af\{(1-3\cos^2\Theta)\sin^2 i + \sin 2i \sin 2\Theta \cos(\lambda+\Phi) - (1+\cos^2 i)\sin^2\Theta\cos 2(\lambda+\Phi)\} \qquad (23a)$$

$$U_c = 2Af\{\sin i \sin 2\Theta \sin(\lambda+\Phi) - \cos i \sin^2\Theta \sin 2(\lambda+\Phi)\} \qquad (23b)$$

while the Stokes Parameters for scattering of light from the companion star are

$$Q_s = \frac{(1-f)\tau_j}{2}\left[\ \ \right] + \frac{(1-f)\tau_d}{2}\{\ \ \}$$

$$U_s = (1-f)\tau_j\left[\ \ \right] + (1-f)\tau_d\{\ \ \} \qquad (24)$$

where the terms in [ ] and { } are the bracketed terms of equations (12) and (15) respectively.

The value of a depends on the masses of the compact object and the companion star. It is, however, rather insensitive and for the sum of the masses $\simeq 50\ M_\odot$, a $\simeq$ 0.4 AU. Since the central source approximates

the light from the inner regions of the disc which is considered to be the more luminous of the two light sources (Kemp et al., 1986), optically and geometrically thick (half-height $\simeq {}^{2}/_{3}$ radius, Margon 1984) $R_c \lesssim 10^{-3}$, seems unjustifiable. $\dot{M}_T$ must be greater than $\dot{M}$. In fact, since the conversion of matter to energy in the environs of a black hole or neutron star is highly inefficient, and since the jet material has such a high kinetic energy, $\dot{M}_T$ is probably at least two orders of magnitude greater than $\dot{M}$. $\dot{M}$ itself cannot be much greater than $10^{-6}\ \dot{M}_\odot\ yr^{-1}$ otherwise the necessary mass loss rate from the companion star ($\gtrsim \dot{M}_T$) becomes so large that SS433 must be less than a few thousand years old - which is the minimum age required to explain the size of W50 (Margon, 1984). Hence, for $\dot{M} = 10^{-7}\ M_\odot\ yr^{-1}$, $a = 0.4$ AU, $R_c\ 10^{-3}$, $R_d = 0.45$, $\dot{M}_T = 100\ \dot{M}$ equations (21) and (22) become

$$\tau_j = 3.225 \times 10^{-6}$$

$$\tau_d = 6.605 \times 10^{-7}\ t$$

and $$A = 2.533 \times 10^{-3} - 6.02 \times 10^{-6}\ t \qquad (25)$$

(Note that t is still measured in seconds).

Therefore, unless $t \lesssim 400$ s, A will be negative i.e. the disc will dominate the polarisation of light from the central source. However, the spiral time, t, of the disc is likely to be of the order of days i.e. 10^5 seconds.

Even if the jet dominates the polarisation from the central source, the disc will still dominate the scattering from the companion (cf. equations 24) since $\tau_d >> \tau_j$ unles $t \lesssim 10^3\ (\frac{\dot{M}}{\dot{M}_T})$ and $t \simeq 10_s$ is completely unreasonable, since the time taken to travel 0.2 AU at the speed of light is 100 s. So for a disc of radius $0.45a$, even radial infall at the speed of light could not give $t < 50$ seconds.

However, these conclusions depend on the assumption that the disc and jet are optically thin. This is unlikely to be true, particularly in the disc. As a result the estimates for the disc density (and hence t) found from data using this model will be many times smaller than the true value. The maximum percentage polarisation predicted by this model for light emitted by the central source and scattered off the disc/jet system is $\sim \quad 2\,|A|\,\%$.

The contribution to the polarisation of the whole system made by the scattering of light from the companion star will be at least an order of magnitude smaller than that from the central source since the terms in [ ] and { } in equations (24) are less than or of the order of 1. $|A|$ will be greater than $\sim 10^{-3}$ even if the effective disc mass (and hence t in equation 25) is reduced by $\sim 10^{2}$ compared to its true mass as a result of the optical thickness of the jet and $\tau_d \simeq 10^{2}\ \tau_j \simeq 10^{-4}$. Hence, unless f is very small, we expect the central source, i.e. the precession period, to be dominant.

If the effect of the companion star is strong enough to show above the noise on the data, it should appear at half the orbital period since the disc will contribute more than the jet (see section 4.3 and above). The precession of the disc will change the shape of the scattering retion, and hence the shape of the Q,U locus on the synodic period. This effect is unlikely to be detected even if the half-orbital period is seen clearly (cf. Figures 10-13).

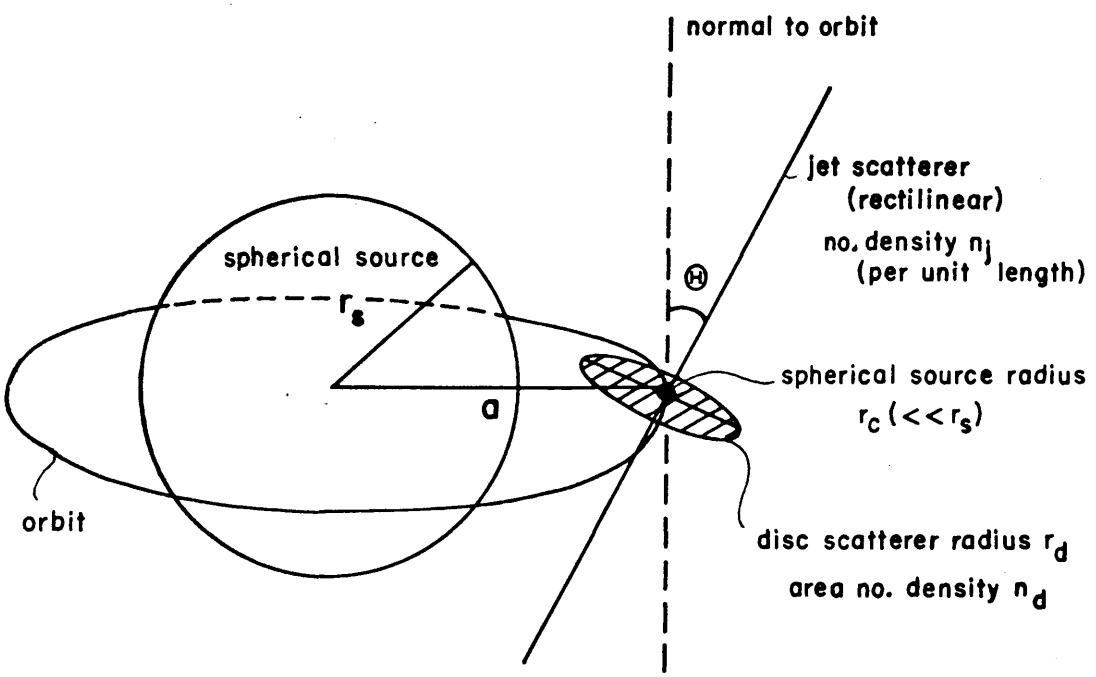

Figure 1: Simple geometrical model for SS433

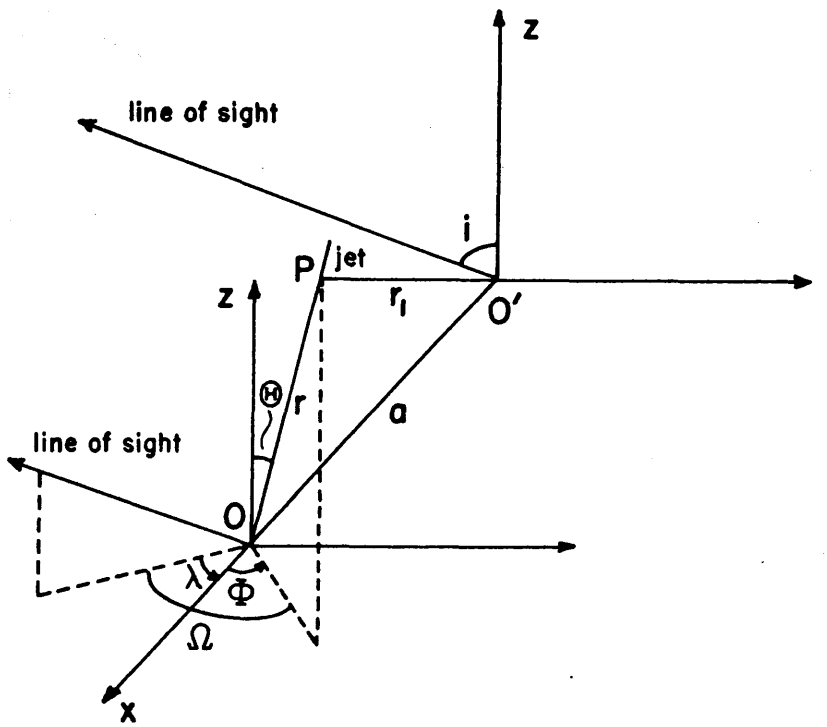

Figure 2: Scattering geometry for an arbitrary point P on the jet. λ is the phase of the orbit, Ω is the phase of precession. P has coordinates (r,Θ,Φ) with respect to O, the centre of the compact object. O' is the centre of the companion star. a is the separation of the sources.

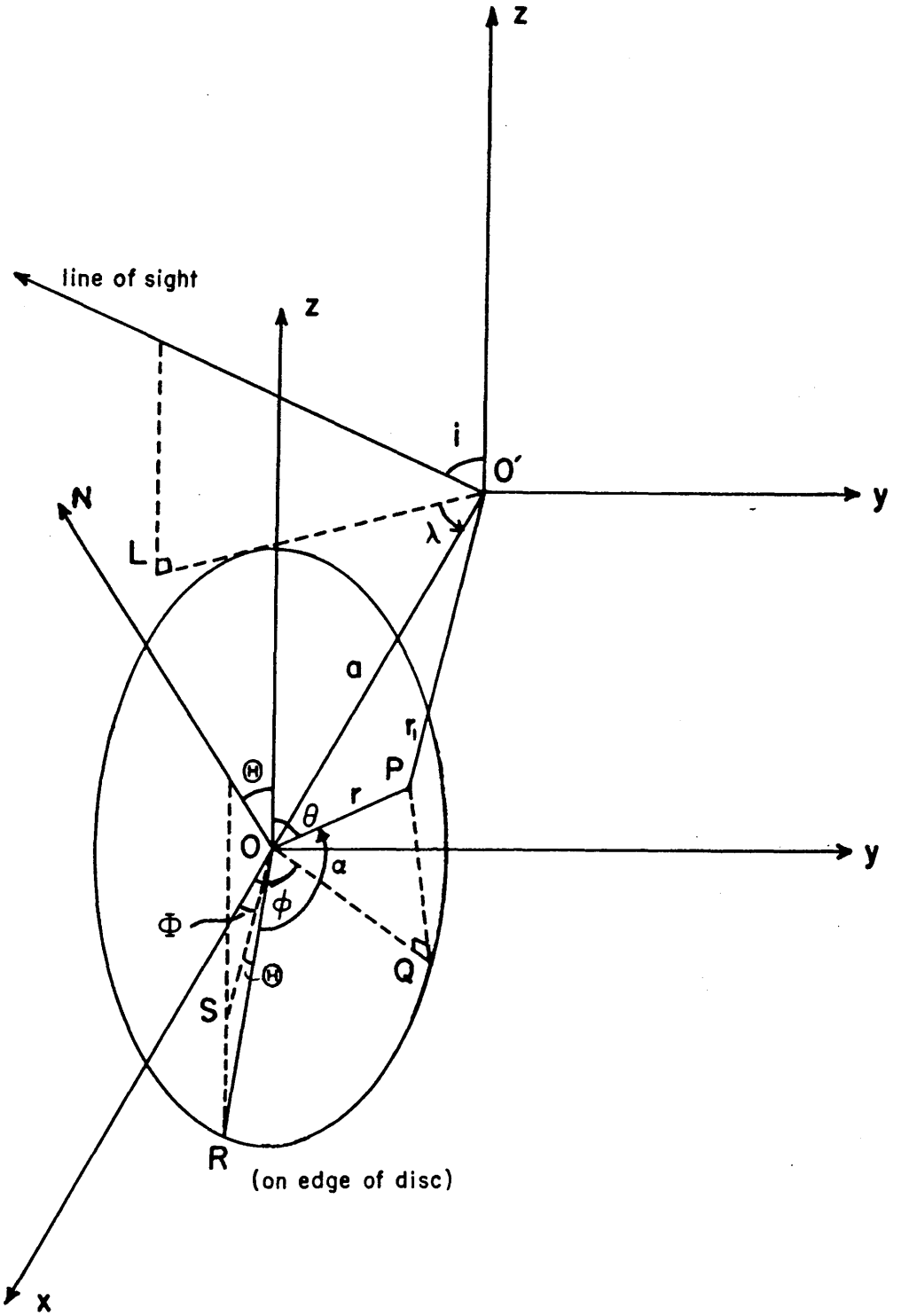

Figure 3: Scattering geometry for an arbitrary point P in the disc. P has coordinates (r,θ,ϕ) with respect to O, the compact object. O' is the centre of the companion star. ON is the normal to the disc, the direction of the jet. OQ is the projection of OP on the x,y plane. OS is the projection of OR on the x,y plane. O'L is the projection of the line of sight on the x,y plane.

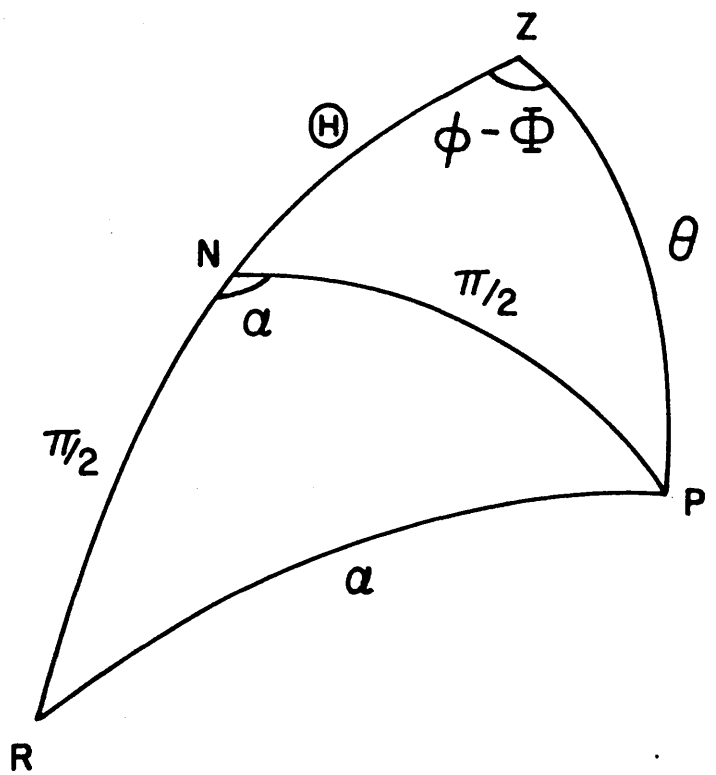

Figure 4: Spherical triangle from Figure 3 for the transformation from (r, θ, ϕ) to (r, α), coordinates in the plane of the disc.

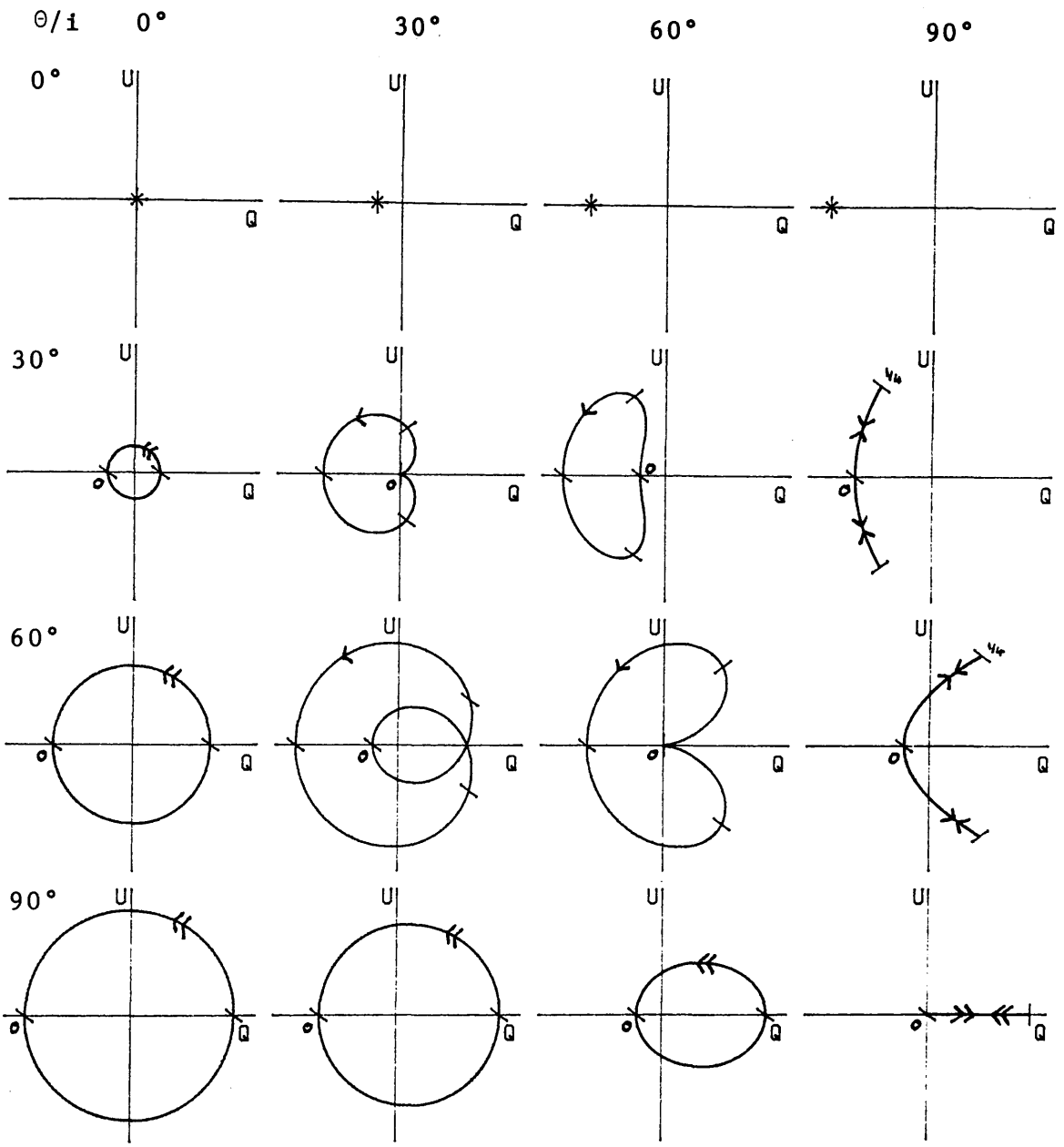

Figure 5: Matrix of Q,U loci for a precessing disc and jet scattering from a central spherically symmetric source. These loci are for jet dominated scattering. Fiduciary marks are shown at quarter precession phase intervals.

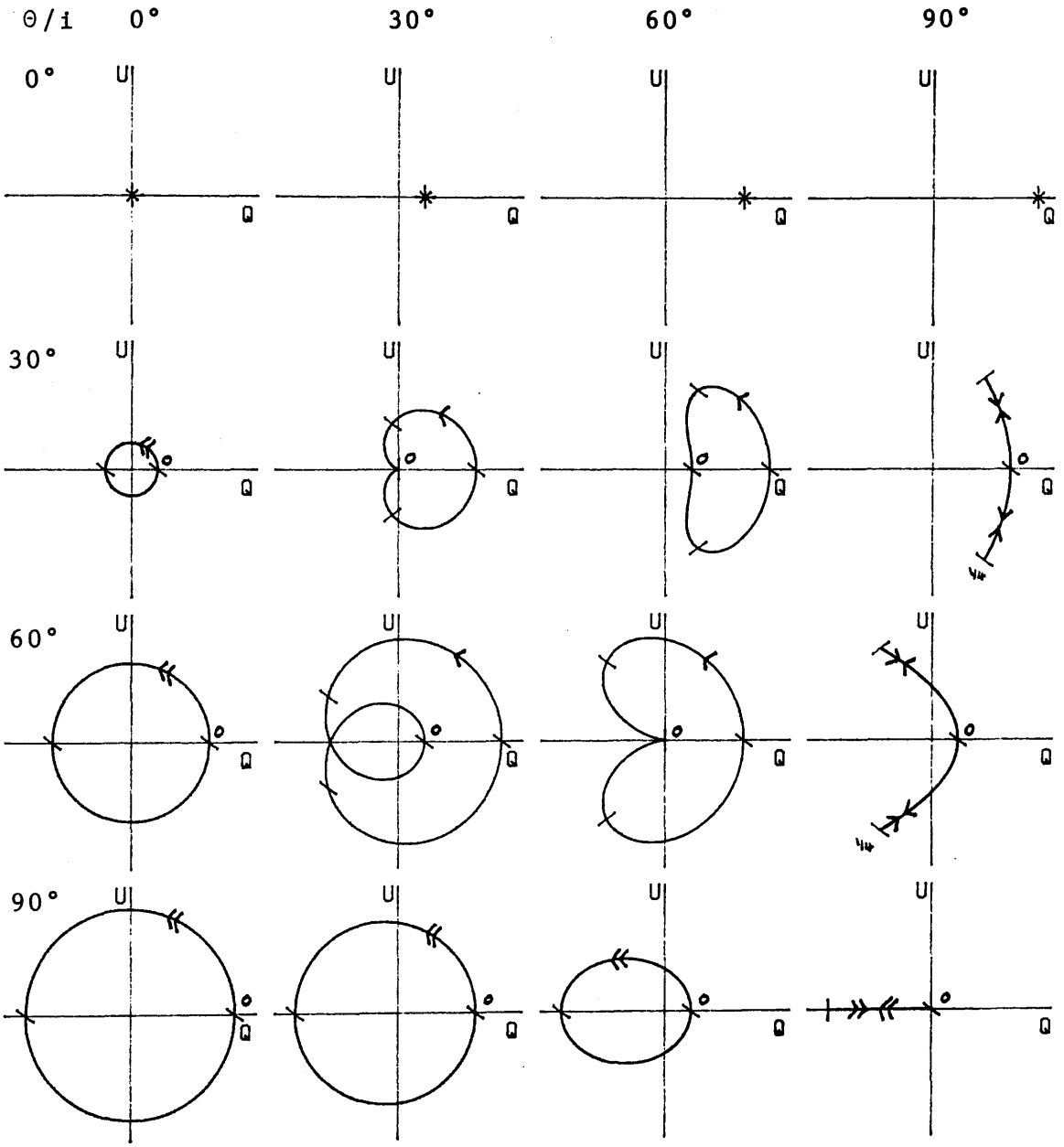

Figure 6: As Figure 5 for disc dominated scattering.

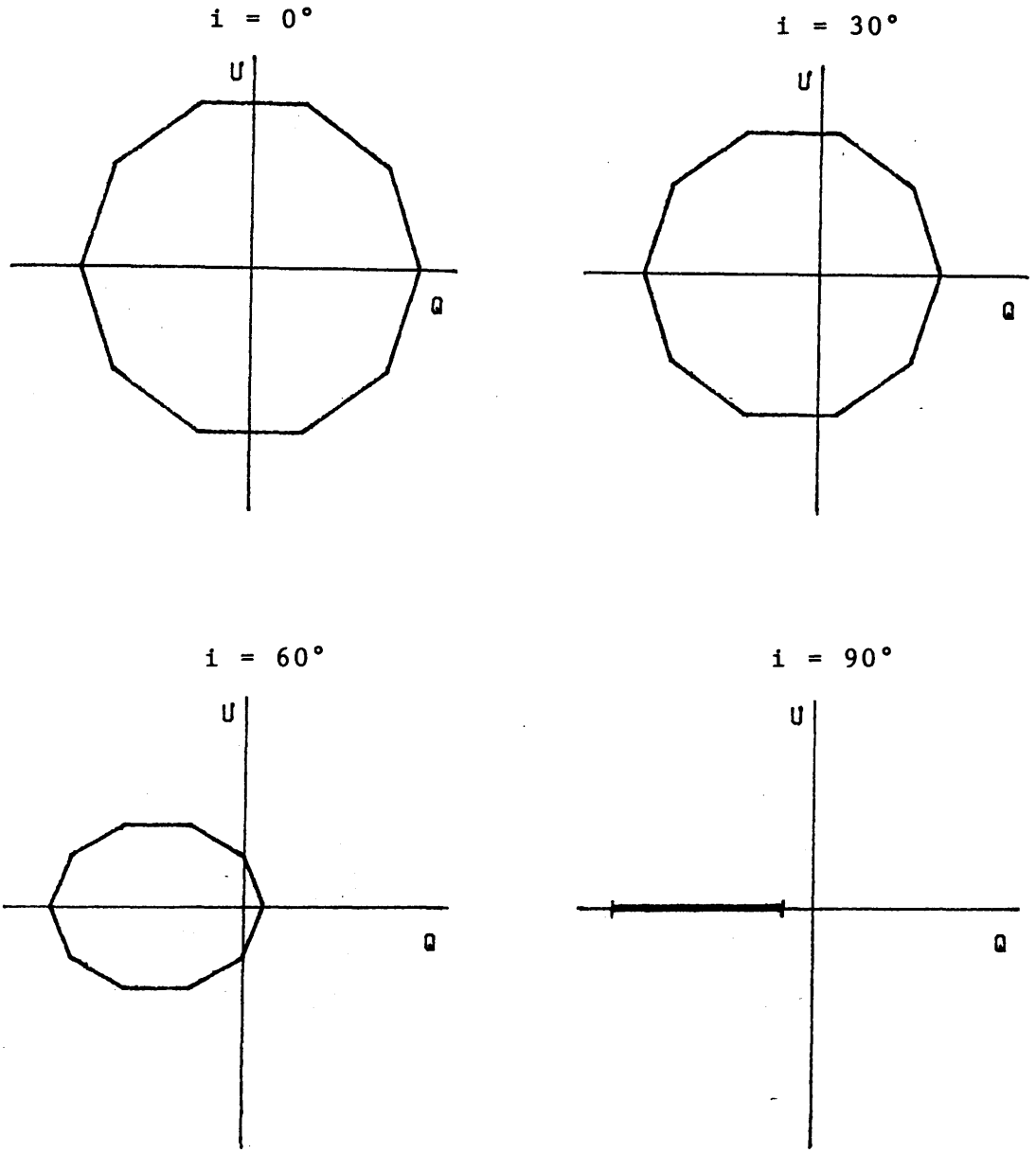

Figure 7: Set of Q,U loci for a precessing jet in a binary system, scattering from a spherically symmetric companion star of radius, $R_s = 0.7$. The binary orbit is circular, of unit radius. The half angle of the precession cone, $\Theta = 0°$.

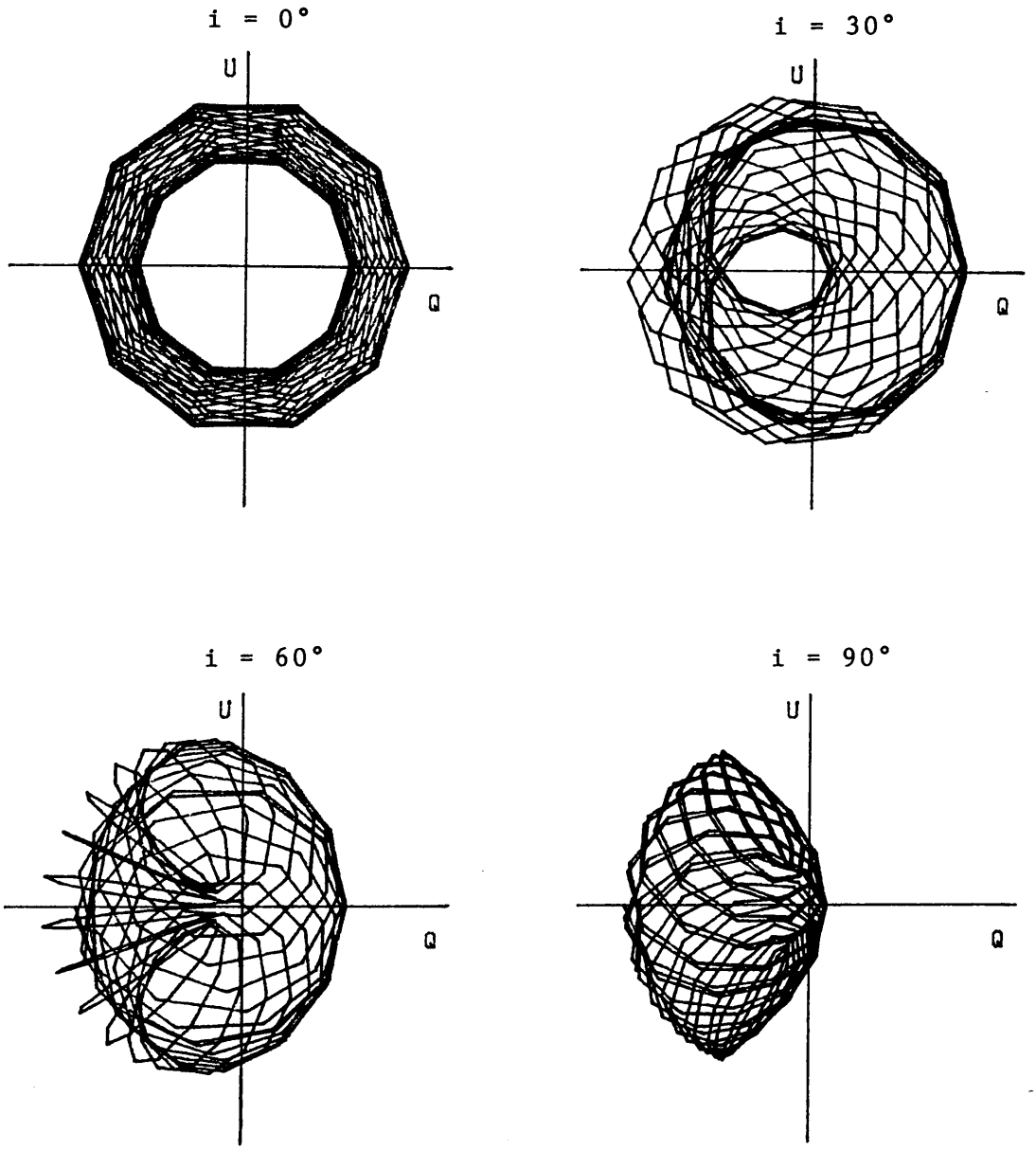

Figure 8: As Figure 7 for Θ = 30°.

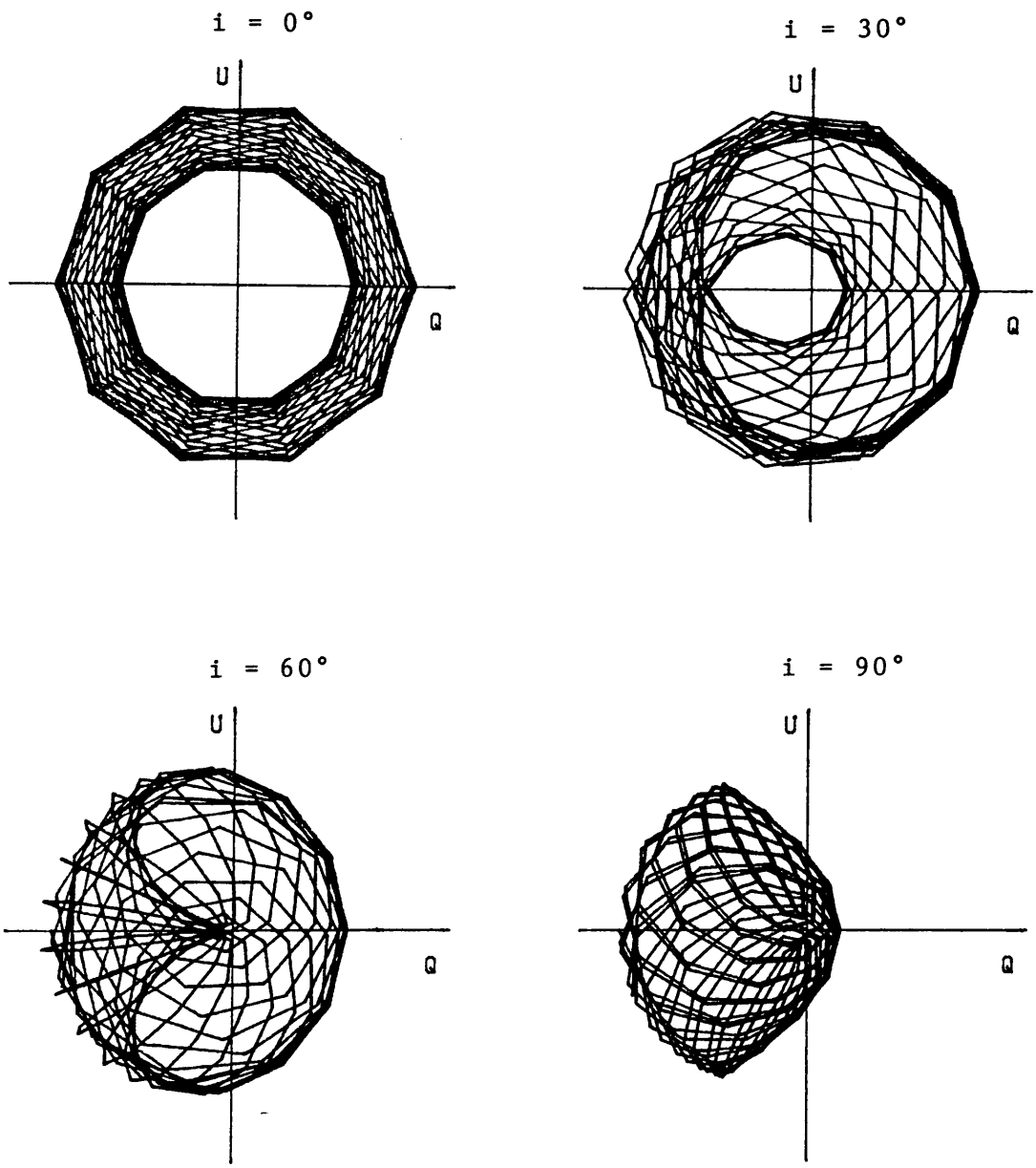

Figure 9: As Figure 7 for R_s = 0.45 and Θ = 30°.

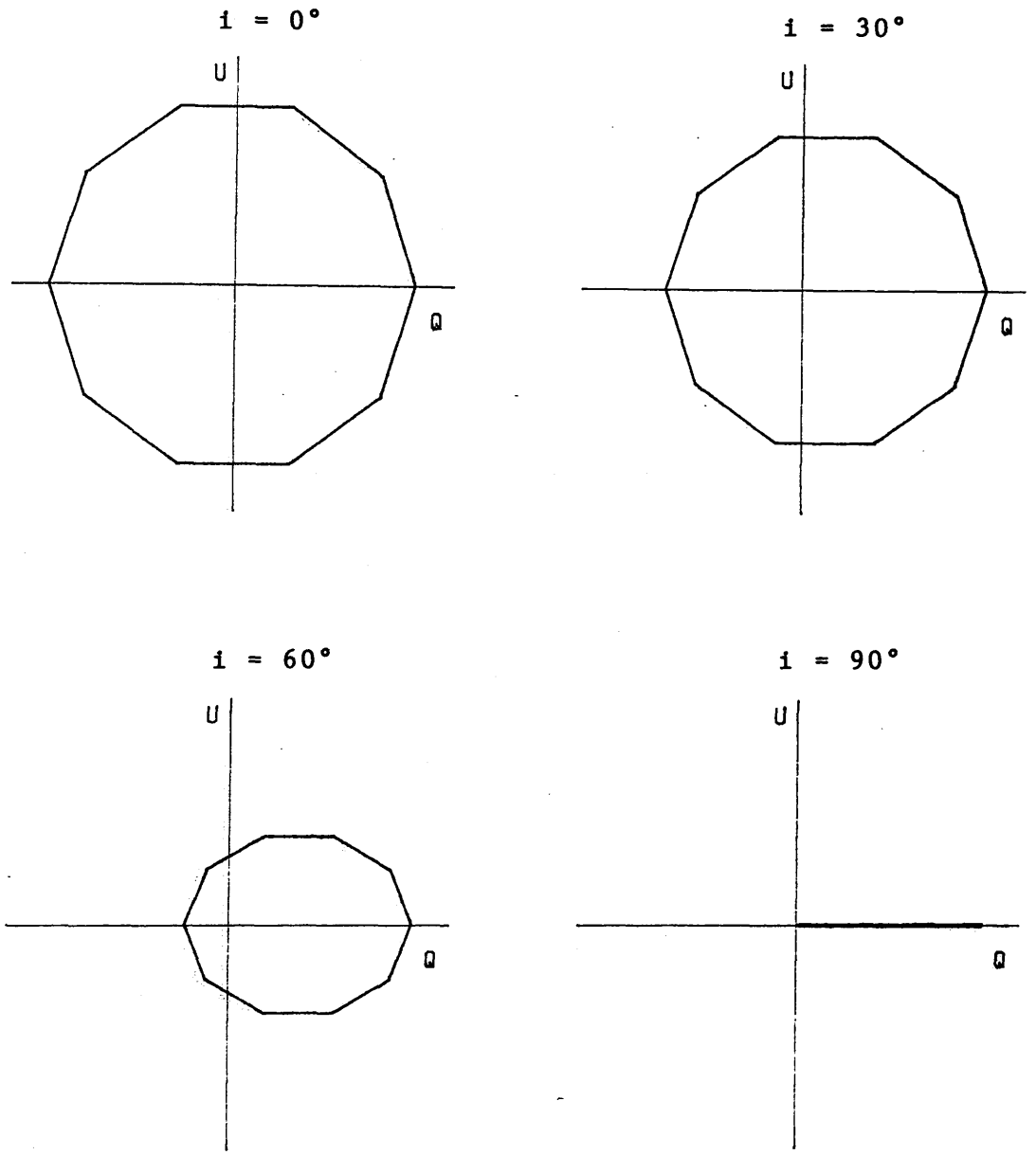

Figure 10: Set of Q,U loci for a precessing disc of outer radius, $R_d = 0.2$ in a binary system, scattering from a spherically symmetric companion star of radius, $R_s = 0.7$. The binary orbit is circular, of unit radius. The half angle of the precession cone, $\Theta = 0°$.

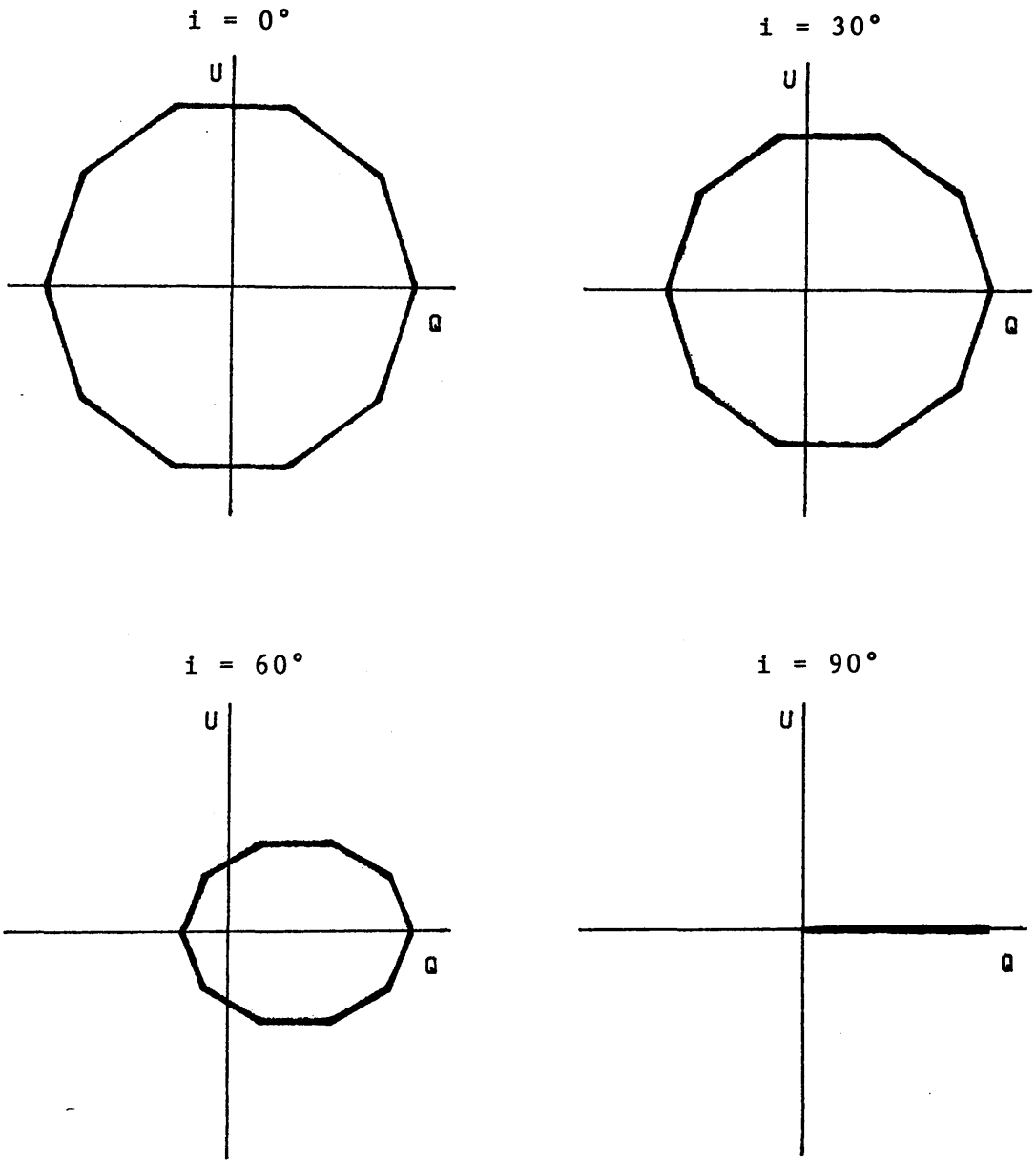

Figure 11: As Figure 10 for $\Theta = 60°$.

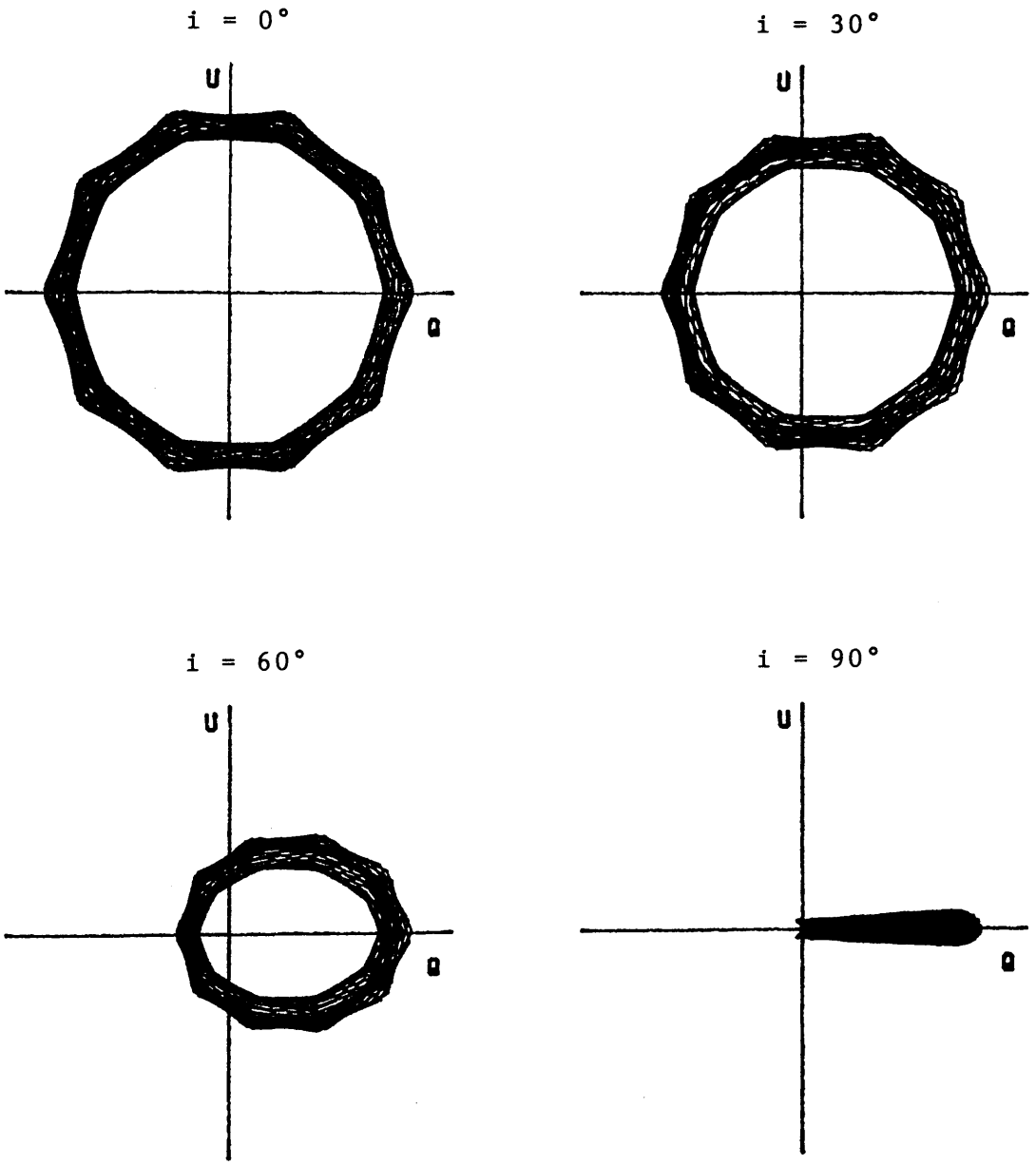

Figure 12: As Figure 10 for $R_d = R_s = 0.45$ and $\Theta = 60°$.

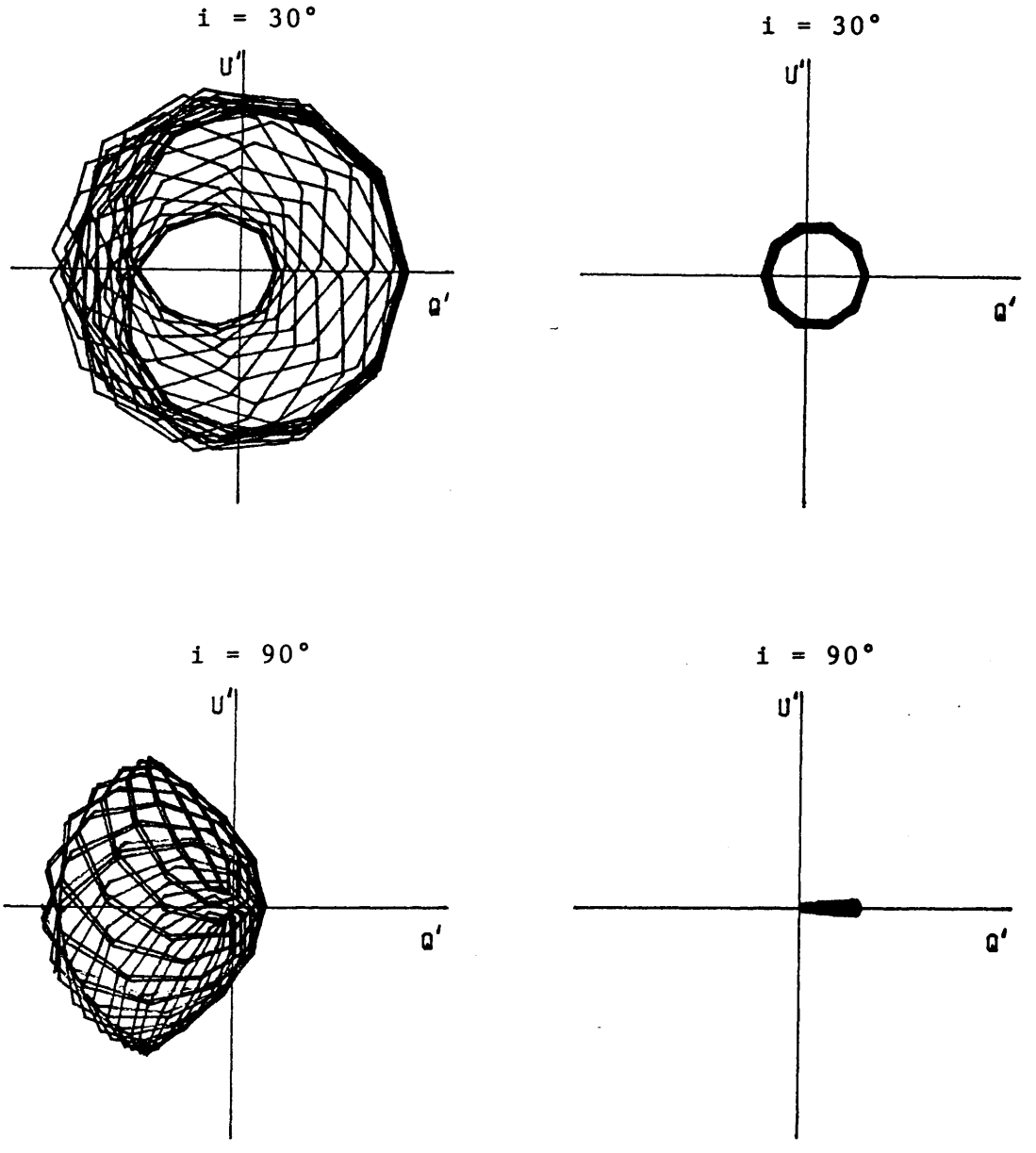

a) jet contribution b) disc contribution

Figure 13: Set of Q,U loci to compare the contributions of a precessing jet or disc to the Stokes Parameters of SS433 due to light scattered from the companion star. The binary orbit is circular, of unit radius and the star has radius 0.45, as has the disc. The half angle of the precession $\Theta = 30°$.

a) $U' (=U_{sj}/\tau_j)$ v $Q' (=Q_{sj}/\tau_j)$ where $\tau_j = n_j \sigma_o / a$

b) $U' (=U_{sd}/\tau_d)$ v $Q' (=Q_{sd}/\tau_d)$ where $\tau_d = n_d \sigma_o$

(see equations 19 and 20)

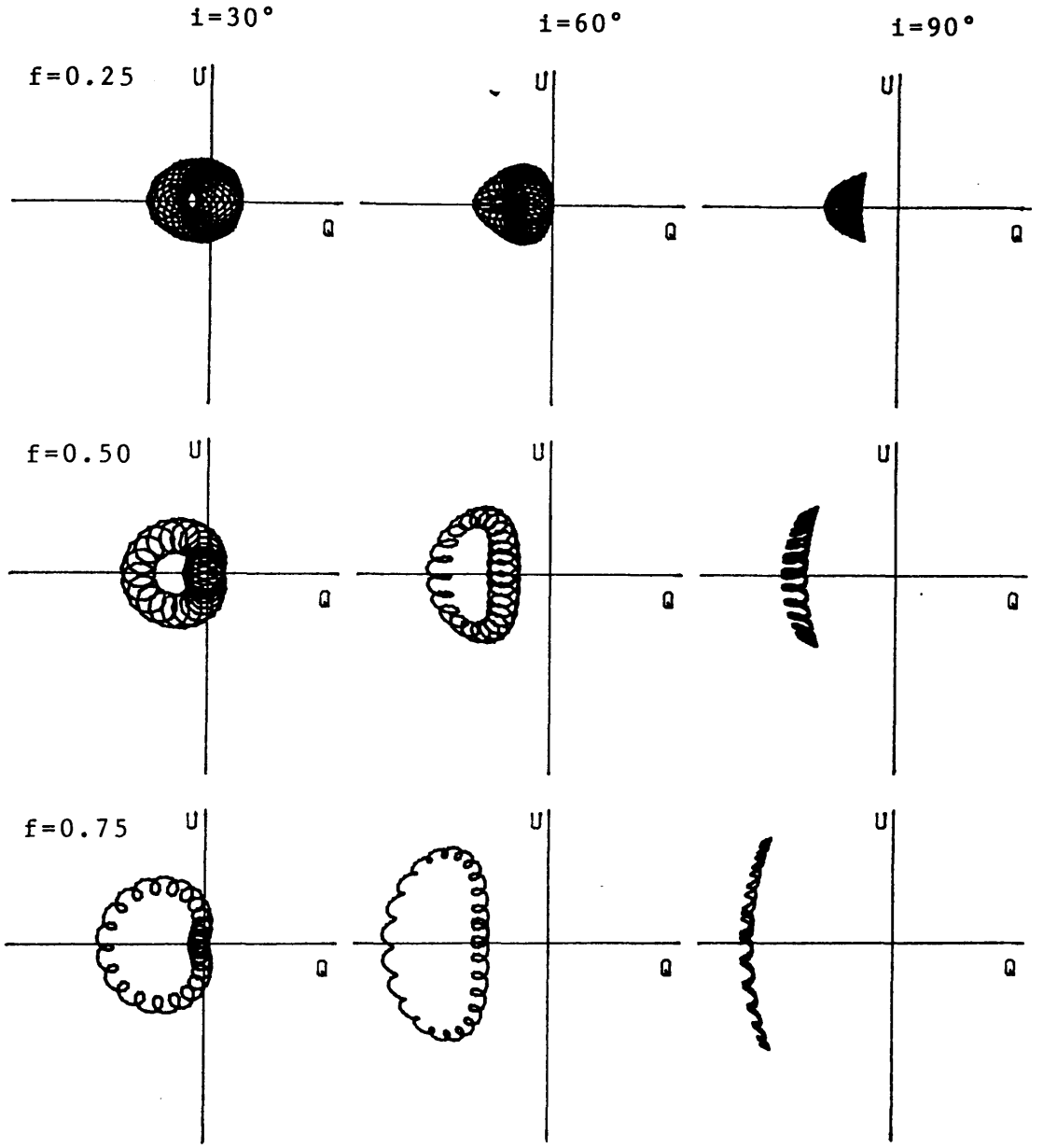

Figure 14: Matrix of Q,U loci for the full model of SS433, where the radii of the disc and the companion star are 0.45 (in units of the orbital radius), the precession cone angle, $\Theta = 20°$, the inclination of the orbit is i, the fraction of the total luminosity emitted by the central source is f, $\tau_j = 0.02$ $\tau_d / \tau_j = 1$ and $A = 0.2$ (τ_j, τ_d and A, are given by equations 19 and 23 respectively).

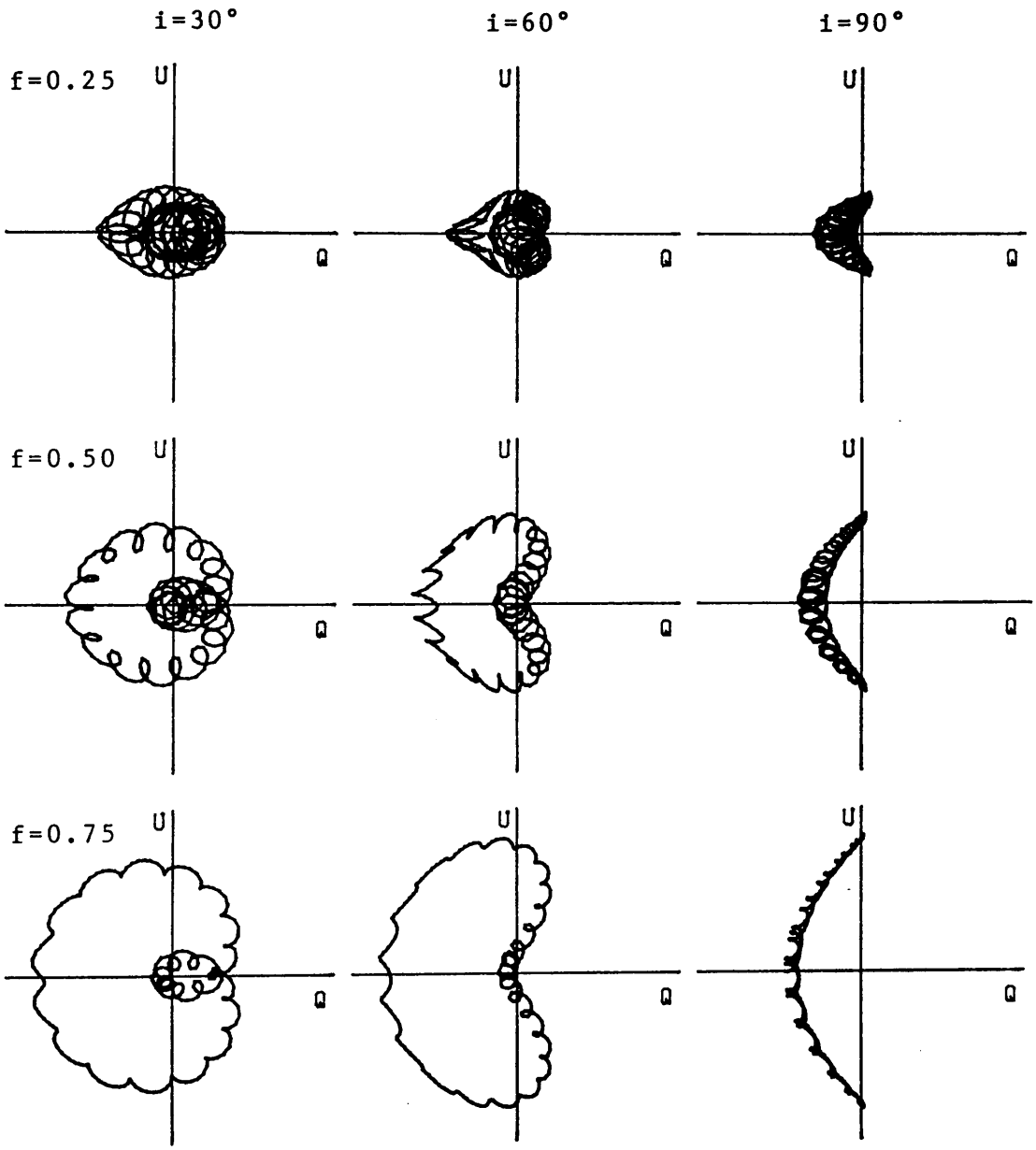

Figure 15: As Figure 14 for Θ = 45°

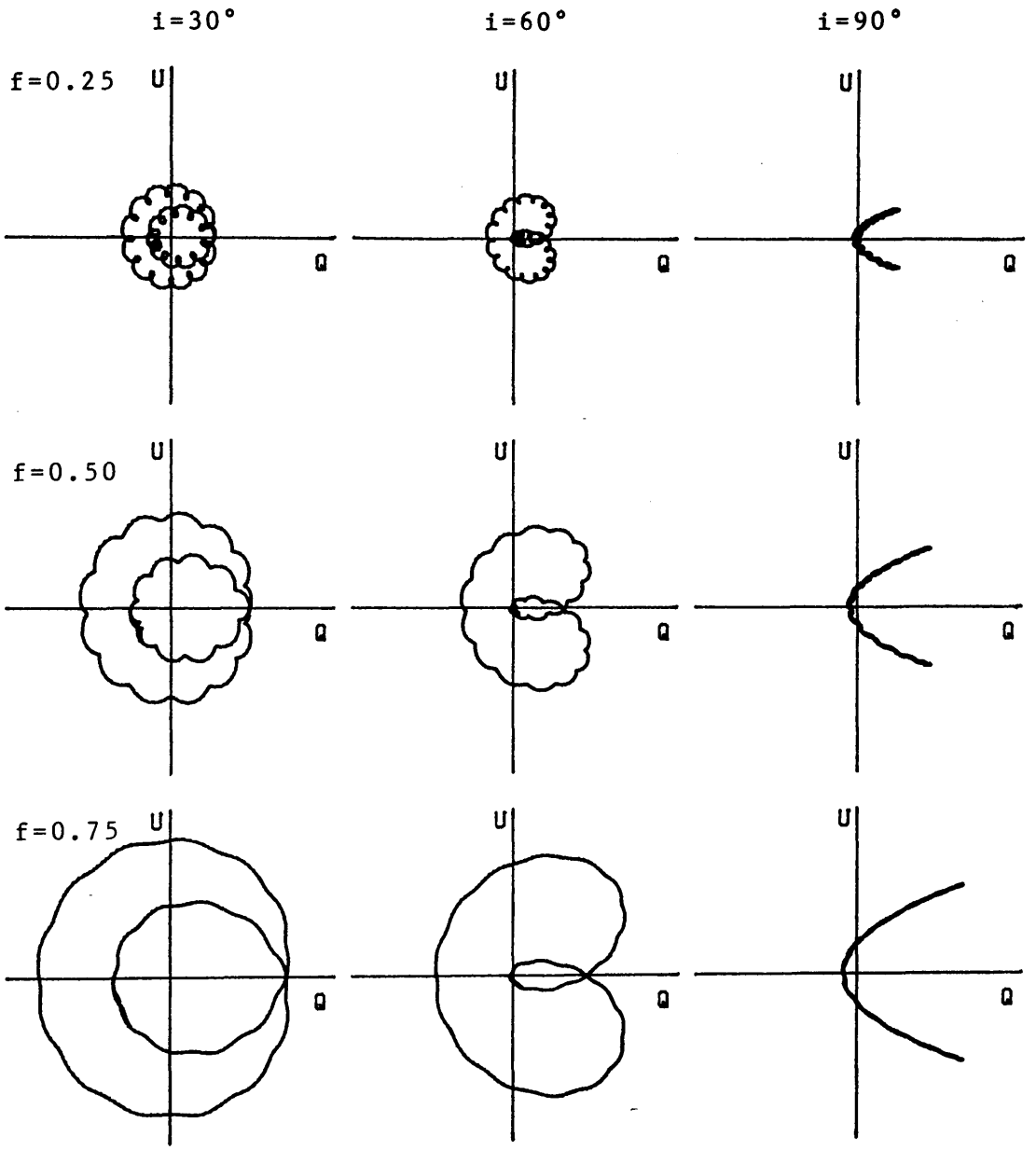

Figure 16: As Figure 14 for $\Theta = 70°$ and $\tau_j = 0$

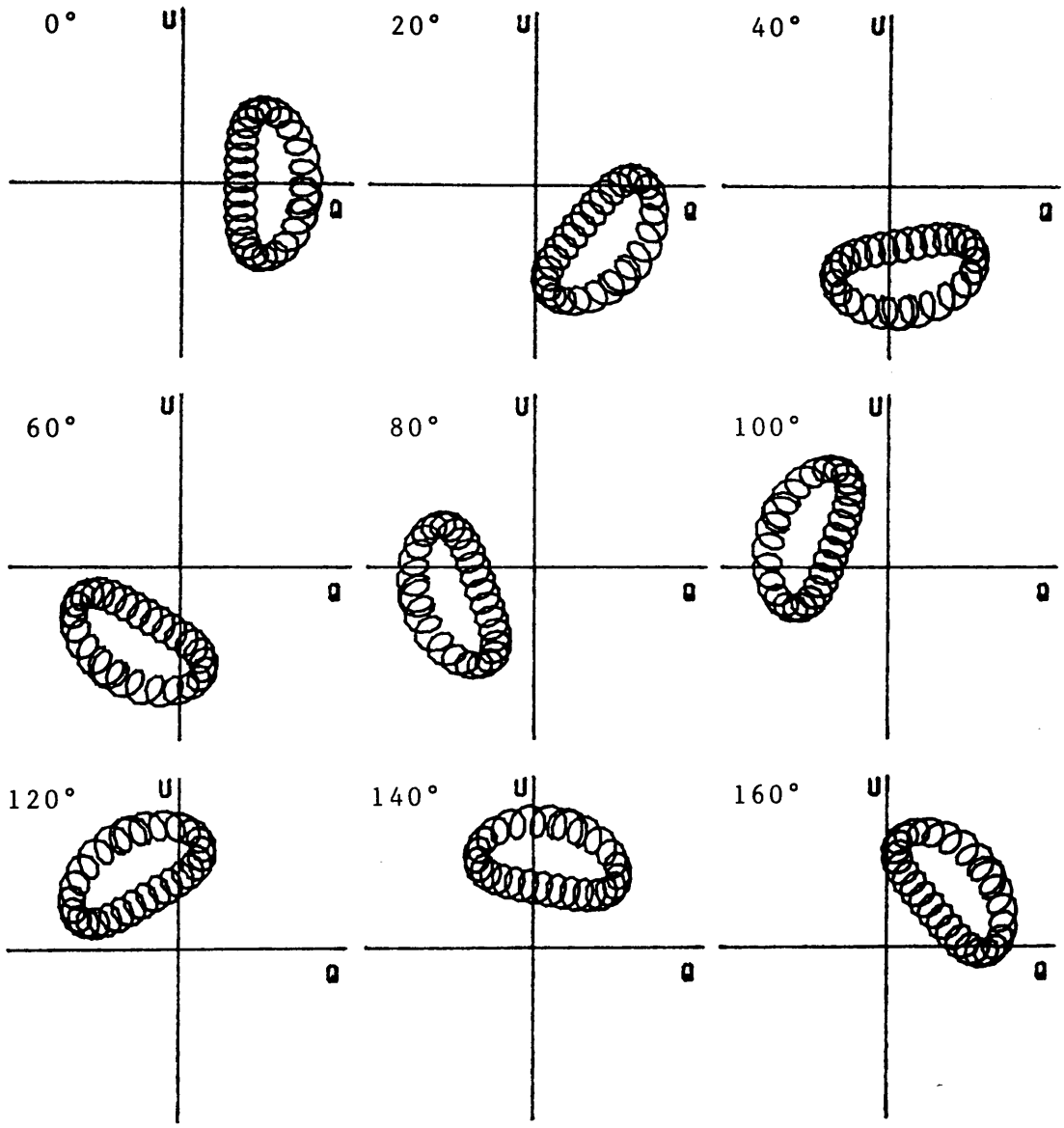

Figure 17: Set of Q,U loci for the full model of SS433 showing the effect of rotating the observer's axes. The radii of the disc and the companion star are 0.45 (in units of the orbital radius), the precession cone angle, $\Theta = 20°$, the inclination of the orbit, $i = 120°$ and $Af = -0.65$, where f is the fraction of the total luminosity emitted by the central source and A is given by equation 23. $(1-f)\tau_j/2 = 0.02$ and $\tau_d/\tau_j = 10$. Since the observer's axes rotate through angle β anticlockwise the locus appears to move through 2β clockwise.

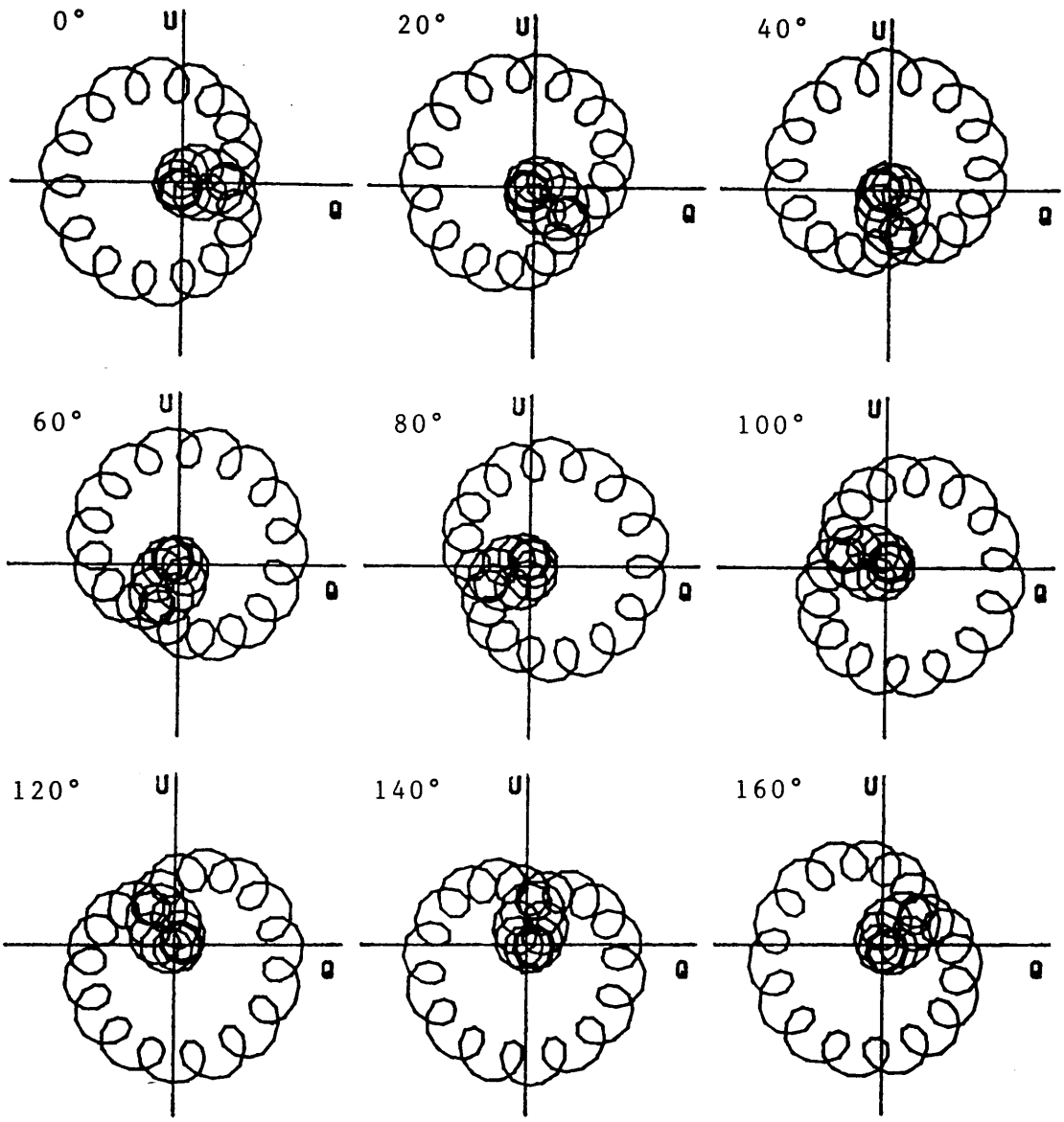

Figure 18: As Figure 17 for Θ = 45°, i = 30° and Af = 0.65

CHAPTER 5

APPLICATION TO DATA

5.1 Introduction

At present, the data available on the optical polarisation of SS433 consists of 84 broadband observations made during the period April 1979 to May 1981 (McLean and Tapia, 1981, McLean, private communication) and 35 multiple waveband observations made during the period June 1979 to October 1982 (Efimov et al., 1984). Of the latter, the 25 R-band measurements are compatible with the McLean and Tapia data giving 109 points spanning 3½ years. A real-time plot of Q and U is shown in Figure 1 and 2. The typical quoted measurement errors are $\sim$ 0.06% for the McLean and Tapia data and $\sim$ 0.12% for the Efimov et al., data. However, inspection of Figures 1 and 2 leads to the conclusion that the scatter of the data points is larger than these typical errors, particularly in Q. This is not unexpected, since SS433 exhibits large aperiodic fluctuations at all wavelengths so far observed. Both the radio observations of the jets and high resolution spectral analysis of the doppler-shifted lines from the jets indicates that the jets are more like a series of 'blobs' than a continuous stream. Since the Thomson scattered polarisation depends on the density distribution of electrons, clumping in the jets and, perhaps, large corresponding fluctuations in the density distribution in the disc, may well account for some of the scatter. Mutual eclipses of the light sources and variable occultation of the scattering regions, particularly the disc, should account for some of the scatter also but these effects should be periodic, depending on the orbital period.

In this chapter, we first investigate the periods present in the

raw data, and the qualitative conclusions that can be drawn from the data. An analytic optimisation procedure is then developed for the precession variation (Section 5.3) and used to obtain the best-fit precession curve. The residuals are analysed for any periods remaining in the data once the best-fit precession curve has been subtracted. Finally, using the best-fit parameters an attempt is made to fit the full theoretical model developed in chapter 4 to the data.

5.2 Power Spectrum and Qualitative Results

The power spectra of the Q and U data of SS433 are shown in Figure 3. They were computed by the Fourier summation method in which first

$$C_\nu \begin{pmatrix} Q \\ U \end{pmatrix} = \frac{2}{N} \sum_{i=1}^{N} \begin{pmatrix} Q_i \\ U_i \end{pmatrix} \cos(2\pi\nu t_i)$$

$$S_\nu \begin{pmatrix} Q \\ U \end{pmatrix} = \frac{2}{N} \sum_{i=1}^{N} \begin{pmatrix} Q_i \\ U_i \end{pmatrix} \sin(2\pi\nu t_i) \qquad (1)$$

is computed, where t_i is the time of the ith observation (Q_i, U_i), and then the spectral power, A_ν, where

$$A_\nu^2 = C_\nu^2 + S_\nu^2 \qquad (2)$$

Here N is the number of data points and the frequency, ν, is the reciprocal of the period. In Figure 3, 1000 search frequencies out to a minimum period of 5 days were used.

In the power spectrum for Q, the highest peak is at $\nu = 0$. This indicates the presence of a strong constant component, part, or all, of which may be due to interstellar polarisation. Apart from this, the highest peak in both the Q and U spectra has a period of 162.5 days. This corresponds to the precession period of SS433 (cf. eg. Margon 1984, Kemp et al., 1986). The U spectrum also shows a strong peak at half the precession period, although this is not clearly seen

above the general noise in Q. The orbital period ($\sim$ 13.1 days) is conspicuous by its absence particularly in U. Neither is there any sign of the (orbital/precessional) synodic period or its second harmonic for either direct or retrograde precession. (14.28 and 12.12 days resp.). There is some evidence of a peak at half the orbital period in U only, but it is not statistically significant (cf. also Section 5.5).

These results are as expected from the model developed in Chapter 4 (cf. section 4.6). It was predicted that the precession period would be dominant in the data, and that the orbital period and its 2nd harmonic would have a much smaller amplitude, if detected at all.

Since the precession period is dominant, we have plotted in Figure 4 the data folded on a period of 162.5 days over two precession cycles. We have defined the precession phase to be zero when the separation of the Doppler shifts of the moving lines is a maximum. This corresponds to a phase of 0.5 by Kemp et al's definition (1986). Hence, we have chosen to use the ephemeris of Kemp et al., 1986 displaced by 0.5 in phase. A quasi-sinusoidal dependence of the U parameter on the precession phase shows clearly in Figure 4. The dependence of the Q parameter on the precession phase is not as clear since the 'noise', particularly in phase interval 0.2 - 0.6 is of the same order as the amplitude of the precession variation.

In the model developed in chapter 4, the precession period and its 2nd harmonic both appear in the expressions for Q and U. (See equations 4.3, 4.7). By inspection of these equations we find that the 1st harmonic is dominant in Q if $|\sin 2i \sin 2\Theta| > (1+\cos^2 i)\sin^2\Theta$ (3)

and in U if $|\sin i \sin 2\Theta| > |\cos i \sin^2\Theta|$ (4)

If the inequalities (3) and/or (4) are reversed then the 2nd harmonic is

dominant in Q and/or U. The regions in the i,Θ plane where one of the harmonics is dominant in both Q and U are shown in Figure 5. Since the 1st harmonic is dominant in both Q and U (Figures 3 and 4) $|\Theta| \lesssim 55^{\circ}$, depending on i. (Note that $-\Theta \equiv \pi - \Theta$ Figure 4.1).

There is a further restriction on the range of the precession cone angle Θ from the geometry of the model of SS433 developed in Chapter 4, namely that precession angles so large that the jets 'collide' with the companion star are proscribed since they result in imaginary integrands in Equations 4.13. Physically such an event should produce clearly observable 'flaring' on half the synodic period. Whether such 'flaring' is observable or not will depend on the column density of the atmosphere of the companion star along the path of the jet. Generally, as Θ increases, the brightness and duration of the 'flare' will increase. Let the minimum distance of the jet from the centre of the companion star such that the column density along the jet path is too low for observable 'flaring' be R_c (measured in units of the orbital radius). Then the maximum permissable precession cone angle such that 'flaring' does not occur is $\cos^{-1} R_e$. For $|\Theta|_{max} = 55^{\circ}$ $R_e < 0.57$. In general, R_e is greater than R_s, since R_s is the radius of the photosphere of the companion.

SS433 does exhibit flaring at most wavelengths (eg. radio Bonsignori-Facondi et al., 1986; X-rays Band and Grindley, 1984) but, so far, there is no reported dependence of these flares on the synodic period. In those models where $R_s \gtrsim 0.8$ (cf. van den Heuval et al., 1980), it is hard to see how there could not be 'flares' since $|\Theta|$ must be non-zero to give any precession variation at all.

5.3 Optimisation procedure for data at unequal phase intervals

This treatment is based on that developed by C. Aspin (1981), which extends that of Simmons et al., (1980) dealing with noisy data binned at equal phase intervals. Such a treatment for the polarisation of SS433 is required because of the present small data set and since SS433 is an eclipsing binary.

As the precession is the dominant frequency in the data (Section 5.2), a model depending on the precession phase only can be used as a first approximation. We use equations 4.3 and 4.7 to give

$$\begin{aligned} Q &= A\{(1-3\cos^2\Theta)\sin^2 i + \sin 2i \sin 2\Theta \cos\Omega - (1+\cos^2 i)\sin^2\Theta\cos 2\Omega\} \\ U &= 2A\{ \sin i \sin 2\Theta \sin\Omega - \cos i \sin^2\Theta \sin 2\Omega \} \end{aligned} \qquad (5)$$

where A is a constant which depends on the optical depth in the disc and jet.

The Stokes Parameters of equations (5) are referred to the natural frame of the system, i.e. Q-axis normal to the orbital plane. With respect to this reference frame, the interstellar polarisation has components (Q_{int}, U_{int}). Hence, the theoretical polarisation of SS433 is

$$Q_t = Q + Q_{int}$$
$$U_t = U + U_{int}$$

Let (Q_{ob}, U_{ob}) be the observed Stokes Parameters of SS433 with respect to the natural frame. Then, with respect to an arbitrary observer's reference frame, rotated with respect to the natural frame by angle β (measured anticlockwise from natural to observer's frame), the observed Stokes Parameters are:

$$\begin{pmatrix} Q'_{ob} \\ U'_{ob} \end{pmatrix} = \begin{pmatrix} \cos 2\beta & \sin 2\beta \\ -\sin 2\beta & \cos 2\beta \end{pmatrix} \begin{pmatrix} Q_{ob} \\ U_{ob} \end{pmatrix} \qquad (6)$$

where the prime denotes the observer's reference frame.

Following the analysis of C. Aspin (1981), we can write the theoretical Stokes Parameters in the natural frame as follows:

$$\begin{aligned} Q_{t,r} &= p_o + p_1 \cos \Omega_r + p_2 \cos 2\Omega_r \\ U_{t,r} &= u_o + v_1 \sin \Omega_r + v_2 \sin 2\Omega_r \end{aligned} \tag{7}$$

where there are certain relationships between the coefficients viz.

$$\begin{aligned} v_1 &= p_i/\cos i \\ v_2 &= -\tan\Theta\, p_1/2 \sin i \\ p_2 &= -\frac{(1+\cos^2 i)\tan\Theta\, p_i}{4 \sin i \cos i} \end{aligned} \tag{8}$$

We wish to find the minimum of the χ^2 function where

$$\chi^2 = \sum_{r=1}^{N} \left(\left[\frac{Q'_{ob,r} - Q'_{t,r}}{\sigma'_r} \right]^2 + \left[\frac{U'_{ob,r} - U'_{t,r}}{\sigma'_r} \right]^2 \right) \tag{9}$$

where N is the number of data points.

σ'_r is the error on the rth measurement

$(Q'_{ob,r}, U'_{ob,r})$ is the rth measurement and phase $\Omega_r/2\pi$

$(Q'_{t,r}, U'_{t,r})$ are the theoretical Stokes Parameters evaluated at phase $\Omega_r/2\pi$.

Since this model does not take account of any orbital effects, such as the contribution of the companion star, and since for SS433 the orbit and precession are not phase locked, then the error on each measurement will be $\tilde{\sigma}$, which will include the characteristic size of the orbital modulation and the stochastic variations in the jets. Now, because of the properties of Stokes Parameters,

$$\sum_{r=1}^{N} [(Q'_{ob,r} - Q'_{t,r})^2 + (U'_{ob,r} - U'_{t,r})^2]$$

is rotationally invarient i.e. independent of the observer's reference frame. Hence the problem reduces to minimising the function

$$F(\underset{\sim}{p};\Theta) = \tilde{\sigma}^2 \chi^2 = \sum_{r=1}^{N} [(Q_{ob,r} - Q_{t,r})^2 + (U_{ob,r} - U_{t,r})^2] \qquad (10)$$

where $\underset{\sim}{p} \equiv (p_o, p_1, p_2, u_o, u_1, u_2)$ and $\theta = 2\beta$.

We rewrite the constraints (8) in the form $g_1 = g_2 = g_3 = 0$ which gives

$$\begin{aligned} g_1 &= p_1 - c\, v_1 \\ g_2 &= t p_1 + 2(1-c^2)^{\frac{1}{2}} v_2 \\ g_3 &= \alpha t p_1 + 2(1-c^2)^{\frac{1}{2}} p_1 \end{aligned} \qquad (11)$$

where $c = \cos i$, $t = \tan \Theta$

and $\alpha = (1+c^2)/2c$ (12)

Using the method of Lagrange multipliers, we obtain 9 additional Lagrange equations, viz:

$$\frac{\partial F}{\partial p} + \sum_{\ell=1}^{3} \lambda_\ell \frac{\partial g_\ell}{\partial p} = 0 \qquad p = p_o, p_1, p_2, u_o, v_1, v_2 \qquad (13)$$

$$\frac{\partial F}{\partial p} + \sum_{\ell=1}^{3} \lambda_\ell \frac{\partial g_\ell}{\partial \theta} = 0 \qquad (14)$$

$$\frac{\partial F}{\partial p} + \sum_{\ell=1}^{3} \lambda_\ell \frac{\partial g_\ell}{\partial t} = 0 \qquad (15)$$

$$\frac{\partial F}{\partial c} + \sum_{\ell=1}^{3} \lambda_\ell \frac{\partial g_\ell}{\partial c} = 0 \qquad (16)$$

Note that $\frac{\partial F}{\partial t} = \frac{\partial F}{\partial c} = 0$.

Since we wish to obtain confidence intervals for i and Θ , we will use only equations (13) and (14) in the following analysis.

Equations (12) and (13) give $\frac{\partial F}{\partial p_o} = \frac{\partial F}{\partial u_o} = 0$ (17)

$$\frac{\partial F}{\partial p_1} + \lambda_1 + t\lambda_2 + \alpha t \lambda_3 = 0 \qquad (18)$$

$$\frac{\partial F}{\partial p_2} + 2(1-c^2)^{\frac{1}{2}} \lambda_3 = 0 \qquad (19)$$

$$\frac{\partial F}{\partial v_1} - c\lambda_1 = 0 \qquad (20)$$

$$\frac{\partial F}{\partial v_2} + 2(1-c^2)^{\frac{1}{2}} \lambda_2 = 0 \qquad (21)$$

Now $\frac{\partial F}{\partial p_o} = -2 \sum_{r=1}^{N} (Q_{ob,r} - Q_{t,r})$ (from equation (10))

$$= 2 \sum_{r=1}^{N} (p_o + p_1 \cos\Omega_r + p_2 \cos 2\Omega_r - Q_{ob,r})$$

$$= 2Np_o + 2p_1 \sum_{r=1}^{N} \cos \Omega_r + 2p_2 \sum_{r=1}^{N} \cos 2\Omega_r - 2 \sum_{r=1}^{N} Q_{ob,r}$$

Let $C_k = \frac{1}{N} \sum_{r=1}^{N} \cos k\Omega_r \qquad k=1,2,3,4$

and $S_k = \frac{1}{N} \sum_{r=1}^{N} \sin k\Omega_r \qquad k=1,2$

and $\bar{p}_o = \frac{1}{N} \sum_{r=1}^{N} Q_{ob,r} \qquad \bar{u}_o = \frac{1}{N} \sum_{r=1}^{N} U_{ob,r}$

Then $\frac{\partial F}{\partial p_o} = 2N(p_o + p_1C_1 + p_2C_2 - \bar{p}_o)$

Sim $\frac{\partial F}{\partial u_o} = 2N(u_o + v_1S_1 + v_2S_2 - \bar{u}_o)$.

Hence equations (17) become

$$p_o = \bar{p}_o - \bar{p}_1C_1 - p_2C_2 \tag{22}$$

$$U_o = \bar{u}_o - \bar{v}_1S_1 - v_2S_2 \tag{23}$$

Substituting for λ_1, λ_2 and λ_3 from equations (19), (20) and (21) into equation (18) gives

$$2c(1-c)^{\frac{1}{2}} \frac{\partial F}{\partial p_1} + 2(1-c)^{\frac{1}{2}} \frac{\partial F}{\partial v_1} - ct \frac{\partial F}{\partial v_2} - \alpha ct \frac{\partial F}{\partial p_2} = 0 \tag{24}$$

Defining $\bar{p}_k = \frac{2}{N} \sum_{r=1}^{N} Q_{ob,r} \cos k\Omega_r \qquad k=1,2$

$$\bar{v}_k = \frac{2}{N} \sum_{r=1}^{N} U_{ob,r} \sin k\Omega_r$$

gives $\frac{\partial F}{\partial p_1} = N[2p_o C_1 + p_1(1+C_2) + p_2(C_1+C_3) - \bar{p}_1]$

$$\frac{\partial F}{\partial p_2} = N[2p_o C_2 + p_1(C_1+C_3) + p_2(1+C_4) - \bar{p}_2]$$

$$\frac{\partial F}{\partial v_1} = N[2u_o S_1 + v_1(1-C_2) + v_2(C_1-C_2) - \bar{v}_1]$$

$$\frac{\partial F}{\partial v_2} = N[2u_o S_2 + v_1(C_1-C_3) + v_2(1-C_4) - \bar{v}_2]$$

Hence equation (24) becomes

$$2c[2(1-c^2)^{\frac{1}{2}}C_1-\alpha t-C_2]p_o+2[2(1-c^2)^{\frac{1}{2}}S_1-ctS_2\ ]u_o+[2(1-c^2)^{\frac{1}{2}}(1+C_2)-$$
$$-\alpha t(C_1+C_3)]cp_1\ +[2(1-c^2)^{\frac{1}{2}}(C_1+C_3)-\alpha t(1+C_4)]cp_2+[2(1-c^2)^{\frac{1}{2}}(1-C_2)-$$
$$-ct(C_1-C_3)]v_1\ +[2(1-c^2)^{\frac{1}{2}}+(C_1-C_3)-ct(1-C_4)]v_2\ =\ 2(1-c^2)^{\frac{1}{2}}(c\bar{p}_1+\bar{v}_1)-$$
$$-ct(\alpha\bar{p}_2+\bar{v}_2)$$

Substituting for p_o and u_o from equations (22) and (23) gives

$$\begin{aligned}
&[2(1-c^2)^{\frac{1}{2}}(1+C_2)-\alpha t(C_1+C_3)-2C_1(2(1-c^2)^{\frac{1}{2}}C_1-\alpha tC_2)]\ cp_1\\
&+[2(1-c^2)^{\frac{1}{2}}(C_1+C_3)-\alpha t(1+C_4)-2C_2(2(1-c^2)^{\frac{1}{2}}C_1-\alpha tC_2)]\ cp_2 \qquad (25)\\
&+[2(1-c^2)^{\frac{1}{2}}(1-C_2)-ct(C_1-C_3)-2S_1(2(1-c^2)^{\frac{1}{2}}S_1-ct\ S_2)]v_1\\
&+[2(1-c^2)(C_1-C_3)-ct(1-C_4)-2S_2(2(1-c^2)^{\frac{1}{2}}S_1-ct\ S_2)]\ v_2\\
&=\ 2(1-c^2)^{\frac{1}{2}}(c\bar{p}_1+\bar{v}_1)-ct(\alpha\bar{p}_2+\bar{v}_2)-2c\bar{p}_o[2(1-c^2)^{\frac{1}{2}}C_1-\alpha tC_2]-2\bar{u}_o[2(1-c^2)^{\frac{1}{2}}S_1-ctS_2]
\end{aligned}$$

Since none of the constraints depend on θ , equation (14) becomes

$$\frac{\partial F}{\partial \theta}\ =\ 0$$

and since $Q_{ob,r} = Q'_{ob,r}\cos\ - U'_{ob,r}\sin\theta.$

$$U_{ob,r} = Q'_{ob,r}\sin\ _r\ U'_{ob,r}\cos\theta \qquad (26)$$

$$\frac{\partial F}{\partial \theta} = 2\sum_{r=1}^{N}[(Q_{ob,r}-Q_{t,r})\frac{\partial Q_{ob,r}}{\partial\theta} + (U_{ob,r}-U_{t,r})\frac{\partial U_{ob,r}}{\partial\theta}]$$

$(Q_{t,r},U_{t,r})$ being independent of θ .

Now, from equations (26)

$$\frac{\partial Q_{ob,r}}{\partial\theta} = -U_{ob,r} \quad \text{and} \quad \frac{\partial U_{ob,r}}{\partial\theta} = Q_{ob,r}$$

Therefore $\frac{\partial F}{\partial\theta} = 2\sum_{r=1}^{N}(U_{ob,r}\,Q_{t,r} - Q_{ob,r}U_{t,r})$

If we define $\bar{q}_k = \frac{2}{N}\sum_{r=1}^{N} Q_{ob,r}\sin k\Omega_r$ $\qquad k=1,2$

and $\bar{u}_k = \frac{2}{N}\sum_{r=1}^{N} U_{ob,r}\cos k\Omega_r$

then we find that

$$2p_o\bar{u}_o - 2u_o\bar{p}_o + p_1\bar{u}_1 + p_2\bar{u}_2 - v_1\bar{q}_1 - v_2\bar{q}_2 = 0 \qquad (27)$$

and, again, substituting for p_o and u_o from equations (22) and (23) gives

$$(\bar{u}_1 - 2\bar{u}_o C_1)p_1 + (\bar{u}_2 - 2\bar{u}_o C_2)p_2 + (2\bar{p}_o S_1 - \bar{q}_1)v_1 + (2\bar{p}_o S_2 - \bar{q}_2)v_2 = 0 \qquad (28)$$

Now, using equations (8) to substitute for v_1, v_2 and p_2 in equation (25) gives

$$\begin{aligned}&[4(1-c^2)O_1 + c^2t^2O_2 - 4ct(1-c^2)^{\frac{1}{2}}O_3]p_1 \\ &= 4c^2(1-c^2)^{\frac{1}{2}}t(\alpha C_2\bar{p}_o + S_2\bar{u}_o) - 8c(1-c^2)(cC_1\bar{p}_o + S_1\bar{u}_o) + 4c(1-c^2)(c\bar{p}_1 + \bar{v}_1) \\ &\quad - 2c(1-c^2)^{\frac{1}{2}}\,t(\alpha\bar{p}_2 + \bar{v}_2)\end{aligned} \qquad (29)$$

where

$$\begin{aligned}O_1 &= c^2(1+C_2) + (1-C_2) - 2(c^2C_1^2 + S_1^2) \\ O_2 &= \alpha^2(1+C_4) + (1-C_4) - 2(\alpha^2C_2^2 + S_2^2) \\ O_3 &= \alpha c(C_1+C_3) + (C_1 - C_3) - 2(\alpha cC_1C_2 + S_1S_2)\end{aligned} \qquad (30)$$

and, similarly, equation (28) becomes

$$4(1-c^2)^{\frac{1}{2}}(S_1\bar{p}_o - c\,C_1\bar{u}_o) + 2(1-c^2)^{\frac{1}{2}}(c\bar{u}_1 - \bar{q}_1) - 2ct(S_2\bar{p}_o - \alpha C_2\bar{u}_o) - ct(\alpha\bar{u}_2 - \bar{q}_2) = 0 \qquad (31)$$

Now, we had $\bar{p}_k = \frac{2}{N}\sum_{r=1}^{N} Q_{ob,r}\cos k\Omega_r \qquad k=1,2$

Substituting for $Q_{ob,r}$ from equations (26) gives

$$\bar{p}_k = \left(\frac{2}{N}\sum_{r=1}^{N} Q'_{ob,r}\cos k\Omega_r\right)\cos\theta - \left(\frac{2}{N}\sum_{r=1}^{N} U'_{ob,r}\cos k\Omega_r\right)\sin\theta$$

$$\left.\begin{aligned}\text{i.e. } \bar{p}_k &= \bar{p}'_k\cos\theta - \bar{u}'_k\sin\theta && k=1,2 \\ \text{Similarly } \bar{q}_k &= \bar{q}'_k\cos\theta - \bar{v}'_k\sin\theta && k=1,2 \\ \bar{u}_k &= \bar{p}'_k\sin\theta + \bar{u}'_k\cos\theta && k=1,2 \\ \bar{v}_k &= \bar{q}'_k\sin\theta + \bar{v}'_k\cos\theta && k=1,2 \\ \bar{p}_o &= \bar{p}'_o\cos\theta - \bar{u}'_o\sin\theta \\ \bar{u}_o &= \bar{p}'_o\sin\theta + \bar{u}'_o\cos\theta\end{aligned}\right\} \qquad (32)$$

where $\bar{p}_k'$, $\bar{u}_k'$ etc are defined in the same way as $\bar{p}_k$, $\bar{u}_k$ etc., using the observed data.

Hence, we can solve equation (31) for $\tan\theta$ to give

$$\tan\theta = \frac{2(1-c^2)^{\frac{1}{2}}(2A_3+B_1)-ct(2A_4+B_2)}{-2(1-c^2)^{\frac{1}{2}}(A_1-2B_3)+ct(A_2-2B_4)} \tag{33}$$

where
$$A_1 = c\bar{p}_1'+\bar{v}_1' \qquad B_1 = c\bar{u}_1'-\bar{q}_1'$$
$$A_2 = \alpha\bar{p}_2'+\bar{v}_2' \qquad B_2 = \alpha\bar{u}_2'-\bar{q}_2' \tag{34}$$
$$A_3 = S_1\bar{p}_o'-cC_1\bar{u}_o' \qquad B_3 = cC_1\bar{p}_o'+S_1\bar{u}_o'$$
$$A_4 = S_2\bar{p}_o'-\alpha C_2\bar{u}_o' \qquad B_4 = \alpha C_2\bar{p}_o'+S_2\bar{u}_o'$$

Also, we can solve equation (29) for p_1, viz.

$$p = \frac{2c(1-c^2)^{\frac{1}{2}}\{[2(1-c^2)^{\frac{1}{2}}(A_1-2B_3)-ct(A_2-2B_4)]\cos\theta- -[2(1-c^2)^{\frac{1}{2}}(2A_3+B_1)-ct(2A_4+B_2)]\sin\theta\ \}}{4(1-c^2)O_1+\ c^2t^2O_2-\ 4ct\ (1-c^2)^{\frac{1}{2}}\ O_3} \tag{35}$$

and hence p_2, v_1, v_2 from equations (8) and p_o, u_o from equations (22) and (23).

From equations (1) and (3) it can be seen that

$$A = p_1/\sin 2i \sin 2\Theta$$
$$Q_{int} = p_o - \frac{p_1(1-3\cos^2\Theta)\sin i}{2\cos i \sin 2\Theta} \tag{36}$$
$$U_{int} = u_o \quad .$$

Hence, from a set of data of known phase, for each Θ and i, (Q_{int}, U_{int}) A, and $\tan\theta$ can be found using equations 33-36. Since $\theta = 2\beta$, there will be two possible values of β in the range 0 to π differing by $\pi/2$. This reflects the basic ambiguity between jet and disc scattering (cf. discussion in section 4.2). There will be two sets of parameters, one for each value of β, since the sign of p_1 will change depending on which value of θ is used. One set will have A positive

and will correspond to a jet dominated solution, the other, having A negative, will correspond to a disc dominated solution (see section 4.2).

The function $\tilde{\sigma}^2\chi^2$ can then be found for each Θ and i . It will be the same for both sets of parameters. By grid-searching through the range of possible values of Θ and i the minimum of the function and confidence intervals can be found.

5.4 Special Cases of the Filting Procedure

5.4.1 Equal Phase Intervals

Should it become possible to bin the data into equal precession phase bins, then considerable simplification of equations (22), (23),(30), (33), (34) and (35) result. For equally spaced, binned data

$$\Omega_r = \frac{2\pi(r-1)}{N}$$

Hence $C_k = \frac{1}{N}\sum_{m=o}^{N-1} \cos\frac{2\pi km}{N}$ and $S_k = \frac{1}{N}\sum_{m=o}^{N-1} \sin\frac{2\pi km}{N}$ $(k=1,\ldots,4)$

and so $C_k = S_k = 0 \qquad (k=1,\ldots,4)$.

from the orthogonality relations for sine and cosine. Therefore, equations (22) and (23) become

$$p_o = \bar{p}_o$$

$$u_o = \bar{u}_o$$

equations (30) become

$$0_1 = 1+c^2$$

$$0_2 = 1+\alpha^2$$

$$0_3 = 0$$

and, from equations (34) $A_3 = A_4 = B_3 = B_4 = 0$.

Hence equation (33) becomes

$$\tan\theta = \frac{2(1-c^2)^{\frac{1}{2}} B_1 - ct\ B_2}{-2(1-c^2)^{\frac{1}{2}} A_1 + ct\ A_2}$$

and equation (35) becomes

$$p_1 = \frac{2c(1-c^2)^{\frac{1}{2}}\{[2(1-c^2)^{\frac{1}{2}}A_1 - ct\ A_2]\cos\theta[2(1-c^2)^{\frac{1}{2}}B_1 - ct\ B_2]\sin\theta}{4(1-c^4) + c^2t^2(1+\alpha^2)}$$

5.4.2 Special Cases of the constraints

a) i=0. The theoretical Stokes Parameters are given by

$$Q_{t,r} = p_o + p_2 \cos 2\Omega_r$$

$$U_{t,r} = u_o + v_2 \sin 2\Omega_r$$

where $p_2 = v_2 = -2A \sin^2\Theta$. Hence the constraints reduce to

$$g = p_2 - v_2$$

Following a similar analysis as in 5.4, we find that

$$p_o = \bar{p}'_o \cos\theta - \bar{u}'_o \sin\theta - p_2 C_2$$

$$u_o = \bar{p}'_o \sin\theta + \bar{u}'_o \cos\theta - p_2 S_2$$

$$p_2 = \frac{[\bar{p}'_2 + \bar{v}'_2 - 2(C_2\bar{p}_o + S_2\bar{u}'_o)]\cos\theta + [\bar{q}'_2 - \bar{u}'_2 - 2(S_2\bar{p}'_o - C_2\bar{u}'_o)]\sin\theta}{1 - 2C_2^2 - 2S_2^2}$$

and $$\tan\theta = \frac{(\bar{q}'_2 - \bar{u}'_2) - 2(S_2 p'_o - C_2 u'_o)}{(\bar{p}'_2 + \bar{v}'_2) - 2(C_2 p'_o + S_2 u'_o)}$$

b) i=90°. The theoretical Stokes Parameters are given by

$$Q_{ob,r} = p_o + p_2 \cos 2\Omega$$

$$U_{t,r} = u_o + v_1 \sin \Omega.$$

where $p_2 = -A \sin^2\Theta$ and $v_1 = 2A \sin 2\Theta$. Hence the constraints reduce to

$$g = 4p_2 + tv_1 \qquad \text{where } t = \tan\Theta \ .$$

Again following the analysis in 5.4, we find

$$p_o = \bar{p}'_o \cos\theta - \bar{u}'_o \sin\theta - p_2 C_2$$

$$u_o = \bar{p}'_o \sin\theta + \bar{u}'_o \cos\theta - v_1 S_1$$

$$v_1 = \frac{4[4v'_1 - t\bar{p}'_2 + 2(tC_2\bar{p}'_o - 4S_1\bar{u}'_o)]}{\cos\theta[16(1-C_2) - t^2(1+C_4) - 32S_1 + 2t^2C_2^2]}$$

$$\tan\theta = \frac{4\bar{q}'_1 + t\bar{u}'_2 - 2(4S_1\bar{p}'_o + tC_2\bar{u}'_o)}{4\bar{v}'_1 - t\bar{p}'_2 + 2(tC_2\bar{p}'_o - 4S_1\bar{u}'_o)}$$

5.5 Results of Optimisation

We evaluated $\sigma^2\chi^2_{min}$ for each (i,Θ) on a 5^o grid on the i,Θ plane, where $0 \leq i \leq 180^o$ and $-90^o < \Theta < 90^o$ ($-\Theta \equiv 180^o - \Theta$). We have displayed the results graphically in Figures 6 and 7. In Figure 6, $\sigma^2\chi^2_{min} \equiv f(i,\Theta)$ defines a three-dimensional surface (cross-hatched) while in Figure 7 the contour levels of the $\sigma^2\chi^2_{min}$ surface have been projected onto the (i,Θ) plane. The shaded area shows the region where $\sigma^2\chi^2_{min} \leq 17.64$ (see below). By searching a smaller area including this region using a finer mesh, the global minimum inf ($\sigma^2\chi^2_{min}$) was found to be 15.746. The 2 sets of parameter values corresponding to the minimum are

$$i=120^o.0,\ \Theta = -13^o.0 \left\{ \begin{array}{llll} \beta_1 = 81.195, & U_{Int}=0.359, & Q_{Int}=-3.018, & A = -0.728 \\ \beta_2 = -8.805, & U_{Int}=-0.359, & Q_{Int}=3.018, & A = 0.738 \end{array} \right. \quad (37)$$

The precession curve corresponding to these parameter sets is superimposed on the data and shown in Figures 1, 2 (Q,U against data), 8(folded data against phase) and 9(U against Q). It is quite clear from Figure 8 that the U parameter is described better by the model than Q. Figure 9 alone is not a good indication of the quality of the fit. Plotting the raw data

on the Q,U plane does not give a sense of the development of the Q,U locus with time. Sufficient data to permit binning and hence simple smoothing of the observed locus is required before a direct comparison of model with data on the Q,U plane can be made. Even then, close attention to the phasing of the locus must be paid.

The root mean square deviation of the Q's and U's from the best fit curve is 0.269. Adopting this value for σ^2gives a value for χ^2 for the best fit of 218 which, for the number of degrees of freedom (215), has a significance of $\sim$45%. The 10% significance level corresponds to a value of χ^2= 242, i.e. all models with $\sigma^2\chi^2 \lesssim 17.64$ have a significance $\gtrsim$10%. An estimate of the variance of the Q and U parameters that is quite independent of any model can be found by binning the data and calculating the variance on the average of each bin. The root mean square of these bin variances is then an estimate of the spread in the data. It should be noted that the final result of such a process does depend on the number of bins originally used. For 20 equally spaced precession phase bins (on the Kemp et al., 1986 ephemeris) of which, for the given data set, 14 contains 2 or more points, the root mean square variances on the Q and U parameters are, respectively, $\bar{\sigma}_Q$ = 0.274 and $\bar{\sigma}_U$=0.192. $\bar{\sigma}_Q$ and $\bar{\sigma}_U$ give a measure of the dispersion in the data which is a few times the value of the quoted measurement errors (cf. Simmons et al., 1980). If the mean of $\bar{\sigma}_Q$ and $\bar{\sigma}_U$ is used for $\bar{\sigma}$ the best fit has a significance of only $\sim$0.1%.

Using the best-fit model defined by the parameter sets (37), the power spectra of the Q and U residuals, (i.e. after removal of the precession variation and interstellar component) were calculated and three

expanded sections of the spectra about ν_p, $2\nu_p$, ν_o and $2\nu_o$ are shown in Figures 10(Q) and 11(U) with the relevant sections of the power spectra of the raw data for comparison. It is clear that the power in the constant terms and the peaks at ν_p ($\frac{1}{P_{precession}}$) and $2\nu_p$ has been dramatically reduced and, in some cases, completely removed. This success is despite the merely moderate statistical significance of the best-fit. So we conclude that the model does describe well the variation due to precession and allows evaluation of the interstellar polarisation.

The significance of the peak near half the orbital period (i.e. near $2\nu_o$) remains marginal in the Q residuals. The expanded scale of Figures 10 and 11 also shows that if the peaks near $2\nu_o$ are genuinely due to a variation at half the orbital period they have been displaced to higher frequencies, which may indeed be the result of the unequally spaced data.

To estimate the errors on the best fit values of i and Θ , we return to Figure 7. The shaded area shows the region of the i,Θ plane which gives model fits with confidence $\gtrsim$10%. From the dimensions of this region we can derive a crude estimate of the 10% confidence interval errors on i and Θ namely

$$i = 120^{o}0 \pm 35^{o} \qquad \Theta = -13^{o}0 \pm 45^{o} \qquad (38)$$

The size of the confidence interval reflects the scatter on the data. As much of this may be caused by stochastic processes in the disc/jet system an increased data set should decrease the relative importance of this scatter allowing for a more precise determination of i and Θ .

5.6 Comparison of Results

The optimisation procedure developed in Section 5.3 to fit the simple precession model to the polarisation data of SS433 resulted in 2 sets of parameters corresponding to a predominantly jet (A>0) and a predominantly disc (A<0) scattering solution. Of the six parameters found by this method, the inclination and precession cone angles can also be derived from the spectroscopic measurements of the Doppler shifted emission lines from the jets and from radio VLA observations. The position angle of the jets on the sky (related to β, see below) can be found from radio and X-ray imaging and the interstellar polarisation can be estimated from measurements of field stars near SS433. However, this last is fraught with uncertainty since there are three underlying assumptions namely that the stars are intrinsically unpolarised, that they are at the same distance as SS433 and that conditions along the different lines of sight are sufficiently similar not to invalidate the estimate. Given that the extinction in the region of W50 is both large and patchy (cf. Margon 1984), this last assumption seems very shaky.

The simple kinematic model for the Doppler shifted emission lines (see e.g. Margon 1984) yield values for i and Θ of $78^{\circ}.82$ and $19^{\circ}.8$, but does not by itself distinguish between i and Θ , nor does it determine their quadrant uniquely as π-i and π-Θ give the same solution. The dynamic model developed by Collins and Newsom (1986) gives $i=78^{\circ}.91$ and $\Theta=19^{\circ}.41$, where now the ambiguity lies in distinguishing between the ascending and descending nodes. Radio observations give values for i and Θ of 80° and 20° respectively (Hjellming and Johnstone 1981a, Fejes 1986) and that the sense of the jet rotation is clockwise.

In the polarisation model the angles i and Θ are measured from the z-axis, the normal to the orbital plane. The precession phase is measured anticlockwise about the z-axis (i.e. the sense of the precession of the jets can be considered to define the direction of the z-axis). Since zero phase is defined to be when the redshifts of the two opposing jets are at maximum separation, if i is in the first quadrant, Θ must be in the first quadrant also and the sense of the jet rotation, as seen by the observer is anticlockwise. Similarly, for i in the 2nd quadrant, Θ is in the same quadrant and the sense of the jet rotation is clockwise. The polarisation best fit parameter sets both have i and Θ in the 2nd quadrant (since $-\Theta \equiv \pi - \Theta$) and hence the polarisation data indicate that the sense of the jet rotation is clockwise, in agreement with the radio data. It can be seen that the best fit values of i and and Θ are in agreement, within the errors, with those found from other observations allowing for the ambiguity in the quadrant of i and Θ , or equivalently the ambiguity in the sense of rotation of the jets in the optical data.

By definition, β is the angle measured anticlockwise from the normal to the orbit to the observer's Q-axis, which is the direction to North. The position angle of the jets has been observed in both radio and X-rays to be $\sim 100^{\circ}$ (eg. Hjellming and Johnston 1981a, Seward et al., 1980). For SS433, the position angle is measured anticlockwise from North to the precession axis of the jets which is assumed to be the normal to the orbital plane. Hence, the position angle is equivalent to $\pi-\beta$. Since there are two equivalent solutions there are two possible values of β corresponding to the best-fit model. Not surprisingly, these differ by 90° since one corresponds to a disc dominated solution and the other to a jet dominated solution. Hence, we require the X-ray and radio obser-

vations of the position angle of the precession axis to resolve the ambiguity in the polarisation solution.

From (37), the value of β which more nearly corresponds to the complement of the observed position angle is $\beta_1 = 81°.195$.

This value of β found from the optimisation procedure is not significantly changed by different input values of Θ and i that are within the 10% significance region. If $\beta = 81°.195$ is the preferred solution, then, $A<0$ i.e. the scattering is disc dominated as expected on the theoretical grounds discussed in Section 4.6. Note that $A = -7.38 \times 10^{-3}$ (best-fit solution (37) gives A in percent) gives from equation 4.25 a value for the infall time in the disc of $t = 1.65 \times 10^3$s. Since the disc is not optically thin, this value of t is a strong lower limit.

The best fit parameters give a value for the interstellar polarisation of 3.04% at position angle 86.61° (disc dominated) or -3.39° (jet dominated). McLean and Tapia (1980) estimate the interstellar polarisation from field stars to be 1.5-2.7% at position angle 30°. However, this estimate is highly uncertain. Until a more accurate independent estimate of the interstellar polarisation is available and the errors on the polarisation fit reduced no definitive conclusions can be drawn.

5.7 Full Model Fit to Data.

We attempted to fit the full theoretical model developed in Chapter 4 to the data using the best fit parameters found from the optimisation procedure of Section 5.3. The same phasing of the precession period was used and the orbital period was phased according to the ephemeris of Kemp et al., 1986. Since $i, \Theta, \beta, Q_I, U_I$ and A have been found already (37) the two remaining unknowns are $(1-f)\tau_d$ and

$(1-f)\tau_j$ (A incorporates f). Now, $0 \leq f \leq 1$ and both τ_d and τ_j are positive. Therefore, these unknowns are positive constants. However, no reduction in $\sigma^2\chi^2$ below its f = 1 value could be found for any positive values of $(1-f)\tau_d$ and $(1-f)\tau_j$ even when an arbitrary phase constant was added to the orbital phasing.

A second attempt to fit the data was made with a restricted model of the form

$$\begin{aligned} Q_\tau &= Q_I + Q_c + a\cos 2\lambda + b\sin 2\lambda \\ U_\tau &= U_I + U_c + c\cos 2\lambda + d\sin 2\lambda \end{aligned} \qquad (39)$$

where (Q_I,U_I) and (Q_c,U_c) are given by the precession best fit (37), being the interstellar polarisation and the contribution of the central source respectively, $\lambda/2\pi$ is the orbital phase and a,b,c,d are unknown constants. Equations 4.12 and 4.15 indicate a relation between these unknowns of the form

$$a = \alpha c \quad , \qquad b = -\alpha d \qquad (40)$$

where $\alpha = (1+\cos^2 i)/2\cos i$ as before (cf. Simmons et al., 1980). This would be the case for scattering of light from the companion star off the disc/jet in the situation where the effect of the precession of the disc/jet system is negligible, or for scattering of light from the central source off the atmosphere of the companion star. Again, using the method of Lagrange multipliers, we find

$$\begin{aligned} a &= \frac{(1+\alpha^2)(1-C_4)D - (1-\alpha^2)S_4E}{(1+\alpha^2)^2(1-C_4^2) - (1-\alpha^2)^2 S_4^2} \\ b &= \frac{(1-\alpha^2)S_4D - (1+\alpha^2)(1+C_4)E}{(1+\alpha^2)^2(1-C_4^2)-(1-\alpha^2)^2S_4^2} \end{aligned} \qquad (41)$$

where $C_4 = \frac{1}{N}\sum_{i=1}^{N} \cos 4\lambda_i$; $S_4 = \frac{1}{N}\sum_{i=1}^{N} \sin 4\lambda_i$

$$D = \frac{2\alpha}{N} \sum_{i=1}^{N} [U_{obs,i} + \alpha Q_{obs,i} - (U_I+U_c)_i - \alpha(Q_I+Q_c)_i] \cos 2\lambda_i$$

$$E = \frac{2\alpha}{N} \sum_{i=1}^{N} [U_{obs,i} - \alpha Q_{obs,i} - (U_I+U_c)_i + \alpha(Q_I+Q_c)_i] \sin 2\lambda_i$$

$(Q_{obs,i}, U_{obs,i})$ is the ith data point at orbital phase $\lambda_i/2\pi$ and N is the number of data points.

Using these equations, we find inf $(\sigma^2\chi^2) = 14.394$ for a = 0.116 and b = 0.023. The best-fit ephemeris corresponds to that given in Kemp et al., 1986 with a possible phase shift of 0.5. To find whether this reduction in $\sigma^2\chi^2$ is greater than could be expected from the addition of two free parameters we use the F-statistic which is 10.00 in this case. For comparison, a value of only $\sim$ 4.8 would correspond to a probability of only 1% that the reduction was due to chance. The rms deviation from this model is 0.257. Using this value for $\tilde{\sigma}$ gives χ^2= 218, which has a significance of 40% for 213 degrees of freedom. The significance of this fit has been marginally reduced compared with (37). However, if we take the bin variance $\tilde{\sigma}$ = 0.233, we find that χ^2= 265, which has a significance of 1%, an order of magnitude improvement. Using the rms deviation for $\tilde{\sigma}$ will always result in a significance of less than 50% for a non zero number of fitted parameters. A model independent estimate of $\tilde{\sigma}$ is, therefore, required to determine if a fit has improved, or the F-statistic should be used where appropriate. The high value of the F-statistic indicates that at least some of the peak near $2\nu_o$ in the power spectra of U, and perhaps Q, is real and due to scattering either of light from the companion star off the disc/jet or of light from the central source off the atmosphere of the companion star. However a further reduction of $\sigma^2\chi^2$ to 12.655 is obtained if constraints

(40) are omitted and this fit, when compared to the precession best fit (37) has an F-statistic of 12.88 (1% level would be $\sim$ 3.4). For $\tilde{\sigma}$ = 0.233, χ^2 = 233 which has a significance of 15%. Further analysis of an increased data base is, therefore, required to distinguish between the possible effects causing this variation (e.g. light source eclipses) which would seem, on the basis of the above results, to be due to more than simple scattering.

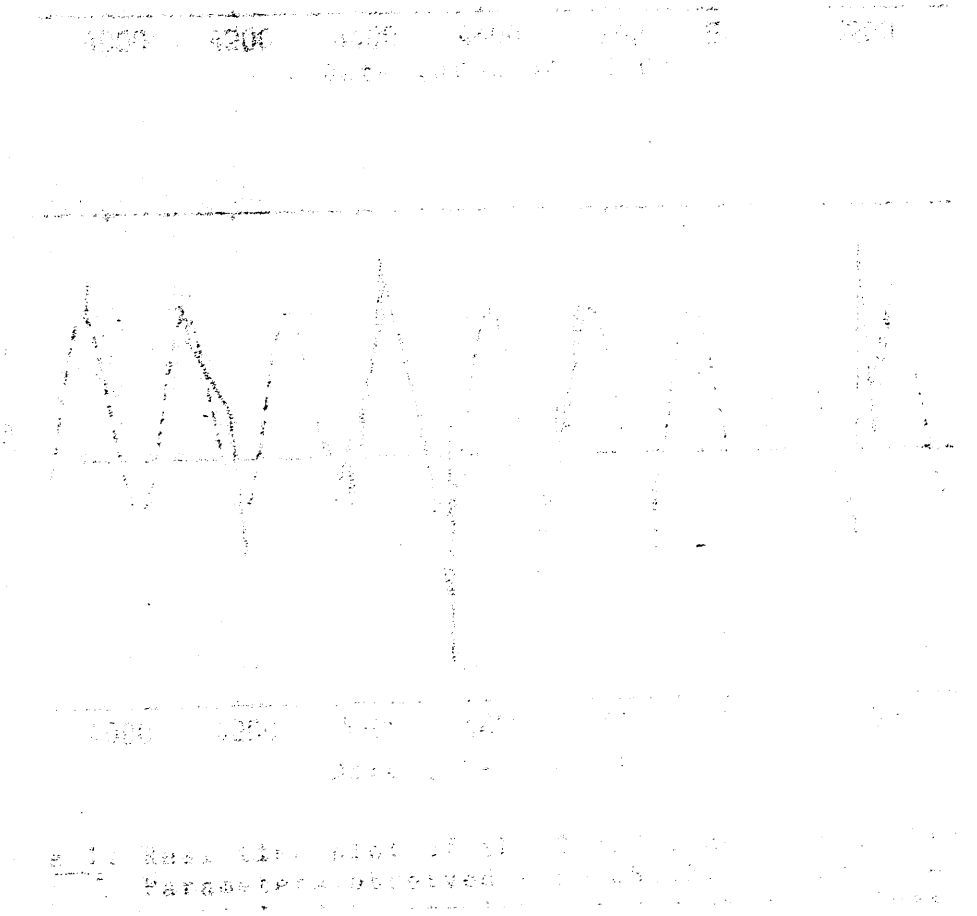

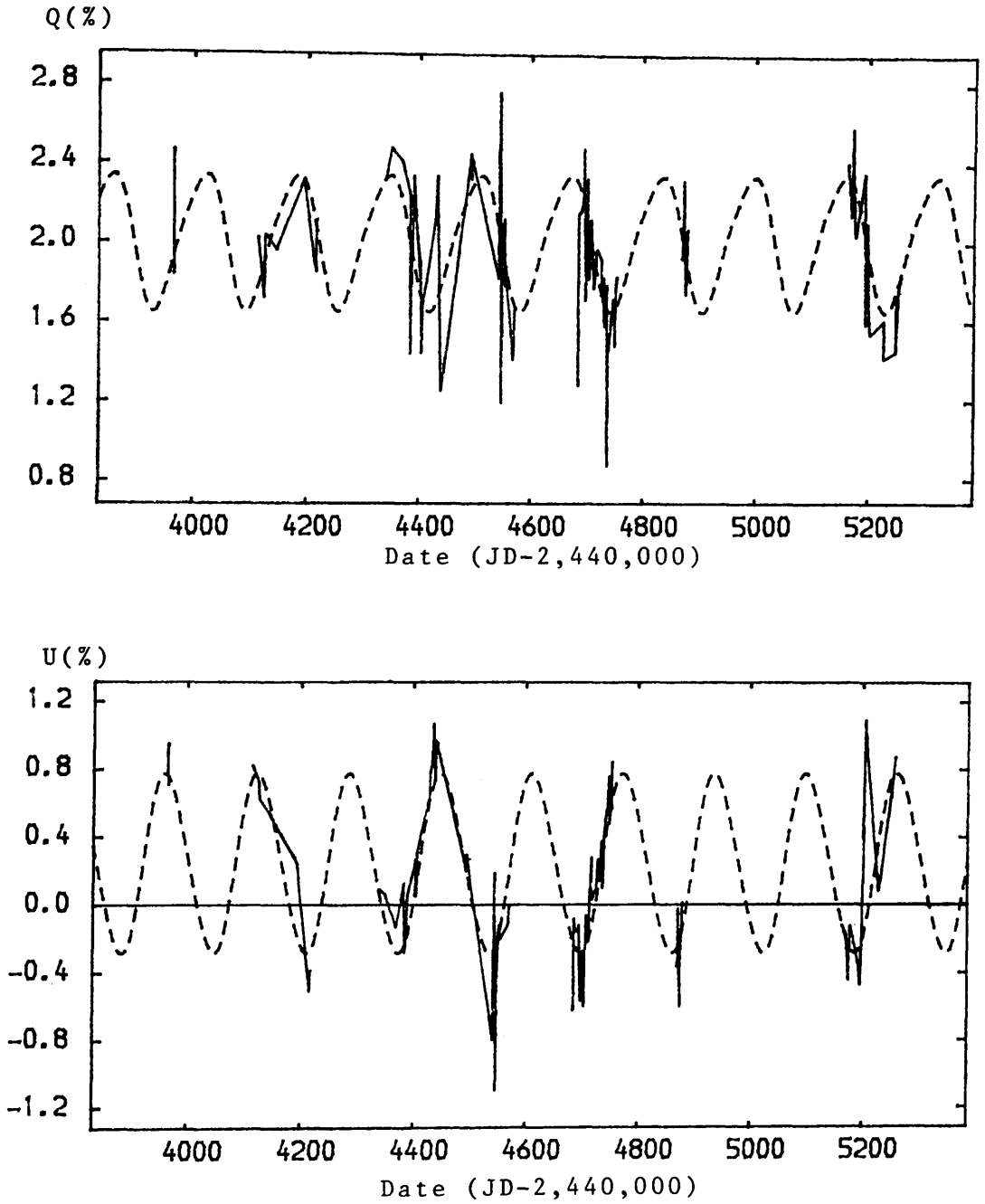

Figure 1: Real time plot of the Q and U normalised Stokes Parameters observed from SS433. The data points are joined by straight line segments unless there were more than 40 days between successive observations. The broken curve is the best-fit precession curve (see Section 5.6).

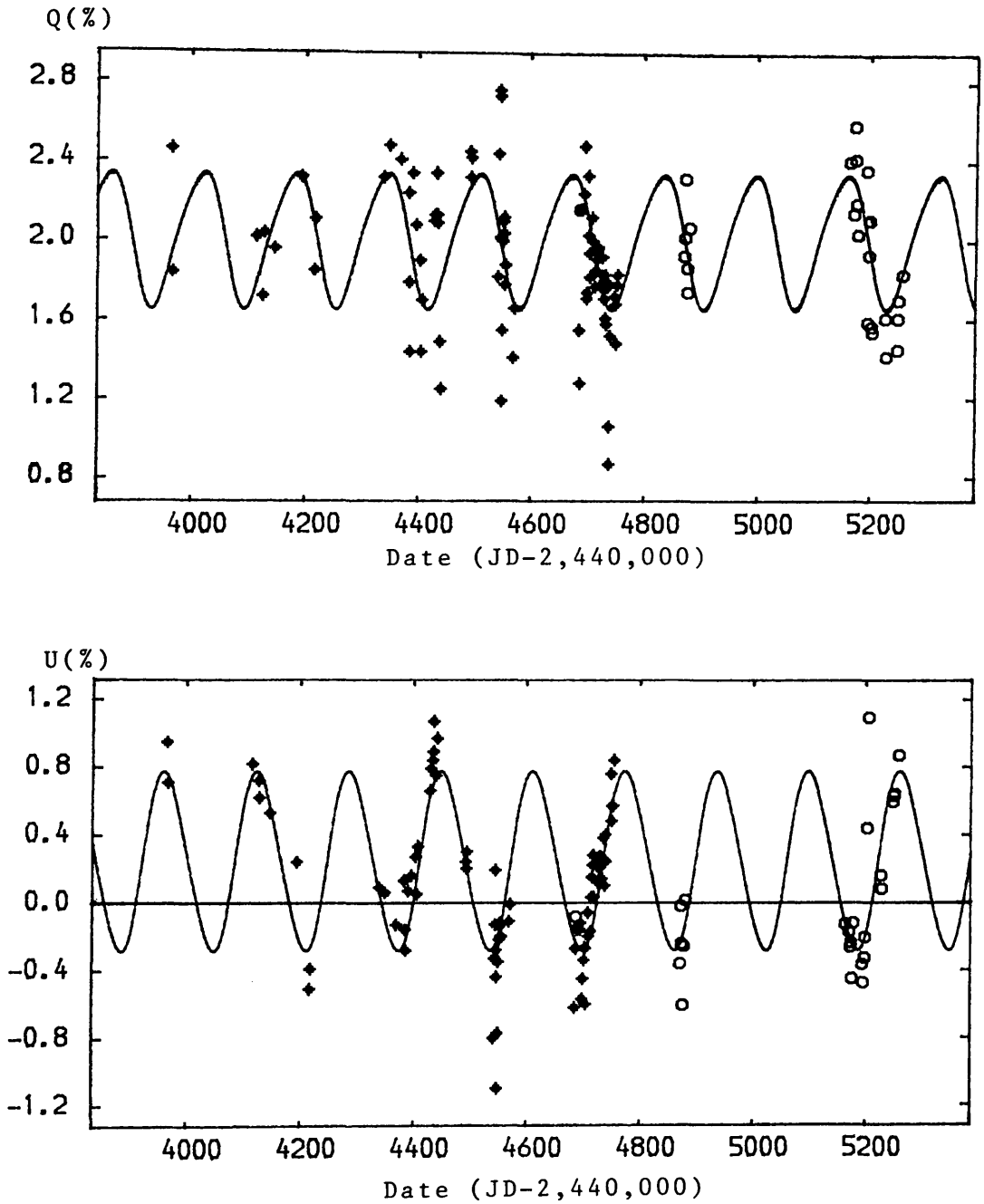

Figure 2: Real time plot of the Q and U normalised Stokes Parameters observed from SS433.
* McLean and Tapia (1981) data
o Efimov et al. (1984) data
The curve is the best-fit precession curve (see Section 5.6).

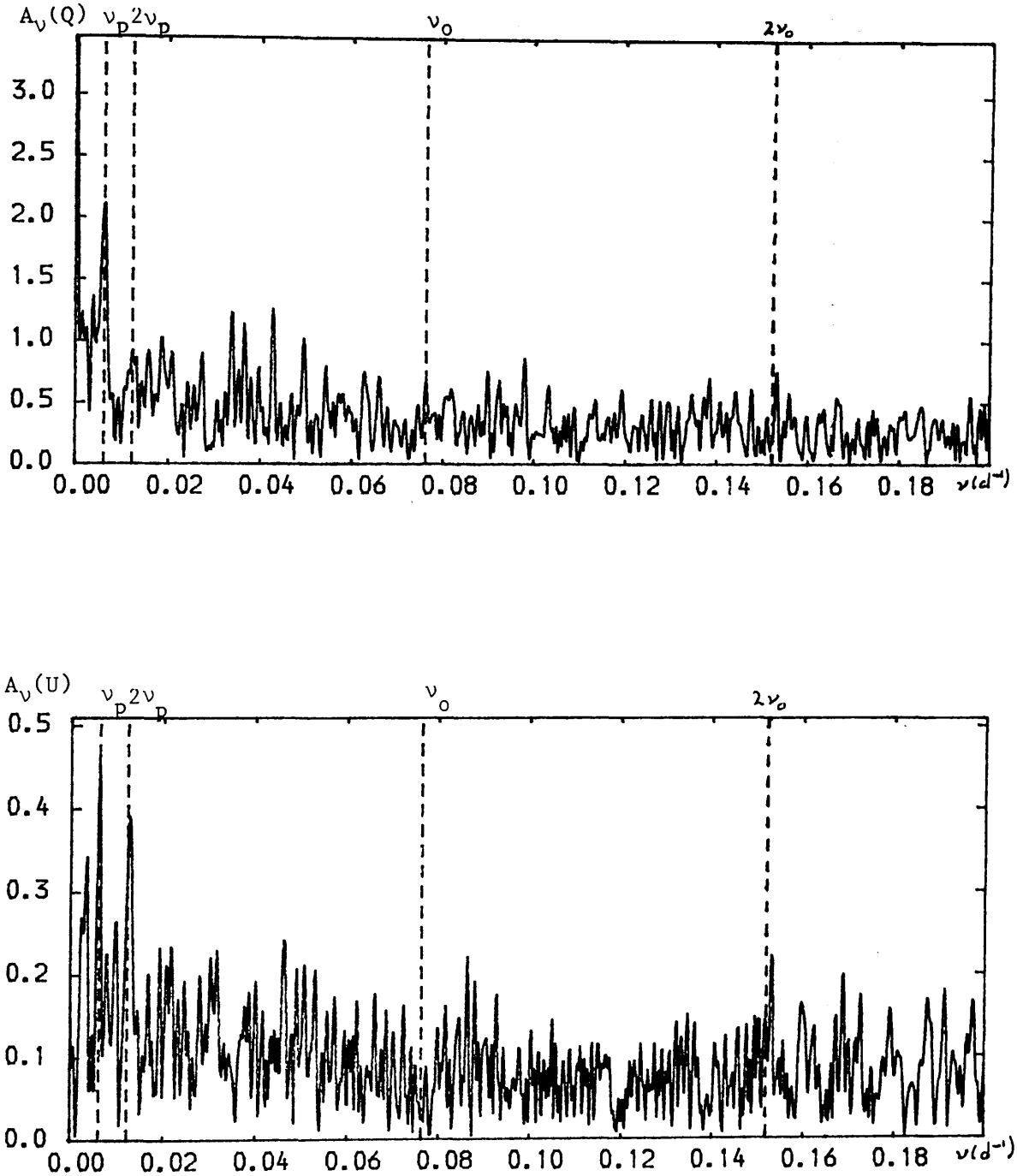

Figure 3: Power spectra of the observed Q and U Stokes Parameters of SS433, based on 109 data points during 1979-1982. 1000 search frequencies, out to the shortest period of 5 days, were used.
$\nu_p \equiv$ precession frequency $\nu_o \equiv$ orbital frequency

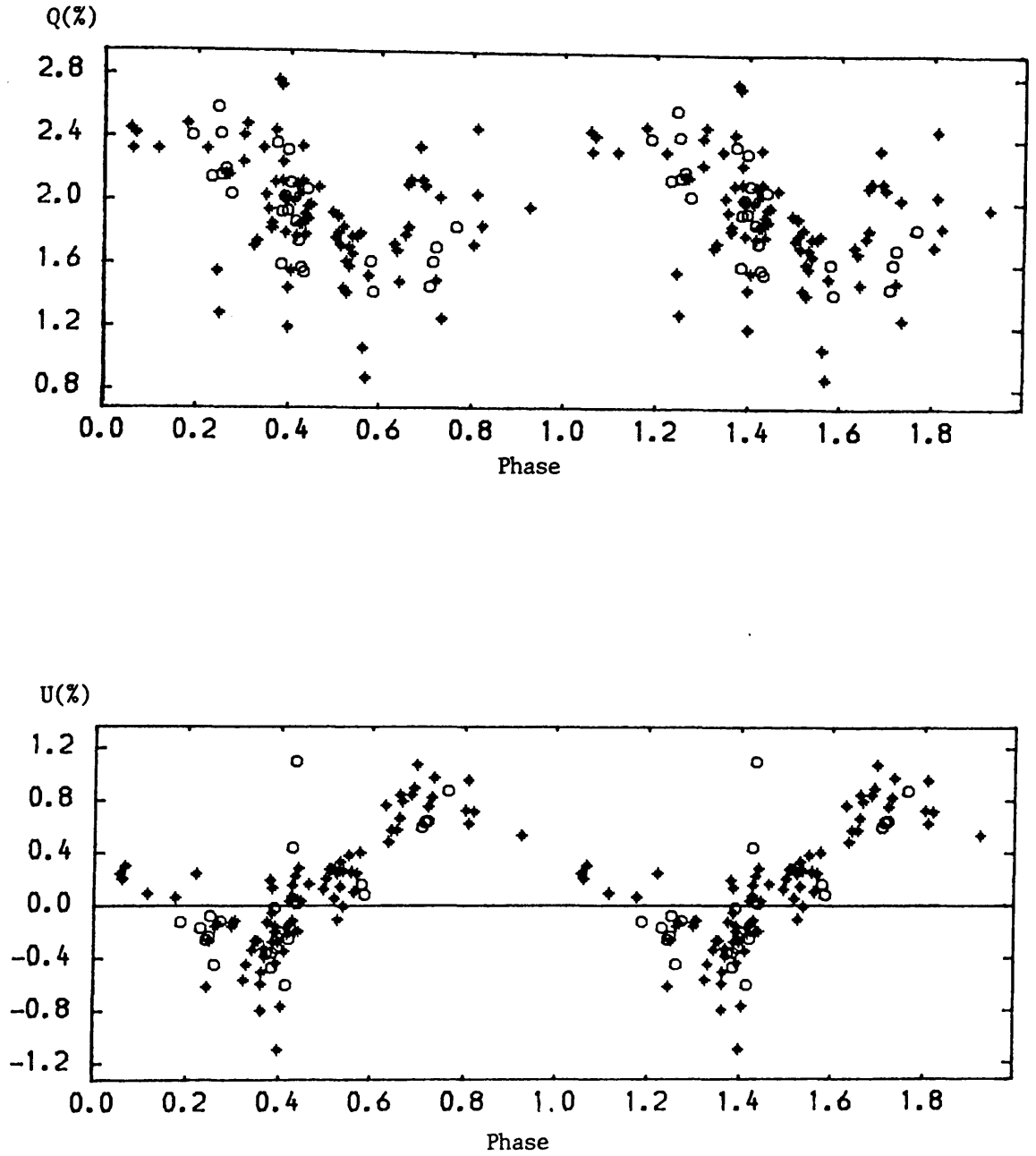

Figure 4: The observed Q and U Stokes Parameters of SS433 folded and plotted against precession phase according to the ephemeris and period given in Kemp et al., 1986. On this scale, the typical quoted errors are smaller than (McLean and Tapia, 1981) or the same size as (Efimov et al., 1984) the characters used to mark the points.
* McLean and Tapia (1981) data
o Efimov et al. (1984) data.

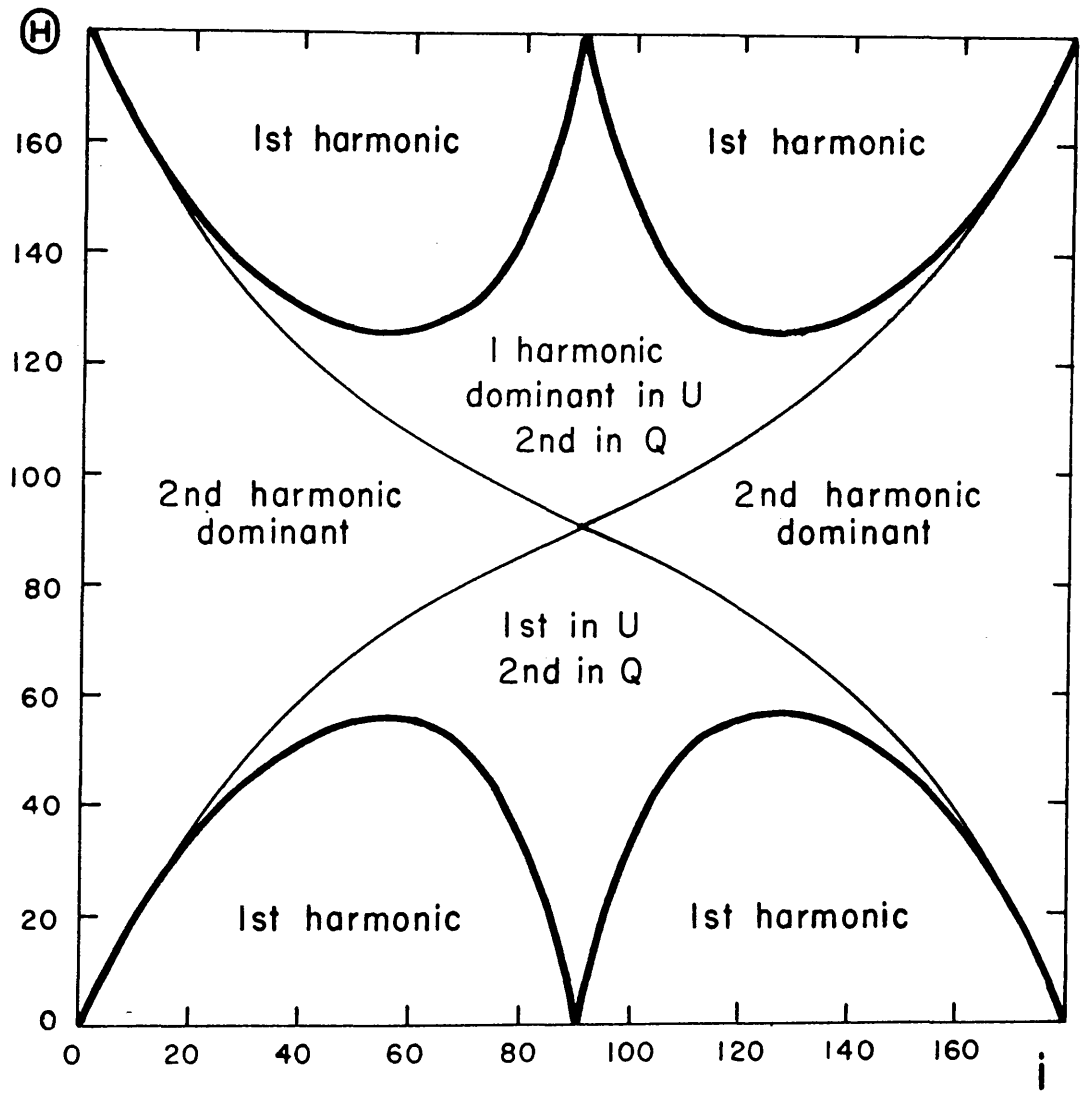

Figure 5: Regions of the i,Θ plane where the precession period or its harmonic is dominant in the Stokes Parameters Q and U.

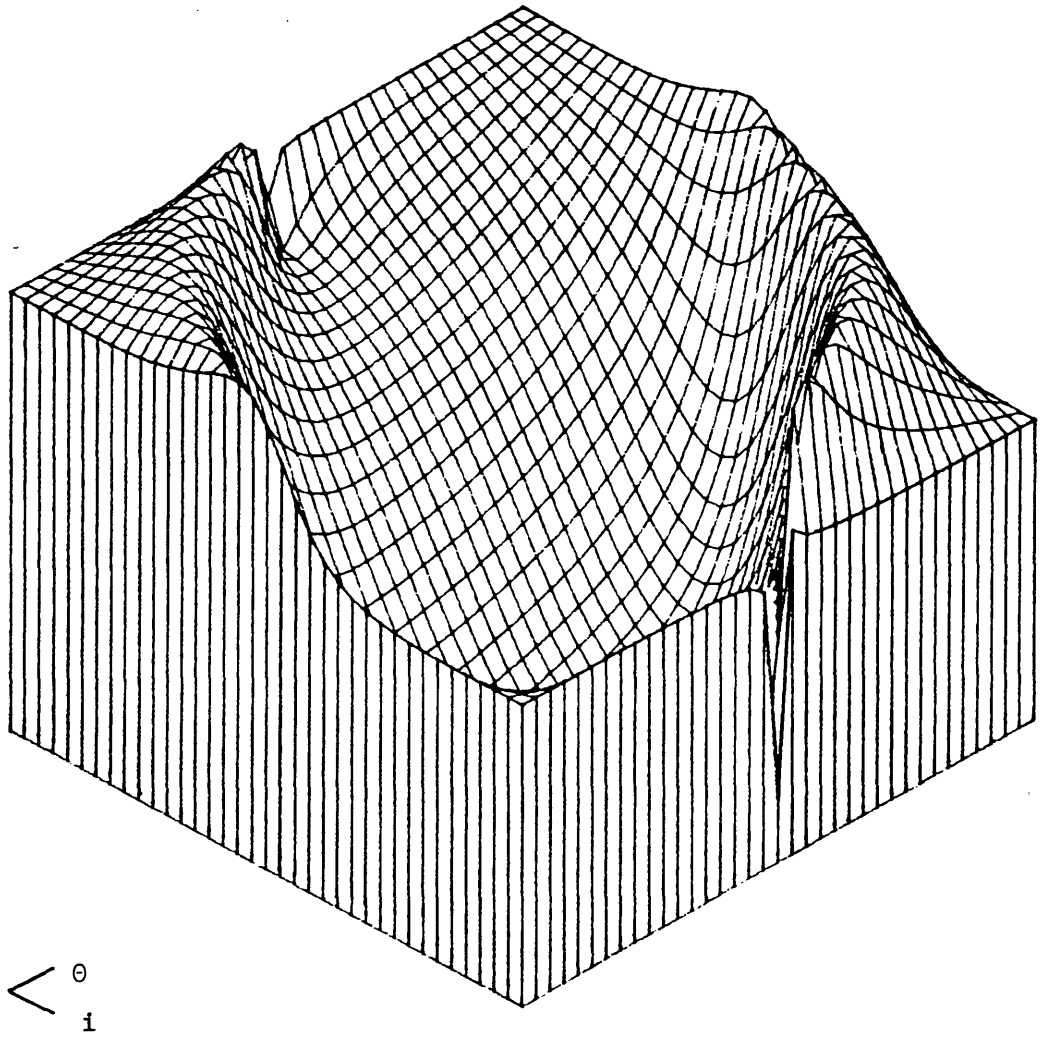

Figure 6: Three dimensional (cross-hatched) surface defined by $f(i, \Theta) = \sigma^2\chi^2_{min}$. The base is the $\sigma^2\chi^2 = 0$ level. The ranges of i and Θ are 0° to 180° and -90° to 90° respectively.

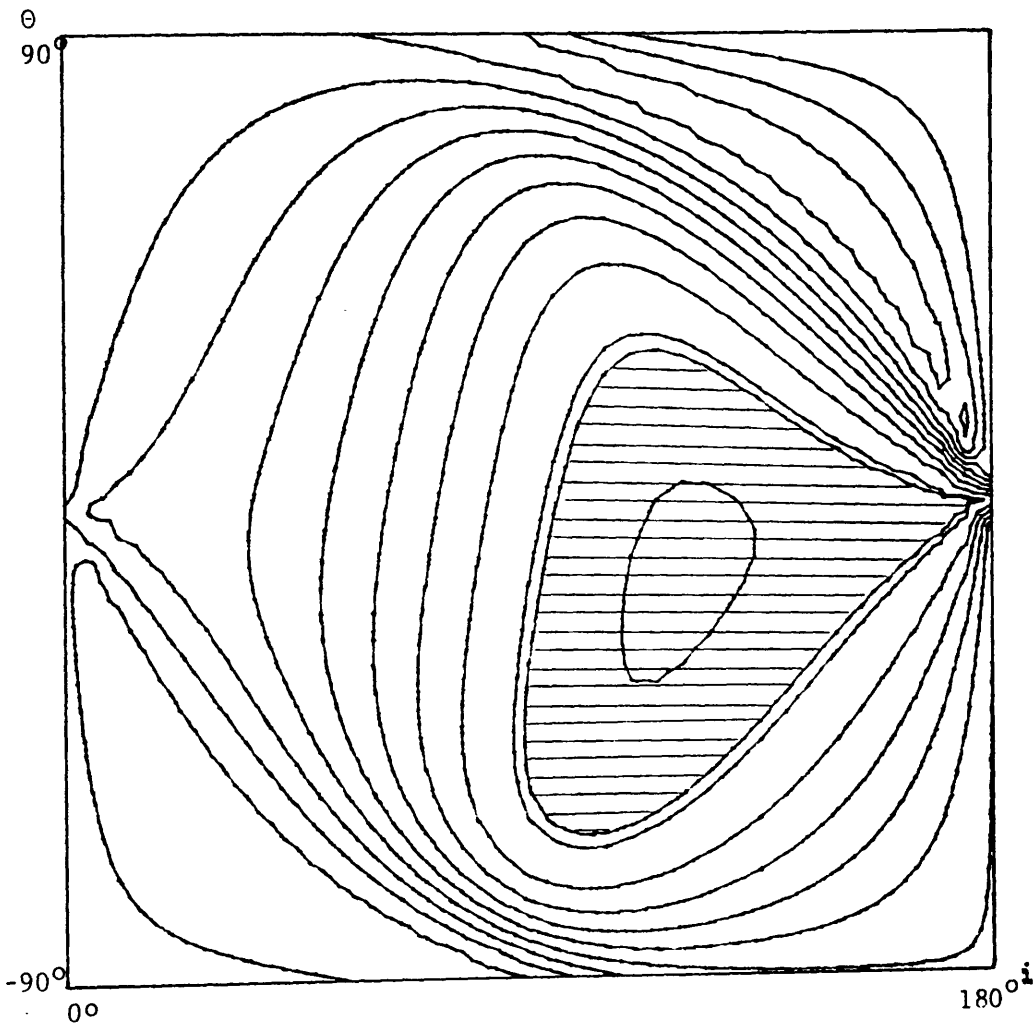

Figure 7: Contour plot of $f(i, \Theta) = \sigma^2 \chi^2_{min}$. The contours have been drawn at intervals of 2 from 16 to 36. An extra level has been drawn at 17.64. The shaded region is, therefore, where $f(i,\Theta) \leq 17.64$ (see section 5.5).

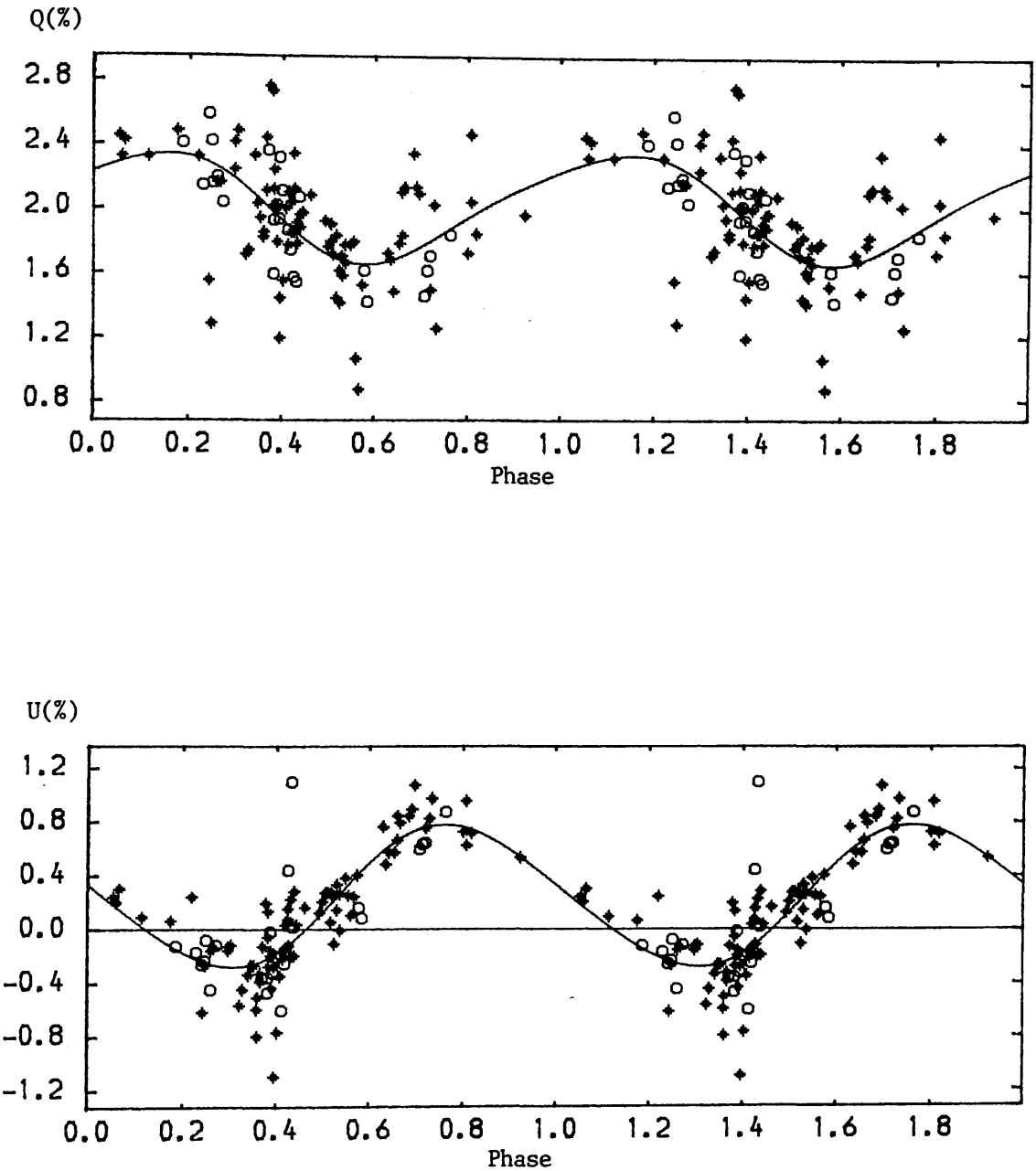

Figure 8: As Figure 4. Solid curve is the best-fit precession curve (see section 5.6)

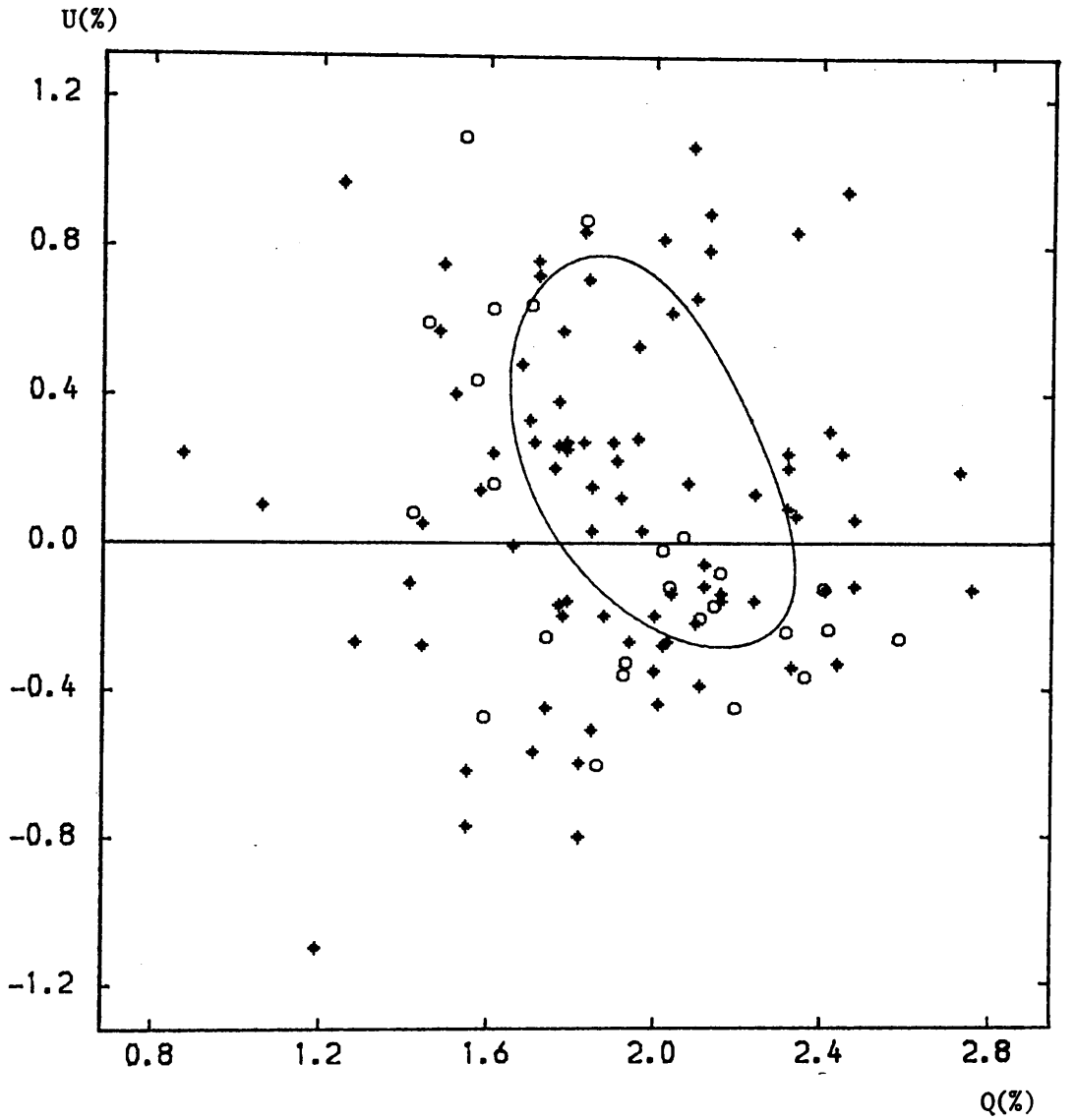

Figure 9: Observed Q and U Stokes Parameters of SS433 with the best fit precession curve sumperimposed (the solid curve).
* McLean and Tapia (1981) data
o Efimov et al. (1984) data

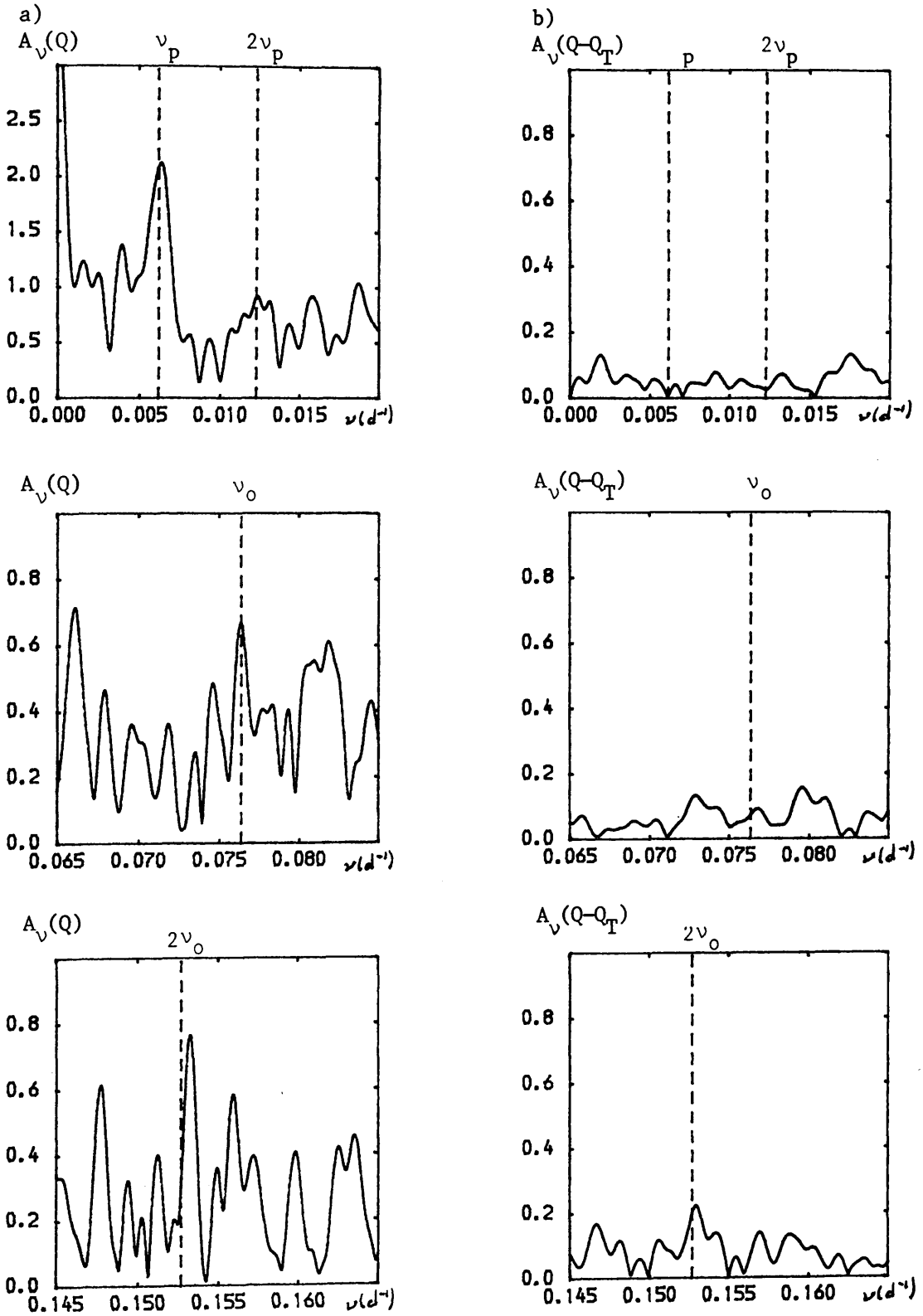

Figure 10: Three expanded sections of the power spectrum of the Q Stokes Parameter of SS433 based on 109 observations for a) the raw data and b) the residuals, ie $Q-Q_T$ where Q_T is calculated from the best-fit solution. Note that the scale of the first graph of a) is three times the others. $\nu_p = 1/P_{precession}$ $\nu_o = 1/P_{orbital}$

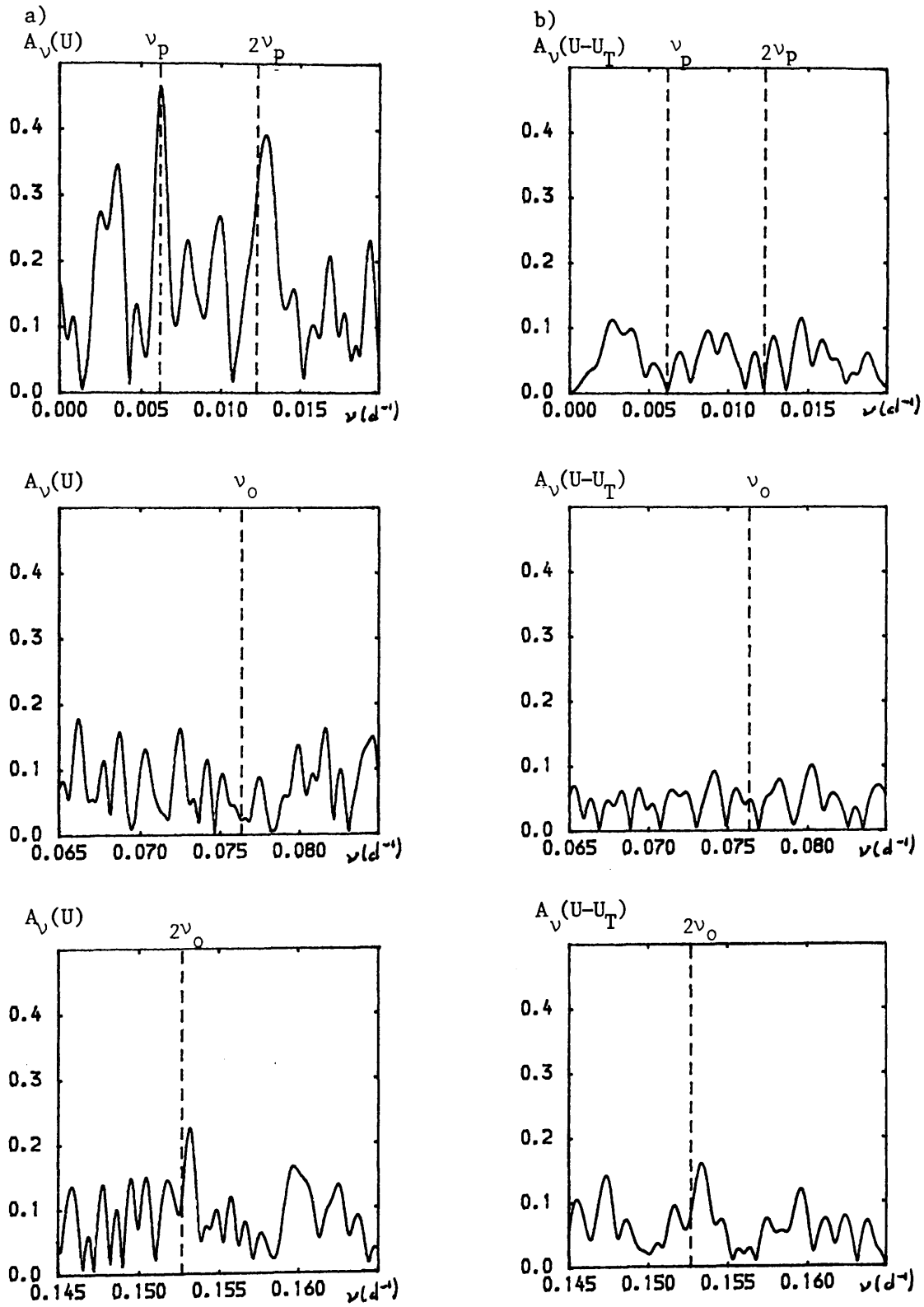

Figure 11: As Figure 10 for the U Stokes Parameter.

CHAPTER 6

GAMMA-RAY LINES FROM SS433?

6.1 Introduction

SS433 is not an unlikely gamma ray source since, at a relative velocity of 0.26c, each proton has a kinetic energy of 30 MeV. The narrow gamma ray lines reported by Lamb et al. (1933) and Lamb (1984), though unconfirmedhave stimulated a number of theoretical models. Boyd et al., 1984 discuss mainly the lines reported by Lamb and co-workers (1983, 1984) near 1.5 and 1.2 MeV, and propose thermonuclear processes in the jets as their most likely source, while Kundt (1984) argues for inverse compton boosting of H_α photons by relativistic electron-positron pairs near the central object. Ramaty et al., (1984),(RKL) on the other hand, consider the lines at about 1.5 and 6.7 MeV. They identify these with nuclear transitions of $^{24}Mg^*$ and $^{16}O^*$, and claim that their very small line widths and high intensities are compatible only with non-thermal excitation of nuclei in solid grains present in the jet, which are presumed to collide with protons in some ambient gas. Helfer and Savedoff (1984) proposed a magnesium jet model for the lower energy line.

We will not concern ourselves here with either the details of the nuclear transitions, nor with the controversy over the observations, but rather with the viability of the RKL grain interpretation of the 1.5 and 6.7 MeV lines in terms of its consistency with theoretical considerations, with data at other wavelengths, and with the most widely accepted model for SS433. Related issues have been discussed recently by Helfer and Savedoff (1986). In essence the RKL model is that nuclei of magnesium and

oxygen, embedded in solid grains that are presumed to be present in the jets of SS433 and carried along with them, collide with protons in an ambient medium supposed to surround the jets. These collisions excite nuclei, which transfer their recoil energy to the grains that contain them before they emit their excitation energy by spontaneous emission. Thus the emitted gamma rays are seen at the red- or blueshift of the jets, and are narrow because the recoil energy has been absorbed by Coulomb collisions in the grains(Lingenfelter and Ramaty 1977). The absence of a ^{12}C line, which ought to appear strongly at 4.4 MeV rest energy but is not observed, is neatly explained by the fact that its de-excitation time is much shorter than the Coulomb stopping time, so that its expected line width of several hundred keV comes out too broad to be detectable. Then RKL derive estimates of the area and mass of the grains, for plausible grain sizes, from the gamma ray intensity and by equating the total Coulomb loss in the jet material with the jet kinetic power. The resulting black body temperature of the grains is then claimed by RKL to be sufficiently low to ensure grain survival.

The possible presence of grains in the jets has implications for the observed optical polarisation of the system. Grain scattering could add significantly to the polarisation produced by the jets, perhaps even changing the balance between the disc and jet scattering (cf. discussion in section 4.6). From the mass of grains required to give the observed luminosity of the gamma ray lines, we estimate in section 6.5.2 the optical polarisation these grains would give, assuming optically thin scattering and using the Rayleigh scattering approximation.

6.2 Consistency with gamma ray data

In their Table 1, RKL present fluxes of eight gamma ray lines expected from the jet grain model to be comparable to that of the strong 1.5 MeV line. For consistency with the few lines apparently observed (Lamb et al. 1983, 1984) most of these are explained away by RKL by invoking for the 4.4 MeV line of ^{12}C an excessive line width (cf. Section 6.1) and for the remainder, low element abundances. Thus they concentrate on the lines at 1.495 and 6.695 MeV, and identify these with the (rest energy) lines at 1.369 MeV from $^{24}Mg^*$ and at 6.129 MeV of $^{16}O^*$, blueshifted by a factor $1+z = 1.092$ in energy appropriate to the phase of SS433 at the time of observation.

We should also expect corresponding redshifted lines at 1.184 and 5.301 MeV from the receding jet, with fluxes reduced by about $[(1-z)/(1+z)]^4$, which is roughly 0.9 at this phase, relative to the blueshifted components. The former energy corresponds to a line detected with less confidence (Lamb et al. 1983, Fig.3), while RKL make no mention of the latter, which line would be an important check on the model. Since the jets are observed almost at right angles to the line of sight, strong absorption of the redshifted gamma way lines seems unlikely (cf. RKL).

In addition to these lines, however, the model should predict features of comparable equivalent width at the rest energies (1.369 and 6.129 MeV) because, just as 'interstellar' protons excite nuclei in jet grains, so should jet protons excite nuclei in 'interstellar'grains. Let n_{pj} and n_{gi} be the number densities of the protons and the grain nuclei (averaged) in the jet, and let n_{pi} and n_{gi} be the corresponding 'interstellar' values; let the volume of interaction of the jet and interstellar material be V. Then the rates of emission of gamma ray photons, from any nuclear transitions

in the jet and 'interstellar' grains, should be in the ratio

$$\frac{I_{\gamma j}}{I_{\gamma i}} = \frac{n_{gj} n_{pi} QvV}{n_{gi} n_{pj} QvV} = \left[\frac{n_{pi}}{n_{gi}}\right]\left[\frac{n_{gj}}{n_{pj}}\right] \qquad (1)$$

where v is the jet speed and Q is the excitation cross-section. It follows from (1) that if the grain/proton number ratio is similar in the jet and in the ambient medium, then the 'interstellar' grains bombarded by the jet protons should produce observable rest energy lines, unless either 'interstellar' grains are so small that recoiling nuclei cannot come to rest in them, or so large that they are optically thick to gamma rays.

These alternatives seem improbable, so that one ought to expect lines with equivalent widths comparable to the moving lines. Again the 1.369 MeV line falls on an instrumental feature (Lamb et al. 1983), but neither these authors nor RKL refer to the expected line at 6.129 MeV, the occurrence or absence of which should be an important test of the model. It is possible that the rest energy lines are too wide to be detected. However, if the width of the very strong H_α line at rest is any indication, the gamma ray line width ought to be about 50 keV, which seems too narrow to escape detection.

6.3 Jet dynamics and grain survival

RKL have calculated the Coulomb energy loss rate $\dot{W}_c$ deposited in the jet due to collisions of jet material with ambient gas, and find (for solar elemental abundances)

$$\dot{W}_{cg} = 3.3 \times 10^5 \, n_{pi} \, M_g \text{ erg s}^{-1} \qquad (2)$$

$$\dot{W}_{cp} = 8.7 \times 10^5 \, n_{pi} \, M_g \text{ erg s}^{-1} \qquad (3)$$

for grains and the gas, respectively, where M_g and M_p are the total masses of the grains and the protons in the jet volume ejected during time $\hat{\tau} \simeq 4$ days of the flaring episode around the time of observation.

The luminosity of the 1.369 MeV line predicted due to collisions of jet grains with interstellar protons is (RKL)

$$L_{1.369} = 16.5\, n_{pi}\, M_g \text{ erg s}^{-1} \qquad (4)$$

so that only a small fraction (about 5×10^{-5}) of the energy lost by collisions within the grains goes into gamma rays, and the rest goes into Coulomb heating of the grains. Substituting the reported value $L_{1.369} = 10^{37}$ erg s^{-1}, and eliminating $n_{pi} M_g$ between (2), (3), and (4), we obtain

$$\dot{W}_{cg} = 2 \times 10^{41} \text{ erg s}^{-1} \qquad (5)$$

$$\dot{W}_{cp} = 5.8 \times 10^{41} (M_p/M_g) \text{ erg s}^{-1} \qquad (6)$$

as the heating rates for grains and gas, respectively. It should be noted that these huge losses apply not only to the grain model but to any non-thermal model due to the basic inefficiency of radiation from a collisional beam (cf. Brown, 1971).

The huge power deposited collisionally, even in the grains alone, poses several fundamental problems for the RKL jet grain model. Firstly this loss is comparable to or greater than the estimated total kinetic luminosity of the jets (eg. Watson et al., 1983) so that the jets would be quickly stopped by collisions unless constantly driven so as to just offset the losses and maintain the observed near constancy of jet speed over large distances. RKL proposed line-locked radiation pressure (eg. Pekarevich et al., 1984) as the possible mechanism. However, secondly, $\dot{W}_{cg}$ and $\dot{W}_{cp}$ exceed the Eddington luminosity of any stellar object by a factor of at

least 100 which would appear to exclude radiative driving as a means to offset these losses particularly as the collisional braking in the interstellar medium could not be expected to decline rapidly with distance as the radiation pressure must. One would then have to invoke some powerful long range mechanical or magnetic driver acting on the jet.

Nevertheless, let us assume that the Coulomb losses can somehow be made good without loss of jet speed or collimation and consider, thirdly, whether the necessary refractory grains could survive in the thermal conditions resulting from the collisional heating. (Problems of how such grains could ever be formed in the jets were discussed at length by Helfer and Savedoff, 1986, and are exacerbated by the recent discovery that the innermost parts of the jets are at X-ray temperatures - Watson et al., 1986). In addressing the question of grain survival, RKL propose that the grains can lose the heat deposited in them by black body radiation near but below their sublimation temperature ($\simeq$ 3000 K). They do so by expressing the total grain area in terms of the grain density, size, and total mass M_g, and by adopting the identity $\dot{W}_{cg} = \frac{1}{2}\dot{M}_g v_j^2$. This last is incorrect as may be seen by noting that $\dot{M}_g = M_g/\tau$ whereas $\dot{W}_{cg} = \frac{1}{2}M_g v_j^2/\tau_{coll}$ where τ_{coll} is the Coulomb stopping time for grain particles. Their expression would only be valid, therefore, if the time τ taken by the central source to eject mass M_g was equal to τ_{coll} which must vary as $1/n_{pi}$ - a conspiracy of equality of two unrelated quantities.

It is possible, however, to arrive at the fundamental problem confronting grain survival much more directly simply by evaluating the grain area A_g needed to match (5) by black body radiation from optically thick grains at $T < 3000$ K viz.

$$A_g = \frac{\dot{W}_{cg}}{\sigma T^4} \gtrsim 4 \times 10^{31} \text{ cm}^2 \qquad (7)$$

If these grains are spherical, then their projected area along any line of sight will be

$$A_{g\perp} = A_g/4 \gtrsim 10^{31} \text{ cm}^2 \qquad (8)$$

which must be compared to the maximum projected area of the blue jet segment. Assuming that the age of the segment, and the time taken to eject it, is small compared to the precession period then the length L_j of the segment is given by

$$L_j = v_j \tau = 2.7 \times 10^{15} \text{ cm} \qquad (9)$$

Denoting the radius of the segment by R_j we therefore have

$$A_{j\perp} = L_j R_j = 2.7 \times 10^{15} R_j \text{ cm}^2 \qquad (10)$$

where $A_{j\perp}$ is the projected area of the jet. Consequently, either $R_j \gtrsim 3.6 \times 10^{15}$ cm $= 1.4\ L_j$ or $A_{g\perp} > A_{j\perp}$. In the former case the jet would be wider than it is long, and hardly able to exhibit jet behaviour such as narrow gamma ray lines. In the other case, the grains become mutually obscuring and (7) must be replaced, for an optically thick jet, by (for total jet area A_j)

$$T_g = (\dot{W}_{cg}/\sigma A_j)^{\frac{1}{4}} = (\dot{W}_{cg}/(\sigma \times 2\pi R_j L_j))^{\frac{1}{4}}$$

$$\cong 3000\ (L_j/R_j)^{\frac{1}{4}} \text{ K} \qquad (11)$$

For $R_j/L_j \lesssim 0.1$, equation (11) implies $T_g \cong 5300$ K, well above the ablation temperature of even the most stubborn grains.

Thus far, we have considered only $\dot{W}_{cg}$ and not $\dot{W}_{cp}$. Since the geometry already demands that the jet be optically thick, addition of $\dot{W}_{cp}$ to the energy input simply demands still higher steady temperatures than (11) by a factor $(1+\dot{W}_{cp}/\dot{W}_{cg})^{\frac{1}{4}} = (1+2.6M_p/M_g)^{\frac{1}{4}}$, using (5) and (6) which would give $T \cong 7300$ K for $M_p = M_g$ and $T \cong 21{,}000$ K for $M_p/M_g = 100$.

It is also instructive to consider the interaction of jet grains with ambient protons in terms of the mean energy E deposited per second per atom of mass m_a in each grain over the interval, namely

$$\Delta E = \frac{\dot{W}_{cg}}{\dot{M}_g \tau} m_a = \frac{m_a}{m_p} \times \frac{1}{(\dot{M}_g/(10^{-4} M_\odot yr^{-1}} \times 100 \text{ eV s}^{-1} \qquad (12)$$

With $m_a/m_p \cong 20$ for grain atoms and $\dot{M}_g < 10^{-4} M_\odot \text{ yr}^{-1}$ (in grains alone) each grain atom would thus have 2 keV s^{-1} delivered to it by 30 MeV protons, resulting in rapid direct ablation unless rapid recondensation can occur.

We, therefore, do not expect grains to survive the large collisional heating they must experience to permit non-thermal production of the reported gamma rays. The only way out of the dilemma would be some non-radiative mode of grain cooling (Helfer and Savedoff 1986 point out that there is a lack of wavelengths in which to hide a radiative loss as large as $\dot{W}_c$). The only such mode we can think of is conversion of thermal energy into mechanical energy of lateral jet expansion - i.e. work done by the jet gas pressure. (We assume that the grains could also be so cooled by being radiatively coupled to the gas in the optically thick jet). The cooling rate by expansion is $\dot{W}_{exp} \lesssim (\frac{1}{2} n_{pj} m_p v_\perp^3)(2\pi R_j L_j)$ where $v_\perp$ is the tranverse proton speed. This is best compared with the jet kinetic luminosity $\dot{W}_K = (\frac{1}{2} n_{pj} m_p v_j^3)(\pi R_j^2)$ so that $\dot{W}_{exp}/\dot{W}_K \lesssim (v_\perp/v_j)^3 \times (L_j/R_j) \lesssim (R_j/L_j)^2$ if the jet angle is determined by free expansion. Since $R_j \lesssim 0.1\ L_j$ the cooling rate by expansion is, therefore, $<< \dot{W}_K$ which we already saw was $\lesssim \dot{W}_{cg}$ and we conclude that this process cannot save the grains.

6.4 Restrictions on the volume of the interaction region

6.4.1 Penetration of the jet by ambient protons

We have assumed so far, following RKL, that the whole mass of the

flaring jet volume (emitted over τ = 4 days) can interact with interstellar protons, but this is not in general the case. A proton of v = 0.26c is brought to rest collisionally after traversing a hydrogen column density along its path of $N_{\parallel} = 10^{23}$ cm^{-2} ($\cong$ 0.17 gm cm^{-2}) - eg. Emslie (1978). Assuming that the volume swept by the precessing jets can constantly refill with gas (cf. discussion by Helfer and Savedoff 1986) then protons will enter the jet 'slug' across both its front and side areas. Those protons entering from the front will penetrate along the jet to longitudinal column density $N_{\parallel}$ while those entering from the sides will penetrate a column density in that direction $N_{\perp} = (v_{\perp}/v_j)N_{\parallel}$ where $v_{\perp}$ is the transverse jet expansion speed, (assuming that $v_{\perp} >> v_t$ where v_t is the interstellar proton thermal speed). Thus the masses of interacting jet material on the side and end surfaces will be in the ratio

$$\frac{M_{\perp}}{M_{\parallel}} = \frac{2\pi R_j L_j N_{\perp}}{\pi R_j^2 N_{\parallel}} = \frac{2L_j}{R} \frac{v_{\perp}}{v_j} \lesssim 2 \qquad (13)$$

where equality holds when R_j is determined by free expansion. Consequently the maximum interacting mass of jet gas is

$$Mp_{max} \cong 3\pi R_j^2 N_{\parallel} m_p \cong 3 \times 10^{26} R_j^2 \text{ (AU) gm} \qquad (14)$$

From (4) and (14) it then follows that to achieve the reported 1.369 MeV line luminosity requires a minimum interstellar density

$$n_{pi} \geq \frac{M_p}{M_g} \times \frac{6 \times 10^9 \text{ cm}^{-3}}{R_j^2 \text{ (AU)}} \qquad (15)$$

which is unbelievably high for any plausible M_p/M_g. Physically this simply means that the gamma ray production rate is at its collisional thick target limit (cf. Brown, 1971) and can only be increased by increased incident flux - i.e. increased n_{pi}. Any increase in the slug mass and density

(i.e. in M_p) beyond (14) for prescribed R_j will simply increase the jet kinetic luminosity without increase in gamma ray production.

6.4.2 Doppler limit on length of the gamma ray slug

We have already noted that the jet cannot be significantly decelerated by Coulomb collisions if the gamma ray lines are not to be broadened; the near constancy of the jet speed is quite well documented (Margon, 1984; Schilizzi, Romney and Spencer, 1984; Vermeulen et al., 1987). On the other hand, if the slug of gamma ray emitting material was ejected, at constant speed, over too long a period of time, the lines would be Doppler broadened by precessional change of the jet direction. The best-fit ephemeris to the moving optical lines of SS433 gives

$$1 + z = \gamma(\beta \sin i \sin\theta \cos\psi + \beta \cos i \cos\theta + 1) \qquad (16)$$

(Margon 1984). By differentiating this with respect to time, we deduce that the redshift spread Δz between the two ends of the slug is, to second order,

$$\Delta z = -\gamma\beta \sin i \sin\theta(\tau \sin\psi + \tau^2 \cos\psi)$$
$$\tau = \omega\Delta t \qquad (17)$$

where $2\pi/\omega$ is the precessional period and Δt is the time elapsed between the ejection of the head and the tail of the slug. At the epoch of the gamma ray observations, $\cos\psi = 0.136$, so that a slug length corresponding to a time interval of four days implies $|\Delta z| = 0.0137$, which means a line width of $\Delta E = 20$ keV at 1.4 MeV, and 84 keV at 6.1 MeV. The line widths reported by Lamb et al., (1983) and used by RKL are all below 10 keV, which is indeed the main basis on which RKL dismiss alternative models for the gamma rays of SS433. To keep the RKL model within the limits imposed by this 'geometric Doppler width', one must require that ejection of the gamma ray emitting slug should last less than about half a day. To achieve the thick

target value (14) of interacting mass in 0.5 days requires

$$\dot{M}_p = (10^{-4}\ M_\odot\ yr^{-1}) \times R_j^2(AU)$$

6.5 Inconsistency with data at other wavelengths

6.5.1 Infrared flux

It is a central consequence of the RKL model that the SS433 jet grains should radiate an infrared luminosity $L_{IR} = 2\times10^{41}$ erg s^{-1}, at a temperature below the survival value (11). If we take the value $T_g = 2750$ K used by RKL, then the infrared flux at 10^{14} Hz should be about 5×10^{26} erg s^{-1} Hz^{-1}. On the other hand, the observed flux density at this frequency is $10^{-23.4}$ erg cm^{-2} s^{-1} Hz^{-1} (McAlary and McLaren 1980), which, at a distance of 5.5 kpc, means an infrared flux of about 10^{22} erg s^{-1} Hz^{-1}: this is fully 50,000 times smaller than the RKL model predicts.

6.5.2 The optical polarisation of SS433

The jet grains required by RKL should scatter optical radiation from the central source, producing a net polarisation because of the non-spherical geometry, which will vary with time as the system rotates (Brown et al., 1978, Simmons, 1982). The amplitude of the variation indicates the mass of scattering material present. As has been shown in Chapters 3 and 4, the general treatment is fairly complicated, but a rough estimate can be obtained by using the Rayleigh scattering approximation, which should be applicable since the grain size we derived above is of the order of the optical wavelengths. In that case, the scattering cross section is about r_g^2 and the polarisation of light singly scattered at right angles is 100%.

Then for a rectilinear jet (cf. Brown and McLean, 1977) the nett polarisation is roughly $P \cong r_g^2 \Gamma / 4\pi r_o$, where Γ is the number of grains per unit jet length and r_o is the effective minimum distance from the light source. Now

$$\Gamma = \dot{M}_g / (4\pi r_g^3 \rho_g v_j) \qquad (18)$$

so that with $\rho_g = 3$ gm cm^{-3}, $r_g(\text{cm}) = 10^{-4} r_{-4}$, we predict $P \cong 50\% \times \dot{M}_g / (10^{-4} M_\odot \text{ yr}^{-1}) / (r_{-4} r_o \text{ (AU)})$ where r_o will be of the order of the size of the primary light source which is certainly < 1AU. Thus the RKL model predicts a grain scattering polarisation much larger than observed (McLean and Tapia, 1980) unless either the grains are much larger than 10^{-4} cm or multiple scattering reduces the polarisation below the optically thin result obtained here. This latter option is equivalent to our previous conclusion on different grounds that the jet is optically thick in grains, which we already saw is incompatible with their survival by radiative cooling.

6.6 Conclusions

In summary, while the RKL model for producing narrow gamma ray lines is in itself quite ingenious, and may have applications elsewhere, closer examination of the physical and observational constraints in the jet system of SS433 shows that the model is untenable as an explanation for the gamma ray lines apparently observed in that source.

Besides the unreasonable demands the model makes on jet energy and mass output and on the interstellar density, the most important among these constraints is that the required size of the radiating area is incompatible

with the narrowness of the lines. This constraint is quite generic as it applies not only to gamma ray emission, but should also provide constraints (albeit possibly weaker) on models for line emission in any wavelength. The point is, that in order to generate the observed intensity, the emitting slugs must be big; on the other hand, the 'geometrical Doppler broadening' requires that the slugs be small, or else the line of sight velocity difference between their head and tail is larger than the observed line width.

Next, there is the fact that the radiating area that is required to keep the grains below 3000 K or so, while they are subject to the Coulomb heating that accompanies the gamma ray producing collisions, is inconsistent with the jet geomtry and with the observed infrared flux. Finally, the RKL jet grain parameters should result in an optical polarisation, due to scattering, that is far larger than observed.

As RKL point out, other models, such as the thermonuclear mechanism proposed by Boyd et al. (1984) are also irreconcilable with the narrow line widths. We have no viable alternative to offer either, but believe to have shown that the possibility of having grains present in the jets does not provide the answer. Indeed the obstacles to any model seem so severe that there seems little other recourse than to take refuge in the uncertainty of the observations.

CHAPTER 7

CONCLUSIONS AND FUTURE WORK

In this thesis, we have shown that the optically thin treatment of Thomson (or Rayleigh) scattering polarisation of light from a point source can be modified, in principle, to apply to arbitrary source shapes. In general, this requires a double integral of scattering expressions over the surface of the source, performed at each scattering point. Only in simple cases, such as that of a uniform sphere, does this integral have an analytic solution, and in these cases the effect of the extended source is a geometrical 'depolarisation' factor which depends only on the angular size of the source as seen from the scattering point and not on the local inclination. This factor, even when analytic, is not always practical (see treatment of limb darkened spherical star, Brown, Carlaw and Cassinelli, 1988). Allowing for the effect of the extended source reduces the unreasonably high contribution to the polarisation of those electrons close to the source, and it removes the singularity as the distance of the electrons from the source tends to zero that is present in the unmodified point source expressions.

The polarisation data of SS433 clearly shows a dependence on the precession period and its first harmonic. The scatter on the points, when folded on this period, is clearly greater than the estimated measurement errors, indicating that effects other than precession are present in the polarimetric data. As a first approximation, however, a simple geometrical model time dependent only on the precession period and its first harmonic was used to make a preliminary fit to the available data. The optimisation procedure developed on the basis of this model yields the best fit solution and a confidence region in the inclination,

precession cone angle plane. The results of the optimisation are in agreement, within the confidence region, with the values of the inclination and precession cone angle derived from other observations, such as the radio observations and the optical doppler shifted emission lines. However, statistically the best fit has a low significance and the confidence region is large so that the parameters are not well determined.

Extending the best fit model found from the optimisation by the addition of a simple dependence on the first harmonic of the orbital period allowed some investigation of the other possible effects present in the data. The results of this investigation indicate that the first harmonic of the orbital period is present in the data but the cause, or causes, of it is uncertain.

To investigate the data further, the optimisation procedure based on the simple model could be redone omitting those data points taken during the orbital eclipses. In principle, this should allow for a more accurate determination of the precession parameters. However, the length of the eclipses is uncertain and a larger data set may be required to determine the parameters with increased accuracy because of the noise on the data. If all the points with orbital phase within 0.05 of phase 0 and 0.5 are omitted then the number of Q,U points is reduced from 109 to 86 and if the length of the eclipses is doubled then the number is further reduced to 69. Access to an extended data set would be valuable.

A theoretical model for SS433 which includes the effects of eclipses and occultation should be developed and fitted to the data. Although the best fit and confidence intervals for the parameters may not be easily determined from such a model, investigation in a localised region about

the best fit simple model already found here may well provide useful information. Estimates for some of the parameters such as the disc radius, obtained from other observations could be used to reduce the number of free parameters.

To investigate the effects of multiple scattering, the assumption of optically thin scattering should be relaxed and a full radiative transfer treatment applied to the system. The circular polarisation of the system should also be investigated since this could provide useful constraints on the effects of multiple scattering and on the contribution to the polarisation from processes other than Thomson scattering such as synchrotron polarisation.

The presence of dust grains in the jets of SS433 as proposed by Ramaty et al., (1984), would have had serious implications for the modelling of the polarisation (cf. Chapter 6). However, we have shown that the dust grain model for the gamma-ray lines is untenable, given the physical and observational constraints on the system. Indeed, further observations are required to test whether SS433 is really the source of such narrow lines and to clearly identify the transitions responsible.

A similar treatment to that developed here could be applied to other binary systems where mass loss/transfer is thought to take place and, in particular, where there may be luminous disks, for example Cyg X-1, Her X-1, where there may be a precessing disk and HD191765 which may be a binary system comprising a WR star and a precessing neutron star.

Although the explanation of dust grains in the jets of SS433 for the narrow gamma-ray lines is not tenable, dust grains may be present in other environments such as the atmosphere of cool stars and young

stellar, or AGN, jets. As a result, a more complete tretment of the polarisation due to grain scattering than that in Chapter 6 should be done for various scattering geometries. This would require the extension of the Thomson scattering treatment to Mie scattering. Further, jets emitting gamma-ray lines, according to the Ramaty et al., (1984) dust grain model, may be possible if some of the conditions applicable to SS433 are relaxed or removed. For example, in SS433 the length of the emitting region is restricted by the requirement that the precessional doppler broadening be less than the observed line width. Also the narrow opening angle ($<5^{o}$) and good collimation of the jets restrict the width of the emitting region. As a result, the cross-section of the emitting region is such that it must be optically thick in grains if gamma-ray lines of the observed luminosity are to be produced. This in turn implies an equilibrium grain temperature far above any plausible sublimation point. A jet with a very long precession period, or that does not precess at all, with a large opening angle, compared to that of the jets in SS433, could allow an emitting region of sufficient volume to allow the grains to radiate the waste energy deposited in them at a temperature low enough for them to survive. Such a jet-grain source of narrow gamma-ray lines would necessarily be an IR source. So far the only objects other than SS433 which may have relativistic precessing jets are those AGN's which have 'twisted' radio jets. Further investigation into the conditions necessary to the emission of detectable, narrow gamma-ray lines is required.

REFERENCES

Abell, G.O., Margon, B.: 1979, Nature 279, 701.

Allen, D.A.: 1979, Nature 281, 284.

Anderson, S.F., Margon, B., Grandi, S.A.: 1983a, Astrophys. J. 269, 605.

Anderson, S.F., Margon, B., Grandi, S.A.: 1983b, Astrophys. J. 273, 697.

Aspin, C.: 1981, Ph.D. Thesis.

Band, D.L., Grindlay, J.E.: 1984, Astrophys, J. 285, 702.

Bedogni, R., Braccesi, A., Marano, B., Messina, A.: 1980, Astron. Astrophys. 84, L4.

Begelman, M.C., Rees, M.J.: 1984, M.N.R.A.S. 206, 209.

Begelman, M.C., Sarazin, C.L., Hatchett, S.P., McKee, C.F., Arons, J.: 1980, Astrophys. J. 238, 722.

Bodo, G., Ferrari, A., Massaglia, S., Tsinganos, K.: 1985, Astron. Astrophys. 149, 246.

Bonsignori-Facondi, S.R., Braccesi, A.: 1986, Astron. Astrophys. 163, 77

Bonsignori-Facondi, S.R., Padrielli, L., Montebugnoli, S., Barbieri, R.: 1986, Astron. Astrophys. 166, 157.

Boyd, R.N., Wiescher, M., Newson, G.H., Collins, G.W.II: 1984, Astrophys. J. 276, L6.

Brown, J.C.: 1971, Solar Physics 18, 489.

Brown, J.C., Carlaw, V.C., Cassinelli, J.P.: 1988 in preparation

Brown, J.C., Henricks, H.F.: 1987, Astron. Astrophys. 182, 107.

Brown, J.C., McLean, I.S.: 1977, Astron. Astrophys. 57, 141.

Brown, J.C., McLean, I.S., Emslie, A.G.: 1978, Astron. Astrophys., 68, 415.

Cassinelli, J.P., Nordsieck, K.H., Murison, M.A.: 1987, Astrophys. J. 317, 290.

Catchpole, R.M., Glass, I.S., Carter, B.S., Roberts, G.: 1981, Nature, 291, 392.

Chandrasekhar,1960, Radiative Transfer, Dover Publications Inc., New York.

Ciatti, F., Mammano, A., Bartolini, C., Guarnieri, A., Piccioni, A., et al.,: 1981, Astron. Astrophys. 95, 177. Erratum in Astron. Astrophys. 100, 300.

Ciatti, F., Mammano, A., Vittone A.: 1981, Astron. Astrophys. 94, 251.

Clark, D.H., Green, A.J., Caswell, J.L.: 1975, Aust. J. Phys. Astrophys. Suppl. 37, 75.

Clark, D.H., Murdin, P.: 1978, Nature 276, 45.

Collins, G.W.II, Newsom, G.H.: 1986, Astrophys. J. 308, 144.

Cox, D.P., Tucker, W.H.: 1969, Astrophys. J. 157, 1157.

Crampton, D., Cowley, A.P., Hutchings, J.B.: 1980, Astrophys. J. Lett. 235, L131.

Crampton, D., Hutchings, J.B.: 1981, Astrophys. J. 251, 604.

Daniel, J.Y.: 1980, Astron. Astrophys. 87, 204.

Daniel, J.Y.: 1980, Astron. Astrophys. 86, 198.

Daniel, J.Y.: 1981, Astron. Astrophys. 94, 121.

Davidson, K., McCray, R.: 1980, Astrophys. J., 241, 1082

De Campli, W.M.: 1980, Astrophys. J. 242, 306.

Dolan, J.F.: 1984, Astron. Astrophys. 138, 1.

Efimov, Y.S., Piirola, V., Shakhovskoy, N.M.: 1984, Astron. Astrophys. 138, 62.

Eichler, D.: 1983, Astrophys. J., 272, 48.

Emslie, A.G.: 1978, Astrophys. J. 224, 241.

Fabian, A.C., Rees, M.J.: 1979, M.N.R.A.S. 187, 13p.

Falomo, R., Boksenberg, A., Tanzi, E.G., Tarenghi, M., Treves, A.: 1987, M.N.R.A.S. 224, 323.

Fejes, I.: 1986, Astron. Astrophys. 168, 69.

Forman, W., Jones, C., Cominsky, L., Julien, P., Murray, S., et al.: 1978, Astrophys. J. Suppl. 38, 357.

Geldzahler, B.J., Downes, A.J.B., Shaffer, D.B.: 1981, Astron. Astrophys. 98, 205.

Geldzahler, B.J., Pauls, T., Salter, C.J.: 1980, Astron, Astrophys.84,237

Geldzahler, B.J., Share, G.H., Kinzer, R.L., Forrest, D.J., Chupp, E.L., Rieger, E.: 1985, 19th International Conference Volume 1, 187.

Gilmore, W.S., Seaquist, E.R., Stocke, J.T., Crane, P.C.: 1981, Astron. J. 86, 864.

Gower, A.C., Gregory, P.C., Hutchings, J.B., Unruh, W.G.: 1982, Astrophys. J. 262, 478.

Gower, A.C., Hutchings, J.B.: 1982a, Astrophys. J. Lett. 253, L1

Gower, A.C., Hutchings, J.B.: 1982b, Astrophys. J. Lett., 258, L63

Gower, J.F.R., Scott, P.F., Wills, D.: 1967, Mem R.A.S. 71, 49.

Grindlay, J.E., Band, D., Seward, F., Leahy, D., Weisskopf, M.G., Marshall, F.E.: 1984, Astrophys. J. 277, 286.

Heeschen, D.S., Hammond, S.E.: 1980, Astrophys. J. Lett. 235, L129

Helfer, H.L., Savedoff, M.P.: 1984, Astrophys. J. 283, L49

Helfer, H.L., Savedoff, M.P.: 1986, Astrophys. J. 304, 581

Hjellming, R.M., Johnstone, K.J.: 1981a, Nature 290, 100

Hjellming, R.M., Johnstone, K.J.: 1981b, Astrophys. J. Lett. 246, L141

Hjellming, R.M., Johnstone, K.J.: 1982, In Extragalactic Radio Sources, I.A.U. Symp. 97, ed. D.S. Heeschen, C.M. Wade, p197,Dordrecht: Reidel.

Hut, P., van den Heuvel, E.P.J.: 1981, Astron. Astrophys. 94, 327.

Johnston, K.J., Santini, N.J., Spencer, J.H., Klepcznski, G.H., Kaplan, G.H., et al.: 1981, Astron. J. 86, 1377.

Johnstone, K.J., Geldzahler, B.J., Spencer, J.H., Waltman, E.B., Klepczynski, W.J., et al.: 1984, Astron. J. 89, 509.

Kaplan, G.H., Kallarakal, V.V., Harington, R.S., Johnstone, K.J., Spencer, J.H.: 1980, Astron. J. 85, 64.

Katz, J.I.: 1980, Astrophys. J. Lett., 236, L127.

Katz, J.I.: 1986, Comments Astrophys., 11, 201.

Katz, J.I., Anderson, S.F., Margon, B., Grandi, S.A.: 1982, Astrophys. J. 260, 780.

Katz, J.I., Piran, T.: 1982, Astrophys. Lett. 23, 11.

Kemp, J.C., Henson, G.D., Kraus, D.J., Carroll, L.C., Beardsley, I.S., et al.: 1986, Astrophys. J. 305, 805.

Kirshner, R.P., Chevalier, R.A.: 1980, Astrophys. J. Lett. 242, L77

Kodaira, K., Lenzen, R.: 1983, Astron. Astrophys. 126, 440.

Kodaira, K., Nakada, Y., Backman, D.E.: 1985, Astrophys. J. 296, 232.

Kundt, W.: 1985, Astron. Astrophys. 150, 276

Kundt, W.: 1987, Astrophys. Space Sci. 134, 407

Lamb, R.C.: 1984, invited talk, AAS, Las Vegas

Lamb, R.C., Ling, J.C., Mahoney, W.A., Reigler, G.R., Wheaton, W.A., Jacobsen, A.S.: 1983, Nature, 305, 37

Leibowitz, E.M.: 1984, M.N.R.A.S. 210, 37

Liebert, J., Angel, J.R.P., Hege, E.K., Martin, P.G., Blair, W.P.: 1979, Nature 279, 384.

Lingenfelter, R.E., Ramaty, R.: 1977, Astrophys. J., 211, L19

Mammano, A., Ciatti, F., Vittone, A.: 1980, Astron. Astrophys. 85, 14.

Margon, B.: 1981, Ann. N. Y. Acad. Sci., 375, 403.

Margon, B.: 1984, Ann. Revs. of Astron. Astrophys., 22, 507.

Margon, B., Anderson, S.A., Aller, L.H., Downes, R.A., Keyes, C.D.: 1984, Astrophys. J. 281, 313.

Margon, B., Ford, H.C., Katz, J.I., Kwitter, K.B., Ulrich, R.K., et al., 1979a, Astrophys. J. Lett. 230, L41.

Margon, B., Ford., H.C., Grandi, S.A., Stone, R.P.S.: 1979b, Astrophys. J. Lett. 233, L63

Margon, B., Grandi, S.A., Downes, R.A.: 1980, Astrophys. J. 241, 306

Marshall, F.E., Swank, J.H., Boldt, E.A., Holt, S.S., Serlemitsos, P.J.: 1979, Astrophys. J. Lett. 230, L145.

Martin, P.G., Rees, M.J.: 1979, M.N.R.A.S. 189, 19p

Matese, J.J., Whitmire, D.P.: 1982, Astron. Astrophys. 106, L9

Matsuoka, M., Takano, S., Makishima, K.: 1986, M.N.R.A.S. 222, 605

Mazeh, T., Kemp, J.C., Leibowitz, E.M., Meningher, H., Mendelson, H.: 1987, Astrophys. J. 317, 824.

McAlary, C.W., McLaren, R.A.: 1980, Astrophys. J., 240, 853.

McClintock, J.E., Canizares, C.R., Tartar, C.B.: 1975, Astrophys. J. 198, 641.

McLean, I.S., Tapia, S.: 1980, Nature, 287, 703.

McLean, I.S., Tapia, S.: 1981, Vistas Astron., 25, 45.

Milgrom, M.: 1978, Astron. Astrophys. 65, L1

Milgrom, M.: 1979, Astron. Astrophys. 76, L3

Milgrom, M.: 1981, Vistas Astron.,25, 141

Milgrom, M., Anderson, S.F., Margon, B.: 1982, Astrophys. J., 256, 222

Murdin, P., Clark, D.H., Martin, P.G.: 1980, M.N.R.A.S. 193, 135

Murdin, P., Clark, D.H.: 1980, M.N.R.A.S. 190, 65p

Neizvestnyi, S.I., Pustil'nik, S.A., Efremov, V.G.: 1980, Sov.Astron. Lett. 6, 368.

Papaloizu, J.C.B., Pringle, J.E.: 1982, M.N.R.A.S. 200, 49

Papaloizu, J.C.B., Pringle, J.E.: 1984, M.N.R.A.S. 208, 72

Pekarevich, M., Piran, T., Shaham, J.: 1984, Astrophys. J., 283, 295

Ramaty, R., Kozlovsky, B., Lingenfelter, R.E.: 1984, Astrophys. J., 283, L13

Rees, M.J.: 1982, In Extragalactic Radio Sources, IAU Symp. 97, ed. D.S. Heeschen, C.M. Wade, p211, Dordrecht: Reidel.

Ricketts, M.J., Hall, R., Page, C.G., Pounds, K.A., Sims, M.R.: 1981, Vistas. Astron. 25, 71

Rudi, R.J.: 1979, M.N.R.A.S. 186, 473.

Rudi, R.J., Kemp, J.C.: 1978, Astrophys. J. 221, 200

Ryle, M., Caswell, J.L., Hine, G., Shakeshaft, J.: 1978, Nature 276, 571

Sarazin, C.L., Begelman, M.C., Hatchett, S.P.: 1980, Astrophys. J. Lett. 238, L129

Schilizzi, R.T., Romney, J.D., Spencer, R.E.: 1984, I.A.U. Symposium 110, 289, (R. Fanti, K. Kellerman and G. Setti, Eds.) Reidel, Dordrecht.

Seaquist, E.R.: 1981, Vistas, Astron. 25, 79.

Seaquist, E.R., Garrison, R.F., Gregory, P.C., Taylor, A.R., Crane, P.C.: 1979, Astron. J. 84, 1037.

Seaquist, E.R., Gilmore, W.S., Johnstone, K.J., Grindlay, J.E.: 1982, Astrophys. J. 260, 220

Seaquist, E.R., Gilmore, W., Nelson, G.J., Payton, W.J., Slee, O.B.: 1980, Astrophys. J. 241, L77

Seward, F.D., Page, C.G., Turner, M.J.L., Pounds, K.A.: 1976, M.N.R.A.S. 175, 39p

Seward, F., Grindlay, J., Seaquist, E., Gilmore, W.: 1980. Nature 287, 806

Shapiro, P.R., Milgrom, M., Rees, M.J.: 1986, Astrophys. J. Suppl., 60, 393

Sikora, M., Wilson, D.B.: 1981, M.N.R.A.S., 197, 529

Simmons, J.F.L.: 1982, M.N.R.A.S., 200, 91

Simmons, J.F.L.: 1983, M.N.R.A.S. 205, 153.

Simmons, J.F.L., Aspin, C., Brown, J.C.: 1980, Astron. Astrophys. 91, 97.

Spencer, R.E.: 1979, Nature, 282, 483.

Stephenson, C.B., Sanduleak, N.: 1977, Astrophys. J. Suppl. 33, 459

Stewart et al.,: 1986, referenced in Kemp et al., 1986.

St-Louis, N., Drissen, L., Moffat, A.F.J., Bastien, P., Tapia, S.: 1987, Astrophys. J. 322, 870.

Thompson, R.I., Rieke, G.H., Tokunaga, A.T., Lebofsky, M.J.: 1979, Astrophys. J. Lett. 234, L135

van den Heuvel, E.P.J., Ostriker, J.P., Petterson, J.A., : 1980, Astron. Astrophys. 81, L7

van Gorkom, J.H., Goss, W.M., Seaquist, E.R., Gilmore, W.S.: 1982, M.N.R.A.S. 198, 757

Vermeulen, R.T., Schilizzi, R.T., Icke, V., Fejes, I., Spencer, R.E.: 1987, Nature, submitted.

Wagner, R.M.: 1986, Astrophys. J. 308, 152.

Watson, M.G., Stewart, G.C., Brinkmann, W., King, A.R.: 1986, M.N.R.A.S. 222, 261

Watson, M.G., Willingdale, R., Grindlay, J.E., Seward, F.D.: 1983 Astrophys. J. 273, 688

Wheaton, W.A., Ling, J.C., Mahoney, W.A., Jacobson, A.S.: 1985, 19th International Cosmic Ray Conference, Volume 1, 183

Whitmire, D.P., Matese, J.J.: 1980, M.N.R.A.S. 193, 707